

DISSERTATION

THE INNOVATIVE APPLICATION OF RANDOM PACKING MATERIAL TO ENHANCE  
THE HYDRAULIC DISINFECTION EFFICIENCY OF SMALL SCALE WATER SYSTEMS

Submitted by

Jessica L. Baker

Department of Civil and Environmental Engineering

In partial fulfillment of the requirements

For the Degree of Doctorate of Philosophy

Colorado State University

Fort Collins, Colorado

Fall 2021

Doctoral Committee:

Advisor: Subhas Karan Venayagamoorthy

Co-Advisor: Susan K. De Long

Jeffrey D. Niemann

Stephen J. Leisz

Copyright by Jessica Baker 2021

All Rights Reserved

## ABSTRACT

### THE INNOVATIVE APPLICATION OF RANDOM PACKING MATERIAL TO ENHANCE THE HYDRAULIC DISINFECTION EFFICIENCY OF SMALL SCALE WATER SYSTEMS

In a world where the quality of our water supplies is declining and our infrastructure is deteriorating, let alone the lack of available water in arid regions, the treatment of drinking water is becoming ever more challenging – especially for small scale systems that lack technical and financial support. The innovative application of random packing material (RPM) has been proposed as a possible tool to aid small water treatment systems (SWTSs) improve their disinfection contact systems in order to meet the Safe Drinking Water Act (SDWA) standards and provide the communities they serve with safe drinking water. While it has been demonstrated at the laboratory-scale that RPM can significantly improve the hydraulic disinfection efficiency of a contact basin in terms of baffling factor (*BF*) there was a lack of fundamental understanding of why RPM is so effective. Conceptually, the RPM slows and spreads the jet flow from a sharp inlet. Yet the mechanics of a jet flow through a highly porous material such as RPM is not well understood. Insight into the dynamics of such a flow is important in order to be able to use RPM in a manner that maximizes the benefits and minimizes the (unintended) drawbacks.

The main aim of this dissertation is to use laboratory-scale experiments to study the mechanics of a turbulent jet flow from a long pipe through RPM and the impact on the hydraulic disinfection efficiency and final water quality for a disinfection contactor. There are three main objectives in this work: (1) To gain fundamental insights regarding turbulent jet flow through a

highly porous media (such as RPM); (2) To address practical concerns for the application of the use of RPM in disinfection contactors; and (3) To provide guidance in terms of best practice for the innovative use of RPM to enhance hydraulic disinfection efficiency in SWTSSs.

The first part of this dissertation focuses on the resulting flow fields of a turbulent jet flow (5-20 gpm) through a wall of RPM of various thicknesses ( $L$ ). An experiment was conducted in a flume using a Particle Image Velocimetry (PIV) system to map the flow fields downstream of the jet up to  $x/d_j \approx 30$  (where  $d_j$  is the diameter of the jet, i.e. inlet pipe). Once the PIV data were verified using a Laser-Doppler Anemometry (LDA) system and validated for a jet into an ambient (provided as a baseline), the velocity fields of the jet flow downstream of the walls of RPM were analyzed. A second order relationship was observed between the thickness of RPM and the spread of the flow. It was also observed that the jet velocities decay exponentially through RPM. With respect to flow rate, the spreading rate increased slightly, but there was a slight decrease in the decay of the jet as the flow rate increased. While the maximum velocities were reduced by over 90% after  $L \approx 5d_j$ , it was only after  $L \approx 15d_j$  that the flow downstream of the RPM was nearly uniform. Furthermore, the coefficients of drag showed a non-monotonic relationship with respect to the particle Reynolds number ( $Re_{dp}$ ) that followed the well-established trend of a uniform flow around an infinitely long cylinder. This relationship provides valuable insight into the different regimes of the highly complex flow within and/or downstream of a highly porous material.

Next, the potential improvement in the hydraulic disinfection efficiency and the possible energy loss as a result of the presence of random packing material in a laboratory-scale chlorine contactor were investigated. Tracer tests were conducted on a 55-gal drum tank filled with RPM in varying amounts in different configurations to measure the efficiency of each setup in terms of

baffling factor. The bulk pressure drop was measured to determine the energy loss for each configuration. The results of this study show that securing RPM near the inlet, in any amount, improves the *BF* by 300% to more than 900%. The amount of RPM begins to have an impact at or above an inlet jet Reynolds number of 27,700. Also, changes in head loss due to the presence of RPM (in any amount, configuration, and/or flow rate) were generally considered to be negligible.

Finally, a concern surrounding the potential for excessive biofilm growth is addressed through a long-term study. The inflow, outflow, and RPM were monitored for heterotrophic bacteria (via heterotrophic plate counts) and *Pseudomonas aeruginosa* as indicators of bacteriological water quality and the presence of biofilm. The results of this study show that there was no substantial biofilm growth in a lab-scale chlorine contactor and no substantial increase in bacterial counts for the bulk outflow over a 10-week period. Thus, the potential for excessive biofilm growth should not be considered a barrier concerning the use of RPM to improve the hydraulic disinfection efficiency of chlorine contactors in small drinking water treatment systems.

Overall, this dissertation work aims to contribute a foundational understanding of turbulent jet flow through a highly porous material such as RPM as well as address some practical concerns for the innovative application of RPM to improve the hydraulic disinfection efficiency. From the results of the studies conducted, best practice guidelines have been developed to maximize the potential benefit of using RPM in disinfection contactors. Ultimately, the hope of this work is to promote the use of RPM to help SWTSs that are struggling to meet SDWA standards and to provide the communities they serve with safe drinking water.

## ACKNOWLEDGEMENTS

I am incredibly grateful for my advisor, Dr. Subhas Karan Venayagamoorthy, who has not only been a good academic advisor but a good mentor holistically. It has been an honor to work with someone who is brilliant and passionate about their research as well as investing in the next generation of engineers. While he holds a high standard he does so with incredible grace, encouragement, and a greater perspective of my purpose for pursuing a PhD. While the research in this dissertation was not directly funded, Dr. Karan constantly advocated for me so that I could complete this work.

I want to show appreciation to my co-advisor, Dr. Susan De Long, for her support and mentorship, especially as a female engineer in academia. She also advocated for me for funding and spent time giving me constructive feedback and encouragement. Her attention to detail to create good science and to communicate that science well is something that I will take with me. I would also like to acknowledge Dr. Jeffrey Niemann and Dr. Stephen Leisz for being on my committee and for the examples they have each set for using their knowledge and expertise to serve communities around the world.

Finally, I would like to express thanks to my community of friends and family (near and far). My fellow lab-mates in the EFML (Dapo Aseperi, Matthew Klema, Joe Pugh, Joey Sinclair, and Harshit) – thank you for your camaraderie and all the help you provided me to complete this work. To the good friendships forged through my graduate school experience at CSU (Cherie Nelson and Jenny Campfield) – thank you support, encouragement, and for being a listening ear. And thank you to Christ and my siblings in Christ who believed in and supported me in all areas of life (including this work) - reminding me to not lose sight of the grander story of redemption.

## TABLE OF CONTENTS

ABSTRACT .....	ii
ACKNOWLEDGEMENTS .....	v
LIST OF TABLES .....	ix
LIST OF FIGURES.....	x
LIST OF ACRONYMS.....	xviii
1 INTRODUCTION .....	1
1.1 Motivation .....	1
1.2 Objectives.....	4
1.3 Dissertation Layout .....	5
1.4 Summary .....	6
2 LITERATURE REVIEW .....	8
2.1 Random Packing Material.....	8
2.1.1 Design .....	8
2.1.2 Current Uses and Applications .....	11
2.2 Relevant Turbulent Flows .....	14
2.2.1 Turbulent Round Jet into an Ambient.....	15
2.2.2 Homogenous Shear Flow .....	19
2.3 Flow Interacting with Obstacles.....	21
2.3.1 Flow around an Infinitely Long Cylinder .....	22
2.3.2 Flow through Packed Beds .....	29
2.4 Hydraulic Disinfection Efficiency .....	38
2.4.1 $CT$ .....	38
2.4.2 Baffling Factor .....	40
2.4.3 Use of RPM to Improve $BF$ .....	41
2.5 Biofilm .....	48
2.5.1 Biofilms in Water Treatment Systems .....	49
2.6 Summary .....	51
3 EXPERIMENTAL METHODS .....	53
3.1 Flow Velocity Measurements.....	53
3.1.1 Introduction.....	53

3.1.2	Laser-Doppler Anemometry .....	54
3.1.3	Particle Image Velocimetry .....	61
3.2	Baffling Factor Measurements .....	69
3.2.1	Introduction.....	69
3.2.2	Tracer Tests.....	69
3.3	Bulk Head Loss Measurements.....	71
3.3.1	Introduction.....	71
3.3.2	Digital Manometers .....	71
3.4	Bacterial Plate Counts .....	72
3.4.1	Introduction.....	72
3.4.2	Bacterial Counts.....	72
3.4.3	Membrane Filtration .....	73
3.5	Summary .....	73
4	TURBULENT ROUND JET FLOW FROM A PIPE THROUGH RPM.....	74
4.1	Introduction .....	74
4.2	Materials and Methods.....	75
4.2.1	Experimental configuration .....	75
4.2.2	Data Collection .....	83
4.2.3	Verification using LDA .....	92
4.3	Results & Discussion .....	94
4.3.1	Turbulent Round Jet into an Ambient.....	94
4.3.2	Turbulent Round Jet Obstructed by RPM.....	110
4.4	Conclusions .....	137
5	EFFICIENCY GAIN AND ENERGY LOSS .....	139
5.1	Introduction .....	139
5.2	Materials and Methods.....	143
5.2.1	Experimental configuration .....	143
5.2.2	Data analysis.....	147
5.3	Results & Discussion .....	148
5.3.1	Efficiency.....	148
5.3.2	Configuration .....	153
5.3.3	Energy Loss .....	157

5.4	Conclusions .....	160
6	POTENTIAL BIOFILM GROWTH .....	162
6.1	Introduction .....	162
6.2	Materials and Methods .....	165
6.2.1	Experimental configuration .....	165
6.2.2	Sample collection.....	166
6.2.3	Removal of biofilm cells from RPM .....	167
6.2.4	Sample processing .....	168
6.2.5	Data analysis .....	169
6.3	Results & Discussion .....	169
6.3.1	HPC results .....	169
6.3.2	Pseudomonas results .....	170
6.3.3	Inactivation results .....	171
6.3.4	Visual results.....	173
6.3.5	Statistical analysis results .....	174
6.4	Conclusions .....	176
7	SUMMARY & CONCLUSIONS .....	178
7.1	Summary of Investigation .....	178
7.2	Conclusions and Key Findings.....	179
7.3	Suggestions for Future Research.....	183
	REFERENCES .....	186
	APPENDIX A.....	A1
	APPENDIX B .....	A31

## LIST OF TABLES

Table 2-1: Random Packing Material Costs (USEPA 2002).....	11
Table 2-2: “ <i>CT</i> values for Inactivation of Viruses by Free Chlorine” (USEPA 2003).....	39
Table 2-3: Baffling Factors by Qualitative Description of Contact Tank (USEPA 2003) .....	41
Table 2-4: Inlet Box Parametric Study Results (Kattnig 2014).....	45
Table 4-1: Experimental Flow Rates .....	81
Table 4-2: Estimated Jet Reynolds number ( $Re_{jet}$ ) values of SWTSS .....	81
Table 4-3: Parameters used for data collection in different PIV windows .....	84
Table 4-4: Parameters used for data collection in different PIV windows .....	92
Table 4-5: Normalized standard deviation of velocities across the vertical profiles just downstream of the RPM walls.....	120
Table 4-6: Percent reduction in maximum Reynolds stresses compared to baseline jet .....	120
Table 4-7: Percent reduction in max turbulent kinetic energy by flow rate .....	121
Table 5-1: Experimental Flow Rates .....	145
Table 5-2: Estimated Jet Reynolds number ( $Re_{jet}$ ) values of SWTSS .....	145
Table 5-3: P-value results of t-test for baffling factor and Kolmogorov-Smirnov test for RTD curves* for the BI/TO configurations. ....	153
Table 5-4: P-value results of t-test for baffling factor and Kolmogorov-Smirnov test for RTD curves* of different %RPM = 50% configurations.....	156
Table 5-5: P-value results of t-test for $\Delta P/P_{baseline}$ for all configurations.....	159
Table 6-1: Percent Inactivation and Outlier Results .....	172
Table 6-2: Median HPC counts (CFU/mL) and t-test results <sup>a</sup> .....	175
Table 6-3: Median PIA counts (CFU/mL) and t-test results <sup>a</sup> .....	176

## LIST OF FIGURES

Figure 1-1: Number of health-based violations, 1982–2015, by contaminant type.....	1
Figure 1-2: Total violations per water system, by housing density category and income group (Allaire et al. 2018).....	2
Figure 2-1: Photograph of a variety of RPM of different size, geometry, and material .....	9
Figure 2-2: Pressure drop vs. C-Factor plots for 2” RPM .....	13
Figure 2-3: Visualization of (a) a jet into an ambient and (b) isotropic turbulence downstream of a grid .....	14
Figure 2-4: A schematic of the free turbulent jet (Abdel-Rahman 2010).....	15
Figure 2-5: (a) Radial profiles of mean axial velocity in a turbulent round jet at $Re = 95500$ (Pope 2000) and (b) Mean axial velocity versus radial distance of a turbulent round jet at $Re \approx 10^5$ (Pope 2000).....	17
Figure 2-6: A sketch of a turbulence-generating grid; $d$ = bar diameter & $M$ = mesh spacing (Pope 2000).....	20
Figure 2-7: The decay of Reynolds stresses in grid turbulence; $\blacksquare = u^2/U_0^2$ , $\bullet = v^2/U_0^2 = w^2/U_0^2$ , $\blacktriangle = k/U_0^2$ (Comte-Bellot & Corrsin 1966) .....	21
Figure 2-8: Plot of base suction coefficients ( $-C_{PB}$ ) versus Reynolds numbers, as a basis for the discussion of various flow regimes of cylinder wake (Williamson 1996).....	24
Figure 2-9: Visualization of flow around a cylinder at $Re = 26$ (Van Dyke 1982).....	25
Figure 2-10: Periodic laminar regime at $Re = 140$ (Van Dyke 1982) .....	25
Figure 2-11: DNS of Mode B three-dimensional instabilities at $Re = 250$ (Thompson et al. 1996) .....	27
Figure 2-12: Generic Schematic of a packed bed .....	29
Figure 2-13: Schematics of a low $A_{ratio}$ (left) and high $A_{ratio}$ (right) (Baker 2011) .....	31
Figure 2-14: Schematic displaying the concept of tortuosity .....	32
Figure 2-15: Schematics to demonstrate ‘plug flow’ (top) versus ‘short-circuiting’ (bottom) (USEPA 2003) .....	39
Figure 2-16: RTD curve of 50-gallon cylindrical tank completely filled with RPM (Barnett 2014) .....	42

Figure 2-17: (a) RTD curves from 1” RPM in a 25-gallon tank and (b) BF for three RPM sizes with different RPM fill amounts (%) (Barnett 2014).....	43
Figure 2-18: (a) Plan View and (b) Side View of a Generalized Inlet Box System (Kattnig 2014) .....	44
Figure 2-19: (a) Plan view and (b) Side view of a generalized turn box system (Kattnig 2014) .	46
Figure 2-20: Resulting RTD Curves for (a) All Tested Systems at a Flow Rate of 20 GPM and (b) the Turn Box System at Various Flow Rates (Kattnig 2014) .....	47
Figure 2-21: A schematic of the formation of a biofilm.....	48
Figure 2-22: Relative abundances of bacterial community composition (phylum level) detected in (a) DWTP bulk water samples; (b) BAC biofilm samples. [Abbreviations: W, wet season; D, dry season; A, raw water; B: grid reaction tank effluent; C: settling pond effluent; D: BAC filter effluent; E: finished water; F0: the top GAC samples; F30: The bottom GAC samples; S: the top sand samples.] (Hou et al. 2018).....	49
Figure 2-23: Photograph of drinking water biofilm under 1000× magnification (left) and a Microcolony (right) on a stainless steel surface after 14 days of exposure to drinking water (Wingender & Flemming 2011).....	50
Figure 2-24: Scanning electron micrograph of a biofilm grown on synthetic rubber in a drinking water system (left) and under magnification (right). (Wingender & Flemming 2011) ....	50
Figure 3-1: Diagrams of (a) the measuring volume [fringe pattern] and (b) how the velocity is determined using a pair of laser beams; where $\theta$ is the angle between the two laser beams, $n_{+/-}$ are the unit normal vectors along/orthogonal to the bisector of $\theta$ , $\alpha$ is the angle between the $u$ and $n$ - vectors, and $\delta$ is the spacing between fringes (Muste et al. 2017) .	55
Figure 3-2: Schematic of an emitting & receiving probe similar to the device in the EFML (Muste et al. 2017) .....	57
Figure 3-3: Example LDA data; Top left: pre-filtered signal, Top right: pedestal (DC component), Bottom left: noise, and Bottom right: Doppler burst (AC component) (Muste et al. 2017) .....	59
Figure 3-4: Doppler frequency signal with a peak of 302.7 Hz after a frequency analysis of the signal (Muste et al. 2017).....	59
Figure 3-5: A schematic of a typical 2C-2D PIV system where CCD stands for ‘charge-coupled device’ (Adrian & Westerweel 2011).....	61

Figure 3-6: A parallel (a) and normal (b) view of the formation of a laser light sheet with the different lenses (including L1, a plano-concave spherical; L2, plano-convex spherical; and L3, plano-concave cylindrical) and the distance ( $s_{12}$ ), which controls the position of the beam waist (Muste et al. 2017) .....	62
Figure 3-7: An example of an interrogation using PIV of flow over a sand ripple with the grid subdivision and close-up of a single interrogation area (where green and red coloring indicate the displacement of the particles between image frames) (Muste et al. 2017) ...	64
Figure 3-8: A single cross correlation interrogation region pair (a) along with cross correlation functions (b & c) with the maximum marked by the dashed dotted lines in (d) (Muste et al. 2017) .....	65
Figure 3-9: A general RTD Curve from a step-tracer test; Note: time $t$ has been normalized by TDT.....	70
Figure 3-10: General Membrane Filtration Steps (reference unknown).....	73
Figure 4-1: Photographs of the acrylic wall set-up (left: front; right: back).....	76
Figure 4-2: Schematic of the $\frac{3}{4}$ " bulkhead tank fitting with dimensions in inches (Grainger®, Lake Forest, IL) .....	76
Figure 4-3: Photographs of the RPM wall apparatus.....	77
Figure 4-4: Schematic of the jet in the flume and PIV set-up with measurement plane coordinate system .....	78
Figure 4-5: Photograph of an experimental set-up of a turbulent jet encountering RPM; from top left to bottom right: $L = 100$ mm, $L = 150$ mm, $L = 200$ mm, $L = 250$ mm, $L = 300$ mm, $L = 300$ mm (uniform flow upstream). .....	80
Figure 4-6: Photographs of the baseline experimental set-ups for a turbulent jet into an ambient with centerline shown using a plug-and-thread apparatus.....	82
Figure 4-7: Photograph of LDA traverse system (left) and lasers (right) with measurement volume located at $r = 0$ and $x = 18$ mm. ....	83
Figure 4-8: RMSE and NRMSE for increasing number of images (vector fields) compared to the LDA measurements along the vertical profile at $x = 98$ mm for a jet of 20 gpm.....	86
Figure 4-9: Schematic of overall data collection time windows for different schemes of sets of images; solid coloring = recording time window & stripped coloring = image writing time (e.g. no recording possible).....	87

Figure 4-10: RMSE and NRMSE for 12 sets of 200 images averaged compared to the LDA measurements along the vertical profile at $x = 98$ mm. ....	88
Figure 4-11: RMSE and NRMSE for 6 sets of 400 images averaged compared to the LDA measurements along the vertical profile at $x = 98$ mm. ....	88
Figure 4-12: RMSE and NRMSE for 4 sets of 600 images averaged compared to the LDA measurements along the vertical profile at $x = 98$ mm. ....	89
Figure 4-13: RMSE and NRMSE for 3 sets of 800 images averaged compared to the LDA measurements along the vertical profile at $x = 98$ mm. ....	89
Figure 4-14: RMSE and NRMSE between an increasing number of images (vector fields) of PIV measurements along the vertical profile at $x = 98$ mm (TP/DF at 400 Hz & $Dt = 300\mu s$ ). .....	90
Figure 4-15: RMSE and NRMSE between increasing number of sets of 200 images averaged of PIV measurements along the vertical profile at $x = 98$ mm (TP/DF at 400 Hz & $Dt = 300\mu s$ ). ....	91
Figure 4-16: RMSE and NRMSE between an increasing number of images of PIV measurements along the vertical profile for SP/SF at 200 Hz & $Dt = 300\mu s$ . ....	91
Figure 4-17: RMSE and NRMSE between increasing number of sets of 200 images averaged of PIV measurements along the vertical profile for SP/SF at 200 Hz & $Dt = 300\mu s$ . ....	92
Figure 4-18: Average streamwise and vertical velocity profiles for consecutive images and sets of 200 images of PIV and LDA measurements along the vertical profile for TP/DF at 400 Hz & $Dt = 300\mu s$ . ....	93
Figure 4-19: Average streamwise and vertical velocity profiles for consecutive images and sets of 200 images of PIV and LDA measurements along the vertical profile for SP/SF at 800 Hz & $Dt = 300\mu s$ . ....	94
Figure 4-20: $\langle U \rangle / U_j$ velocity scalar plot for the baseline jet at 20 gpm jet. The x & y-axis are in mm and the color scale ranges from $-0.1 \leq \langle U \rangle / U_j \leq 1.10$ (blue $\rightarrow$ red). ....	96
Figure 4-21: Streamwise ( $\langle U \rangle$ ) velocity profiles at increasing distances downstream of wall. ....	97
Figure 4-22: Lateral ( $\langle V \rangle$ ) velocity profiles at increasing distances downstream of wall (horizontal axis tick marks = $\pm 0.03$ ). ....	97
Figure 4-23: Plots of streamwise velocity profiles at select $x/d_j$ locations. ....	98
Figure 4-24: Plots of similar streamwise velocity profiles at select $x/d_j$ locations. ....	99

Figure 4-25: Plots of streamwise normal stress profiles at select $x/d_j$ locations. ....	100
Figure 4-26: Plots of lateral normal stress profiles at select $x/d_j$ locations. ....	101
Figure 4-27: Plots of Reynold's shear stress profiles at select $x/d_j$ locations. ....	102
Figure 4-28: Plots of turbulent kinetic energy profiles at select $x/d_j$ locations. ....	103
Figure 4-29: Turbulence intensities along the centerline (max). ....	104
Figure 4-30: Ratio of the turbulent fluctuations along the centerline. ....	104
Figure 4-31: The variation in normalized half-width ( $r_{1/2}$ ) along the centerline (max) moving downstream. ....	105
Figure 4-32: The variation in normalized mean velocity along the centerline (max) moving downstream (normalized by the jet diameter [left] and effective radius [right]). ....	106
Figure 4-33: The variation in normalized mean velocity along the centerline (max) moving downstream (a modified effective radius): left: this study; right: Papadopoulos & Pitts study (1998). ....	106
Figure 4-34: Normalized entrainment downstream of jets. ....	108
Figure 4-35: Normalized mass flux across vertical profiles downstream of jets for a smooth contracting ( $M$ = mass flux; Mi et al, 2007) ....	109
Figure 4-36: Normalized momentum flux across vertical profiles of the jet. ....	110
Figure 4-37: $\langle U \rangle / U_j$ velocity scalar plot for the 20 gpm jet downstream of a RPM wall of thickness $L = 4.78d_j$ . The x & y-axis are in mm and the color scale ranges from $-0.020 \leq \langle U \rangle / U_j \leq 0.100$ (blue $\rightarrow$ red). ....	111
Figure 4-38: $\langle U \rangle / U_j$ velocity scalar plot for the 20 gpm jet downstream of a RPM wall of thickness $L = 7.17d_j$ . The x & y-axis are in mm and the color scale ranges from $-0.020 \leq \langle U \rangle / U_j \leq 0.100$ (blue $\rightarrow$ red). ....	112
Figure 4-39: $\langle U \rangle / U_j$ velocity scalar plot for the 20 gpm jet downstream of a RPM wall of thickness $L = 9.56d_j$ . The x & y-axis are in mm and the color scale ranges from $-0.005 \leq \langle U \rangle / U_j \leq 0.040$ (blue $\rightarrow$ red). ....	113
Figure 4-40: $\langle U \rangle / U_j$ velocity scalar plot for the 20 gpm jet downstream of a RPM wall of thickness $L = 11.94d_j$ . The x & y-axis are in mm and the color scale ranges from $-0.005 \leq \langle U \rangle / U_j \leq 0.012$ (blue $\rightarrow$ red). ....	114

Figure 4-41: $\langle U \rangle / U_j$ velocity scalar plot for the 20 gpm jet downstream of a RPM wall of thickness $L = 14.33d_j$ . The x & y-axis are in mm and the color scale ranges from $-0.0050 \leq \langle U \rangle / U_j \leq 0.0083$ (blue $\rightarrow$ red).....	115
Figure 4-42: $\langle U \rangle / U_j$ velocity scalar plot of uniform flow at 20 gpm downstream of a RPM wall of thickness $L = 14.33d_j$ . The x & y-axis are in mm and the color scale ranges from $-0.0050 \leq \langle U \rangle / U_j \leq 0.0083$ (blue $\rightarrow$ red).....	116
Figure 4-43: Normalized streamwise velocity profiles for $Q = 20$ gpm. Note the $\langle U \rangle / U_j$ scales decrease from left to right. ....	118
Figure 4-44: Normalized lateral velocity profiles for $Q = 20$ gpm. Note the $\langle V \rangle / U_j$ scales decrease from left to right. ....	119
Figure 4-45: Turbulent kinetic energy normalized by $U_j$ (the initial velocity) for $Q = 20$ gpm as the distance downstream of the RPM wall increases.....	122
Figure 4-46: Maximum Turbulence intensities for $Q = 20$ gpm.....	122
Figure 4-47: Ratio of the turbulent fluctuations along the centerline.....	124
Figure 4-48: The normalized standard deviation of the fluctuations along the vertical profiles for $Q = 20$ gpm. ....	125
Figure 4-49: The variation in normalized half-width ( $r_{1/2}$ based on $\frac{1}{2}U_{max}$ ) moving downstream. The dashed line indicates ‘fully-spread’ based on the width of the flume. ....	126
Figure 4-50: Spreading rate within RPM.....	127
Figure 4-51: The variation in normalized maximum velocity moving downstream. ....	128
Figure 4-52: Inverse Decay Rate within RPM.....	129
Figure 4-53: Normalized entrainment downstream of jets. ....	130
Figure 4-54: Normalized momentum flux across vertical profiles of the jet.....	131
Figure 4-55: Drag coefficients ( $C_D$ ) versus amount of RPM ( $L$ ; in terms of $x/d_j$ ).....	132
Figure 4-56: Drag coefficients ( $C_D$ ) versus amount of jet Reynolds number ( $Re_j$ ).....	133
Figure 4-57: The particle Reynolds number compared to the amount of RPM ( $L$ ). The dashed line [--] indicates laminar ( $Re_{dp} < 10$ ), transitional ( $10 < Re_{dp} < 300$ ) and turbulent ( $Re_{dp} > 300$ ) flow in a packed bed. The dashed-dotted line [-·] indicates the Recrit values of different wake regimes for flow around an infinitely long cylinder:	

Laminar Steady Regime ( $Re_{crit} < 49$ ), Vortex Shedding Laminar Regime ( $49 < Re_{crit} < \sim 140$ ), and the Wake Transition Regime ( $Re_{crit} > \sim 140$ ).....	134
Figure 4-58: Drag coefficients ( $C_D$ ) versus amount of particle Reynolds number ( $Re_{dp}$ ) with Plot of base suction coefficients ( $-C_{PB}$ ) versus Reynolds numbers (Williamson 1996).....	136
Figure 5-1: Schematic of experimental set-up for an energy loss versus baffling efficiency gain study: A = BI/TO, B = BI/TO Split, C = TI/BO. Arrows indicate direction of inlet/outlet flow. ....	144
Figure 5-2: Photographs of 55-gallon tank (BI/TO) filled with 2" spherical RPM; A = 25%, B = 50%, C = 75%, D = 90%, E = 100%, F = 25/25% (before RPM filled near outlet).....	146
Figure 5-3: Graph of $BF$ of varying %RPM as a function of turbulent jet Reynolds number ( $Re_{jet}$ ) for the BI/TO configurations. ....	148
Figure 5-4: Graph of $BF$ of various flow rates as a function of % RPM for the BI/TO configurations. ....	149
Figure 5-5: Average RTD curves of various %RPM for 5 gpm ( $Re_{jet} = \sim 13,800$ ) for the BI/TO configurations. ....	150
Figure 5-6: Average RTD curves of various %RPM for 10 gpm ( $Re_{jet} = \sim 27,700$ ) for the BI/TO configurations. ....	151
Figure 5-7: Average RTD curves of various %RPM for 15 gpm ( $Re_{jet} = \sim 41,500$ ) for the BI/TO configurations. ....	151
Figure 5-8: Graph of $BF$ compared with various $Re_{jet}$ 's of different configurations of %RPM = 50%; secured near inlet (50% BI/TO), split between inlet & outlet (25/25% BI/TO), and reverse direction (50% TI/BO) .....	154
Figure 5-9: Average RTD curve of different configurations of %RPM = 50% at ~5 gpm ( $Re_{jet} = \sim 13,800$ ); secured near inlet [50% (BI/TO)], split between inlet & outlet [25/25% (BI/TO)], and reverse direction [50% (TI/BO)]. ....	155
Figure 5-10: Graph of $\Delta P$ of all experimental scenarios compared to Q.....	158
Figure 5-11: Graph of $\Delta P$ (left) and normalized $\Delta P$ (right; dashed lines on indicate accuracy bounds of digital manometer) from various flow rates through varying fill amounts of RPM .....	158
Figure 6-1: Experimental Set-up Schematic .....	166

Figure 6-2: Photograph of Sonication Set-up for RPM samples .....	168
Figure 6-3: Average heterotrophic plate counts (HPC) with standard deviation error bars for bulk water inflow and outflow and randomly selected RPM surface .....	170
Figure 6-4: Average <i>Pseudomonas</i> plate counts (PIA) with standard deviation error bars for bulk water inflow and outflow and randomly selected RPM surface .....	171
Figure 6-5: Percent of inactivation of heterotrophic and <i>Pseudomonas</i> bacteria based upon average counts.....	172
Figure 6-6: Photograph of residue on membrane filter from a sonicated RPM sample towards the end of the study .....	173
Figure 6-7: Before (left) and after (right) photographs of 2” RPM used in experiment.....	174

## LIST OF ACRONYMS

<i>BF</i>	Baffling Factor
CDPHE	Colorado Department of Public Health and Environment
CFD	Computational Fluid Dynamics
CSU	Colorado State University
DBP	Disinfection By-Products
EFML	Environmental Fluid Mechanics Laboratory
RPM	Random Packing Material
RTD	Residence Time Distribution
SDWA	Safe Drinking Water Act
SWTS	Small Water Treatment System
TDT	Theoretical Detention Time
US	United States of America
USEPA	United States Environmental Protection Agency

# CHAPTER 1

*“The engineer is a mediator between the philosopher and the working mechanic and, like an interpreter between two foreigners, must understand the language of both, hence the absolute necessity of possessing both practical and theoretical knowledge.”*

Henry Palmer, 1818

## 1 INTRODUCTION

### 1.1 Motivation

In the US, and around the world, we are faced with aging infrastructure, decreasing source water quality, and limited financial resources, which pose a challenge in providing safe drinking water. In 2015, close to 21 million people in the US relied on community water systems that violated health-based quality standards as stipulated by the Safe Drinking Water Act (SDWA) (Allaire et al. 2018). Of the different health-based violations, 37% were from total coliform and 36% from disinfection byproducts (DPBs), etc. (Figure 1-1).

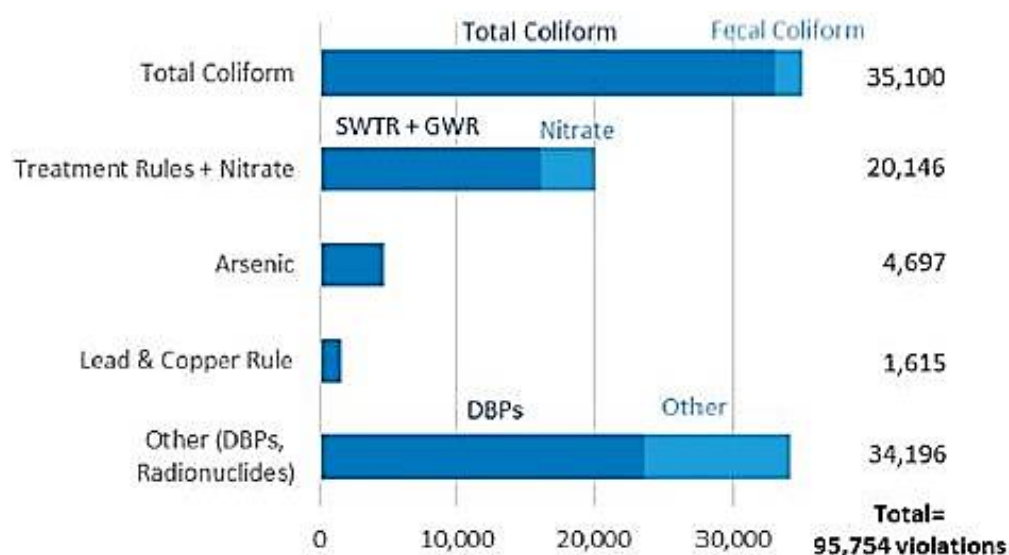
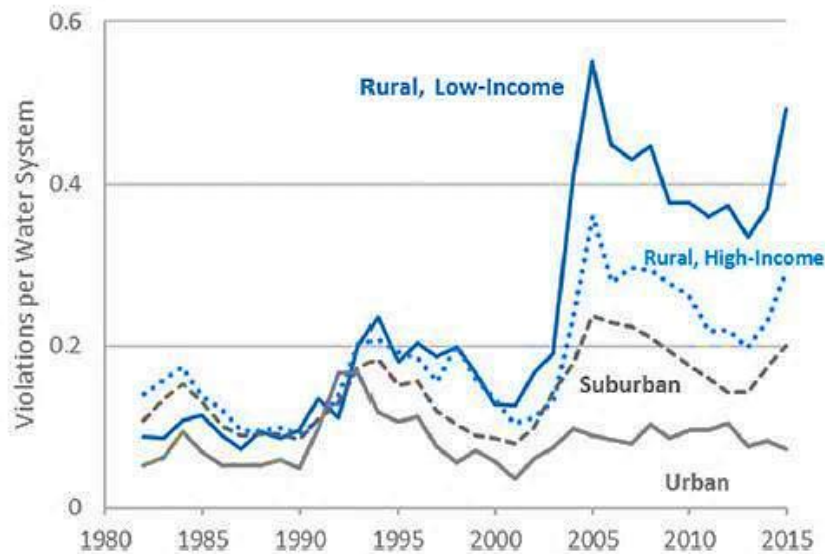


Figure 1-1: Number of health-based violations, 1982–2015, by contaminant type (Allaire et al. 2018)

Additionally, *Figure 1-2* shows that the highest prevalence of violations occurred in small water treatment systems (SWTSs) in rural areas (Allaire et al. 2018). From these statistics it can be concluded that, on the national scale, the majority of SDWA violations are related to the disinfection stage in SWTSs.



*Figure 1-2: Total violations per water system, by housing density category and income group (Allaire et al. 2018)*

There are multiple methods to eliminate pathogens from drinking water including chemical disinfection processes such as chlorination, chloramination, and ozone treatment, as well as physical removal processes such as the use of membranes (Crittenden et al. 2012). Chemical disinfection, specifically chlorination, is still the most widely used method of disinfection in the US and around the world (Crittenden et al. 2012). When using chemicals for disinfection (or other water treatment processes including coagulation), the chemical must be dispersed uniformly. Effective mixing is necessary to ensure that all the water, which is continuously flowing through a system, receives its proportionate share of the disinfectant. The injection of a disinfectant inline is often not sufficient and therefore requires a mechanical mixing device to achieve the desired uniform distribution of disinfectant throughout the water. (NRCSDWC 1980)

In addition to mixing, the time in which the water remains in the treatment system, or residence time, after a disinfectant is injected is just as important (Crittenden et al. 2012). The time requirement is based upon the chemical reaction rate of the particular disinfectant used and the particular microorganisms present in the water that require inactivation (Crittenden et al. 2012). Most drinking water treatment systems include a ‘contact’ basin that is designed to retain the water long enough to meet the required  $CT$ , the designated parameter to ensure microbial inactivation (USEPA 2003). While there are multiple designs of contact basins used in small water treatment systems, simple cylindrical tanks are commonly used due to low cost, relatively small footprint, and easy maintenance, particularly in an international context (often used as storage tanks simultaneously). These cylindrical tanks, however, suffer greatly from short-circuiting and large recirculation or ‘dead zones’ due to the jet of water from the inlet pipe into the ambient tank. The presence of short-circuiting and dead zones is considered to be hydraulically inefficient, meaning that not all of the available volume in the tank is being utilized (Barnett et al. 2014). Therefore, the water is not remaining within the system as long as ideally possible based upon the dimensions of the tank used. Short-circuiting and dead zones also prevent thorough mixing within the tank itself.

The *Baffling Factor Guidance Manual* proposed multiple simple and cost-effective modifications and innovative technologies to improve the hydraulic disinfection efficiency of contact basins for SWTSs (CDPHE 2014). One of the innovative technologies proposed was the use of random packing material (RPM). There are many different designs of RPM, but the basic design principles include a relatively high porosity (60 - 98%) and high surface area. A laboratory-scale study was conducted demonstrating that filling a cylindrical tank with RPM created near plug flow conditions (Barnett et al. 2014), which is ideal for chemical disinfection

purposes in terms of microbe inactivation as well as reduction of disinfection byproducts (DBPs) (Wilson & Venayagamoorthy 2010). Another study conducted created “porous walls” using RPM located at the inlet and turns in a baffled tank. Results of this study indicated a 35-62% improvement in the hydraulic disinfection efficiency (Kattnig 2014; Kattnig & Venayagamoorthy 2015).

Despite the promising benefit in terms of decreased short-circuiting and increased residence time, which results in improved disinfection, there is limited understanding of jet flow through a highly porous material such as RPM. Without a better understanding of the flow dynamics in this context, it remains an ad-hoc modification without any guidelines for the vast variability of SWTSs that could benefit from using RPM. At this time, this technology has not been adopted in SWTSs due to the lack of best practice application as well as practical concerns surrounding the use of RPM in this context. The lack of knowledge of the characteristic jet flow through RPM as well as some practical concerns for implementation provide the focus of this dissertation research.

## 1.2 Objectives

This dissertation research employs physical experimentation at the lab scale to study the use of random packing material (RPM) to improve hydraulic disinfection efficiency in SWTSs. The main objectives are as follows:

- 1) *To gain a more fundamental understanding of turbulent jet flow through RPM.* The motivation of this objective is to physically explain the increase in baffling factors observed in lab scale disinfection contactors. To date, there has been little research

conducted on obstructed turbulent jet flow, none in an engineered water system context.

The physical insights from a laboratory scale study of a turbulent jet from a long pipe through RPM are presented in Chapter 4.

- 2) *To address practical concerns for the application of the use of RPM to improve hydraulic disinfection efficiency in SWTS.* With any engineered solution, there are typically unintended consequences/results that need to be addressed and weighed. The second objective of this dissertation is to address two of the practical concerns of the innovative use of RPM in disinfection contactors. One of the practical concerns involves the added energy requirement (pumping cost) as a result of the increased drag the flow within a disinfection contactor experiences due to the presence of RPM is presented in Chapter 5. The other practical concern, presented in Chapter 6, is the potential for excessive biofilm growth due to the substantial added surface area of RPM.
- 3) *To provide guidance in terms of best practice for the innovative use of RPM to enhance hydraulic disinfection efficiency.* On the basis of a fundamental understanding of the unique flow dynamics along with the practical concerns regarding the unintended consequences addressed, best practices are developed. The need for best practice guidelines is crucial for the adoption and implementation the innovative use of RPM in the water sector. The recommended amount and location of RPM within a disinfection contactor are presented in chapters 4 and 5, respectively.

### 1.3 Dissertation Layout

The remainder of this dissertation is organized according to the following chapters:

- Chapter 2 contains a literature review covering RPM, flow interacting with obstacles, relevant turbulent flows, hydraulic disinfection efficiency, and biofilms in order to establish a foundational framework to better understand turbulent jet flow through RPM and how it can be applied to improve the hydraulic disinfection efficiency of SWTSSs.
- Chapter 3 provides a background on the experimental methods used in the laboratory scale experiments for the completion of this dissertation.
- Chapter 4 presents the study of turbulent jet flow from a long pipe through RPM in line with the first (and third) objective of this dissertation.
- Chapter 5 presents the laboratory scale study investigating the efficiency gain along with the energy loss due to the presence of RPM in a cylindrical tank. This is in line with the second and third objectives.
- Chapter 6 presents the practical concern of biofilm growth on RPM in the context of a chlorine contact basin commonly used in SWTSSs in line with the second objective of this dissertation.
- Chapter 7 provides a summary and conclusion to this dissertation. Suggested best practice guidance for the use of RPM in disinfection contactors is provided as a part of this chapter – in line with the third objective of this dissertation work.

## 1.4 Summary

This dissertation presents both the published and unpublished work on the study of RPM to improve the hydraulic disinfection efficiency of SWTSSs. Multiple physical experiments were conducted using an appropriate range of flowrates, in terms of the non-dimensional jet Reynolds numbers, representative of typical SWTSSs. The overarching goal of this dissertation is to gain a

fundamental understanding of turbulent jet flow through RPM as well as address practical concerns for the use of RPM in the context of a disinfection contact basin. The hope is that this work will promote the adoption of the use of RPM as a viable modification to SWTSs struggling to meet the SDWA standards related to disinfection.

## CHAPTER 2

### 2 LITERATURE REVIEW

#### 2.1 Random Packing Material

##### 2.1.1 Design

The general design concept for random packing material (RPM) is to have a high surface area and void fraction that allows fluid to flow through its pores (or void spaces). The reason they are called ‘random’ is that each unit does not lie within the same plane as the others (Cannon 1952) thus creating a random flow pattern by forcing the fluid to flow through the void spaces arbitrarily. For the purpose of enhancing hydraulic disinfection efficiency, the forcing of the flow through RPM reduces short-circuiting in a tank by dissipating the incoming jet, promoting plug flow conditions. Also, the added shear stress resulting from the high surface area of the RPM promotes turbulence. An important outcome of turbulence is mixing, which is key for disinfecting water through the use of chemicals such as chlorine.

##### 2.1.1.1 Geometry

There are multiple different geometries (and sizes) of RPM available including (but not limited to) different types of rings (e.g. raschig, pall, cascade, beta, or helix), saddle, snowflake/star, tellerette, polyhedral hollow, and spherical. *Figure 2-1* shows examples of various manufactured RPM.



*Figure 2-1: Photograph of a variety of RPM of different size, geometry, and material*  
(Image credit: <https://www.walcoom.com/products/filtering/mass-transfer/random-packing.html>)

#### 2.1.1.2 Geometric Surface Area

The geometric (or specific) surface area ( $a_p$ ) is defined as the surface area per unit volume of packing ( $V_p$ ) ( $[L^2/L^3]$ ). The greater the geometric surface area the greater the contact area and as a result a greater mass transfer efficiency and shear stress.

#### 2.1.1.3 Void Fraction (Space)

The void fraction (or space) refers to the porosity ( $\epsilon$ ) of the RPM which is the volume of the voids divided by the total volume ( $\epsilon = V_v/V$ ). Typical RPM have a void fraction between 0.6 to 0.98 (or 60-98%; various RPM manufacture product bulletins).

#### 2.1.1.4 Packing Factor

The packing factor ( $F_p$ ) is defined as the RPM's surface area per unit volume divided by the cube of the void fraction ( $F_p = a_p/\epsilon^3$ ;  $[L^{-1}]$ ). The greater the surface area per unit volume the higher the

packing factor. This correlates to more efficient RPM in terms of mass transfer but also a larger pressure drop. The packing factor correlates to the permeability of the RPM, e.g. the higher the packing factor the lower the permeability.

#### 2.1.1.5 Material

RPM can be made from different types of material including polyvinyl chloride (PVC/C-PVC), polypropylene (PP), polyethylene (PE), stainless steel, ceramic, etc. There are many different RPM manufacturers, both in the U.S. and internationally, for which some RPM meet the National Sanitation Foundation/ American National Standard (NSF/ANSI) 61 criteria. The NSF/ANSI 61 certification ensures that a product (i.e. any water system component) meets the regulatory requirements of the US and Canada such that it is fit for use in drinking water applications. Specifically, this certification “*establishes minimum health effects requirements for the chemical contaminants and impurities that are indirectly imparted to drinking water from products, components, and materials used in drinking water systems*” (NSF/ANSI 2016).

#### 2.1.1.6 Cost of Random Packing Material

The cost of RPM varies depending on the manufacturer, the type (i.e. size and geometry) and material. *Table 2-1* shows the average cost of RPM ranges from about \$6/ft<sup>3</sup> for polypropylene to \$100/ft<sup>3</sup> for stainless steel (USEPA 2002).

Table 2-1: Random Packing Material Costs (USEPA 2002)

Nominal Diameter (inches)	Construction material	Packing Type	Packing cost (\$/ft <sup>3</sup> )	
			< 100 ft <sup>3</sup>	> 100 ft <sup>3</sup>
1	304 Stainless Steel	Pall Rings, Raschig Rings, Ballast Rings	70 - 109	65 - 99
1	Ceramic	Raschig Rings, Berl Saddles	33 - 44	26 - 36
1	Polypropylene	Tri-Pak®, Pall Rings, Ballast Rings, Flexisaddles, Berl Saddles, Raschig Rings	141 - 37	12 - 34
2	Ceramic	Tri-Pac®, Lanpac®, Flexiring, Flexisaddle	13 - 32	10 - 30
2	Polypropylene	Tellerette, Ballast Rings	3 - 20	5 - 19
3.5	304 Stainless Steel	Tri-Pak®, Lanpac®, Ballast Rings	30	27
3.5	Polypropylene		6 - 14	6 - 12

### 2.1.2 Current Uses and Applications

Packing material was originally invented for use in phase reaction devices. RPM was designed such that a substituent (fluid) of one phase (e.g. gas) would be brought into contact with a substituent of a different phase (e.g. liquid) (Cannon 1952). Phase reaction devices or columns are commonly used for purposes of distillation, extraction, or absorption where the interface between the wetted surfaces of the RPM and the vapor promotes mass transfer (Cannon 1952).

RPM is also used for drinking and waste-water treatment purposes – aeration/air-stripping (Kavanaugh and Trussell 1980) and trickling filters (Richards and Reinhart 1986) respectively.

The water treatment processes of air-stripping, where gas is removed from water, and aeration, when air or oxygen is transferred to the water, both exploit the aeration process. Aeration is used in order to oxidize compounds such as iron and manganese while air-stripping is used to remove volatile organic compounds (VOCs), trihalomethanes (THMs), taste and odor causing substances, etc. (USEPA 2019). A trickling filter is a biological aerobic system used to remove

organics from wastewater. Trickling filter technologies, such as packed bed reactors (bio-towers), are known as attached-growth processes. Wastewater flows over a media, such as RPM, such that microorganisms in the water attach and grow on the RPM surfaces that eventually form a biological film or slime layer. Microorganisms in the outer part of the slime layer degrade organic material in the wastewater. (USEPA 2000)

### 2.1.2.1 Typical Performance Specifications

Performance specifications include those relevant to the particular application and to the fluid dynamics. The performance specifications relevant to application typically include (but are not limited to) the number of theoretical units (NTU), height of mass-transfer unit (HTU), and volumetric mass-transfer coefficient ( $K_G a$ ). The performance specification relevant to the fluid dynamics include the pressure drop, liquid holdup, and flooding (from various RPM manufacture product bulletins). Despite the fact that RPM was developed over a century ago, due to the complex two-phase countercurrent flow through RPM, it is still difficult to predict the fluid dynamics and mass transfer efficiency. Therefore, empirical models are used but they typically have limited ranges of validity. There are a few models based on a tube/capillary or particle model (see Section 2.3.2.2) that have been developed such that they could be applied to all types and sizes of RPM, however, most still rely strongly on empirical parameters (Engel et al. 2001). For the purpose of this dissertation research, only the fluid dynamics performance specifications for pressure drop are of interest.

#### 2.1.2.1.1 Pressure Drop

Flow through RPM experiences a drop in pressure due to frictional and form drag (discussed in Section 2.3). The main focus for the improvement in RPM has been (and continues to be) on

reducing the pressure drop due to the associated operational costs (McNulty 1988). In *Figure 2-2* below there are example pressure drop graphs (compared to the C-factor; [L/T]) for 2” spherical RPM that was used in the laboratory scale experiments presented in this document.

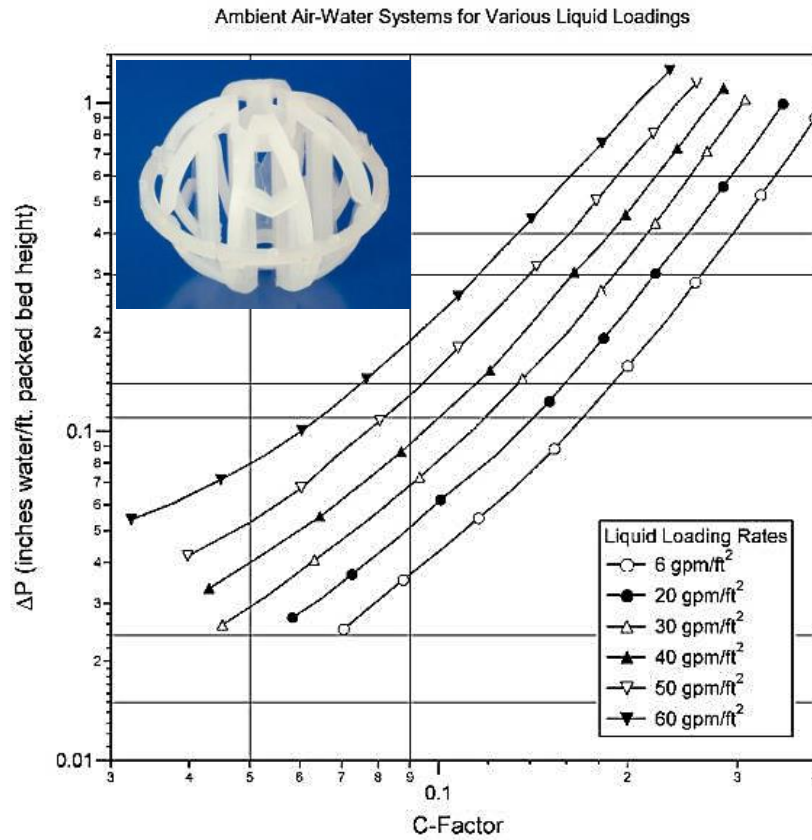


*Figure 2-2: Pressure drop vs. C-Factor plots for 2” RPM (image credit: RJT 2019)*

The flow in contact basins for drinking water disinfection involves a single-phase, turbulent jet flow. However, at this time, the pressure drop models, empirical studies, and specifications reported only concern the current applications that involve uniform, countercurrent two-phase (uniform) flow. Therefore the specifications provided are not necessarily transferable to flow through RPM in a disinfection contact basin.

## 2.2 Relevant Turbulent Flows

Turbulence is an important aspect for chemical disinfection as one of the main symptoms is mixing (Pope 2000). Whenever there is a sharp inlet (e.g. inflow pipe) into a tank, the result is a turbulent jet. The simplest case studied is a turbulent round jet entering an ambient of the same fluid (*Figure 2-3a*). Understanding how a turbulent round jet decays and spreads in an ambient is foundational to researching how a turbulent jet would decay and spread through RPM. The goal of using RPM is to disperse the turbulent jet quickly in order to reduce short-circuiting and increase the effective volume of the tank thereby improving the hydraulic disinfection efficiency of the SWTSSs. Also, when considering the typical operational flow rates of SWTSSs, it is possible that the flow within a contact tank (closed-conduit) could be laminar (Wilson & Venayagamoorthy 2010), which is not beneficial in terms of mixing. However, assuming that the turbulent jet is spread uniformly across the cross-sectional area of the tank by the presence of RPM, the flow downstream of the RPM layer would ideally be homogenous and conceivably mimic flow downstream of a grid (i.e. grid turbulence) as seen in *Figure 2-3b*, commonly used to study the decay of homogenous shear flows.

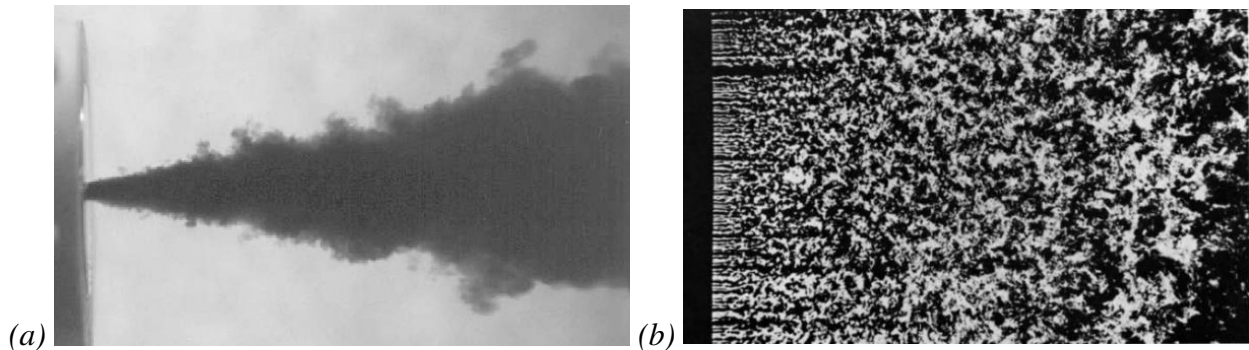


*Figure 2-3: Visualization of (a) a jet into an ambient and (b) isotropic turbulence downstream of a grid (image credit: <http://www.dartmouth.edu/~cushman/courses/engs43/Chapter3.pdf>)*

## 2.2.1 Turbulent Round Jet into an Ambient

When a round jet enters an ambient, the velocity difference creates free shear which causes turbulence and mixing to occur (Abdel-Rahman 2010). The mixing of the fluid from the jet with the surrounding quiescent fluid dissipates and spreads the jet. There are three regions of a round jet: the near-field, the intermediate-field, and the far-field (*Figure 2-4*).

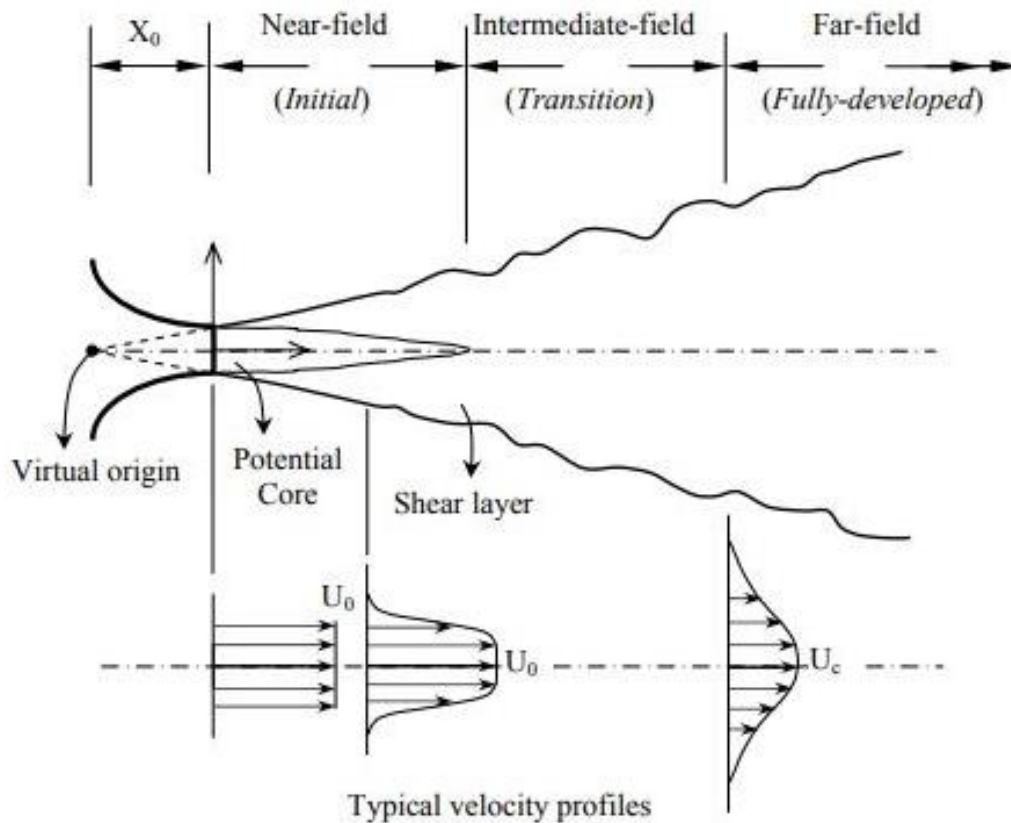


*Figure 2-4: A schematic of the free turbulent jet (Abdel-Rahman 2010)*

The near-field region contains the potential core of the jet and therefore the flow characteristics mimic those of the nozzle-exit. This region typically ranges between  $0 < x/d_j < 6$ , where  $x$  is the distance from the nozzle exit along the center line and  $d_j$  is the diameter of the nozzle (jet). The intermediate-field typically ranges from  $6 < x/d_j < 30$ , beyond the potential core but

where the jet is still developing. Beyond  $x/d_j = 30$  is considered the far-field and begins around where the jet is fully developed. (Fielder et al. 1998)

### 2.2.1.1 Parameters

The flow of a steady jet with Newtonian fluid through a round smooth-contracting nozzle is statistically stationary and axisymmetric. This allows the flow to be simply defined by the velocity of the jet ( $U_j$ ), the diameter of the jet ( $d_j$ ), and the viscosity of the fluid ( $\nu$ ). Therefore, the jet Reynolds number ( $Re_j$ ) is the important non-dimensional parameter when studying turbulent round jets. (Pope 2000)

$$Re_j = \frac{U_j d_j}{\nu} . \quad 2-1$$

In the mean axial velocity field ( $\langle U(x, r, \theta) \rangle$ ) the main velocity of interest is the centerline velocity ( $U_0(x)$ ) which is defined as:

$$U_0(x) = \langle U(x, 0, 0) \rangle . \quad 2-2$$

Another important parameter is the jet's half width ( $r_{\frac{1}{2}}(x)$ ) which is defined such that:

$$\langle U(x, r_{\frac{1}{2}}(x), \theta) \rangle = \frac{1}{2} U_0(x) . \quad 2-3$$

### 2.2.1.2 Self-Similarity

Through experimentation it has been found that as  $x$  increases  $U_0(x)$  decreases (i.e. decays) and  $r_{\frac{1}{2}}(x)$  increases (i.e. spreads). As the jet decays and spreads the mean velocity profile changes (*Figure 2-5a*). (Pope 2000) However, it is observed that the shape of the profiles remain the same. When the jet is fully developed (in the far-field) the non-dimensional mean velocity profiles collapse when compared to the non-dimensional radial distance as seen in *Figure 2-5b* below. This is described as 'self-similarity'. (Pope 2000)

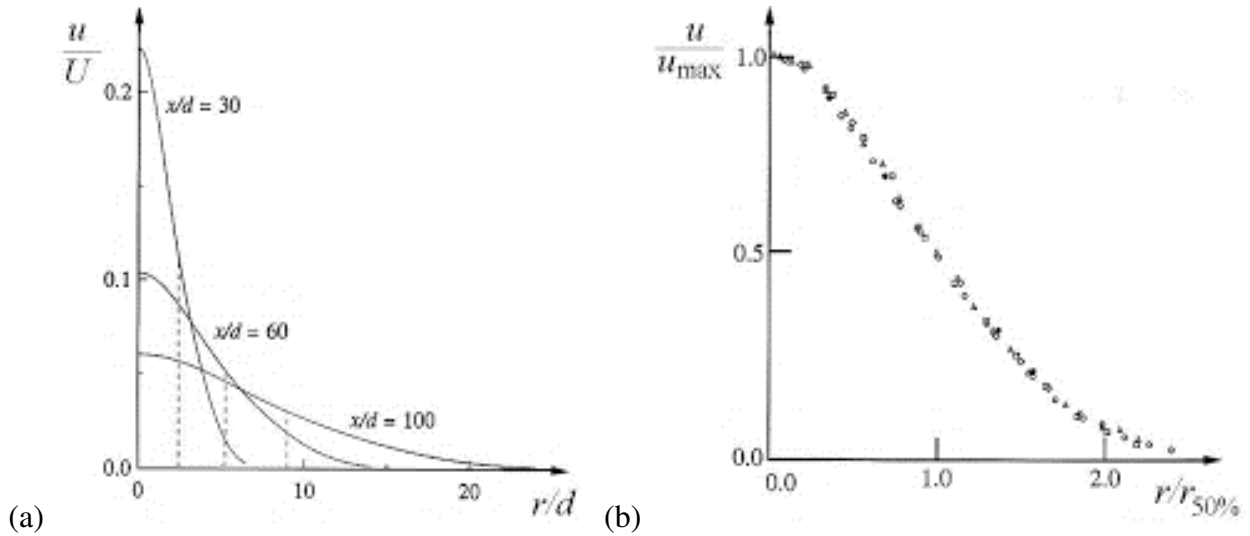


Figure 2-5: (a) Radial profiles of mean axial velocity in a turbulent round jet at  $Re = 95500$  (Pope 2000) and (b) Mean axial velocity versus radial distance of a turbulent round jet at  $Re \approx 10^5$  (Pope 2000)

When considering the axial variation of  $U_0(x)$  and  $r_{\frac{1}{2}}(x)$  in the far-field, experimental results indicate two linear relationships where  $B$  is an empirical constant indicating an inverse decay rate,  $S$  is the spreading rate, and  $x_0$  is the virtual origin of the jet. (Pope 2000)

$$\frac{U_0(x)}{U_j} = \frac{B}{(x-x_0)d_j'} , \quad 2-4$$

$$r_{\frac{1}{2}}(x) = S(x - x_0) . \quad 2-5$$

From experimental data by Panchapakesan & Lumley (1993a), Hussien et al. (1994), and Mungal & Hollingsworth (1989) it was observed that the mean velocity profile and spreading rate of a turbulent round jet from a smooth converging nozzle are independent of  $Re_j$  (Pope 2000).

### 2.2.1.3 Mean Momentum

In turbulent flows, though statistically stationary, the fluid velocity varies significantly and irregularly in space and time. Therefore, a statistical analysis of the flow is invoked and the mean velocities are considered. The Reynolds decomposition of an instantaneous velocity ( $\mathbf{U}$ ) is

performed:  $\mathbf{U} = \langle \mathbf{U} \rangle + \mathbf{u}$  where  $\langle \mathbf{U} \rangle$  is the mean velocity and  $\mathbf{u}$  is the difference from the mean, or its fluctuation. In an axial flow field (e.g. a round jet), the coordinates  $x$  (axial),  $r$  (radial),  $\theta$  (circumferential) and correspond to  $U$ ,  $V$ , and  $W$ . On the basis of the axisymmetric assumption, the radial and circumferential velocity components are equal, therefore only the  $U$  &  $V$  velocity components are of concern. In turbulent round jets, the dominant mean flow ( $\langle U \rangle$ ) is in the  $x$  direction and the lateral (or radial) flow ( $\langle V \rangle$ ) is relatively small (by two orders of magnitude). This allows the use of the 2D Turbulent Boundary Layer Equations, which are simplified and Reynolds-averaged versions of the continuity and Navier-Stokes equations of fluid motion. For turbulent round jets which are statistically axisymmetric, stationary, and non-swirling the following continuity and momentum equations (Eqns 2-6 & 2-7 respectively) in cylindrical coordinates are used (Pope 2000):

$$\frac{\partial \langle U \rangle}{\partial x} + \frac{1}{r} \frac{\partial r \langle V \rangle}{\partial r} = 0, \quad 2-6$$

$$\langle U \rangle \frac{\partial \langle U \rangle}{\partial x} + \langle V \rangle \frac{\partial \langle U \rangle}{\partial r} = \frac{\nu}{r} \frac{\partial}{\partial r} \left( r \frac{\partial \langle U \rangle}{\partial r} \right) - \frac{1}{r} \frac{\partial}{\partial r} (r \langle uv \rangle). \quad 2-7$$

The term  $\langle uv \rangle$  is referred to as the Reynolds shear stress and can be determined by the following equation where  $\nu_T(x, r)$  is the turbulent viscosity:

$$\langle uv \rangle = -\nu_T \frac{\partial \langle U \rangle}{\partial r}. \quad 2-8$$

Due to the self-similarity,  $\nu_T(x, r)$  scales with  $U_0(x)$  and  $r_{\frac{1}{2}}(x)$  where  $\eta = r/(x - x_0)$ :

$$\nu_T(x, r) = r_{\frac{1}{2}}(x) U_0(x) \hat{\nu}_T(\eta). \quad 2-9$$

It is observed that  $\hat{\nu}_T(\eta)$  is a constant and the product of  $r_{\frac{1}{2}}(x) U_0(x)$  is independent of  $x$ .

Therefore  $\nu_T$  can be taken to be uniform. Thus the boundary-layer momentum equation simplifies to:

$$\langle U \rangle \frac{\partial \langle U \rangle}{\partial x} + \langle V \rangle \frac{\partial \langle U \rangle}{\partial r} = \frac{\nu_T}{r} \frac{\partial}{\partial r} \left( r \frac{\partial \langle U \rangle}{\partial r} \right). \quad 2-10$$

Additionally, from experimental observations the spreading rate ( $S$ ) can be determined by:

$$S = 8(\sqrt{2} - 1)\hat{v}_T . \quad 2-11$$

### 2.2.1.4 Mean Flow and Turbulent Kinetic Energy

The mean kinetic energy of a fluid (per unit mass) can be decomposed into the kinetic energy of the mean flow ( $\bar{E} = \frac{1}{2}\langle \mathbf{U} \rangle \cdot \langle \mathbf{U} \rangle$ ) and the turbulent kinetic energy ( $k = \frac{1}{2}\langle \mathbf{u} \cdot \mathbf{u} \rangle$ ):

$$\langle E(x, t) \rangle = \bar{E}(x, t) + k(x, t) \quad 2-12$$

The equations for the evolution of  $\bar{E}$  and  $k$  can be written as:

$$\frac{\bar{D}\bar{E}}{\bar{D}t} + \nabla \cdot \bar{\mathbf{T}} = -\mathcal{P} - \bar{\varepsilon} , \quad 2-13$$

$$\frac{\bar{D}k}{\bar{D}t} + \nabla \cdot \mathbf{T}' = \mathcal{P} - \varepsilon , \quad 2-14$$

where  $\mathcal{P}$  is the term associated with the production ( $\mathcal{P} = v_T \frac{\partial \langle U \rangle}{\partial r}$ ),  $\mathbf{T}$  is the term associated with transport, and  $\varepsilon$  is the term associated with dissipation of kinetic energy. (Pope 2000)

### 2.2.2 Homogenous Shear Flow

A homogenous shear flow occurs when the fluctuating velocity components ( $\mathbf{u}(\mathbf{x}, t)$ ) and fluctuating pressure ( $p'(\mathbf{x}, t)$ ) are statistically homogeneous under a uniform shear rate ( $S = \partial \langle U_i \rangle / \partial x_j$ ). In homogenous shear (or turbulent) flow the transport of energy is absent and therefore  $\mathbf{T}$  is zero. From experimental studies by Tavoularis & Corrsin (1981) and computational (DNS) studies by Rogallo (1981) and Rogers & Moin (1987), it has been concluded that homogenous shear flows are also self-similar. When the statistics are normalized by  $S$  and  $k(t)$ , they become independent of time (Pope 2000). Therefore the turbulent kinetic energy equation simplifies to:

$$\frac{dk}{dt} = \mathcal{P} - \varepsilon . \quad 2-15$$

This equation can also be written as:

$$\frac{\tau}{k} \frac{dk}{dt} = \frac{P}{\varepsilon} - 1 . \quad 2-16$$

Since  $P/\varepsilon$  and the turbulent timescale ( $\tau$ ) are constant there is an analytical solution:

$$k(t) = k(0) \exp \left[ \frac{t}{\tau} \left( \frac{P}{\varepsilon} - 1 \right) \right] . \quad 2-17$$

### 2.2.2.1 Grid Turbulence

When the mean velocity gradient is absent in homogenous turbulence, i.e.  $S$  is zero, then the Reynolds shear stresses ( $\langle uv \rangle$ ) are zero and there is no production ( $P = 0$ ). Therefore the turbulence simply decays i.e. only  $\varepsilon$  remains (Pope 2000):

$$\frac{dk}{dt} = -\varepsilon . \quad 2-18$$

This is practically achieved by passing a uniform stream ( $U_0$  in the  $x$ -direction) through a ‘grid’ or mesh (*Figure 2-6*). This is known as grid turbulence and is statistically stationary, varying only in the  $x$ -direction.

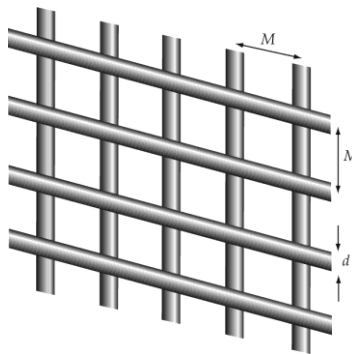


*Figure 2-6: A sketch of a turbulence-generating grid;  $d$  = bar diameter &  $M$  = mesh spacing (Pope 2000)*

Experimental results seen in *Figure 2-7* below indicate that the normal stresses ( $\langle u^2 \rangle$ ) and turbulent kinetic energy ( $k$ ) decay according to a power law where  $A$  is a constant (highly dependent on grid geometry and Reynolds number) and  $n$  is typically taken to be 1.3 (Mohamed & LaRue 1990):

$$\frac{k}{U_0^2} = A \left( \frac{x-x_0}{M} \right)^{-n} . \quad 2-19$$

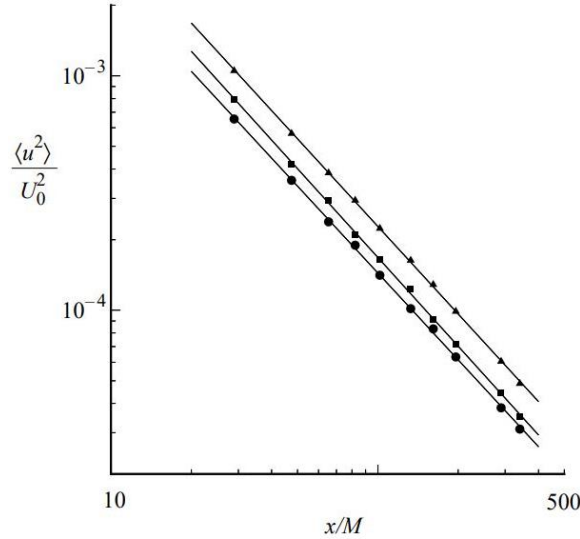


Figure 2-7: The decay of Reynolds stresses in grid turbulence; ■ =  $\langle u^2 \rangle/U_0^2$ , ● =  $\langle v^2 \rangle/U_0^2$ , ▲ =  $k/U_0^2$  (Comte-Bellot & Corrsin 1966)

In a moving frame, the previous equation can be re-cast as the following where  $t_0$  and  $k_0$  are arbitrary references: (Pope 2000)

$$k(t) = k_0 \left( \frac{t}{t_0} \right)^{-n} . \quad 2-20$$

By differentiating, this equation becomes:

$$\frac{dk}{dt} = \left( \frac{nk_0}{t_0} \right) \left( \frac{t}{t_0} \right)^{-(n+1)} . \quad 2-21$$

Plugging Eqn 2-18 in to Eqn 2-21, the dissipation decays according to the power law where  $\varepsilon_0 = n(k_0/t_0)$ :

$$\varepsilon(t) = \varepsilon_0 \left( \frac{t}{t_0} \right)^{-(n+1)} . \quad 2-22$$

### 2.3 Flow Interacting with Obstacles

Understanding jet flow dynamics in a quiescent fluid is essential, but RPM are obstacles that the flow interacts with and have a significant impact on the flow dynamics. This requires an

investigation into the drag due to the flow interacting with obstacles. Our world is full of obstacles that flows encounter, whether in the atmosphere, such as buildings and wind farms, or in rivers or ocean, such as bridge piers and aquaculture. These flows create wakes and vortices that produce turbulence, which subsequently impacts drag. Flows interacting with obstacles involves three types of shear flows: boundary layers, free shear layers, and a wake making them incredibly complex (Williamson 1996).

### 2.3.1 Flow around an Infinitely Long Cylinder

The emphasis of work done concerning wake-vortex dynamics is on the simplest case: steady, uniform flow past an infinitely long cylinder. Studies have consisted of both physical and computational (e.g. direct numerical simulations (DNS)) experiments. Hotwire anemometry, specifically ‘flying’ hotwire in order to gain both magnitude and directional information, has typically been used to measure velocities in physical experiments. To visualize the flow, smoke (air) or hydrogen bubbles (water) have been used.

#### 2.3.1.1 Parameters

There are a plethora of parameters used in the study of flow around obstacles. Some of the relevant measurements include the flow velocity ( $U$ ), the diameter of the cylinder ( $d$ ), and the width of wake ( $d_w$ ). Additionally, there is the length of formation ( $L_f$ ), which is the axial distance downstream of the cylinder where the root mean square-velocity fluctuations ( $u_{rms}$ ) are maximum, and the diffusion length ( $L$ ), which is the thickness of shear layer at the end of the formation region where the layer is drawn across the wake (Gerrard 1966). There are also a number of relevant non-dimensional parameters discussed below.

### 2.3.1.1.1 Reynolds Number

The most important non-dimensional number in flow interacting with an obstacle is the Reynolds number ( $Re$ ).  $Re$  is the ratio of the inertial to viscous forces in a flow and is defined below (where  $\nu$  is the kinematic viscosity of the fluid and  $L$  is the appropriate characteristic length scale):

$$Re = \frac{UL}{\nu}. \quad 2-23$$

For flow around a cylinder the appropriate length scale is the diameter of the cylinder such that:

$$Re = \frac{Ud}{\nu}. \quad 2-24$$

### 2.3.1.1.2 Strouhal Number

The Strouhal number ( $St$  or  $S$ ) describes the oscillation of flow and is defined below (where  $f$  is a frequency):

$$St = \frac{fU}{d}. \quad 2-25$$

### 2.3.1.1.3 Drag Force and Coefficients

Drag is the resultant force due to friction that resists motion. The drag force of an object moving through a fluid is dependent on the properties of the fluid (i.e. density and viscosity) and the object (i.e. size, shape, velocity, etc.). The equation often used for drag is given below where  $F_D$  is the drag force,  $\rho$  is the density of the fluid,  $\mathbf{U}$  is the velocity (relative to the fluid),  $A$  is the projected cross-sectional of the object, and  $C_D$  is the (dimensionless) drag coefficient:

$$F_D = \frac{1}{2}\rho\mathbf{U}^2C_D A. \quad 2-26$$

The  $F_D$  is the sum of two components, the drag due to skin friction (i.e. due to contact of fluid and solid boundary) and the form drag which is due to the pressure difference between the front

and back caused by boundary layer separation. For flow around an infinitely long cylinder, the form drag is much larger than the skin drag and is therefore is of main concern. As in much of fluid mechanics, non-dimensional numbers are more practical and so the base pressure (sometimes referred to as suction) coefficient ( $C_{PB}$ ; where  $P = F/A$ , a.k.a. pressure) is the relative value of interest:

$$C_{PB} = \frac{2\Delta P}{\rho U^2}. \quad 2-27$$

### 2.3.1.2 Observations of Flow Regimes

In the study of flow around an infinitely long cylinder, the common comparisons made are  $Re$  versus  $St$  and  $Re$  versus  $-C_{PB}$ ; in line with the objectives of this work only the latter is considered. As  $Re$  is increased, the flow around the cylinder moves through different regimes, transitioning at what are called ‘critical  $Re$ ’ ( $Re_{crit}$ ). A graph of  $\log_{10} Re$  versus  $-C_{PB}$  by Williamson (1996), as seen below in *Figure 2-8*, shows the transition of flow from one regime to the next.

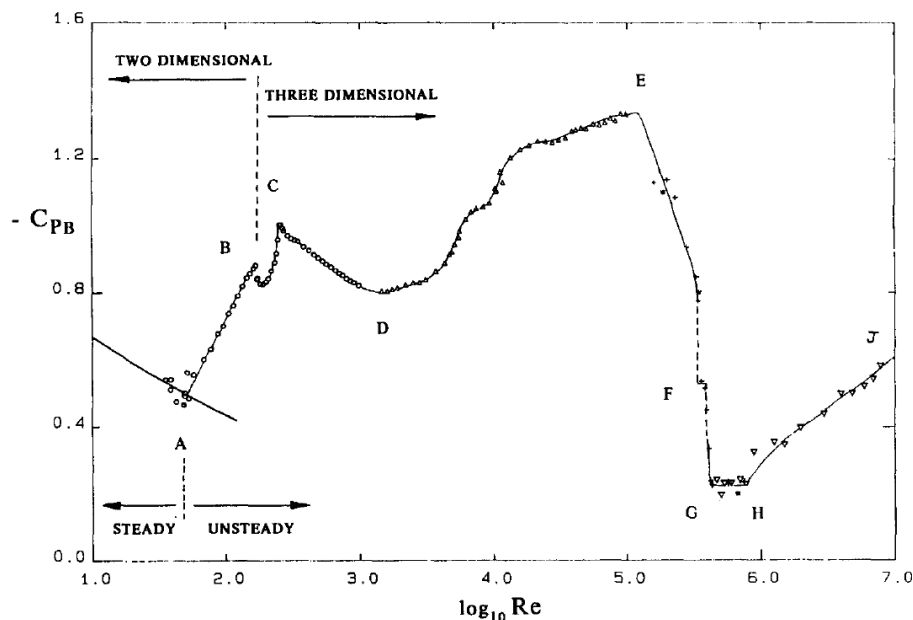


*Figure 2-8: Plot of base suction coefficients ( $-C_{PB}$ ) versus Reynolds numbers, as a basis for the discussion of various flow regimes of cylinder wake (Williamson 1996)*

### 2.3.1.2.1 Laminar Steady Regime

The first regime is called the Laminar Steady Regime that occurs for  $0 < Re < 49$  (up to point A in *Figure 2-8*). This regime is viscosity dominated with two symmetric recirculation cells in the closed near-wake region (or ‘bubble’ of length  $L_f$ ). The free shear layers meet at a confluence point at end of the near-wake as seen in *Figure 2-9*. In this regime, as  $Re$  increases  $L_f$  increases. This régime is the only steady regime in that the flow is globally stable with respect to all three dimensions.

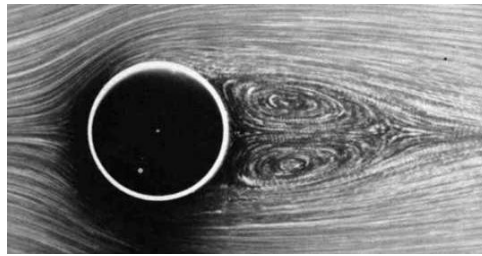


*Figure 2-9: Visualization of flow around a cylinder at  $Re = 26$  (Van Dyke 1982)*

### 2.3.1.2.2 Periodic Laminar Regime

This regime is also referred to as the Vortex Shedding Laminar Regime and is from point A to B in *Figure 2-8*. At the first  $Re_{crit}$ ,  $Re = 49$ , the flow becomes linearly unstable with respect to 2D disturbances. The flow experiences a supercritical Hopf bifurcation, or a critical point where system stability switches and solution becomes periodic, at the downstream end of the bubble. In this regime Von Karman vortex sheets, or vortex shedding, appear (see *Figure 2-10*).



*Figure 2-10: Periodic laminar regime at  $Re = 140$  (Van Dyke 1982)*

Gerrard (1966) proposed that the growing vortex pulls the shear layer from the opposite side of the wake across the wake until it is strong enough to cut off the supply forcing the vortex to shed. The same process then ensues on the opposite side of the wake, following an oscillatory pattern. The frequency at which the wake oscillates is described by the  $St$ . As  $Re$  increases, the wake stability is amplified, the 2D Reynolds stresses in the near-wake region increases, and the  $L_f$  decreases resulting in an increase in  $-C_{PB}$ . (Williamson 1996)

### 2.3.1.2.3 Wake Transition Regime

There is another  $Re_{crit}$  that occurs at some point between  $Re = 140$  and  $194$  (until  $Re = 260$ ; from point B to C in *Figure 2-8*) where the flow transitions from 2D laminar to 3D through a subcritical bifurcation. The large range of  $Re_{crit}$  has yet to be explained. As  $Re$  increases there is a decrease in  $-C_{PB}$  and in the 2D Reynolds stresses as well as an increase in  $L_f$  (from point C to D in *Figure 2-8*). There are two discontinuities in the wake formation in this regime. At the first discontinuity, the flow is characterized as Mode A instability where the wake becomes linearly unstable due to an elliptical instability of the primary vortex core during the process of vortex shedding/dislocation (Williamson 1996). Essentially, part of the vortex is pulled back towards the body, caused by the strain-rate field, forming a vortex loop. These vortex loops form streamwise vortex pairs with a spanwise length scale of  $\lambda_s = 3D$  to  $4D$  (Williamson 1996). As the  $Re$  increases to about 230 to 260 there is a gradual transfer of energy from Mode A to Mode B instability. Mode B is characterized by fine-scale streamwise vortices of spanwise length scale,  $\lambda_s \approx 1D$ . At  $Re = 260$  there is a supercritical bifurcation leading to increasing 3D disorder (*Figure 2-11*). (Williamson 1996)

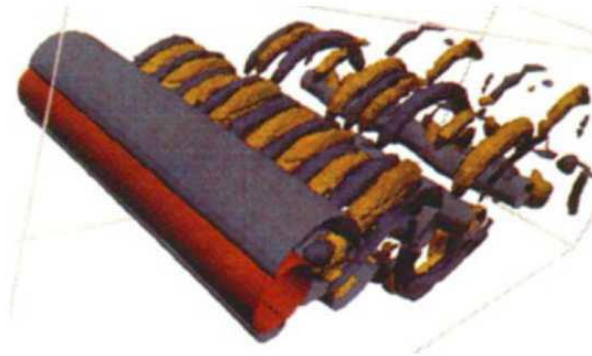


Figure 2-11: DNS of Mode B three-dimensional instabilities at  $Re = 250$  (Thompson et al. 1996)

#### 2.3.1.2.4 Shear Layer Transition Regime

From  $Re \approx 1,000$  to  $200,000$  the flow is said to be in the Shear Layer Transition Regime (from point D to E in Figure 2-8). A Kelvin-Helmholtz instability appears that contributes to the increase in 2D Re stresses and  $-C_{PB}$ . The point where the separating shear layer becomes turbulent moves upstream as Re increases. There is also a decrease in  $L_f$  and the frequency of shedding roughly scale as  $Re^{3/2}$ . (Williamson 1996)

#### 2.3.1.2.5 Asymmetric Reattachment Regime

This regime, also referred to as the Critical Transition Regime, ranges from  $2 \times 10^3 < Re < 5 \times 10^5$  (from point E to F in Figure 2-8) and is characterized by a separation-reattachment bubble. This bubble forms on one side of the cylinder due to the detachment and further reattachment of the boundary layer (Rodríguez et al. 2015). The revitalized boundary layer then separates further downstream. This leads to a reduced  $d_w$ . In this régime there is a drastic decrease in  $-C_{PB}$  and drag. A phenomenon occurs at point F in Figure 2-8 where there is a bistable, one-sided reattachment causing a large lift ( $C_L$ ) on the cylinder. (Williamson 1996)

### 2.3.1.2.6 Symmetric Reattachment Regime

At  $Re \approx 5 \times 10^5$  the flow switches to a Symmetric Reattachment or Supercritical Regime as two separation-reattachment bubbles (symmetric) appear (from point F to G in *Figure 2-8*). It is also referred to as the ‘Drag Crisis’ where the drag remains reasonably constant ( $C_D = 0.2$ ) throughout the entire regime (Rodríguez et al. 2015). The substantially higher Reynolds stresses in the boundary layer downstream of the bubble allows the boundary layer to survive a greater adverse pressure gradient, remaining attached longer and resulting in a smaller  $d_w$ . (Williamson 1996)

### 2.3.1.2.7 Boundary-Layer Transition Regime

This is the last observed regime, also referred to as the Post-critical Regime for  $Re > 10^6$  (from point H to J in *Figure 2-8*). This regime is characterized by a reappearance of periodic turbulent vortex shedding. The point of boundary layer separation moves upstream until the boundary layer itself becomes turbulent. This results in an increase in  $-C_{PB}$ , drag, and  $d_w$  as  $Re$  increases. (Williamson 1996)

### 2.3.1.2.8 General Trends

While the exact mechanism of vortex-wake dynamics is not well understood, particularly why and/or what happens at the  $Re_{crit}$  that makes the flow dynamics change, throughout the different regimes there are some consistent relationships. For instance, as the length of formation ( $L_f$ ) increases, the frequency of vortex shedding decreases. A similar relationship has been found between the diffusion length ( $L$ ) and frequency ( $f$ ) (Gerrard 1966). Also, as  $L_f$  increases, the base pressure coefficient ( $C_{PB}$ ; and subsequently the  $C_D$ ) decreases (Williamson 1996). Also, an over-arching pattern in vortex-wake dynamics is that the point of transition to turbulence moves

upstream as the flow transitions: first the wake becomes turbulent, then the free shear layers, and finally the boundary layer. While the study of flow around an infinitely long cylinder has resulted in significant insight, it is often the case that flows interact with an array of obstacles of various geometries where the individual shear layers and wakes interact increasing the complexity. This is the case in flows through porous media such as packed beds.

### 2.3.2 Flow through Packed Beds

The bulk of the theory of flow through a porous material is focused on ground water flow (flow through soils and/or porous rock) and flow through packed beds (or columns). The flow through packed beds is the closest to single-phase flow through RPM and therefore will be discussed in this section. Packed beds are defined as a number of particles dumped into a container where fluid can flow through the void spaces between the particles (*Figure 2-12*). These packed beds can be ‘fixed’ where the particle bed is static, unable to move, or ‘fluidized’ where the particles are in motion. While the packed columns for liquid/gas contacting (for which the RPM is typically used) are fixed, they are often modeled as fluidized due to the variable porosities as a result of the liquid holdup that occurs (Stichmair et al. 1988).

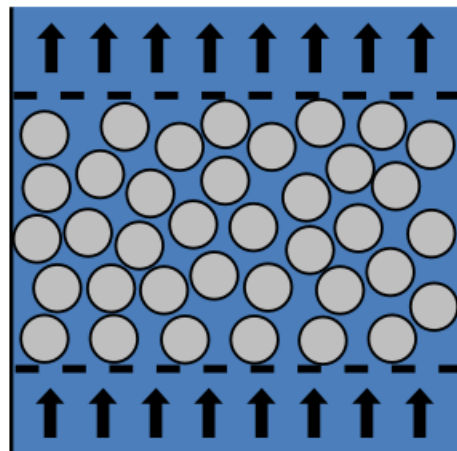


*Figure 2-12: Generic Schematic of a packed bed*  
(image credit: [https://neutrium.net/fluid\\_flow/pressure-drop-through-a-packed-bed/](https://neutrium.net/fluid_flow/pressure-drop-through-a-packed-bed/))

### 2.3.2.1 Parameters

For spherical particles, there are four different packing regimes: hexagonal, face centered cubic, simple cubic, and unstructured. The packing regime of interest is an unstructured or ‘random’ packing regime where the particle packing is heterogeneous and statistically cannot be replicated (Baker, 2011). This poses a challenge when researching flow phenomena. In order for packed beds to be studied mathematically, they are described using a variety of parameters.

#### 2.3.2.1.1 Particle Equivalent Diameter

The particles can be uniform in size and/or shape or irregular. The simplest case is a spherical particle which can be defined by its diameter. If the particles are not spherical, they can be represented by a sphere of equivalent volume which can then be described by the equivalent diameter and by the sphericity (a particle’s deviation from a sphere,  $\phi_s$ ) (Sissom & Pitts 1972).

The particle equivalent diameter ( $d_p$ ) is defined below where  $a_p$  is the specific particle surface area and  $\varepsilon$  is the porosity:

$$d_p = \frac{6(1-\varepsilon)}{a_p}. \quad 2-28$$

The particle equivalent diameter, though useful, does not eliminate the effect of the geometry of the particle shape (Aris 1957).

#### 2.3.2.1.2 Hydraulic Radius

The hydraulic radius ( $R_h$ ) of a packed bed is defined as the fluid volume ( $V_v$ ) divided by the wetted surface area of the particles. Simplified, the equation becomes:

$$R_h = \frac{d_p}{6} \left( \frac{\varepsilon}{1-\varepsilon} \right). \quad 2-29$$

### 2.3.2.1.3 Aspect Ratio

The primary dimensionless geometric property used to characterize a packed bed is the aspect ratio ( $A_{ratio}$ ). The  $A_{ratio}$  is the ratio of the  $d_p$  to the diameter of the column ( $D$ ):

$$A_{ratio} = \frac{D}{d_p}. \quad 2-30$$

Packed beds are often categorized as having either a high  $A_{ratio}$  or a low  $A_{ratio}$ ; *Figure 2-13* below illustrates the difference. Intuitively, the velocity profile through a packed bed with a high  $A_{ratio}$  will be objectively uniform across and is often represented as a pseudo-homogenous network of capillaries of uniform flowrates. A low  $A_{ratio}$ , however, is in-homogeneous with varying sizes of void spaces and therefore a more ‘disordered’ flow network. Though not well defined, an  $A_{ratio}$  greater than 50 is considered to be ‘low’ and less than 50 ‘high’. (Baker 2011)

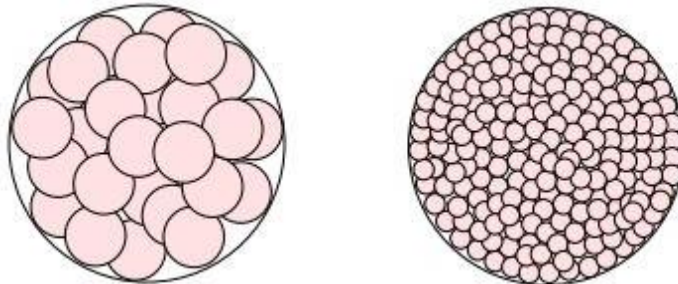


*Figure 2-13: Schematics of a low  $A_{ratio}$  (left) and high  $A_{ratio}$  (right) (Baker 2011)*

The bed length ( $L$ ) is also non-dimensionalized by the equivalent particle diameter as defined below:

$$H_{ratio} = \frac{L}{d_p}. \quad 2-31$$

### 2.3.2.1.4 Porosity

The porosity ( $\varepsilon$ ) of a packed column is defined as the ratio of the volume of the voids within the bed ( $V_v$ ) to the total volume ( $V$ ):

$$\varepsilon = \frac{V_v}{V}. \quad 2-32$$

### 2.3.2.1.5 Tortuosity

The tortuosity ( $\beta$ ) describes the indirect path a fluid particle can take from the entrance of the packed column to the exit as seen in *Figure 2-14* and is defined by the following equation where  $L_e$  is the route of the particle. It should be noted that  $L_e$  is difficult to determine.

$$\beta = \frac{L_e}{L} . \quad 2-33$$

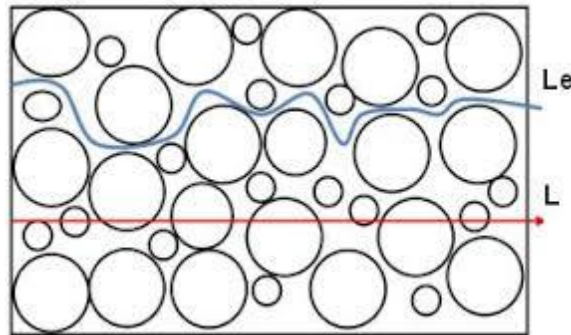


*Figure 2-14: Schematic displaying the concept of tortuosity*  
(image credit: [http://www.groundwatersoftware.com/v9\\_n10\\_tortuosity.htm](http://www.groundwatersoftware.com/v9_n10_tortuosity.htm))

### 2.3.2.1.6 Superficial Velocity

The superficial velocity ( $U$ ) is the velocity of the flow that would occur in the absence of any particles. It is determined by the volumetric flow rate ( $Q$ ) divided by the cross-sectional area of the column ( $A$ ):

$$U = \frac{Q}{A} . \quad 2-34$$

### 2.3.2.1.7 Interstitial Velocity

The interstitial velocity ( $u$ ) is the (global) average velocity of the flow through the pores between particles and is calculated by dividing the superficial velocity by the porosity:

$$u = \frac{U}{\varepsilon} . \quad 2-35$$

### 2.3.2.1.8 Packed Bed Reynolds Number

The Reynolds number ( $Re$ ) of flow in a closed conduit (i.e. pipe flow) is defined using the diameter of the conduit as the characteristic length:

$$Re = \frac{UD}{\nu} . \quad 2-36$$

For pipe flow, a  $Re < 2,300$  is considered to be laminar (White 2003). In a laminar flow the fluid shear layers are orderly and parallel, viscosity effects are dominant, and the velocity profile is parabolic. If the  $Re > 4,000$  then the pipe flow is considered to be turbulent. Turbulent flow is described as chaotic, random, and highly three-dimensional (with the formation of vortices). For  $2,300 < Re < 4,000$ , the flow is considered transitional. (Cengel & Cimbala 2006)

In a packed bed or column (e.g. a pipe filled with particles), the flow can similarly be described using a  $Re$ . There are, however, various  $Re$  based upon different parameters and length scales.

The particle  $Re$  ( $Re_{dp}$ ) uses the equivalent particle diameter as the characteristic length such that:

$$Re_{dp} = \frac{Ud_p}{\nu} . \quad 2-37$$

Using the  $Re_{dp}$ , the flow is considered to be laminar for  $Re_{dp} < 10$  and turbulent if  $Re_{dp} > 300$  (transitional if  $10 < Re_{dp} < 300$ ) (Ziolkowska & Ziolkowska 1988). Since the pore spaces are variable in a random packing regime it is likely that the flow could be laminar in one location and turbulent in another within the internal structure. Furthermore, due to the variable void spaces a flow converging from a larger pore to a smaller pore would dampen larger scale vortices and consequently 're-laminarize'. The issue with the dye-injection studies used to determine the  $Re_{crit}$  values above is that once the streakline has broken up it cannot return to a streakline and the re-laminarization is not detected.

Generally, for a low  $A_{ratio}$  bed, it is unlikely that the entire bed would experience turbulent flow. On the other hand, for a very high  $A_{ratio}$  bed ( $A_{ratio} > 500$ ), it is likely that the flow would almost always be laminar since the pore size is smaller than the smallest turbulent structures governed by the Kolmogorov length scale. (Baker 2011)

### 2.3.2.2 Theory of Flow through Packed Beds

The pressure drop ( $\Delta P$ ) associated with flow through packed beds (or columns) is of primary importance for scientists and engineers. The best way to determine the  $\Delta P$  through a packed bed is an experimental investigation of the particular system. This, of course, is tedious and time consuming. Simple mathematical models have been developed to approximate the  $\Delta P$  within acceptable engineering requirements. Packed beds are essentially a ‘partially blocked pipe’ in which the blockage causes a back pressure (or  $\Delta P$ ). The  $\Delta P$  is dependent upon the ease with which the fluid can flow through the porous media. In pipe flow the pressure drop is associated with the head loss ( $h_L$ ) where  $\gamma$  is the specific weight of the fluid:

$$h_L = \frac{\Delta P}{\gamma}. \quad 2-38$$

The  $\Delta P$  in a packed bed is a function of properties of the bed, fluid, and flow. Theoretical and empirical correlations have been derived to connect these parameters and form a  $\Delta P$  equation:

$$\Delta P = f(\varepsilon, \beta, d_p, D, L, Re). \quad 2-39$$

There are both linear and non-linear models that have been developed over the course of the last 200 years.

#### 2.3.2.2.1 Linear Flow Models

The earliest theory for flow through a (fixed) porous media is based on a ‘theoretical tubes model’ wherein the voids in a porous media are likened to a series of pipes of varying lengths.

Darcy's law was developed empirically and supported using dimensional analysis (Darcy 1856). Darcy's law is analogous to Ohm's law of resistance and Fick's law of diffusion (Dullen 1992). Due to the assumption that the flow through the porous media is a Hagen-Poiseuille flow, Darcy's law can only be applied at low  $Re$  (laminar flow). For steady, laminar, Newtonian flow, the  $\Delta P$  is related to the velocity by the following equation where  $\mu$  is the dynamic viscosity of the fluid and  $k_p$  is the permeability of the porous media:

$$\frac{\Delta P}{L} = -\frac{\mu u}{k_p} . \quad 2-40$$

Brinkman (1947) added a viscous shear term to Darcy's law to describe the boundary layers within a porous media. The Brinkman extended Darcy's Law is defined as:

$$\nabla P = -\frac{\mu u}{k} + \mu' \nabla u . \quad 2-41$$

The Deprit-Forcheimer Relation was proposed by Blake (1922) who modified Darcy's equation by using the superficial velocity ( $U$ ) instead of the interstitial velocity ( $u$ ). Blake (1922) also determined the permeability of the porous media empirically using the hydraulic radius ( $R_h$ ):

$$k = \frac{R_h^2 \varepsilon}{k_2} . \quad 2-42$$

In order to extend the applicability to larger  $Re$ , Kozeny modeled a packed bed as a 'bundle of small diameter tubes' (capillary model) (Kozeny & Sitzber 1927; Strigle 1994) which led to the modified Hagen-Poiseuille relationship which assumes the tubes to be of equal length:

$$\frac{\Delta P}{L} = 72 \frac{U \mu L (1-\varepsilon)^2}{d_p \varepsilon^3} . \quad 2-43$$

Flow through a packed column, however, is a complex network of heterogeneously interconnecting flow paths, thereby taking a longer path than the theoretical tubes (Strigle 1994). From empirical data, Carmen (1937) added a coefficient of 25/12 to the modified Hagen-

Poiseuille relationship to account for the tortuosity. This is known as the Carmen-Kozeny (or Blake -Kozeny) Equation:

$$\frac{\Delta P}{L} = 150 \frac{U\mu(1-\varepsilon)^2}{d_p^2 \varepsilon^3} \quad 2-44$$

If rearranged, the non-dimensional coefficient becomes:

$$C_{C-K} = 150 \frac{(1-\varepsilon)^2}{\varepsilon} \quad 2-45$$

Still, when the flow is turbulent the Carmen-Kozeny Equation does not hold when there are larger kinetic energy losses (Strigle 1994). This led to the development of non-linear models.

### 2.3.2.2.2 Non-Linear Flow Models

While the Hagen-Poiseuille relationship models laminar flow through a pipe, the Darcy-Weisbach Equation models laminar and turbulent flow through a pipe:

$$\Delta P = f \left( \frac{L}{D} \right) \frac{u^2}{2g} . \quad 2-46$$

Using the Darcy-Weisbach relation, Burke & Plummer (1928) substituted in the superficial velocity and the hydraulic radius and through an empirical study determined the following for (fixed) packed beds (only valid for  $Re_p > 1,000$  (Bird et al. 1960)):

$$\Delta P = 1.75 \left( \frac{L}{d_p} \right) \frac{U^2(1-\varepsilon)}{\varepsilon^3} . \quad 2-47$$

Ergun (1952) combined the Carmen-Kozeny and Burke & Plummer equations to get:

$$\frac{\Delta P}{L} = 150 \frac{U\mu(1-\varepsilon)^2}{d_p^2 \varepsilon^3} + 1.75 \frac{U^2(1-\varepsilon)}{d_p \varepsilon^3} . \quad 2-48$$

Similarly, if rearranged, the non-dimensional coefficient becomes:

$$C_{B-P} = 1.75 \frac{(1-\varepsilon)}{\varepsilon^3} . \quad 2-49$$

The coefficients of the Ergun equation ( $C_{C-K}$  and  $C_{B-P}$ ) are based on empirical studies by Carmen (1937) and Burke & Plummer (1928) which were mostly on packed beds with high  $A_{ratio}$ . Further studies have suggested that the Ergun equation is only valid for  $Re_{dp}/(1 - \varepsilon) < 500$  (Hicks 1970) and that it under predicts at low  $Re_{dp}$  ( $Re_{dp}/(1 - \varepsilon) < 10$ ) (Choi et al. 2008). Studies by Handley & Heggs (1968) concluded that the coefficients in the Ergun equation are limited to  $1000 < Re_{dp}/(1 - \varepsilon) < 5000$ . The coefficients have received much attention with conflicting observations (Leva 1959; MacDonald et al. 1979; Plessis & Woudberg 2008; etc.). Within the accepted range of  $Re_{dp}$ , the Ergun equation (based on the capillary model) has shown to fit well for  $0.35 < \varepsilon < 0.55$  (Nemec & Levec 2005). However, Rumpf & Gupte (1971) through studying a larger range of porosity ( $0.35 < \varepsilon < 0.7$ ) determined a different dependence on porosity that agrees closer to the fluidized bed model. Since the porosities of the RPM of interest are higher ( $0.6 < \varepsilon < 0.98$ ), the fluidized bed model is often considered a better fit.

For a fluidized bed, Richardson & Zaki (1954) developed a relationship between the fluid velocity and the porosity where  $U_s$  is the superficial velocity to suspend a multitude of particles,  $U_0$  is the superficial velocity required to suspend a single particle, and  $n$  is a function of  $Re_{dp}$  ( $n = 4.65$  for laminar and  $\approx 4.65/2$  for turbulent; Richardson & Zaki 1954).

For all of the studies of packed and fluidized beds (or columns) the flow upstream of the bed is uniform across the cross-sectional area of the column containing the particles. This, however, is not the case for RPM being used to enhance the hydraulic disinfection efficiency of SWTSSs. The inflow into a contact basin comes from a pipe which creates a turbulent jet. A jet of water entering a ‘bed’ of RPM would behave differently than a uniform flow and subsequently the  $\Delta P$  would most likely be different as well.

In order to increase the effective volume of a disinfection contact tank, it is vital to slow down and disperse the incoming turbulent jet at the inlet. However, in relation to the added head loss due to drag, it is not cost effective to completely fill the tank with RPM to achieve greater hydraulic disinfection efficiency because even SWTSs use relatively large tanks; not to mention the upfront cost of RPM. This requires an investigation into how the hydraulic disinfection efficiency is related to how the turbulent jet spreads and decays as well as the ‘cost-benefit-analysis’ with the added drag.

## 2.4 Hydraulic Disinfection Efficiency

### 2.4.1 $CT$

The method of ‘ $CT$ ’ is used in the US to ensure that drinking water is fully disinfected before it reaches any consumer’s tap (USEPA 2003).  $CT$  is a product of the disinfectant residual concentration at the outlet of the contact system ( $C$ , typically measured in mg/L) multiplied by the characteristic time ( $T$  (min)) in which the disinfectant is in contact with the water. The required  $CT$  ( $CT_{req}$ ) to ensure sufficient disinfection of drinking water varies based on the disinfectant used, the type of microorganism, temperature, and pH. An example table of  $CT$  values is shown in *Table 2-2*. Then there is the calculated  $CT$  ( $CT_{calc}$ ) that is dependent upon the particular system. In the US, the characteristic time used in  $CT_{calc}$  calculations is ‘ $T_{10}$ ’, which is the time at which 10% of a given disinfectant concentration is observed at the outlet of the system (USEPA 2003).

$$CT = CT_{10} . \qquad 2-50$$

This  $T_{10}$  is used as a conservative estimate due to the inefficient internal hydraulics of contact basins demonstrated in *Figure 2-15*.

*Table 2-2: “CT values for Inactivation of Viruses by Free Chlorine” (USEPA 2003)*

	Log Inactivation					
	2.0		3.0		4.0	
pH	6-9	10	6-9	10	6-9	10
Temperature (°C)						
0.5	6	45	9	66	12	90
5	4	30	6	44	8	60
10	3	22	4	33	6	45
15	2	15	3	22	4	30
20	1	11	2	16	3	22
25	1	7	1	11	2	15

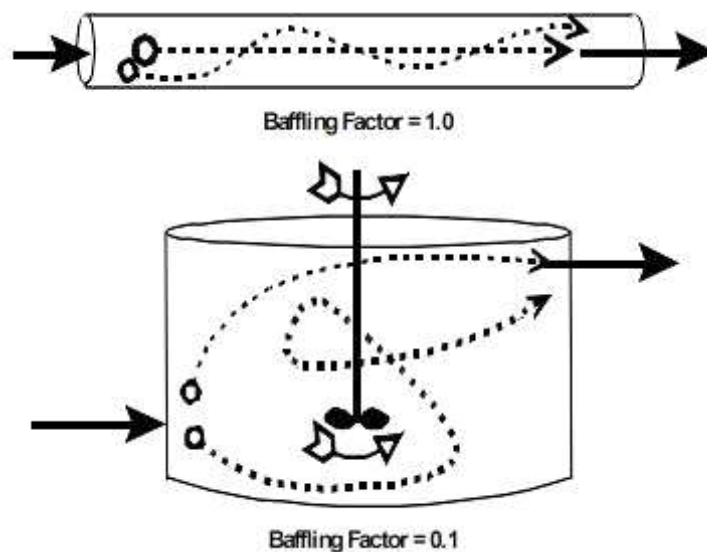


*Figure 2-15: Schematics to demonstrate ‘plug flow’ (top) versus ‘short-circuiting’ (bottom) (USEPA 2003)*

The  $CT_{req}$ , dictated by the microbiological requirements, and the  $CT_{calc}$ , dependent on the system, are used to determine the ‘actual’ log inactivation (USEPA 2003) of pathogenic microorganisms:

$$Actual\ Log\ Inactivation = (log\#) \left( \frac{CT_{calc}}{CT_{req}} \right). \quad 2-51$$

## 2.4.2 Baffling Factor

The USEPA has designated a parameter to measure hydraulic disinfection efficiency, e.g. revealing the effects of short-circuiting, called the baffling factor ( $BF$ ). The  $BF$  is the ratio of  $T_{10}$  over the theoretical detention time ( $TDT$ ):

$$BF = \frac{T_{10}}{TDT}, \quad 2-52$$

where  $TDT$  is calculated from the system volume during operation ( $V$ ) divided by the maximum flow-rate of the system ( $Q$ ):

$$TDT = \frac{V}{Q}. \quad 2-53$$

As a normalized parameter, a  $BF$  of 1 is indicative of ideal ‘plug flow’ conditions, which implies that the fluid moves with a uniform velocity over the cross-sectional area of the tank. Of course, in practical application some level of short-circuiting and recirculation, or ‘dead zones’, occur. The differing extent of short-circuiting that occurs is influenced by the geometry of the tank as well as the incoming flow velocity, inlet location, and inlet-outlet orientation. The inclusion of the  $BF$  of a contact basin adjusts the  $TDT$  to a more realistic value of the characteristic contact time.

The USEPA suggests that the  $BF$  of a system can be estimated using *Table 2-3* (USEPA 2003). However, preliminary tracer studies and computational flow modeling studies performed on full-scale SWTSSs ranging in volume from 25 gallons to 1500 gallons indicate that the  $BF$ s listed in *Table 2-3* are not necessarily applicable to SWTSSs, and often over predict the  $BF$  for both small and large systems (CDPHE 2014). Hence, it appears that *Table 2-3* should not be blindly used as a justification for claiming credit of a  $BF$  unless more detailed descriptions of a SWTSS is given. This, however, would be difficult due to the wide variety of SWTSSs designs.

Table 2-3: Baffling Factors by Qualitative Description of Contact Tank (USEPA 2003)

<b>Baffling Condition</b>	<b>BF</b>	<b>Baffling Description</b>
Unbaffled (mixed flow)	0.1	None, agitated basin, very low length to width ratio, high inlet and outlet flow velocities
Poor	0.3	Single or multiple unbaffled inlets and outlets, no intra-basin baffles
Average	0.5	Baffled inlet or outlet with some intra-basin baffles
Superior	0.7	Perforated inlet baffle, serpentine or perforated intra-basin baffles, outlet weir or perforated launders
Perfect (plug flow)	1.0	Very high length to width ratio (pipeline flow), perforated inlet and outlet, and intra-basin baffles

### 2.4.3 Use of RPM to Improve *BF*

The *Baffling Factor Guidance Manual* proposed multiple simple and cost-effective modifications and innovative technologies to improve the hydraulic disinfection efficiency in terms of *BF* of contact basins for SWTS (CDPHE 2014). One of the innovative technologies proposed was the use of RPM. There have been two studies conducted at the laboratory-scale investigating the use of RPM to improve the *BF* of (1) a cylindrical tank and (2) a baffled concrete tank.

#### 2.4.3.1 Random Packing Material in a Cylindrical Tank

An initial study of the use of RPM in a cylindrical tank was conducted by Barnett et al. (2014). In this laboratory-scale study, two laboratory-scale (25 and 50-gallon) tanks, with varying sizes and amounts of spherical RPM were investigated at multiple flow rates. Results of this study showed first and foremost that the presence of RPM in a cylindrical tank created near plug flow conditions ( $BF \sim 0.9$ ) as seen in the residence time distribution curve (RTD curve; see Section 3.2.2.1.1) in *Figure 2-16* below (Barnett et al. 2014). The different sizes of RPM studied had

similar porosities (~90%) but the smaller RPM is able to become intricately packed making the space between the RPM elements smaller, decreasing the permeability. The size of the RPM, while it had some effect, did not influence the  $BF$  considerably (Barnett et al. 2014).

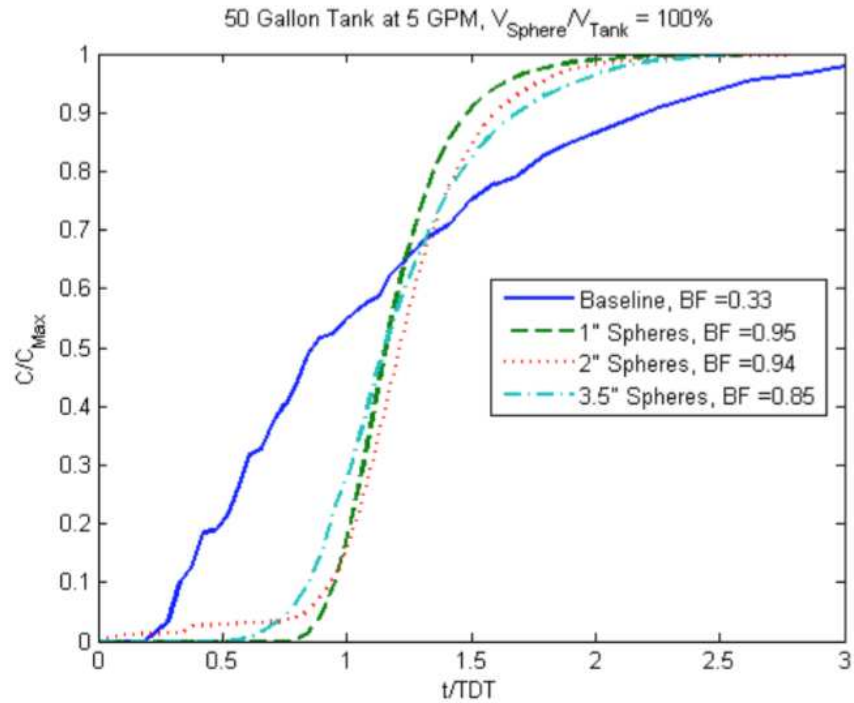


Figure 2-16: RTD curve of 50-gallon cylindrical tank completely filled with RPM (Barnett 2014)

As the amount of RPM ( $V_{packing}/V_{tank}$ ) was increased, the shape of the RTD curves seen in Figure 2-17a indicated that the flow became more uniform. A positive linear correlation between the amount of RPM and the  $BF$  was also determined (Figure 2-17b) (Barnett et al. 2014). It was noted in the Barnett et al. (2014) study that the RPM were not secured in any particular location. Due to the material composition (PP) the RPM used floated near the outlet. Therefore, the greater the  $V_{packing}/V_{tank}$  ratio, the closer to the inlet the RPM was, and therefore, the sooner the turbulent jet caused by the sharp inlet was dispersed. The sooner the inflow jet is dispersed, the more of the total volume of the tank ( $V_{tank}$ ) becomes ‘effective’. The effective volume ( $V_{eff}$ ) was calculated as follows (Barnett et al. 2014):

$$V_{eff} = BF \left( V_{tank} - (1 - \varepsilon) \left( \frac{V_{packing}}{V_{tank}} \right) (V_{tank}) \right). \quad 2-54$$

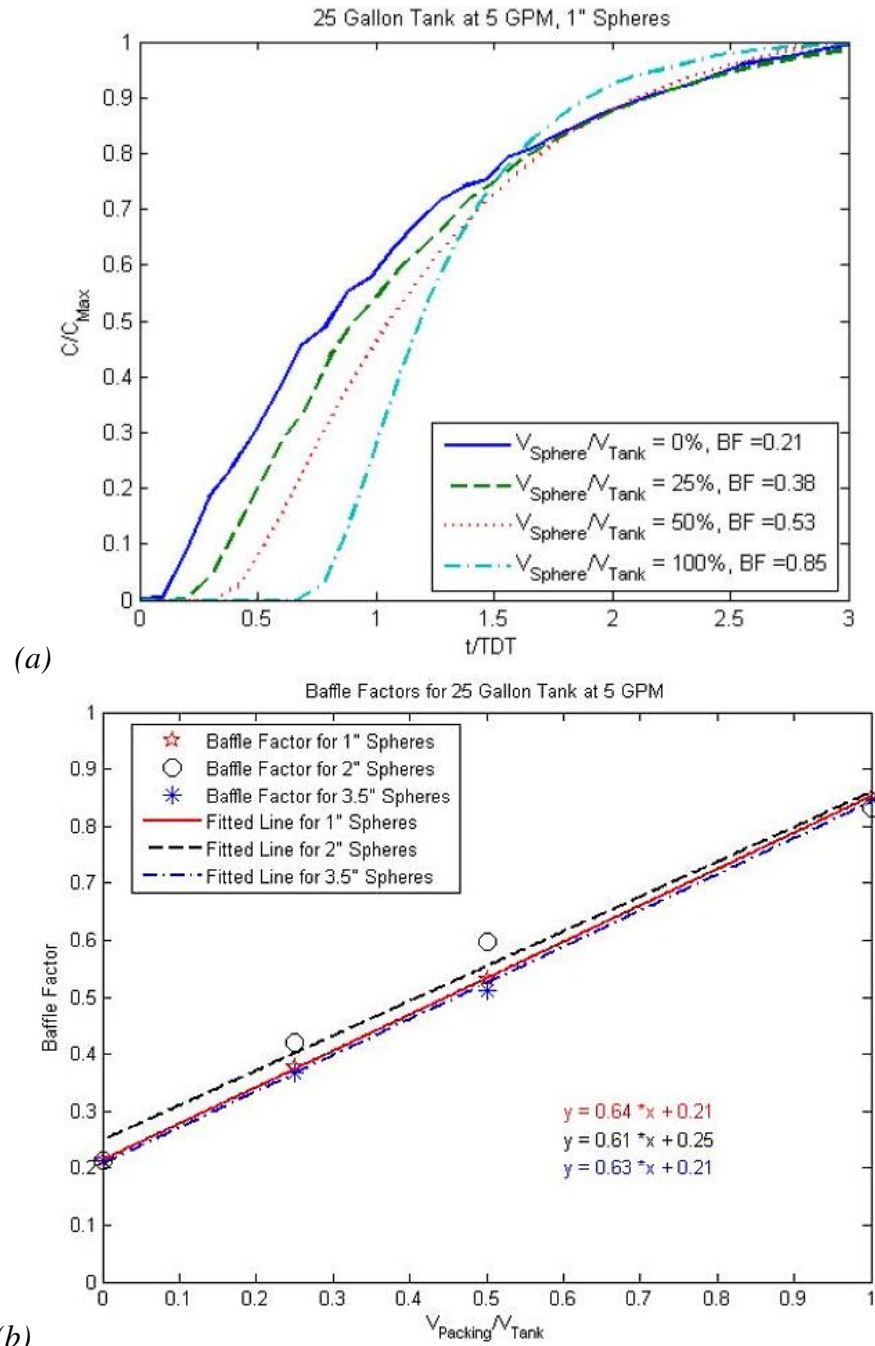


Figure 2-17: (a) RTD curves from 1" RPM in a 25-gallon tank and (b) BF for three RPM sizes with different RPM fill amounts (%) (Barnett 2014)

While cylindrical tanks are frequently used they are not the only type of contact basin used in SWTS; baffled tanks are also common (where the term ‘baffling factor’ is derived). The

geometry of a baffled tank is different, which means that the flow within the tank will also be different. While the RPM showed promising results in cylindrical tanks, this study did not cover how RPM could be applied in a rectangular and/or baffled tank.

### 2.4.3.2 Random Packing Material Used to Create ‘Porous Walls’ in a Baffled Tank

Similar to a cylindrical tank, the inlet to a rectangular and/or baffled tank is typically a sharp inlet that produces a turbulent jet that induces short-circuiting and areas of recirculation or ‘dead zones’. This phenomena results in a poor  $BF$ , reducing the  $V_{eff}$  of the contact tank (Kattnig 2014). Based on the results of the previous study (Barnett et al. 2014), RPM was used to disperse the inflow jet and thereby enhance the hydraulic disinfection efficiency of a rectangular tank. Inlet boxes (filled with 2” spherical RPM) of different arbitrary dimensions for the length ( $L_B$ ) and height ( $H_B$ ) were constructed and secured at the inlet of a 1500 gallon rectangular concrete tank as seen in *Figure 2-18*.

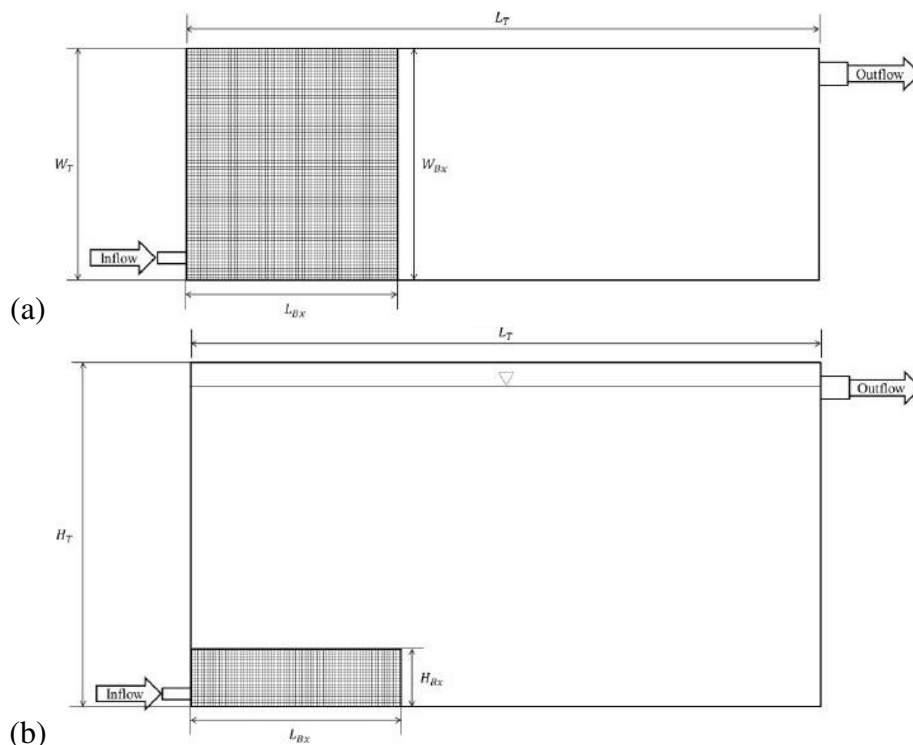


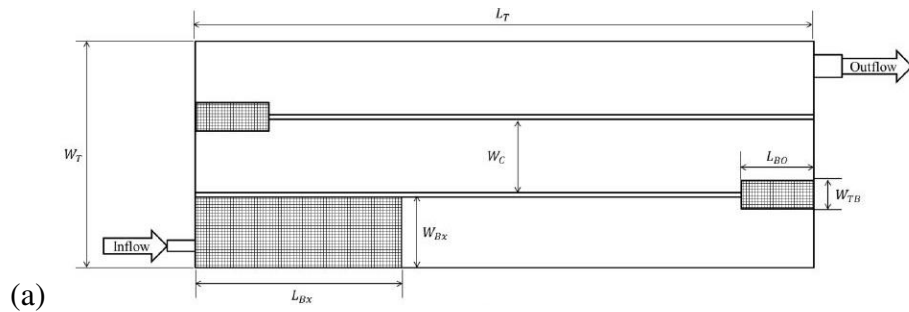
*Figure 2-18: (a) Plan View and (b) Side View of a Generalized Inlet Box System (Kattnig 2014)*

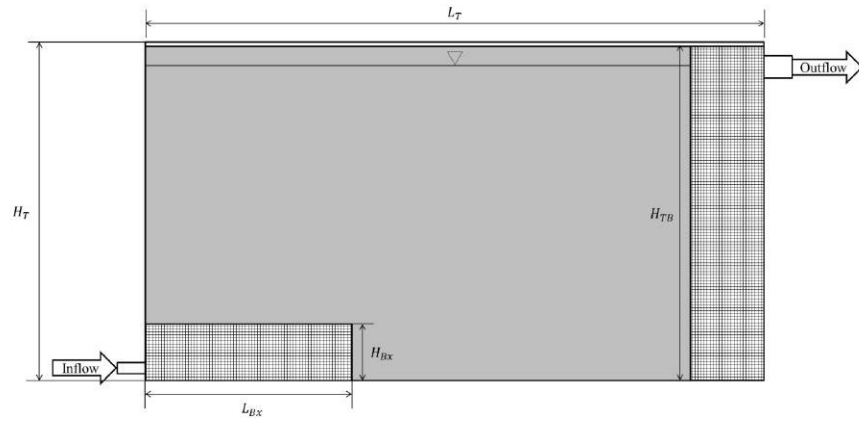
The results of this study shown in *Table 2-4* indicated that the presence of an inlet box significantly improved the *BF* of that particular system by 300-720% (Kattnig 2014). The results also showed that the *BF* increased as the length of the inlet box increased. The fact that the length of the inlet box had a substantial influence makes sense when considering that the length of the inlet box was parallel with the direction of the turbulent jet and consequently the direction the majority of the momentum of the inflow (Kattnig 2014). The height of the inlet box, however, did not have a major influence (Kattnig 2014).

*Table 2-4: Inlet Box Parametric Study Results (Kattnig 2014)*

Flow Rate ( $Q$ , ft <sup>3</sup> /s)	Box Dimensions ( $H_B \times L_B$ ) <i>BF</i>					
	Base Case (no box)	1 ft X 1 ft	1 ft X 2 ft	1 ft X 4 ft	2 ft X 1 ft	2 ft X 2 ft
10	0.05	0.19	0.21	0.26	0.25	0.22
20	0.05	0.21	0.30	0.33	0.25	0.28
40	0.05	0.24	0.34	0.36	0.28	0.15

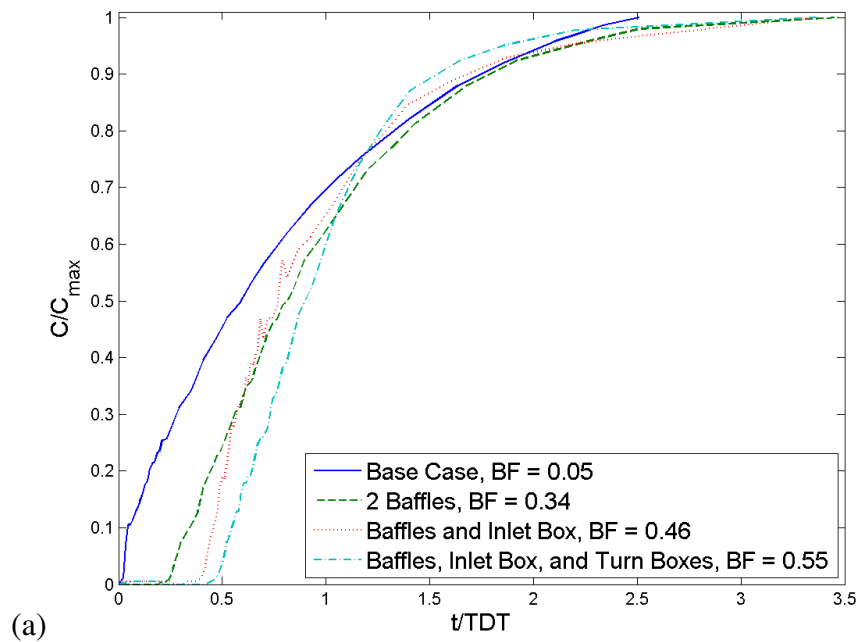
Besides the turbulent jet at the inlet of the tank, locations of substantial flow separation occur at the ends of baffle walls (baffle turns) due to the momentum of the fluid flow. Based on this knowledge, turn boxes filled with RPM to create porous walls were constructed and installed to promote uniform flow in these critical locations (see *Figure 2-19*).

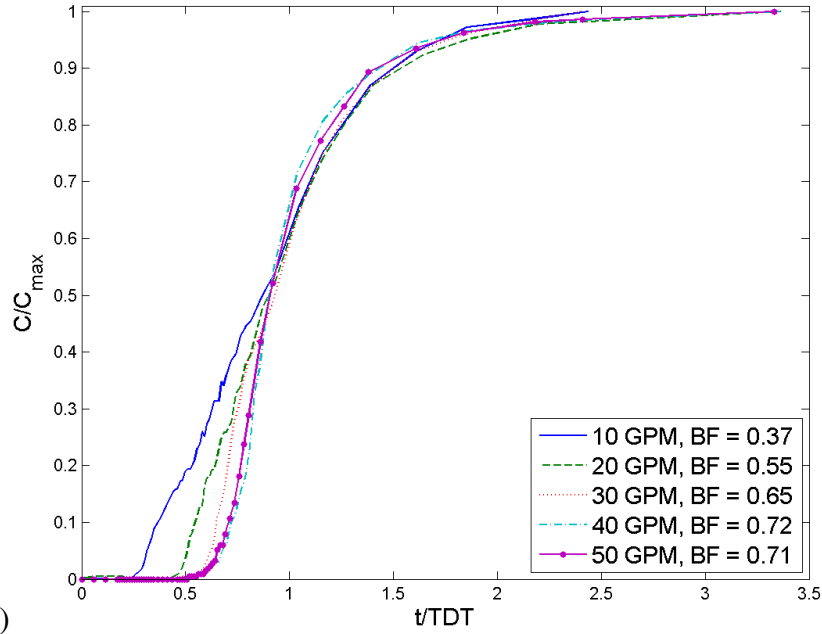




(b) Figure 2-19: (a) Plan view and (b) Side view of a generalized turn box system (Kattnig 2014)

Compared to the rectangular tank with unmodified baffle walls, the presence of inlet and turn boxes filled with RPM improved the *BF* of this system by 35-62% (Figure 2-20a). The flow rate through this system was also varied. The results in Figure 2-20b show that the higher the flow rate the greater the impact the porous walls (RPM) had in enhancing the hydraulic disinfection efficiency. In this system, the *BF* peaked around 0.7 (at 40 gpm) indicating that there is a practical ceiling of enhancement in terms of operational flow rates. (Kattnig & Venayagamoorthy 2015)





(b)

Figure 2-20: Resulting RTD Curves for (a) All Tested Systems at a Flow Rate of 20 GPM and (b) the Turn Box System at Various Flow Rates (Kattnig 2014)

This study demonstrated that RPM can be used to enhance the hydraulic disinfection efficiency (1) in contact basins other than cylindrical tanks and (2) by strategic placement in critical locations such as near the inlet (turbulent jet) and baffle tips (where flow separation occurs). It should be noted, however, that the designs of the inlet and turn boxes in this study were arbitrary, as there is no theory of jet flow through a highly porous media as of yet, and were specific to the tank used for the study. The  $H_B$  and  $L_B$  of the inlet box were compared to the diameter of the turbulent jet (inlet pipe) ( $D_{inlet}$ ) in an attempt produce a generalized design recommendation, leading to the recommendation for the inlet box design to be  $20 < L_B/D_{inlet} < 30$  and  $H_B/D_{inlet}$  (Kattnig & Venayagamoorthy 2015). A more extensive study is necessary to develop better design criteria based on a fundamental understanding of turbulent jet flow through a highly porous media such as RPM.

Despite the promising benefit in terms of decreased short-circuiting and increased residence time, which results in improved  $BF$  (and therefore  $CT$ ), there are practical concerns surrounding

the use of RPM in this context. While the NSF/ANSI 61 certification ensures the chemical safety for use in drinking water, it “*does not establish performance, taste and odor, or microbial growth support requirements for drinking water system products, components, or materials*” (NSF/ANSI 2016). The relevant concern of using RPM in contact tanks, even if NSF/ANSI 61 certified, is the potential for substantial biofilm growth due to the quality of water entering a contact basin combined with the high surface area of RPM (exploited in trickling filters, see Section 2.1.2). This requires an investigation into the formation and growth of biofilms, particularly in water systems.

## 2.5 Biofilm

A biofilm is a natural phenomenon where individual bacteria interact to form ‘highly structured matrix-enclosed communities’ that protect the individual bacteria that make up the biofilm (Stoodley et al. 2002). There are multiple mechanisms by which a biofilm can form including redistribution of attached cells, binary division of attached cells, and/or aggregation of cells from the bulk fluid to the developing biofilm (Stoodley et al. 2002). There are five stages in the formation of a biofilm (see *Figure 2-21*) beginning with individual bacteria attaching to a surface that start to form microcolonies.

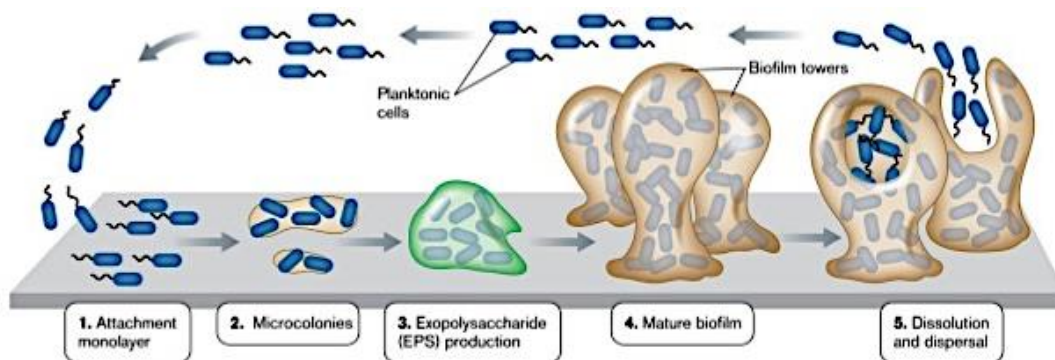


*Figure 2-21: A schematic of the formation of a biofilm (image credit: hiimtia 2012)*

As these microcolonies grow, exopolysaccharides (EPS) are produced which create a structure or ‘film’ that results in a firmer attachment. Once a biofilm is mature, sections will start to dissociate from the surface, known as sloughing. At this stage, any bacteria from a biofilm will be detectable in a water sample. From a hydraulics perspective, intuition suggests that a turbulent flow may prevent the formation of a biofilm; however, studies have shown that biofilm structures become elongated and form ‘mats’ as well as become denser and stronger in turbulent flows (Stoodley et al., 2002).

### 2.5.1 Biofilms in Water Treatment Systems

Biofilms are ubiquitous throughout water treatment and distribution systems (Hou et al., 2018). A number of studies have been conducted that indicate the presence of biofilms in filters (specifically granulated activated carbon (GAC) filters), after disinfection, and in distribution systems (Schwartz et al., 1998). A study by Hou et al. (2018) looked at the microbial community and activity throughout an entire water treatment system – how it changed from treatment stage to stage (spatially) as well as season to season (temporally). The results below (*Figure 2-22*) show that not only are bacteria prevalent, but diverse and variable.

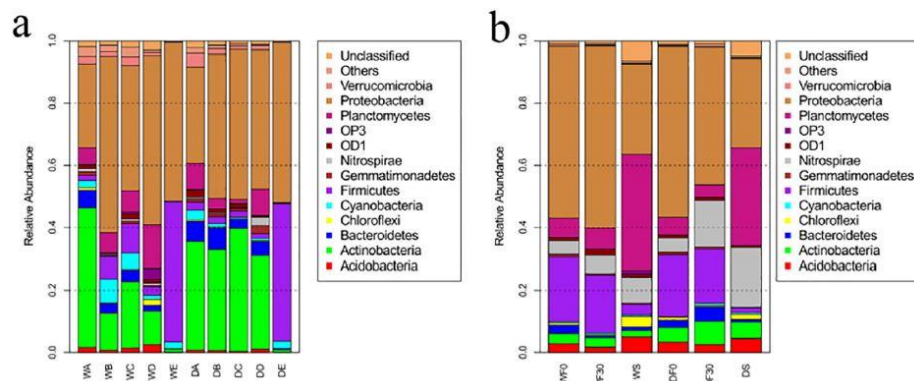


*Figure 2-22: Relative abundances of bacterial community composition (phylum level) detected in (a) DWTP bulk water samples; (b) BAC biofilm samples. [Abbreviations: W, wet season; D, dry season; A, raw water; B: grid reaction tank effluent; C: settling pond effluent; D: BAC filter effluent; E: finished water; F0: the top GAC samples; F30: The bottom GAC samples; S: the top sand samples.] (Hou et al. 2018)*

Biofilms will develop on inert surfaces including stainless steel and PVC, which are commonly used in water treatment systems. Even when drinking water is treated with free chlorine, biofilms have still been shown to develop (Pedersen 1990). The EPS matrix that biofilms produce protect bacteria from the oxidative effects of disinfectants such as chlorine (Christensen et al. 1990). Below are photographs of stainless steel and rubber surfaces in drinking water systems (*Figure 2-23* and *Figure 2-24*) where the presence of biofilms are visible. Moreover, bacteria from chlorinated water systems have been reported to be more resistant to chlorine than bacteria in non-chlorinated water systems (Pedersen 1990). Therefore, it is not surprising that the contamination of drinking water (coliform bacteria) often originates from biofilms, particularly re-contamination due to the high prevalence of biofilms throughout the drinking water distribution systems (Kilb et al. 2003).

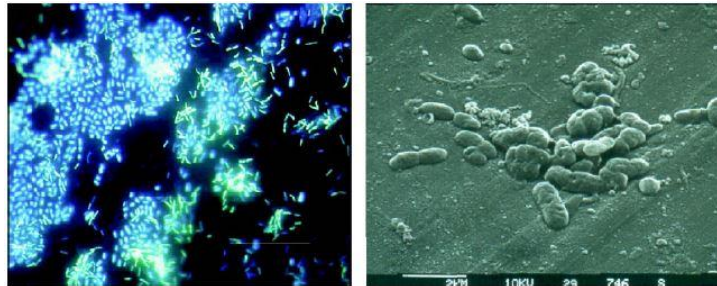


*Figure 2-23: Photograph of drinking water biofilm under 1000× magnification (left) and a Microcolony (right) on a stainless steel surface after 14 days of exposure to drinking water (Wingender & Flemming 2011)*

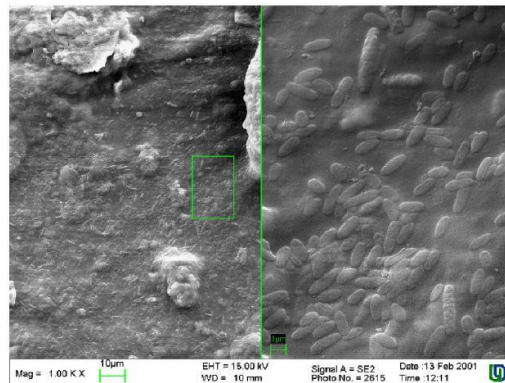


*Figure 2-24: Scanning electron micrograph of a biofilm grown on synthetic rubber in a drinking water system (left) and under magnification (right). (Wingender & Flemming 2011)*

## 2.6 Summary

The several sections in this chapter present an introduction to RPM, relevant turbulent flows, flows interacting with obstacles, hydraulic disinfection efficiency, and biofilms that create the backbone of the new research presented in this dissertation. Relevant equations, parameters, and terminology are presented as well as a brief review of the basic theoretical models, experimental data, and observational trends.

While there has been a substantial amount of research done on RPM, turbulent jets, packed beds, and biofilms, and the contexts of application are all different. For example, RPM is specifically designed for liquid-gas contacting, not hydraulic enhancement. In trickling filters, the high surface area of RPM is exploited and used as a scaffold to intentionally grow biofilms for wastewater treatment. The presence of biofilms in drinking water treatment, however, are typically an issue in that they are a major source of (re-)contamination. When looking at packed beds, the inflow is uniform across the cross-sectional area of the column, but this would not be the case when using RPM to improve the hydraulic disinfection efficiency of a contact basin. The water entering a contact basin is usually from a pipe that creates a sharp inlet resulting in a turbulent jet. The study of a turbulent jet into an ambient has been significant in understanding the phenomena of turbulence. However there has been little research on turbulent jets into a highly porous media. The dynamics of a jet through RPM would be different simply due to the boundary shear that is not present when a jet flows into an ambient.

To re-purpose RPM to improve the hydraulic disinfection efficiency of SWTSs requires a fundamental study of turbulent jet flow through RPM and empirical studies addressing the practical concerns of the use of RPM in this context (including drag/head loss and biofilm

formation). In order to conduct these studies, appropriate experimental methods must be used. The following chapter presents the experimental methods utilized in the various studies conducted.

# CHAPTER 3

## 3 EXPERIMENTAL METHODS

### 3.1 Flow Velocity Measurements

#### 3.1.1 Introduction

When investigating the hydraulics of a system, whether natural or built, the most important component necessary in order to understand a said system is the velocity field. Therefore, it is paramount that velocity measurements are obtained with adequate accuracy and resolution (spatial and temporal). Spatial resolution refers to the smallest flow scales that can be measured and resolved, whereas the temporal resolution refers the highest data acquisition rate possible (Muste et al. 2017). There are a multitude of different devices available for velocity measurement, which include point-, planar-, and volume-based methods, for different purposes (i.e. field and/or laboratory experiments) (Muste et al. 2017). As most flows of interest are turbulent, the task of velocity measurement can prove to be complex. Therefore, it is important that the researcher understands the method of measurements in order to determine the most appropriate method and/or device for a particular study as well as the procedure of collecting and analyzing data.

Historically, hot-wire anemometry (HWA), which are well suited for low-intensity turbulent flows, and laser-Doppler anemometry/velocimetry (LDA/V), used for long-time averaged high-

intensity fluctuations, have been the most important point-wise methods of velocity measurement. Since the early 2000's, particle image velocimetry (PIV) - a planar-based method, has become the most dominate approach in experimental fluid mechanics (Westerweel et al. 2013).

The velocity measurement devices that were used for this dissertation research include a Laser Doppler Anemometer (LDA) and Particle Image Velocimetry (PIV). The Environmental Fluid Mechanics Laboratory (EFML) at CSU is equipped with a *Dantec FiberFlow* pumped, solid-state, two-dimensional 60 mm diode LDA that is mounted on an *Isel* automated traverse system. The LDA data is collected with *Dantec Burst Spectrum Analyzer* processor and software. The EFML also has a 2D-PIV system with *DaVis 10* software by *LaVision*. Brief description of the method of measurement of these devices are given in the following sections.

### 3.1.2 Laser-Doppler Anemometry

#### 3.1.2.1 Fundamentals of Doppler Shift Method

Laser-Doppler Anemometry (LDA) is an indirect, particle-based technique to attain point-based velocity measurements. LDA is a non-intrusive method that uses laser light to detect the movement of small particles (i.e. tracers) within a fluid flow using the Doppler Effect. Tracers 'scatter' the light from the laser creating a Doppler-shift between the light source and the particle as well as between the particle and the receiver. The Doppler-shift is calculated using the following equation where  $f$  is the frequency ( $f = c/\lambda$  with  $c =$  speed of light),  $\mathbf{u}$  is the velocity,  $n_{sp/pr}$  is the unit-normal vector from the source to the particle/particle to the receiver, and  $\lambda$  is the wavelength:

$$f_0 - f_2 = \frac{\mathbf{u} \cdot (\mathbf{n}_{sp} - \mathbf{n}_{pr})}{\lambda_0} \quad 3-1$$

More often, LDA systems use a pair of intersecting laser beams, which is the case for the LDA in the EFML. As tracers flow through the cross-section (i.e. measuring volume) of the laser beams (Figure 3-1a), they scatter the fringe wavelengths generating Doppler frequencies that are proportional to the particle (and therefore flow) speed (Figure 3-1b). (Muste et al. 2017)

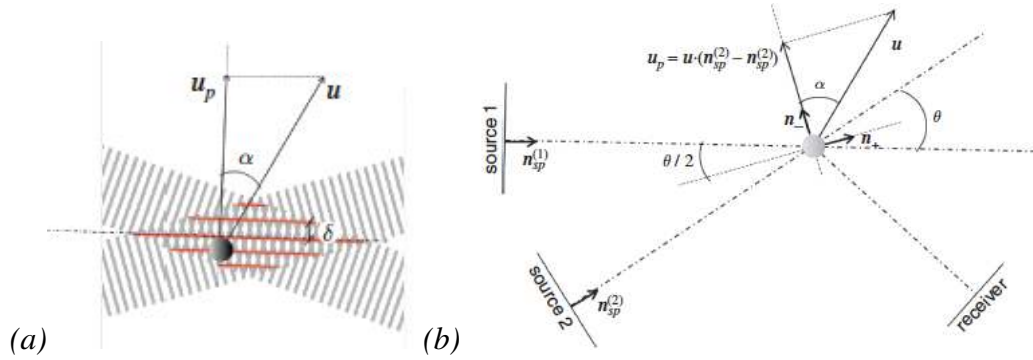


Figure 3-1: Diagrams of (a) the measuring volume [fringe pattern] and (b) how the velocity is determined using a pair of laser beams; where  $\theta$  is the angle between the two laser beams,  $\mathbf{n}_+$  are the unit normal vectors along/orthogonal to the bisector of  $\theta$ ,  $\alpha$  is the angle between the  $\mathbf{u}$  and  $\mathbf{n}_+$  vectors, and  $\delta$  is the spacing between fringes (Muste et al. 2017)

The ‘beat’ or Doppler frequency ( $f_D$ ) can be calculated by taking the difference between the frequencies detected at the receiver ( $f_2$ ) from the two beams:

$$f_D = f_2^{(1)} - f_2^{(2)} = \frac{\mathbf{u} \cdot (\mathbf{n}_{sp}^{(2)} - \mathbf{n}_{sp}^{(1)})}{\lambda_0} = \frac{|\mathbf{u}| |\mathbf{n}_{sp}^{(2)} - \mathbf{n}_{sp}^{(1)}|}{\lambda_0} \cos(\alpha) \quad 3-2$$

It should be noted that the component of the velocity of the particle perpendicular to the bisector in the plane defined by the two laser beams ( $\mathbf{n}_{sp}^{(1)}$  and  $\mathbf{n}_{sp}^{(2)}$ ) is  $u_p = |\mathbf{u}| \cos(\alpha)$ . Since  $|\mathbf{n}_{sp}^{(2)} + \mathbf{n}_{sp}^{(1)}| = 2 \sin(\theta/2)$ , Eqn 3-2 [fringe model] becomes:

$$u_p = f_D \frac{\lambda_0}{2 \sin(\frac{\theta}{2})} \left[ = \frac{\delta}{t} \right] \quad 3-3$$

where  $t$  is the ‘time necessary for a particle to travel between two points with the same phase within the fringe pattern’ (Muste et al. 2017). The benefit of using the dual-beam mode is that

the velocity of the tracer particle is independent of the location of the receiver and therefore the accuracy of the method simply depends on the light wavelength and beam arrangement. Another benefit is that an LDA does not require calibration and is simply a linear function of the Doppler frequency. (Muste et al. 2017)

### 3.1.2.2 Instrument Configuration

A typical LDA system contains a continuous laser source, transmitting optical components (including beam splitters, frequency shifters, and color splitters), receiving optical components, a photodetector, and signal processing components. The laser beams, which are typically Gaussian beams (with a beam quality factor,  $M^2$ , closer to 1 considered to be good quality), are then split with one beam undergoing a frequency shift via a Bragg cell (proportional to the frequency of the acoustic wave ( $\varepsilon_a$ ); ~40 MHz) which reduces directional ambiguity of the detected velocities. It is common for the split beams to then pass through a color-splitter prism. The different colors are used for the different velocity directions; they generally include green, blue, and violet.

In contemporary systems, such as the LDA in the EFML, mirrors are used to deflect the colored beams into single mode optical fibers that conduct the light to emitting (and receiving) probes as seen in *Figure 3-2*. The positioning of the receiving optics  $180^\circ$  from the emitting optics is considered a ‘backscattering’ functioning mode. The beams are then focused through a spherical lens that is calibrated (by the manufacturer) such that the beams cross at the beam waist (the smallest beam radius). It should be noted that if a broad range of Doppler frequencies ( $f_D$ ) is measured, it is possible that the beams may be out of focus and can result in an overestimation of turbulence.

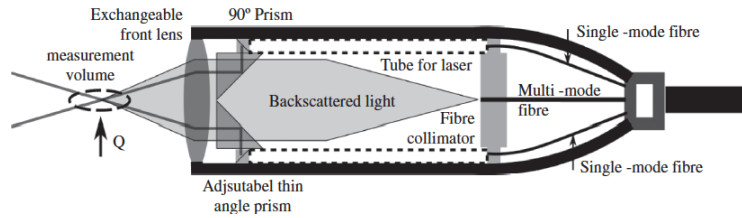


Figure 3-2: Schematic of an emitting & receiving probe similar to the device in the EFML (Muste et al. 2017)

There is a system of lenses and pinholes that focus the light from the scattered fringe patterns by the tracer particles onto the receiver optics. It is then carried through an optical fiber to the receiver module which contains another color-splitter, interference filters, and photodetectors for each color. The photodetector is what converts the scattered light into an electrical signal which is processed to determine the Doppler frequencies through a spectral analysis.

A traversing system enables the researcher to precisely position the control LDA volume, set a reference location, and more easily move the probe along x-y-z coordinates for multiple point measurements. The probe should be positioned such that the largest direction of the measuring volume is aligned with the direction with the smallest gradients of the mean flow. The focal locus of the control volume must be calculated with respect to the material the laser is shown through (e.g. the glass walls of a flume).

### 3.1.2.3 Tracer Particles

As previously mentioned, the LDA requires the use of tracer particles in the fluid flow to scatter the light from the laser. Tracers can be spherical or non-spherical (cheaper but limited knowledge of dynamic interaction with the fluid) in shape but should be inert and non-toxic as well as 'passive', meaning that the presence of the particles does not affect the flow.

There are a number of general criteria for tracers for use with LDA (and PIV) to consider. The particle density should be close to the fluid density yet have a refractive index noticeably

different from that of the fluid. The tracers should also be small enough to provide good signal modulation and show the small-scale details (resolution) of the flow desired. Yet, the tracer should also be large enough to avoid unpredictable kinematic behaviors (such as Brownian motions) and scatter enough light that the photodetector can detect without any signal amplification. A common criterion used is that the particle diameter should be less than the fringe spacing, which is dependent on the angle between the beams and the laser wavelength.

A final practical issue involves particle-induced fringe distortion. This distortion is due to the passage of a particle through a laser beam just outside of the measuring volume. This can affect the burst generated by a particle passing through the measuring volume resulting in an overestimation of turbulence similar to that of the beams not being focused.

#### 3.1.2.4 Signal Processing

The electric signal from the photodetector encompasses irregular ‘bursts’ from one or more particles traversing the measuring volume as well as multiple forms of noise. In order to correctly determine the  $f_D$ , the noise needs to be removed with respect to the spatial shape of the light beam intensity, also referred to as the signal pedestal. For a Gaussian beam, the signal pedestal resembles a Gaussian curve as seen in the top right graph in *Figure 3-3*. A burst is detected by setting an amplitude threshold on the pedestal signal. Noise can be linked to the instruments (including the photodetector, laser generation, and/or system electronics) or from several particles passing through the measuring volume simultaneously but out of phase.

Generally, the sources of noise are uncorrelated and considered white noise. Unfortunately, the noise affects the resolution of small-scale turbulent motions thus should be evaluated.

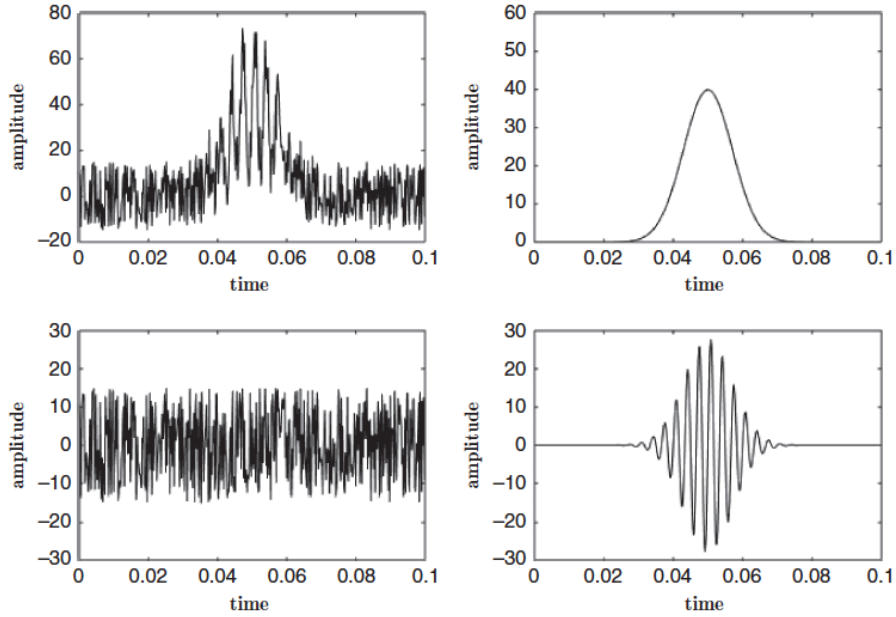


Figure 3-3: Example LDA data; Top left: pre-filtered signal, Top right: pedestal (DC component), Bottom left: noise, and Bottom right: Doppler burst (AC component) (Muste et al. 2017)

The signal-to-noise ratio (SNR) is used to indicate the quality of a signal. The SNR is a ratio of the power of the signal to the power associated with the noise which can be estimated from the value of the auto-correlation function at the origin. Frequency analysis, i.e. an analysis of the energy spectrum of the signal by Fourier techniques, is most commonly used to determine the  $f_D$  as seen in Figure 3-4.

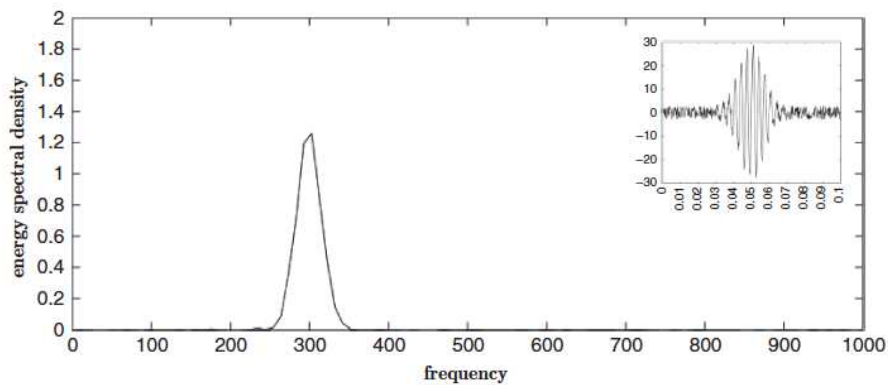


Figure 3-4: Doppler frequency signal with a peak of 302.7 Hz after a frequency analysis of the signal shown in Figure 7 (Muste et al. 2017)

### 3.1.2.5 Basic Statistical Analysis

The velocities from an LDA are obtained at time intervals of  $10^1$ - $10^3$   $\mu\text{s}$ , which is smaller than the relevant turbulent time scales and are therefore considered to be ‘instantaneous’. Since the LDA takes a time series of measurements at relatively high mean data rates in combination with the chaotic, random nature of turbulent flows, a statistical analysis of the instantaneous velocities and power spectral density function are necessary. A weighting-average technique is used to compensate for the bias of larger velocity. The sample mean of the velocity ( $\bar{u}$ ; first moment) is determined by the following equation where  $N$  is the number of samples in the time series and  $\Delta t_k$  is the residence time associated with the particle velocity  $u_{pk}$ .

$$\bar{u} = \frac{\sum_{k=1}^N u_{pk} \Delta t_k}{\sum_{k=1}^N \Delta t_k} \quad 3-4$$

The second (i.e. variance) and higher moments can be acquired by to following where  $a + b = n$  (the order of moment) and  $u_i$  and  $u_j$  are the  $i^{\text{th}}$  and  $j^{\text{th}}$  components of the velocity field:

$$\sigma_{u_i^a u_j^b}^n = \frac{\sum_{k=1}^N (u_{ik} - \bar{u}_i)^a \Delta t_{ik} (u_{jk} - \bar{u}_j)^b \Delta t_{jk}}{\sum_{k=1}^N \Delta t_{ik} \Delta t_{jk}} \quad 3-5$$

The sample-and-hold (S+H; a zero-order polynomial data reconstitution) and/or refined sample-and-hold (RS+H) techniques are commonly used to re-sample LDA data into equally spaced time series to simplify the calculations of autocorrelation, structure, or power spectral density functions.

### 3.1.3 Particle Image Velocimetry

#### 3.1.3.1 PIV Measurement Process

Particle image velocimetry (PIV) is a non-intrusive method of estimating the mean velocity vector fields (or higher order moments of the velocity probability distribution) of a region of flow. This is particularly ideal for studying coherent structures within a flow. PIV measurements typically require tracer particles (seeding of the flow; See Section 3.1.2.3), the illumination of the flow region of interest by a laser light sheet, capturing images of the illuminated flow in pairs (or sequences), and finally processing the images (tracking the displacement of seeding particles).

Figure 3-5 below depicts this procedure. (Muste et al. 2017)

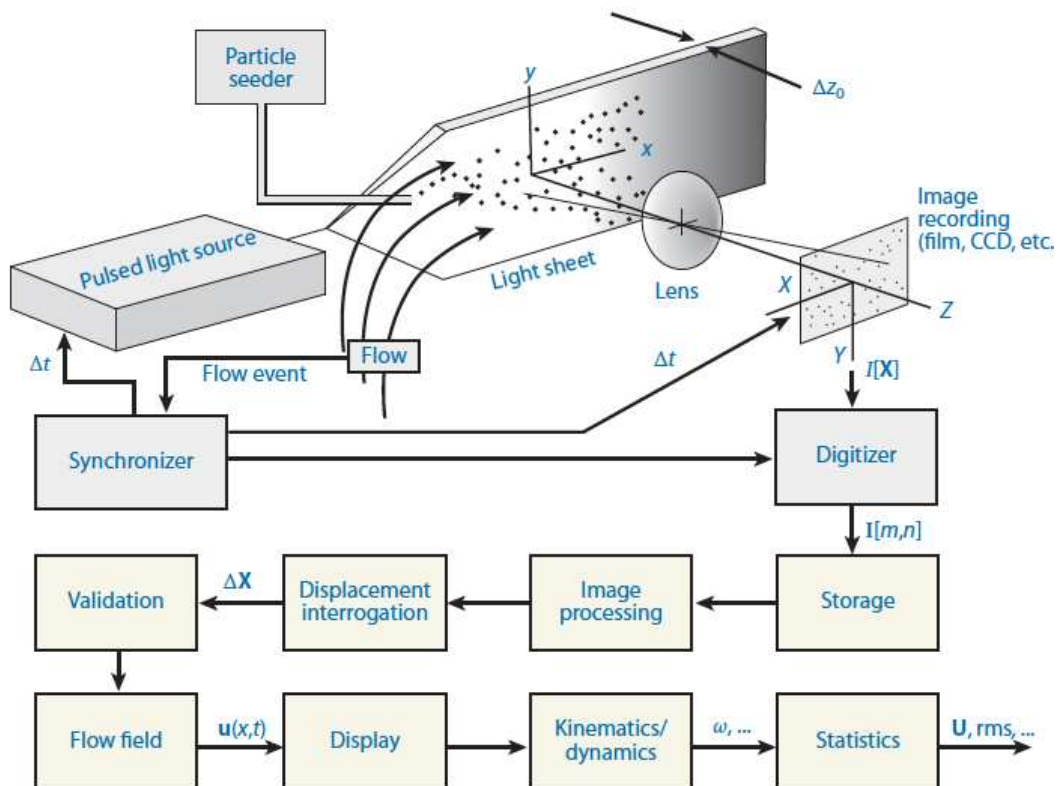
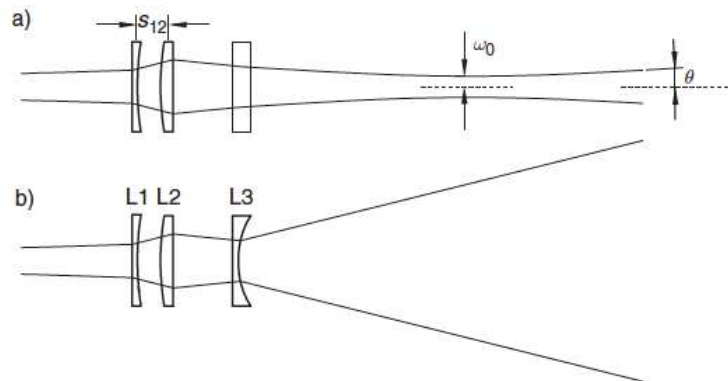


Figure 3-5: A schematic of a typical 2C-2D PIV system where CCD stands for 'charge-coupled device' (Adrian & Westerweel 2011)

### 3.1.3.2 Laser and Image Capturing Specifications

A pulsed Nd:YAG laser (with pulse energies 10-200 mJ, durations 5-10 ns, and repetition rates 10-10,000 Hz) such as in the EFML or dual cavity lasers are commonly used in PIV systems. PIV requires a pulse separation time between 0.1-10 ms which limits the displacements of particle images between exposures. It is important that the laser pulses once per frame that an image is captured. A synchronizing device is often required as the necessary pulse time of the laser may be shorter than the duration of the camera. A strategy known as “frame straddling” is used which involves synchronizing the laser and camera such that the first laser pulse is triggered near the end of the first image exposure and the second pulse at the beginning of the second image exposure.

In order to create a laser light sheet, spherical and cylindrical lenses are strategically place (as seen in *Figure 3-6* in such a way that the thickness and the expansion of the beam can be adjusted. Due to diffraction, the thickness of the sheet will vary slightly with the distance from the laser. Because of this, the entire light sheet is not usable, but only the area that has a reasonably uniform thickness.



*Figure 3-6: A parallel (a) and normal (b) view of the formation of a laser light sheet with the different lenses (including L1, a plano-concave spherical; L2, plano-convex spherical; and L3, plano-concave cylindrical) and the distance ( $s_{12}$ ), which controls the position of the beam waist (Muste et al. 2017)*

The minimum thickness ( $T$ ) is defined by Eqn 3-6 where  $\omega_0$  is the waist radius and  $\theta$  is the far field beam divergence angle. From this equation, it is apparent that there is a tradeoff between the thickness and the divergence angle.

$$T = 2\omega_0 \approx \frac{2M^2\lambda}{\pi\theta} \quad 3-6$$

For PIV, the quality of the laser(s) used are higher than for LDA with a  $M^2$  factor of 5-50.

Similar to the LDA, the light from the laser is scattered by the seeding particles in the flow. The difference is that the light scattered in a PIV system is then focused onto the camera sensor by a lens which then forms an image from the discrete photosites (sensor pixels). Similar to the LDA, the properties (i.e. size and shape) of the tracer particles matters in terms of accuracy. However, for PIV accuracy is also a function of lens aberrations and diffraction (the limiting factor for lens with  $f_\# > 8$ ). Diffraction limited is ideal for PIV as the particle images are reasonably predictable and repeatable in various scenarios.

### 3.1.3.3 Image Processing

In order to determine the velocities using PIV, the position of the particles is compared between two or more consecutive images. The PIV images are divided into a grid of interrogation areas as seen in *Figure 3-7* below. The grid velocity vector is given by

$$\vec{V} = M \cdot \frac{\vec{d}}{\Delta_t} \quad 3-7$$

where  $\vec{d}$  is the displacement of the image pixels,  $M$  is the magnification factor, and  $\Delta_t$  is the image separation time. This process is repeated for each interrogation area in the field of view in order to determine the final velocity vector field.

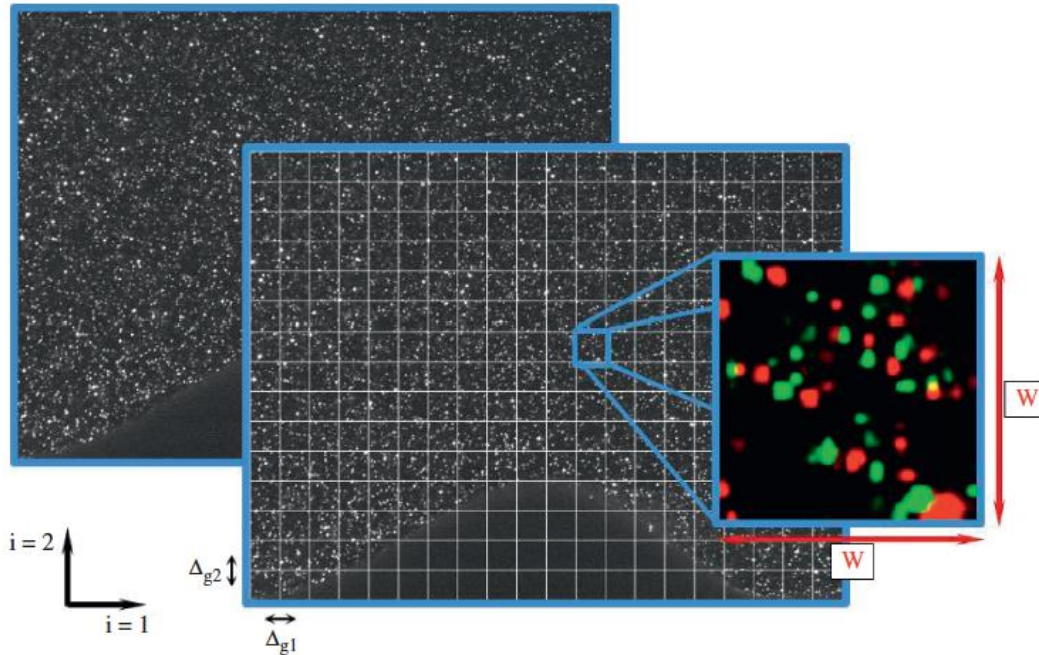


*Figure 3-7: An example of an interrogation using PIV of flow over a sand ripple with the grid subdivision and close-up of a single interrogation area (where green and red coloring indicate the displacement of the particles between image frames) (Muste et al. 2017)*

An algorithm is used to process each interrogation area (or grid window) which results in a single displacement measurement for that grid. It is common for the grid dimensions to be square and multiples of 2 (i.e. 16x16, 32x32, or 64x64 pixels) as it is typically more efficient for some algorithm integration. The two-dimensional correlation of the interrogation region between the two successive images is measured and used to statistically determine the displacement of the particles. To solve the cross-correlation function directly is computationally expensive, therefore a Fourier transform based method (such as FFT) is often used. After the cross-correlation function is calculated using FFT, the highest peak is located, and its position estimated. A common interpolation method used is the three-point Gaussian fit which is depicted in *Figure 3-8* below.

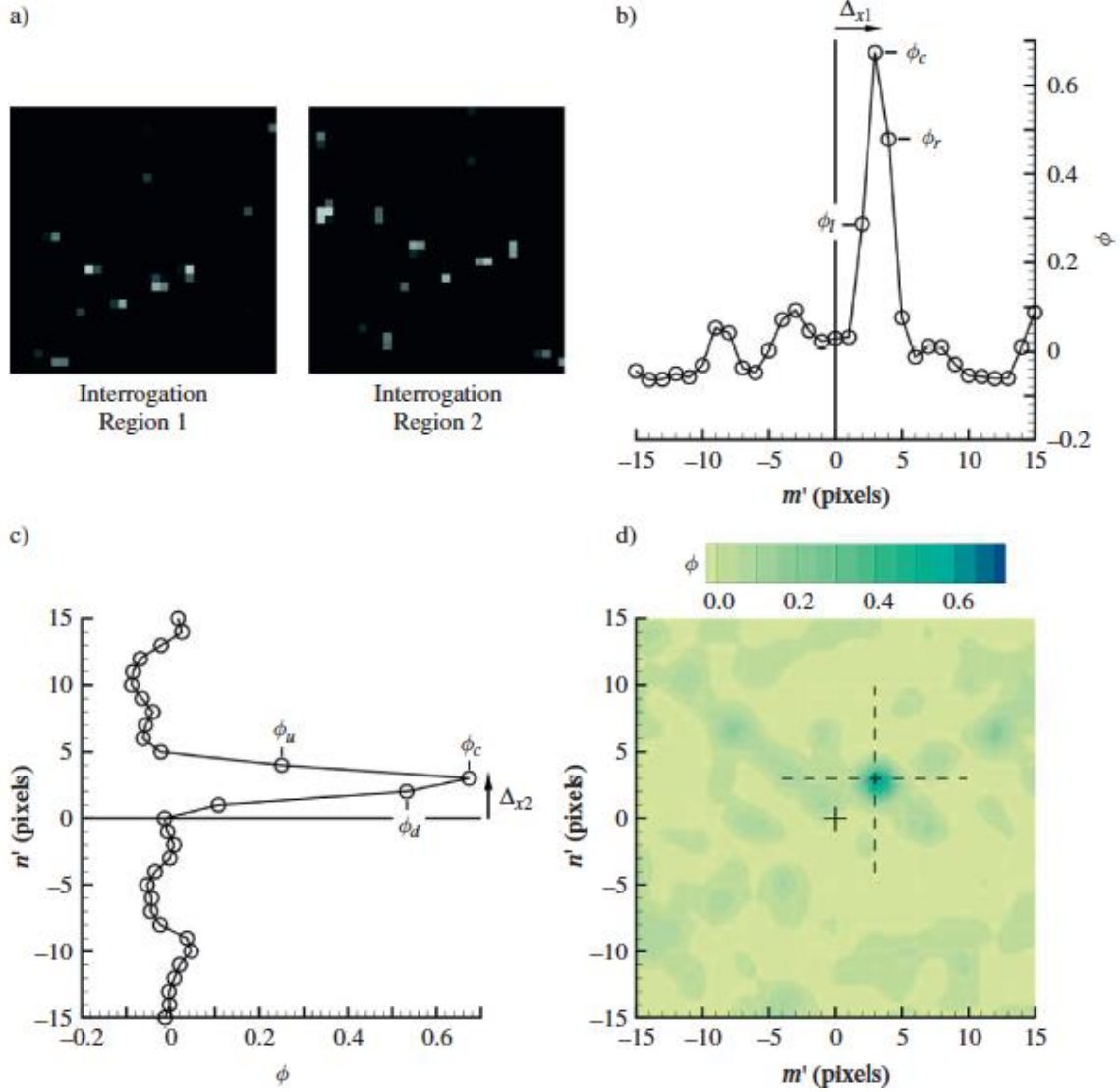


Figure 3-8: A single cross correlation interrogation region pair (a) along with cross correlation functions (b & c) with the maximum marked by the dashed dotted lines in (d) (Muste et al. 2017)

The displacement estimates ( $\Delta_{xi}$ ) are related to their respective velocity components ( $u_i$ ) such

that  $u_1 = \frac{\Delta_{x1}}{S\Delta_t}$  and  $u_2 = \frac{\Delta_{x2}}{S\Delta_t}$  where  $S = M/P$  ( $P = \text{pixel pitch}$ ) and

$$\Delta_{x1} = m'_{\phi_c} + \frac{\ln\phi_l - \ln\phi_r}{2\ln\phi_l - 4\ln\phi_c + 2\ln\phi_r} \quad 3-8$$

$$\Delta_{x2} = n'_{\phi_c} + \frac{\ln\phi_d - \ln\phi_u}{2\ln\phi_d - 4\ln\phi_c + 2\ln\phi_u} \quad 3-9$$

As algorithms have improved, two classes of multi-pass algorithms have emerged: the ‘iterative discrete shift’ (IDS; e.g. Westerweel et al. 1997) method and the ‘iterative deformation method’ (IDM; e.g. Nogueira et al. 1999, Scarano & Riethmuller 2000, Astarita 2007, Cameron 2011). Both methods reduce the in-plane loss of particle images. The IDS method allows the first and second interrogation regions to be offset. How much they are offset is determined by rounding the displacement measured from the previous iteration to the nearest integer.

Additionally, the size of the interrogation window can be altered with each iteration, usually requiring 2-3 pass to achieve a stable solution. The IDM algorithm, on the other hand, works by deforming the images in order to correct for the in-plane losses and velocity gradients. For IDM, 8-20 iterations (depending on parameters used) are typically needed to converge on a solution. IDS is simple to implement and fast to compute compared to IDM, but IDM is able to handle larger velocity gradients and can achieve higher resolution.

### 3.1.3.4 Resolution

The temporal resolution of a PIV system is influenced by the exposure method, camera sensitivity, camera frame rate, and illumination source. Typically, the collection rate is limited based on the standard repetition rates of the digital camera (the images are collected in pairs) and the frequency of the laser that make up the PIV system.

The limit for spatial resolution is set by the Nyquist wavenumber  $k_{Ni} = 1/2\Delta_{gi}$ , where  $\Delta_{gi}$  is the grid spacing and the wavenumber is defined as one over the wavelength. Flow scales less than the Nyquist wavenumber can be resolved; however, they are often attenuated because of spatial averaging, the light sheet thickness ( $L_S(x_3)$ ), and the displacement of particles between exposures defined by the particle displacement transfer function,  $|T_\Delta(k_1)| = \frac{\sin(\pi k_1 \Delta x_1)}{\pi k_1 \Delta x_1}$ . The

amount of attenuation of the turbulence at each wavelength is described by the transfer function,  $T_{CC}(k)$ , which can completely describe the resolution of the PIV system. This is also known as the ‘modulated transfer function’ (MTF) or the PIV system gain factor, and is the ratio of output (measured) to input (actual) amplitudes for the Fourier components of the wavenumber ( $k$ ). The cutoff wavenumber ( $k_{Ci}$ ) should ideally be greater than the Kolmogorov length scale ( $\zeta$ ), but this is rarely possible leading to the measured velocity variance often being biased low due to the lack of spatial resolution.

### 3.1.3.5 Sources of Error

Measurement error ( $\varepsilon_i$ ) for PIV systems is defined as the difference between the measured and actual velocity fluctuations ( $\varepsilon_i = u_i^m - u_i$ ) and is calculated after processing images with a PIV code of a prescribed motion of known velocity fields (e.g. Lecordier & Westerweel 2004, Raffel et al. 2007). The  $\varepsilon_i$  has both mean ( $\bar{\varepsilon}_i$ ) and fluctuating ( $\varepsilon_i'$ ) components and is normally distributed with a standard deviation of  $\sigma_{\varepsilon i} = \sqrt{\overline{\varepsilon_i'^2}}$ . The mean component is considered the ‘bias’ or systematic error while the fluctuating component is called the measurement noise, which is link to the spatial resolution. For scales that are large compared to the mean particle spacing, the power spectrum of PIV measurement noise is defined in *Eqn 3-10* where  $S_{\varepsilon i}$  is the spectral saturation level for the  $i^{th}$  displacement (velocity) component.

$$\phi_{\varepsilon i}(k_1, k_2) = S_{\varepsilon i} |T_{CC}(k_1, k_2)|^2 \quad 3-10$$

In order to be able to assess the system noise separately from the spatial resolution, the noise level of PIV systems, given by  $S_{\varepsilon i}$ , are compared by normalizing the noise variance with the equivalent noise bandwidth ( $E$ ) such that  $S_{\varepsilon i} = \phi_{\varepsilon i}^2 / E$ , where  $E$  is defined as

$$E = \int \int_{-\infty}^{\infty} |T_{CC}(k_1, k_2)|^2 dk_1 dk_2. \quad 3-11$$

Assuming uniform  $\Delta_{x3}$ , the primary two sources of (random) errors come from image aliasing (more so an issue for small particle image diameters) and the change of brightness (for large particle image diameters and large relative out-of-plane displacements,  $\Delta_{x3}/T$ ). An optimum image diameter can be determined in order to minimize the total error. The image aliasing error can be described using the periodic functions below where  $A$  and  $B$  (which scales  $\propto 1/N$ ) are coefficients dependent upon the particle image diameter and the correlation algorithm.

$$\bar{\varepsilon}_i = A \sin(2\pi\Delta_{xi}) \quad \sigma_{\varepsilon_i}^2 = B[1 - \cos(2\pi\Delta_{xi})] \quad 3-12$$

The change of brightness error is due to the overlap of ‘false peaks’ with the ‘true peak’ after the decomposition of the cross-correlation function  $\phi(m', n')$ . This normally occurs when there is a velocity component in the out-of-plane direction ( $u_3$ ) causing particles to move from a bright (i.e. near the center of the light sheet) to a less bright (i.e. near the edge of the light sheet) region. Therefore, the change of brightness error is proportional to  $\Delta_{x3}/T$  as well as to the particle image diameter.

If  $\Delta_{x3}$  is not uniform, i.e. when there are velocity gradients present in the flow, if using the IDS method, the cross-correlation peak is distorted and the error is proportional to the velocity gradients. If there are large displacements in comparison to the image diameter (i.e.  $\sigma_{W1}/d_p < 0.2$ ), the correlation peak can split into several peaks leading to unpredictable results. The measurement error for IDM, however, is comparatively unaffected to any velocity gradient due to iterative corrections for varying displacement. It is tough to fully account for all possible errors, especially considering the conflicting contributions of measurement errors and limited spatial resolution to the variance of velocities.

### 3.1.3.6 Practical PIV Configurations

In general, PIV systems can be assembled based upon the concepts discussed above, but in a variety of different ways. Despite their configurations, the PIV systems can be characterized by specific system parameters.

In the EFML (2C-2D PIV system), the laser sheet is oriented in the normal and streamwise plane of flow in a 5-meter long flume. The camera is secured on the outside of the flume wall with the viewing direction perpendicular to the laser sheet. The PIV is calibrated simply by recording an image of a known scale that is aligned with the illuminated plane. In this set-up, only two directions of the flow can be resolved; in the EFML this includes the streamwise (x) and normal (z) directions with 'y' being the out-of-plane direction.

## 3.2 Baffling Factor Measurements

### 3.2.1 Introduction

In order to determine the  $BF$  of a system,  $T_{10}$  must be measured (see Section 2.2.2). Tracer tests are a common method of evaluating a system's internal hydraulics, from which the characteristic time  $T_{10}$  can be determined.

### 3.2.2 Tracer Tests

There are two types of physical tracer tests: step-dose and pulse. For either option, an appropriate tracer must be detectable and measurable (for example Lithium or Sodium Chloride). Both tracer methods theoretically will give the same results, however each has its own pros and cons. For this dissertation work, only step-dose tracers were conducted.

### 3.2.2.1 Step-Dose

A step-dose tracer test is performed by continuously injecting a stable concentration of a tracer (e.g. a concentrated sodium chloride solution) into a system while measuring the tracer concentration (e.g. conductivity) at the outlet until the tracer concentration stabilizes. The purpose of a step-dose tracer is that it results in a residence time distribution curve described in the section below.

#### 3.2.2.1.1 Residence Distribution Curves

A residence time distribution (RTD) curve (*Figure 3-9*) can be generated by plotting the normalized concentration of tracer ( $C/C_0$  where  $C_0$  is the 'final' stable concentration) from a step-dose tracer test as a function of the normalized time ( $t/TDT$ ). *Figure 3-9* shows an example of an RTD curve of a step dose tracer test for a hypothetical contact system.

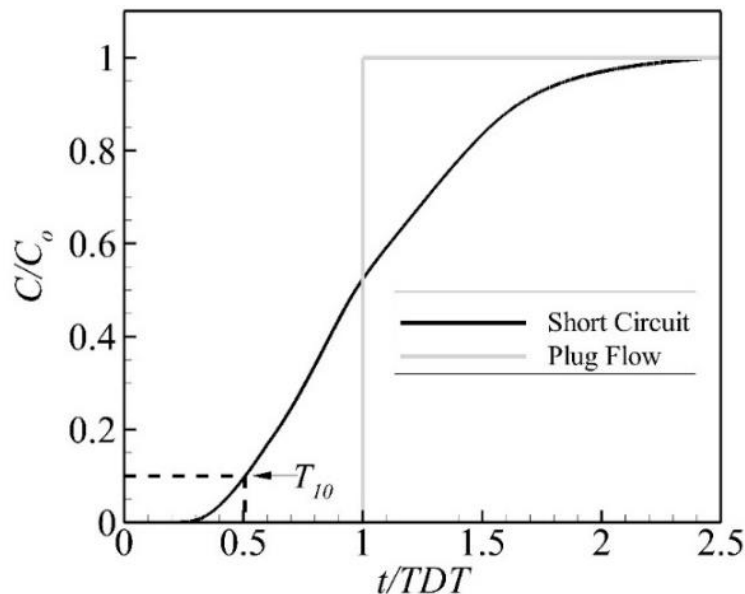


*Figure 3-9: A general RTD Curve from a step-tracer test; Note: time  $t$  has been normalized by TDT*

This RTD curve would be associated with a moderately efficient disinfection contact basin, having a  $BF$  of 0.5, indicating a moderate extent of short circuiting. In contrast, the plug flow

line shown in depicts the idealized case when all of the tracer material sent through the contact basin reaches the outlet at the *TDT* of the contact system.

### 3.3 Bulk Head Loss Measurements

#### 3.3.1 Introduction

In any and every scenario, fluid flow experiences resistance (or ‘drag’) due to the shearing and/or the separation of fluid layers as a result of the viscosity of the fluid and the no-slip condition at a boundary. There are two components of drag; friction (parallel) and form (normal; see Section 2.4). Drag is measured in terms of head loss ( $h_L = \Delta P/\gamma$ ), where  $\Delta P$  is the differential pressure and  $\gamma$  is specific weight. In closed (or pressurized) conduit flow systems the flow experiences both types of friction. Friction drag is related to the amount of surface area and the roughness of the surfaces that the fluid contacts while form drag is related to the system design and fittings used (often referred to as local losses). Determining the origin (type) of friction and its contribution to the overall  $h_L$  in a system is tedious and in the grand scheme unnecessary. For this reason bulk  $h_L$  measurements (in terms of  $\Delta P$ s) are considered representative.

#### 3.3.2 Digital Manometers

While traditional manometers rely on the hydrostatic balance of a fluid (typically water or mercury), digital manometers use pressure transducers. In a differential digital manometer, a pressure transducer converts the observed pressure at two sensors (typically strain gauges) to an electrical signal that is a proxy for the magnitude of the difference in pressure observed, the output measurement.

## 3.4 Bacterial Plate Counts

### 3.4.1 Introduction

As discussed in Section 2.5, biofilms are ubiquitous throughout water treatment and distribution systems and are often the source of bacteria in the bulk water due to sloughing. For the purposes of this dissertation, Heterotrophic Plate Counts (HPC) and *Pseudomonas aeruginosa* (*P. aeruginosa*) counts were conducted.

### 3.4.2 Bacterial Counts

#### 3.4.2.1 Heterotrophic Bacteria

The concern of using RPM in a chlorine contactor is the potential for excessive biofilm growth that would ultimately impact the bacteriological quality of the finished water. Heterotrophic bacteria is a broad category of bacteria often used as an indicator of the effectiveness of water treatment processes, or as an indirect indication of pathogen removal (WHO, 2003). For this reason, HPC were deemed an appropriate indicator for the finished water quality.

#### 3.4.2.2 *Pseudomonas aeruginosa*

Though *P. aeruginosa* levels are not considered a drinking water parameter, they are commonly found in biofilms and are typically used as indicators of biofilm presence in pools and spas (Mena & Gerba, 2009). Since the focus was the potential for excessive biofilm growth on the RPM in a chlorine contactor, *P. aeruginosa* was considered an appropriate indicator for the presence of biofilm. In order to further distinguish *P. aeruginosa* from other *Pseudomonas* species, only the green fluorescent colonies were counted under ultraviolet (UV) light (380nm) (King et al., 1954; WHO, 2004).

### 3.4.3 Membrane Filtration

Due to the expected low CFU counts (< 1 to 10 CFU/mL) for chlorinated water, the membrane filtration method was used (*Figure 3-10*), a common method for bacterial cultures. For consistency, a filter membrane techniques was used for all samples. The downside to this method is the expense of the membranes and the possible cell damage due to excessive vacuum pressure.

(**Standard Methods**, 2017)

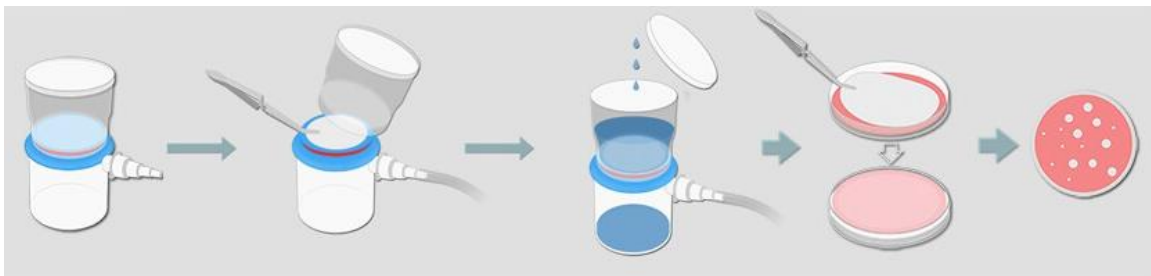


*Figure 3-10: General Membrane Filtration Steps (reference unknown)*

### 3.5 Summary

The experimental methods used for this dissertation research, expounded upon in this chapter, were selected on the basis of the intended information acquired and access. A sound understanding of how each method works is imperative to proper interpretation of the measurement data collected for analysis. The methods used range from rather simple and direct measurements (i.e. digital manometer) to more complex and indirect measurement (i.e. PIV) that require computational processing. Care was taken to ensure each measurement device employed for this dissertation research was used in an appropriate manner on the basis of understanding the method behind the measurement device.

## CHAPTER 4

### 4 TURBULENT ROUND JET FLOW FROM A PIPE THROUGH RPM

#### 4.1 Introduction

Section 2.3 provides a brief overview of flow interacting with obstacles, specifically of flow around an infinitely long cylinder and flow through packed beds. This includes a discussion on the formation of a wake as well as why there is a pressure drop and how it has been modeled. As mentioned previously, however, all the models assume a uniform flow entering the bed. In the case of using RPM in a contact basin, the inflow would be a jet due to a sharp inlet from the incoming pipe. While a jet into an ambient experiences free-shear flow dynamics (as discussed in Section 2.2.1), a jet into a highly porous media, such as RPM, would experience a complex combination of free, wall-bounded, and wake shear flow dynamics. The goal of using RPM is to (1) ‘kill’ the jet in order to reduce short-circuiting and (2) produce a well-mixed uniform (plug) flow, which would likely mimic ‘grid turbulence’ which is a type of homogenous shear flow that would allow the determination of the dissipation ( $\epsilon$ ). There are two aspects to this study:

- 1) to determine how a turbulent round jet decays and spreads through RPM and
- 2) to visualize and characterize the wake (turbulent flow) downstream of the RPM which would provide insight into the associated drag.

The knowledge gained from this study will help to determine the amount of RPM sufficient to kill the jet and achieve plug (or homogenous shear) flow conditions without filling an entire tank with RPM, thus improving the hydraulic disinfection efficiency of a contact basin.

## 4.2 Materials and Methods

### 4.2.1 Experimental configuration

#### 4.2.1.1 Jet in a Flume

The study of a turbulent round jet from a pipe through RPM was conducted in a 5-m long 300 mm wide flume (S6-MKII; Armfield, Hampshire, UK) in the EFML at CSU. The jet was produced by a 3/4 " PVC pipe ( $d_j = 0.824$ " [20.93 mm]; 64 cm long to ensure fully developed flow at the highest tested flow rate) was attached to bulkhead tank fitting fixed in an acrylic sheet (300 x 450 mm) - centered laterally and  $5 \frac{15}{16}$ " (150.8 mm) from the flume floor - seen in *Figure 4-1* below. A small level was attached to the PVC pipe to ensure the jet remained horizontal and parallel to the flume walls. Aluminum angles covered with neoprene stripping were attached to the acrylic sheet to help secure the wall perpendicularly in the flume (taped to help prevent leaking [backflow]). This set up was to create a reservoir with the gate on the downstream end raised up. The PVC pipe was then connected to 1" flexible tubing joined to a submersible pump (1/3 hp, cast iron, 120VAC; model #: 4HU68; Dayton Water Systems, West Carrollton, OH) located in the storage tanks of the recirculating flume. The gate was adjusted to maintain a water depth greater than the width of the flume to take into account any potential effects of the free surface. The gate was sealed to ensure that all water flowed over the gate (i.e. no leakage between the movable gate and flume walls) thereby preventing a current along the floor of the flume.



Figure 4-1: Photographs of the acrylic wall set-up (left: front; right: back).

The flume was filled with water upstream of the wall to balance the hydrostatic forces on the wall. Using the wall as the reference ( $x = 0$ ), the origin of the turbulent jet from the long pipe ( $x_0$ ) is located at  $x = -1.62''$  ( $-41.3$  mm) based on the schematic of the bulkhead tank fitting in Figure 4-2.

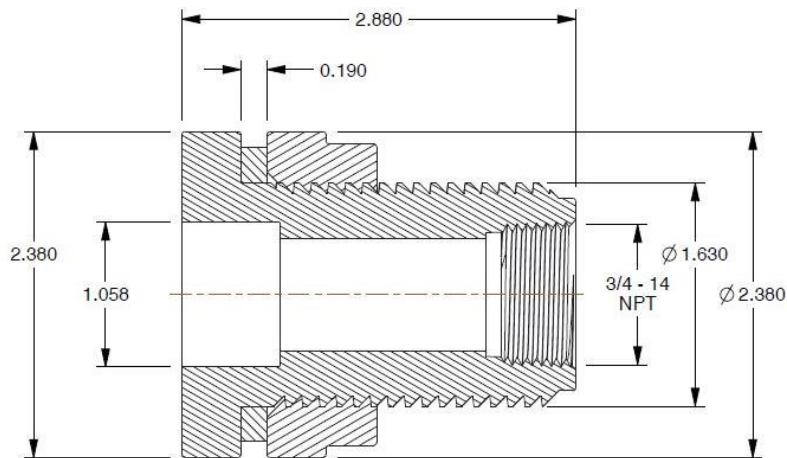


Figure 4-2: Schematic of the  $\frac{3}{4}''$  bulkhead tank fitting with dimensions in inches (Grainger®, Lake Forest, IL)

#### 4.2.1.2 RPM Wall

The RPM (Polypropylene NSF-61 certified with 93.5% void space [or porosity;  $\epsilon$ ]; Raschig USA, Inc., Arlington, TX; RTJ, 2020) was secured as a wall (or ‘bed’) with thickness  $L$  using a mesh frame(s) (See *Figure 4-3*). The mesh frame(s) was constructed from PVC-coated galvanized steel wire cloth using 304 stainless-steel wire to secure the mesh to routing eyebolts (300 stainless-steel, Trade size 214) held in a frame made of 1” acrylic half-round. Neoprene rubber stripping was adhered to the outside edges of the frame to protect the glass flume walls. The height of the RPM wall matched the height of the flume channel ( $\sim 450$  mm) to ensure all water flowed through the RPM.



*Figure 4-3: Photographs of the RPM wall apparatus.*

#### 4.2.1.3 Particle Image Velocimetry

A DM Series Nd:YLF diode pumped laser (single cavity, dual head, 100mJ, with a repetition rate of 1-10,000 Hz; Model No. DM-527-30, Photonics Industries International, Inc., Ronkonkoma, NY) in combination with a Phantom VEO-E 340L high-speed camera (up to 800 fps at a resolution of 2,560 x 1,600 pixels; Vision Research, Inc., Wayne, NJ) with a AF Micro-Nikkor

60mm f/2.8D lens (Nikon Inc., Melville, NY) formed the PIV system used to measure the time-resolved velocity field(s). The laser sheet was centered laterally (z-direction) and parallel (x-direction) in the flume channel in order to measure the centerline profile of the jet in the  $x - y$  plane as seen in *Figure 4-4*. A ‘coupler’ (made of optical glass with dimensions 1” x 1” x 12”) was used to make sure the laser sheet, which is brought from above the flume, would not refract through the free surface, thus skewing the PIV data (Harshit et al. “tentative”). A single PIV window was about 120 mm in the streamwise (x) direction, from the coupler to the floor of the flume (the vertical [y] direction). The camera was set level approximately 700 mm from the flume wall - close enough to focus the seeding particles while still covering the full water depth in a single window.

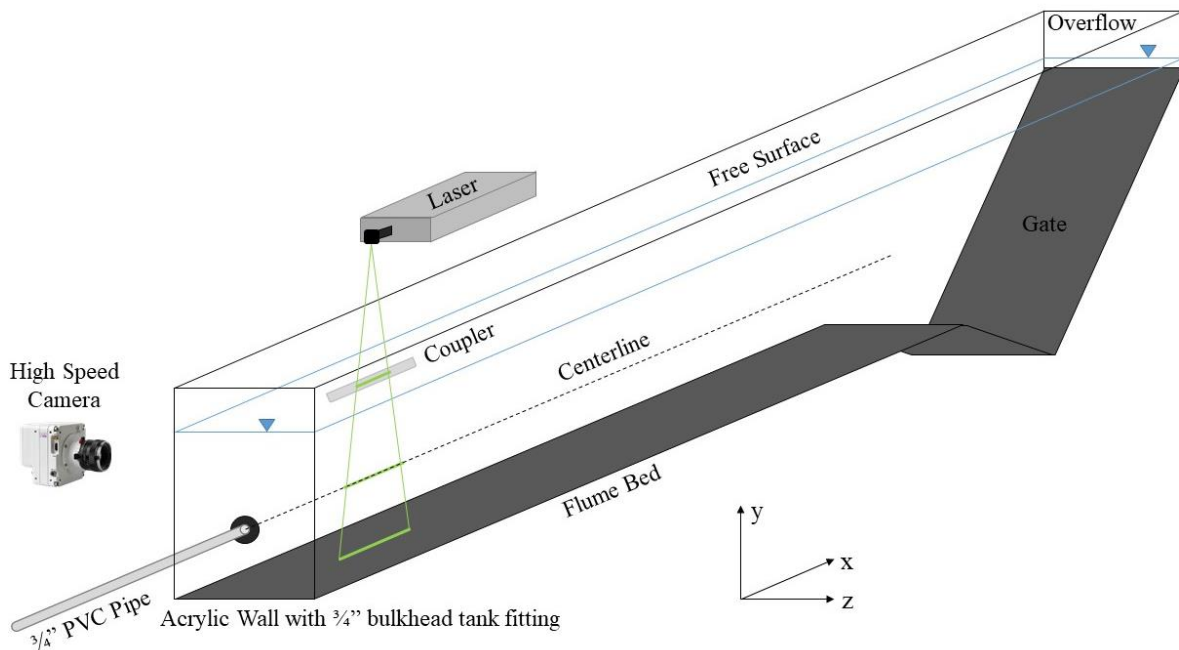


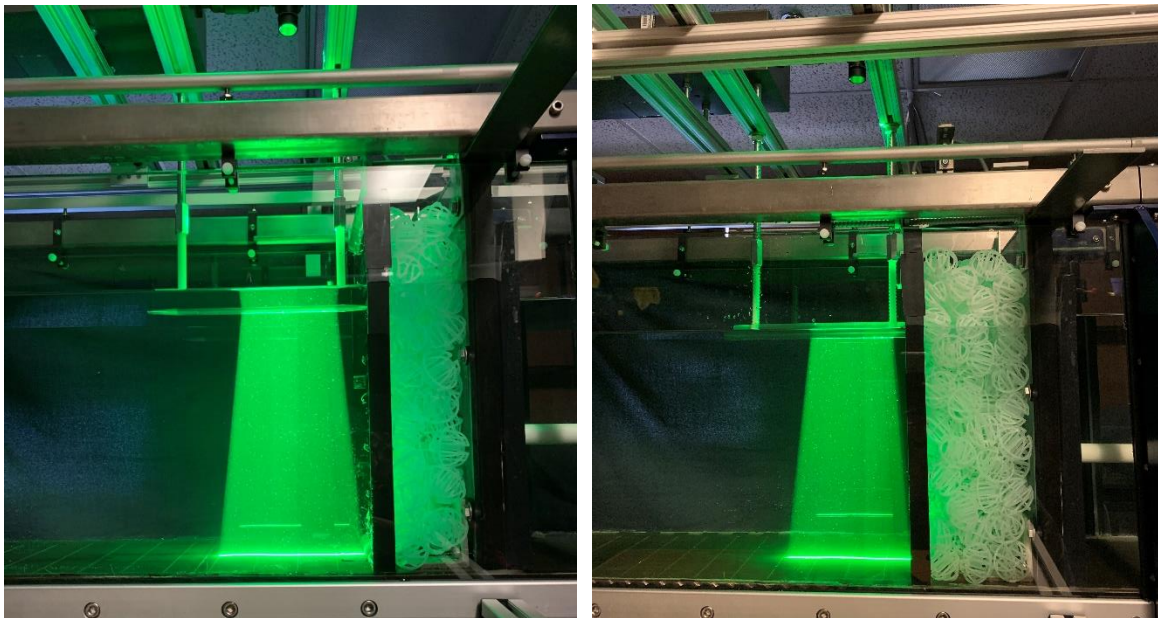
*Figure 4-4: Schematic of the jet in the flume and PIV set-up with measurement plane coordinate system*

Polyamide particles (20- $\mu\text{m}$  with a perfectly spherical particle [PSP] shape; Part Number: 1108892, LaVision Inc., Ypsilanti, MI) were used as seeding particles - added according to standard PIV best-practice guidelines (Raffel et al., 2007). Small circulation/wave pumps were

placed in each flume storage tank to ensure the seeding particles remained in suspension since the submersible pump did not create much turbulence at the relatively low velocities for the flume design.

#### 4.2.1.4 Scenarios

Five different RPM wall thicknesses ( $L = 100\text{ mm}$  [ $x/d_j = 4.78$ ],  $150\text{ mm}$  [7.17],  $200\text{ mm}$  [9.56],  $250\text{ mm}$  [11.94], and  $300\text{ mm}$  [14.33]; see *Figure 4-5*) were evaluated at the four different flow rates ( $Q = 0.315, 0.631, 0.946, 1.577\text{ l/s}$  [or  $\sim 5, 10, 15, \& 20\text{ gpm}$ ]) based on the operating range of the submersible pump used. The flow rates of the jet scenarios were varied using a DART Variable AC Voltage Supply (10 max. amps, 120VAC input/output; model #: 55AC10E; DART Controls, Zionsville, IN) and measured using an inline flowmeter (1" BL 240.34; Master Meter, Inc., Mansfield, TX).



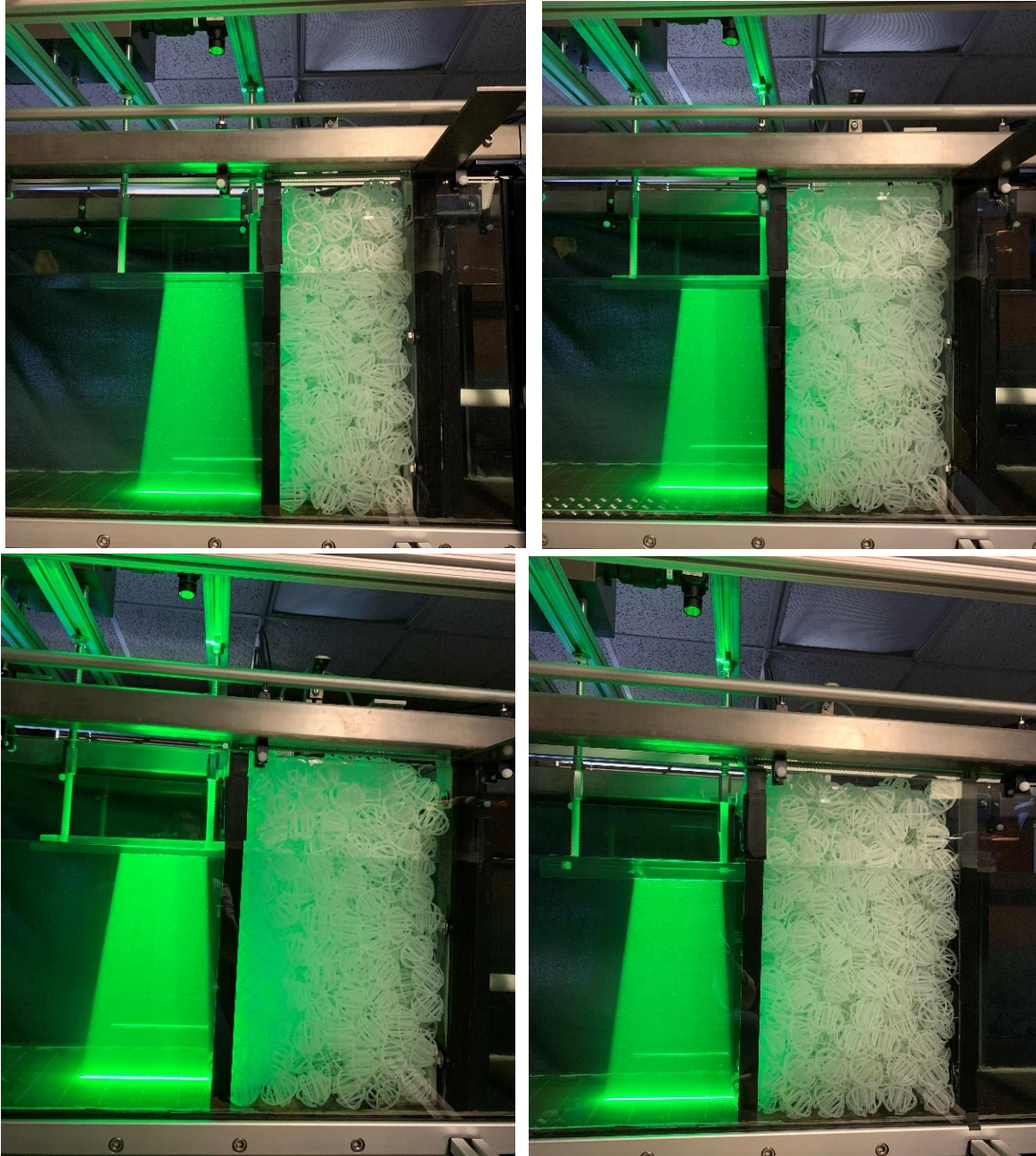


*Figure 4-5: Photograph of an experimental set-up of a turbulent jet encountering RPM; from top left to bottom right:  $L = 100$  mm,  $L = 150$  mm,  $L = 200$  mm,  $L = 250$  mm,  $L = 300$  mm,  $L = 300$  mm (uniform flow upstream).*

The downstream gate was raised to create an average water depth ( $H$ ) of  $334.2 \pm 3.2$  mm which was sufficient to allow the equivalent height of water as the width with an extra allowance for

any free surface effects (Harshit et al. “tentative”). The corresponding Reynold’s numbers

( $Re_{jet} = \frac{U_{jd}}{\nu}$  and  $Re_{flume} = \frac{U_{\infty D}}{\nu}$ ) of the flows are given in *Table 4-1* below.

*Table 4-1: Experimental Flow Rates*

$Q$ (gpm)	$Re_{jet}^*$	$Re_{flume}^*$
5	20,350	310
10	40,700	630
15	61,050	940
20	81,400	1,260

\*Note: Reynolds number values presented are based on average water temperature during all trials (22.6°C)

On the basis of the range of jet Reynold’s numbers, this laboratory study is representative of flow conditions found in SWTSSs seen in *Table 4-2* below.

*Table 4-2: Estimated Jet Reynolds number ( $Re_{jet}$ ) values of SWTSSs*

Nominal Inlet dimensions	$Q$ (gpm)				
	10	20	30	40	50
1”	33,350	66,700	100,060	133,420	166,770
1 ¼”	25,240	50,470	75,710	100,940	126,180
1 ½”	21,590	43,170	64,760	86,340	107,930
2”	16,770	33,530	50,300	67,070	83,830
2 ½”	14,040	28,070	42,110	56,150	70,190
3”	11,280	22,570	33,850	45,130	56,410
3 ½”	9,750	19,500	29,240	38,990	48,740
4”	8,590	17,170	25,750	34,340	42,920
5”	6,840	13,690	20,530	27,370	34,210
6”	5,690	11,380	17,070	22,760	28,450

\*Note: 1. blue shading indicates  $Re_{jet}$  values represented through this laboratory-scale study  
 2. Reynolds number values based on average water temperature during trials (22.6°C)

Two baseline scenarios were conducted: (1) for turbulent round jets from a long pipe with no

RPM present (*Figure 4-6*) and (2) for a uniform flow through a RPM wall of thickness  $L =$

300 mm [ $x/d_j = 14.33$ ] seen in *Figure 4-5*. For the uniform flow baseline, the flow rate was set

using the flume pump ( $Q = 15$  and  $20$  gpm [0.946 and 1.577 l/s] only).

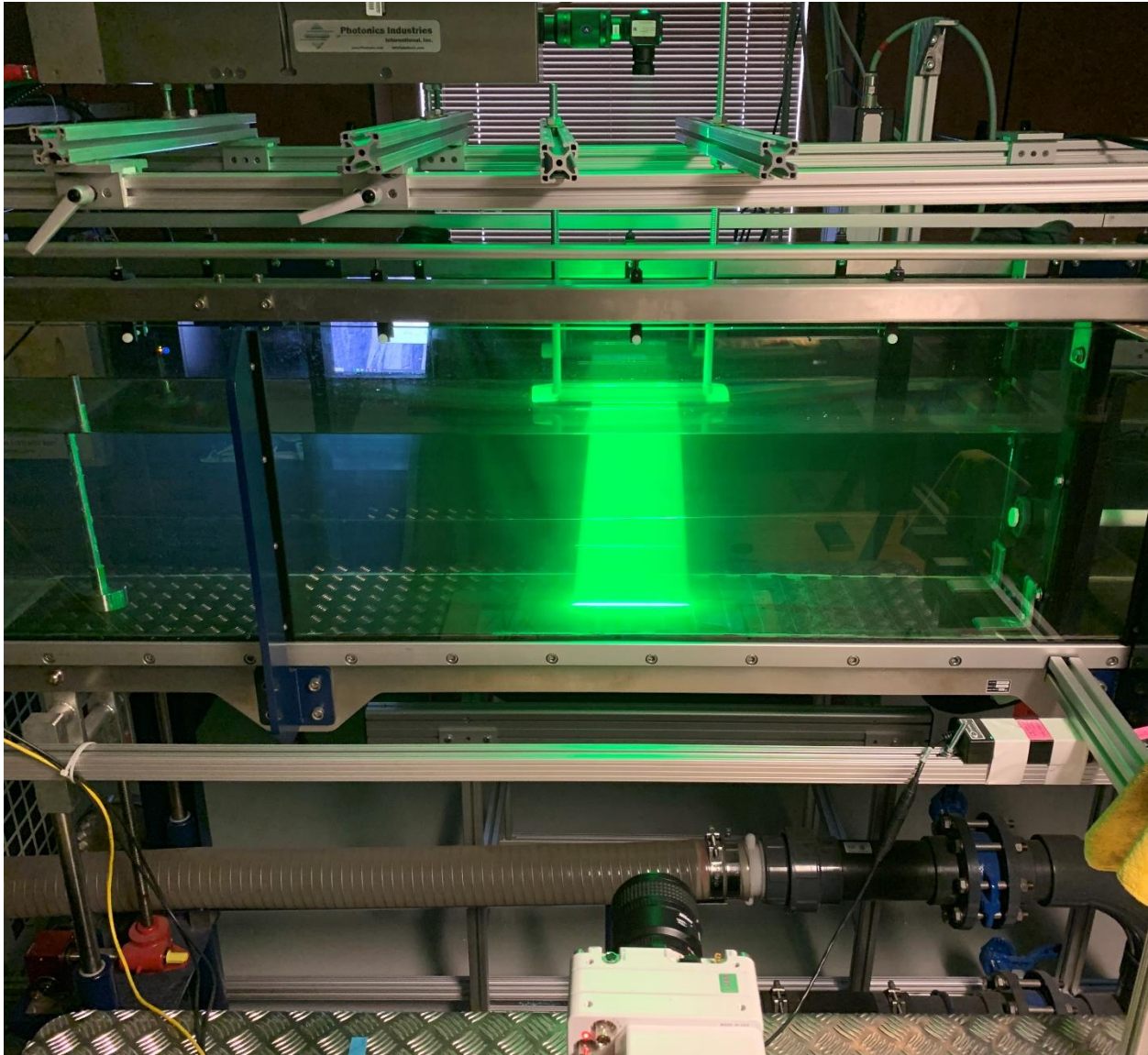


*Figure 4-6: Photographs of the baseline experimental set-ups for a turbulent jet into an ambient with centerline shown using a plug-and-thread apparatus.*

Since there is a steep shear layer in jet flow, it is important to make sure the laser sheet captures the centerline. A few millimeters off and the difference in velocities is significant – for example there is a  $\sim 0.3$  m/s difference if only 4 mm off the centerline at 20 gpm. A plug-and-thread apparatus was created to ensure the laser sheet captured the centerline of the jet. The thread was tied to a weighted rod at the height of the center of the tank fitting opening ( $5 \frac{15}{16}$ " or 150.8125 mm) and was placed within the flume such that the distance from the back wall to the thread was

the same as the center of the bulkhead tank fitting from the same wall ( $5 \frac{7}{8}$ " or 149.225 mm). The laser head was then adjusted so that the thread (i.e. the centerline) was illuminated.

#### 4.2.2 Data Collection

The closest position measurable with the PIV was  $\sim 35$  mm downstream of the reservoir (or RPM) wall due to the coupler. Therefore the LDA was used to measure points along the vertical profile at  $x = 18$  mm - just downstream of the bulkhead tank fitting ( $x/d_j = 2.78$ ; see *Figure 4-7*).

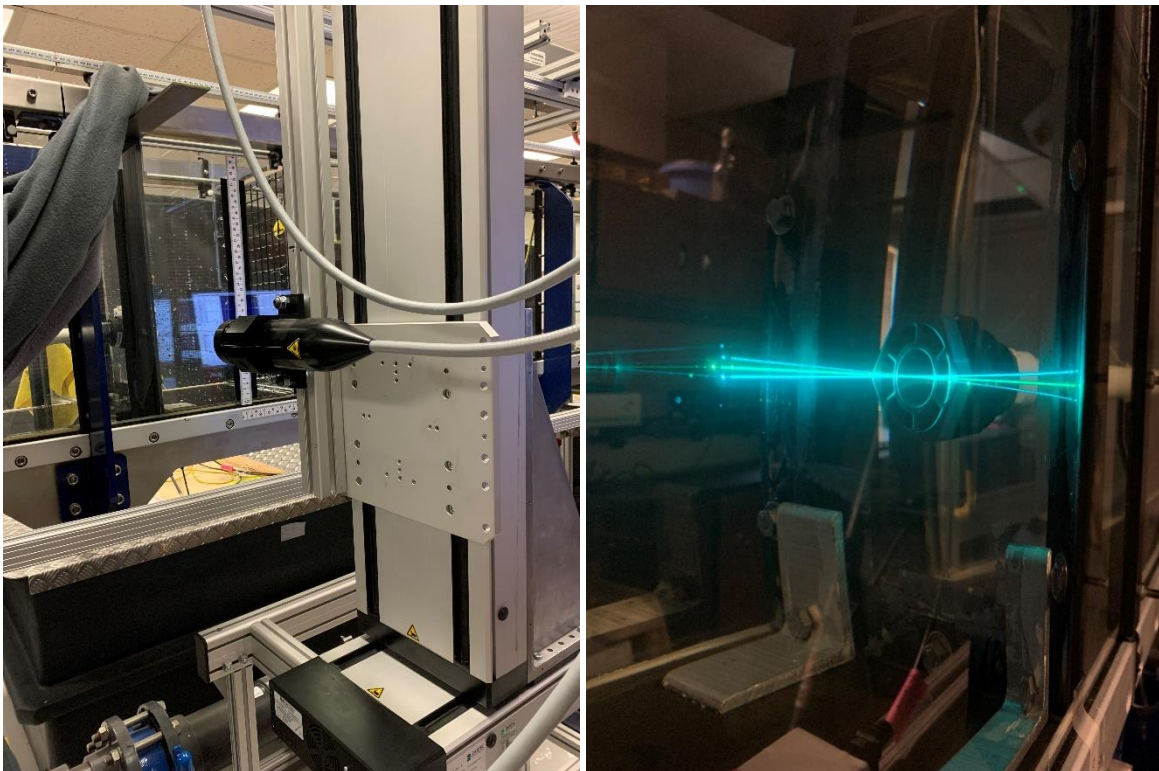


*Figure 4-7: Photograph of LDA traverse system (left) and lasers (right) with measurement volume located at  $r = 0$  and  $x = 18$  mm.*

Enough PIV windows were set up in order to capture the velocity field downstream of the jet (or RPM wall) up to  $\sim x/d_j = 30$  (covering the near, transition, and into the fully developed

regions). For the experimental trials, no measurements were taken for locations located within the RPM wall (i.e. when  $x/d_j < L$ ) (see *Figure 4-5*).

Preliminary data was collected to determine the maximum expected velocities in each window. This was important to determine the proper settings for the PIV including mode (i.e. Twin Pulse – Double Frame [TP/DF] or Single Pulse – Single Frame [SP/SF] mode), frequency (200-800 Hz), the time between pulses (Dt), etc. such that the pixel length of the maximum expected velocity was  $\sim 8 - 10$  pixels (Wilson & Smith 2013). On the basis of the maximum expected velocities from the preliminary run, ten different parameter settings were determined that would cover all windows for all scenarios where the velocities ranged 4 orders of magnitudes ( $O(-3)$  to  $O(1)$ ; *Table 4-3*).

*Table 4-3: Parameters used for data collection in different PIV windows*

Parameter ID	Max Expected Velocity (m/s)	PIV Mode	Frequency (Hz)	Dt ( $\mu$ s)
A	3.8 – 4.7	TP/DF	400	300
B	2.3 – 2.8	TP/DF	400	500
C	1.6 – 2.0	TP/DF	400	700
D	1.0 – 1.3	TP/DF	400	1100
E	0.9 – 1.1	SP/SF	800	300
F	0.7 – 0.9	SP/SF	600	300
G	0.6 – 0.7	SP/SF	500	300
H	0.5 – 0.6	SP/SF	400	300
I	0.3 – 0.4	SP/SF	300	300
J	< 0.3	SP/SF	200	300

#### 4.2.2.1 Data Processing

The DaVis 7.2 from LaVision GmbH PIV software was used to calculate the velocity fields using the Time-resolved 2D-PIV (2C2D) with one camera system. The camera was oriented in portrait mode in order to capture the entire depth of flow such with the minimum focal length to

achieve the highest resolution possible. This orientation is not automatically detected by the DaVis software (images showed flow in the negative  $y$ -direction) therefore the images were mirrored and rescaled so that the flow was oriented in the positive  $x$ -direction within the software. A geometric (rectangular) mask was added to process only the illuminated flow from the bottom of the coupler to the floor of the flume and the width (minimum) of the laser sheet at the coupler. A multi-pass correlation was used with an initial interrogation window size of  $96 \times 96$  pixels (1:1  $\square$  weighting; 50% overlap) and a final interrogation window size of  $32 \times 32$  pixels (with a spatial resolution of  $\sim 4.5$  mm) (2 passes; 1:1  $\circ$  weighting; 75% overlap) for all PIV windows with the universal outlier detection median filter and the anisotropic denoising enabled (medium). For more detailed information about the performance of the PIV algorithm used in the commercial software refer to Stanislas et al. (2008).

#### 4.2.2.2 Statistical Analysis to Determine Number of Images Necessary

As discussed in Section 3.1.3.5, the systematic error of a PIV system is dependent upon the parameters selected. Therefore a statistical analysis was necessary in order to determine the data collection methodology such that it would capture the true average nature of the flow for the various sets of parameters used. Given the PIV system, there were also practical limitations that needed to be taken into consideration including the number of consecutive images possible, the time required to write (upload) the images, the computational time to calculate the velocity fields, etc. Initially, the average velocity field of increasing number of images ( $N$ ; with the number of vector fields  $n = N - 1$ ) was compared to LDA data. The root mean squared error (RMSE) and normalized RMSE (NRMSE; normalized using the average streamwise velocity of the vertical profile) at corresponding points from data collected using the PIV system and the

LDA show little difference ( $\sim 0.29$  m/s and  $\sim 0.2$  respectively for  $\langle U \rangle$ ) as the number of images processed increases seen *Figure 4-8*.

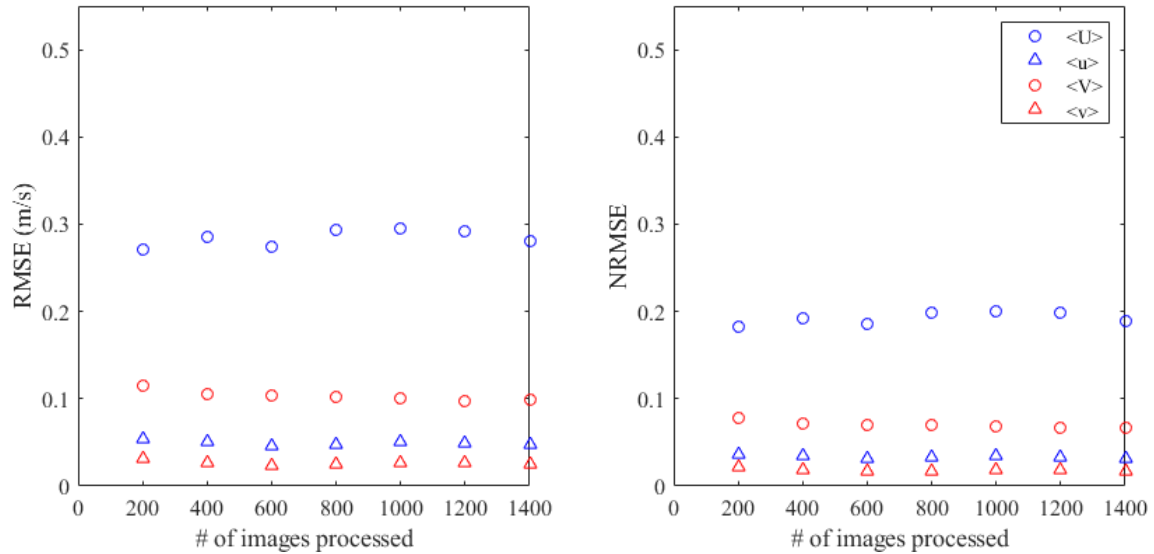


*Figure 4-8: RMSE and NRMSE for increasing number of images (vector fields) compared to the LDA measurements along the vertical profile at  $x = 98$  mm for a jet of 20 gpm.*

Due to the turbulent nature of the flow, it was to be determined if taking all images consecutively or taking multiple sets of a reduced number of images would best capture the average nature of the flow. Also, if multiple sets of images are taken, the number of sets as well as the number of images per set matter. The frequency (and  $\Delta t$  for TP/DF mode) along with the number of images taken determine the time sampling window over which the time-averaged velocity fields are measured. For the example profile shown in *Figure 4-8* above, the time sampling window ranges from 0.5 to 3.5 seconds for 200-1400 images. Once the images are recorded, the PIV system required  $\sim 0.14$  s/image to write in preparation to be processed. While the images are being written, the PIV software is unable to record images. If multiple sets of images are taken, then there is a waiting period before the next set can be recorded which is dependent upon the number of images in the set. This also means that data is collected in snapshots over a longer window of time. To explore how the number of sets and number of images per set affects the time-averaged

results four different schemes of the same number of images overall were considered: 12 sets of 200 images, 6 sets of 400 images, 4 sets of 600 images, and 3 sets of 800 images (See *Figure 4-9*).

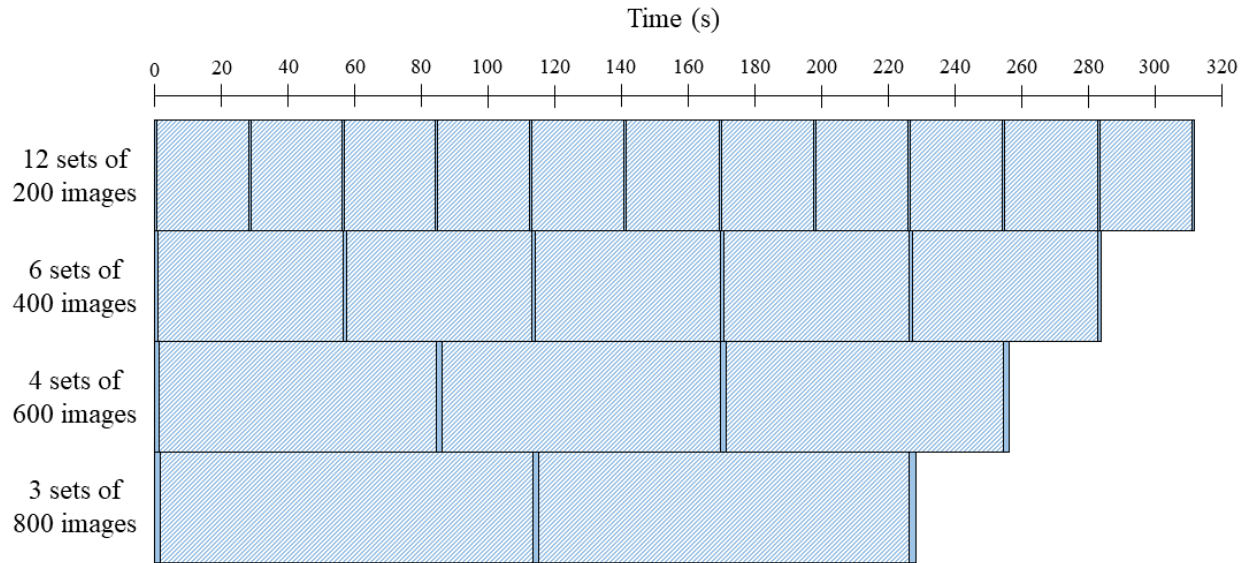


*Figure 4-9: Schematic of overall data collection time windows for different schemes of sets of images; solid coloring = recording time window & striped coloring = image writing time (e.g. no recording possible).*

The RMSE and NRMSE of the difference schemes of PIV image sets as compared to the LDA data are shown in *Figure 4-10 to 13* below. The first thing to note is that the RMSE and NRMSE are the same if not less for all image set scenarios compared to taking all images consecutively. The lowest RMSE and NRMSE for  $\langle U \rangle$ , for multiple sets of images, is  $\sim 0.2$  m/s and  $\sim 0.15$  respectively. This was expected since the LDA data was collected over a 4-minute (240-second) window to ensure that a statistically significant number of measurements were made; i.e. the sample variance being equal to the population variance (Klema et al. 2020). When considering the streamwise and lateral average velocities and fluctuations, the scheme that stands out is the multiple sets of 200 images; with only 7 sets of 200 images are necessary to achieve the lowest RMSE and NRMSE – 1400 images total. Conceptually, while the snapshot is shorter (only 0.5 s)

there are more snapshots over a  $\sim 2.86$ -min interval (171.5 s). For these reasons, the multiple sets of 200 images scheme was selected.

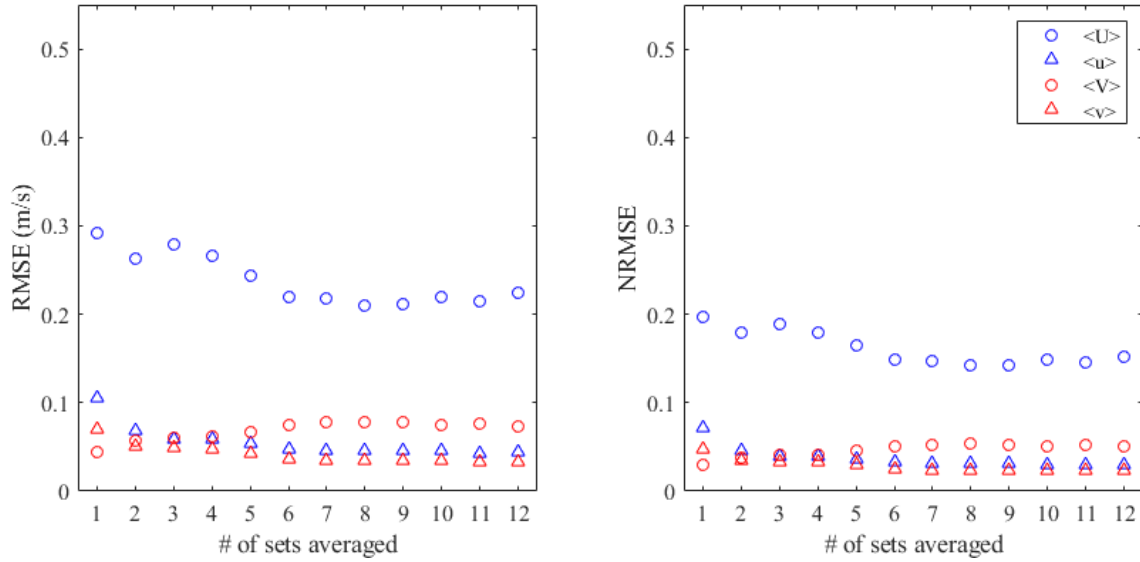


Figure 4-10: RMSE and NRMSE for 12 sets of 200 images averaged compared to the LDA measurements along the vertical profile at  $x = 98$  mm.

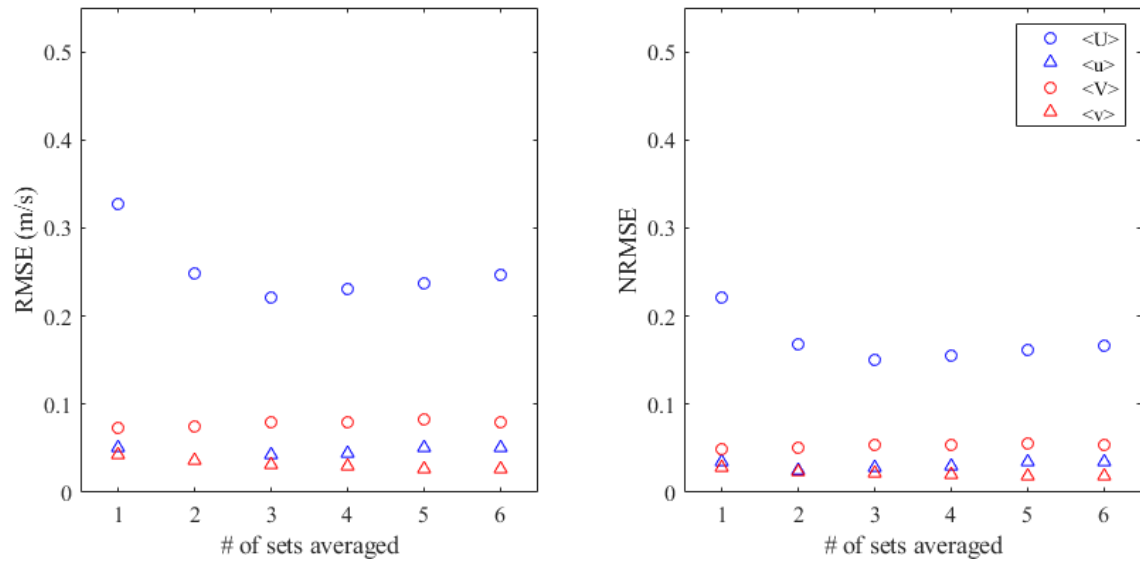


Figure 4-11: RMSE and NRMSE for 6 sets of 400 images averaged compared to the LDA measurements along the vertical profile at  $x = 98$  mm.

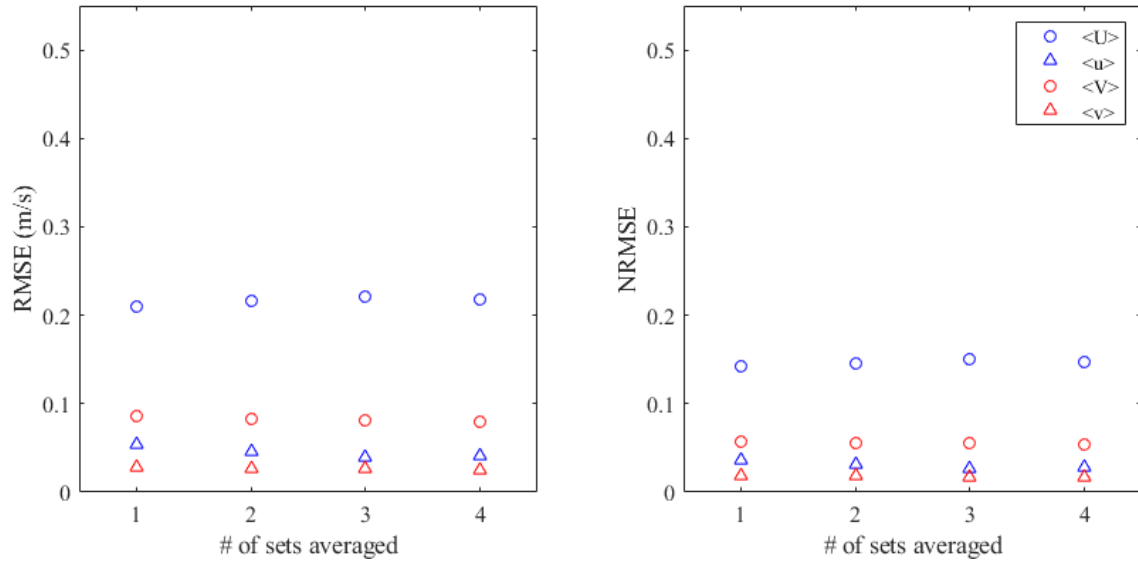


Figure 4-12: RMSE and NRMSE for 4 sets of 600 images averaged compared to the LDA measurements along the vertical profile at  $x = 98$  mm.

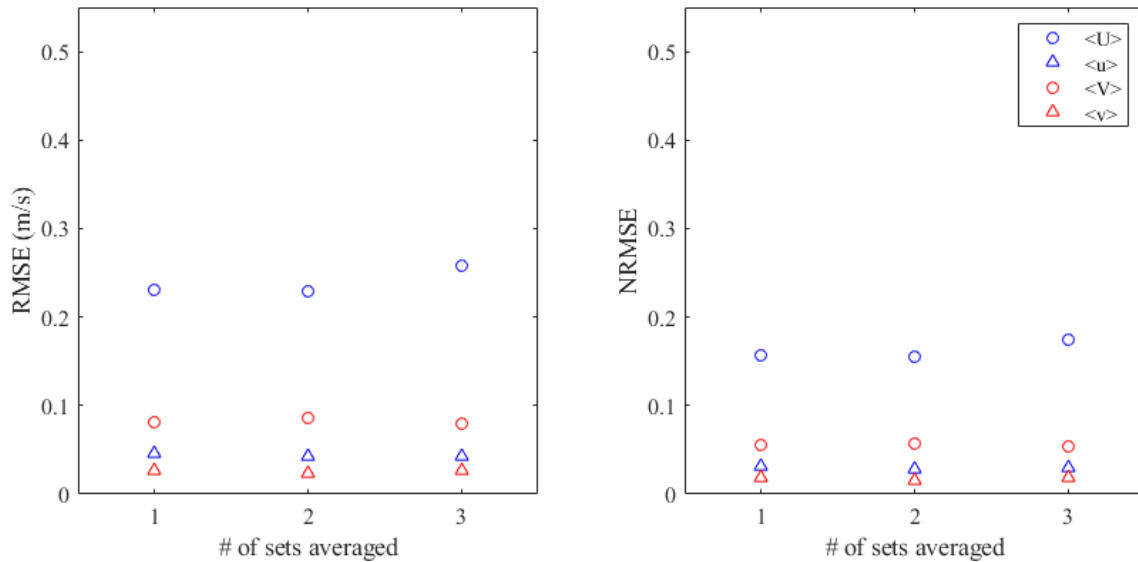
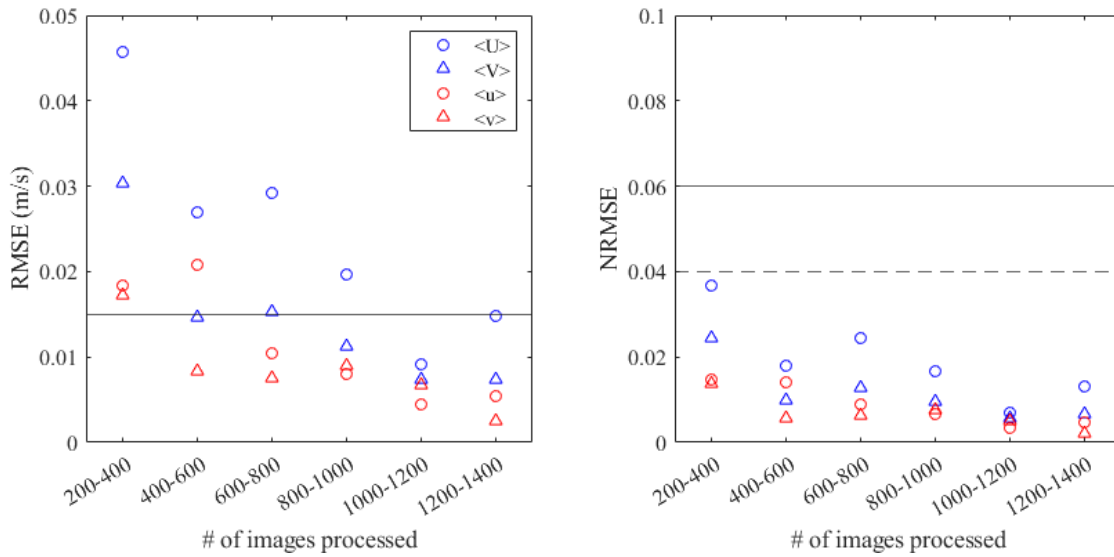


Figure 4-13: RMSE and NRMSE for 3 sets of 800 images averaged compared to the LDA measurements along the vertical profile at  $x = 98$  mm.

A similar error analysis was conducted for all the PIV parameter settings that were determined previous (see Table 4-3). Since the LDA only takes point measurements and was only used to verify, the PIV data was compared against itself – a common practice when LDA data is not available (Capone et. al. 2013; Aleyasin et al. 2017; etc.). The RMSE and NRMSE along a

vertical profile within a PIV window was determined between an increasing number of images as well as an increasing number of sets of 200 images. Depending on the PIV mode, the maximum number of consecutive images possibly taken was 1400 images in TP/DF mode and 2800 images in SP/SF mode. Since these are internal comparisons a reasonable error cut-off was determined by book ending the error under the settings required for the highest and lowest maximum expected flow rates. For higher velocities the RMSE cut-off was set at 0.015 m/s (see *Figures 4-14 & 15*).



*Figure 4-14: RMSE and NRMSE between an increasing number of images (vector fields) of PIV measurements along the vertical profile at  $x = 98$  mm (TP/DF at 400 Hz &  $DT = 300\mu s$ ).*

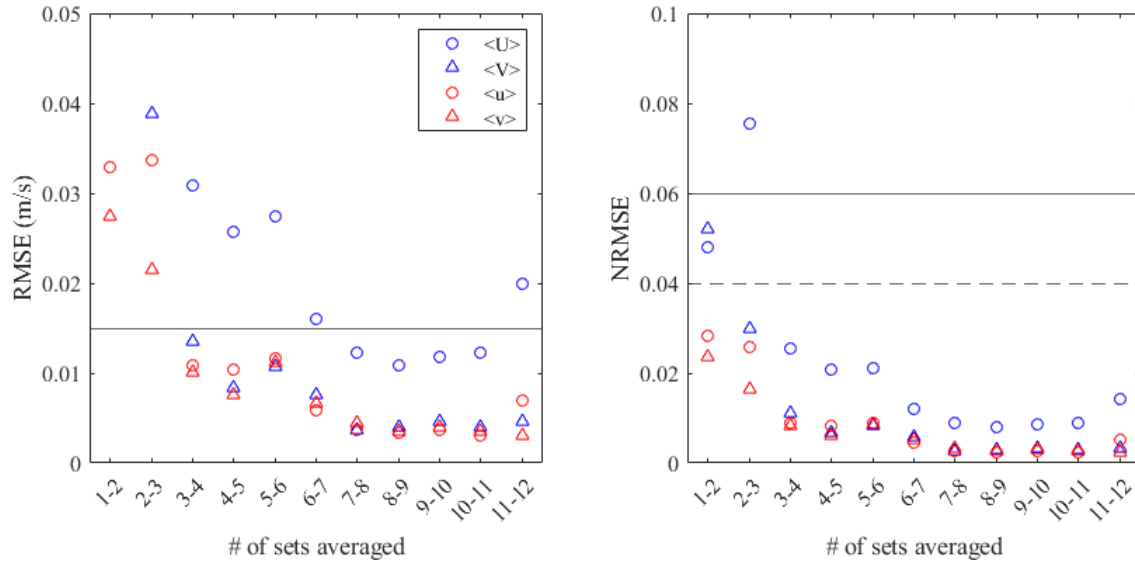


Figure 4-15: RMSE and NRMSE between increasing number of sets of 200 images averaged of PIV measurements along the vertical profile at  $x = 98 \text{ mm}$  (TP/DF at 400 Hz &  $DT = 300\mu\text{s}$ ).

For lower flow rates the NRMSE cut-off was set at 0.06 (see Figures 4-16 & 17). While the NRMSE for lower velocities was less (0.04) when taking more images consecutively, it was decided that it was better to be consistent in the method of data collection (i.e. taking multiple sets of 200 images for all PIV parameter settings) for all PIV windows.

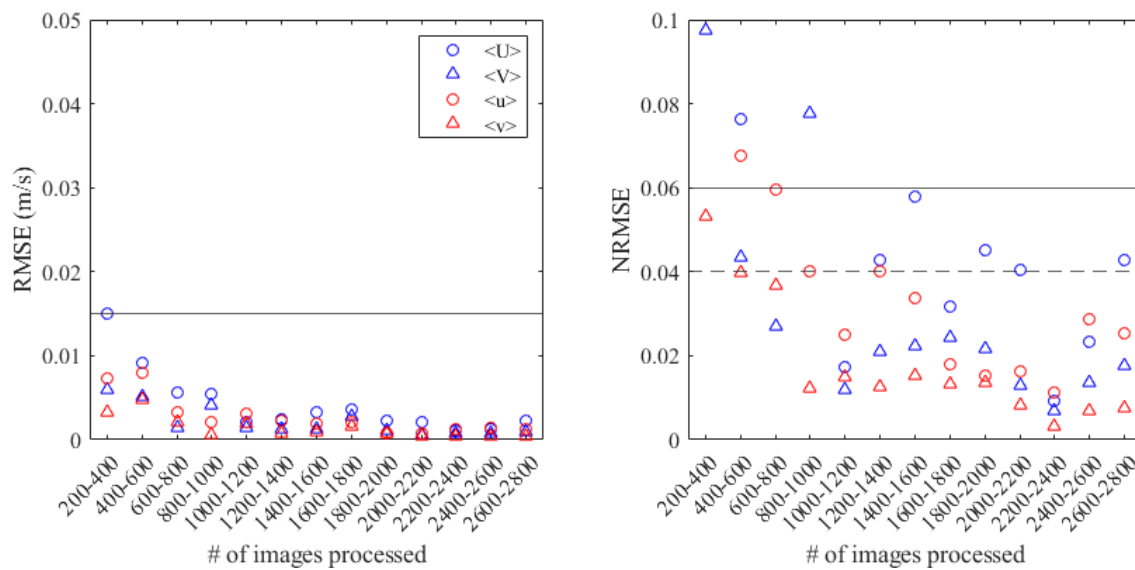


Figure 4-16: RMSE and NRMSE between an increasing number of images of PIV measurements along the vertical profile for SP/SF at 200 Hz &  $DT = 300\mu\text{s}$ .

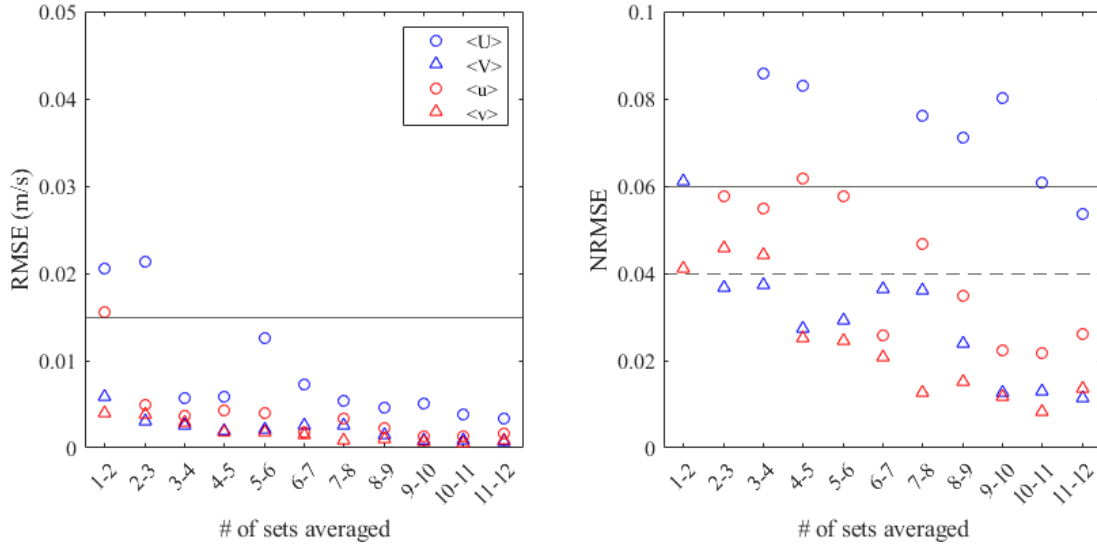


Figure 4-17: RMSE and NRMSE between increasing number of sets of 200 images averaged of PIV measurements along the vertical profile for SP/SF at 200 Hz & DT = 300us.

The computation time required to process the larger number of images was also taken into consideration. The final PIV data collection schemes based upon parameter settings can be found in Table 4-4. (See Appendix A for additional PIV parameter setting plots and tables).

Table 4-4: Parameters used for data collection in different PIV windows

Parameter ID	A	B	C	D	E	F	G	H	I	J
# of sets	7	7	7	7	7	7	8	9	10	12
Total # of images	1400	1400	1400	1400	1400	1400	1600	1800	2000	2400
Sampling Time (s)	0.50	0.50	0.50	0.50	0.25	0.33	0.40	0.50	0.67	1.00
Overall Sampling Time Window (min)	2.86	2.86	2.86	2.86	1.43	1.44	1.69	1.94	2.21	2.77

### 4.2.3 Verification using LDA

The LDA was used to verify the calculated velocities using the PIV data collection scheme(s) determined above. LDA data was collected at various points along vertical profiles spanning the majority of the expected Gaussian curve of a turbulent round jet at 20 gpm. Multiple vertical profiles were taken at multiple locations downstream of the jet, each in a window with a different

parameter ID (A:  $x/d_j = 6.65$ , B:  $x/d_j = 11.76$ , C:  $x/d_j = 14.61$ , D:  $x/d_j = 22.56$ , E:  $x/d_j = 25.86$ , F:  $x/d_j = 30.64$ ). The streamwise and lateral velocity data from the PIV generally tends to be less than the LDA, however, the fluctuation data lines up well. Overall there is considered to be good agreement between the LDA point measurement data and the corresponding vertical profile data extracted from the PIV software as seen in *Figures 4-18 & 19* below. (See Appendix A for additional LDA verification plots).

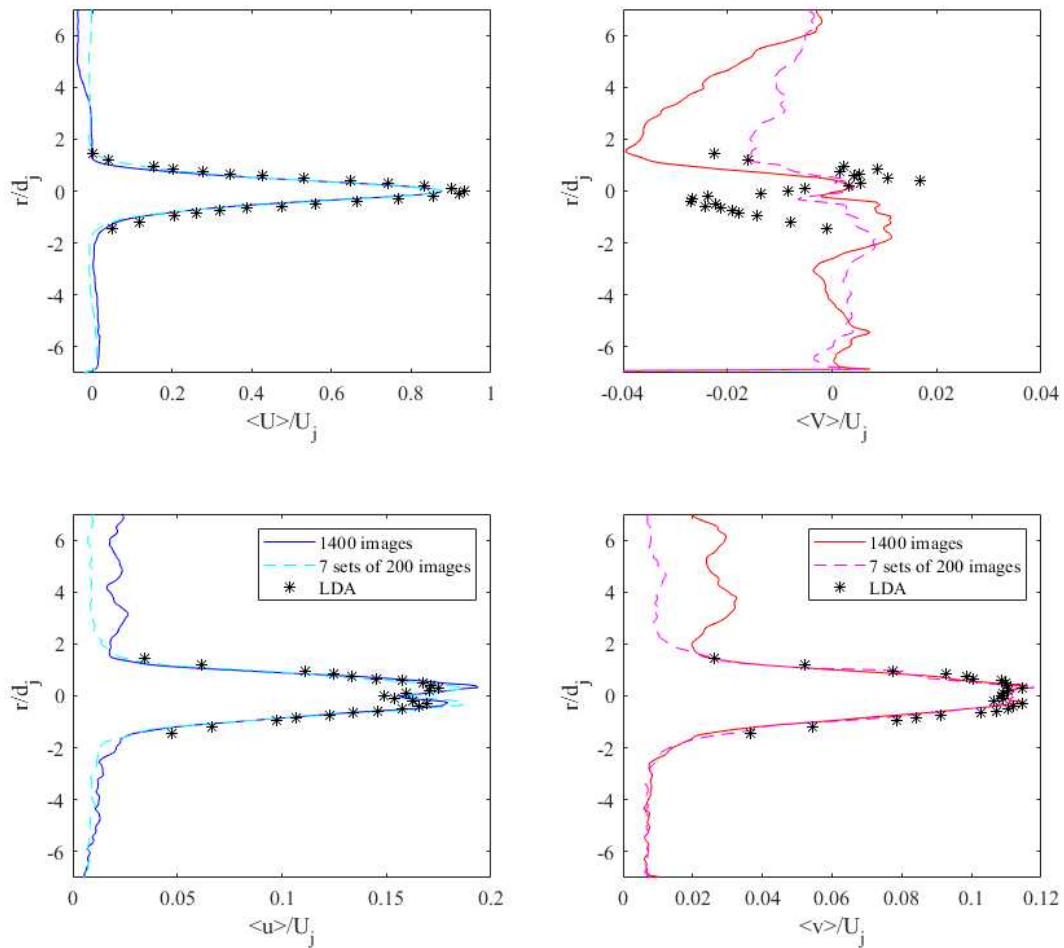


*Figure 4-18: Average streamwise and vertical velocity profiles for consecutive images and sets of 200 images of PIV and LDA measurements along the vertical profile for TP/DF at 400 Hz &  $DT = 300\mu s$ .*

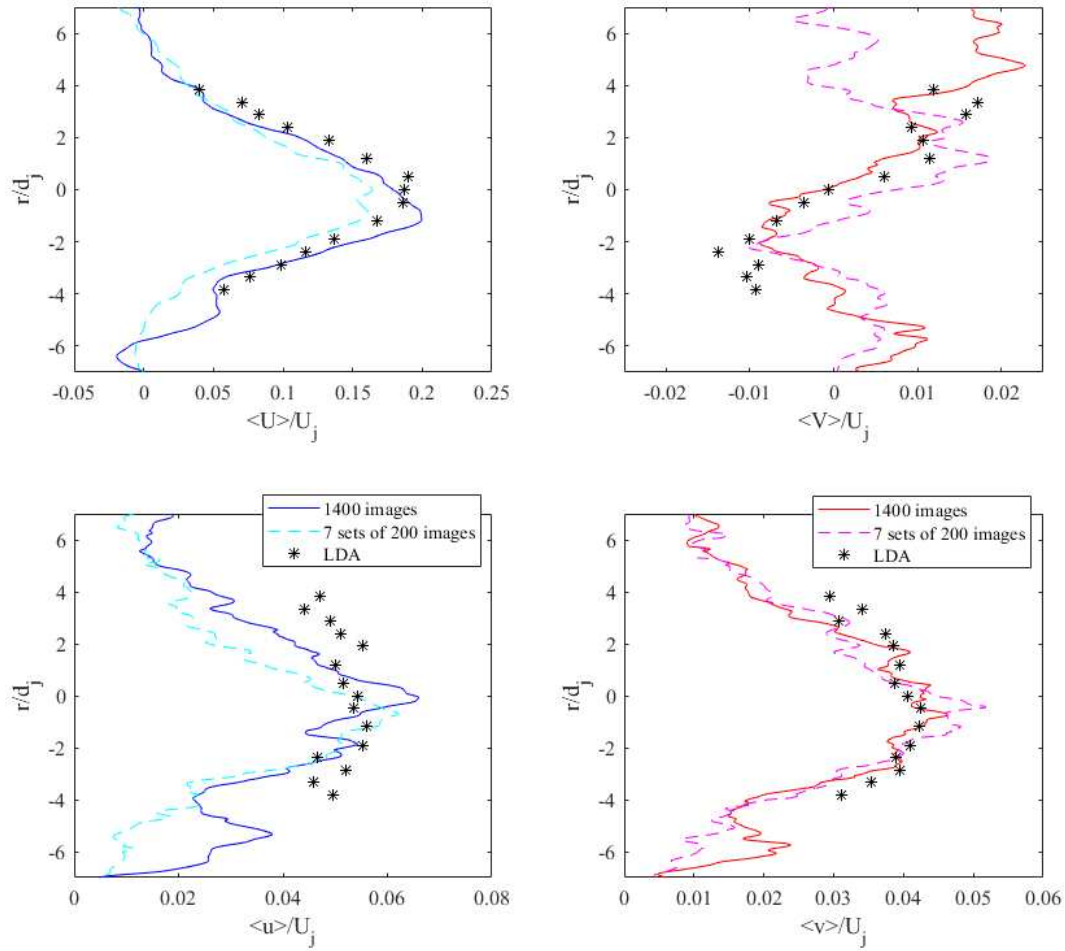


Figure 4-19: Average streamwise and vertical velocity profiles for consecutive images and sets of 200 images of PIV and LDA measurements along the vertical profile for SP/SF at 800 Hz &  $DT = 300\mu s$ .

## 4.3 Results & Discussion

### 4.3.1 Turbulent Round Jet into an Ambient

The baseline of this study consisted of a turbulent round jet into an ambient – a widely studied phenomena as discussed in Section 2.2.1. This baseline is not only representative of a sharp inlet entering a contact tank without any RPM but is also used as validation of results with the PIV data collection methodology employed. The primary results of the PIV measurements are

velocity fields. From the velocity fields additional information can be obtained using the PIV software including the Reynold's stresses and turbulent kinetic energy. Additional post processing (using MATLAB) was performed to determine the jet spreading & decay rates along with the mass & momentum fluxes.

#### 4.3.1.1 Velocities

Scalar plots (across 6 windows) of the average streamwise velocity of the baseline jet at 20 gpm normalized using the average streamwise jet velocity ( $U_j$ ; determined from the flowmeter) can be seen in *Figure 4-20*. The decay and spread of the jet are evident with a potential core visible up until  $x/d_j \approx 8$ . The  $\langle U \rangle / U_j$  and  $\langle V \rangle / U_j$  along vertical profiles are seen *Figures 4-21 & 22*.

While there is some variability, more so in the lateral ( $V$ ) velocities, the average velocity profiles generally collapse onto similar curves along the downstream streamwise direction. The  $\langle U \rangle$  velocities follow a Gaussian shape and the  $\langle V \rangle$  velocities are much less (an order of magnitude or more) than the  $\langle U \rangle$  velocities as expected (Pope 2000). The  $\langle V \rangle$  velocities increase moving away from the centerline until the edge of the jet where the direction reverses (most evident closer to the jet exit). This is also consistent with the expected self-similarity of the round turbulent jets (Pope 2000). When plotted on top of one another in *Figure 4-23 & 24*, the  $\langle U \rangle$  velocities show a similar pattern to *Figures 2-5(a) & (b)*.

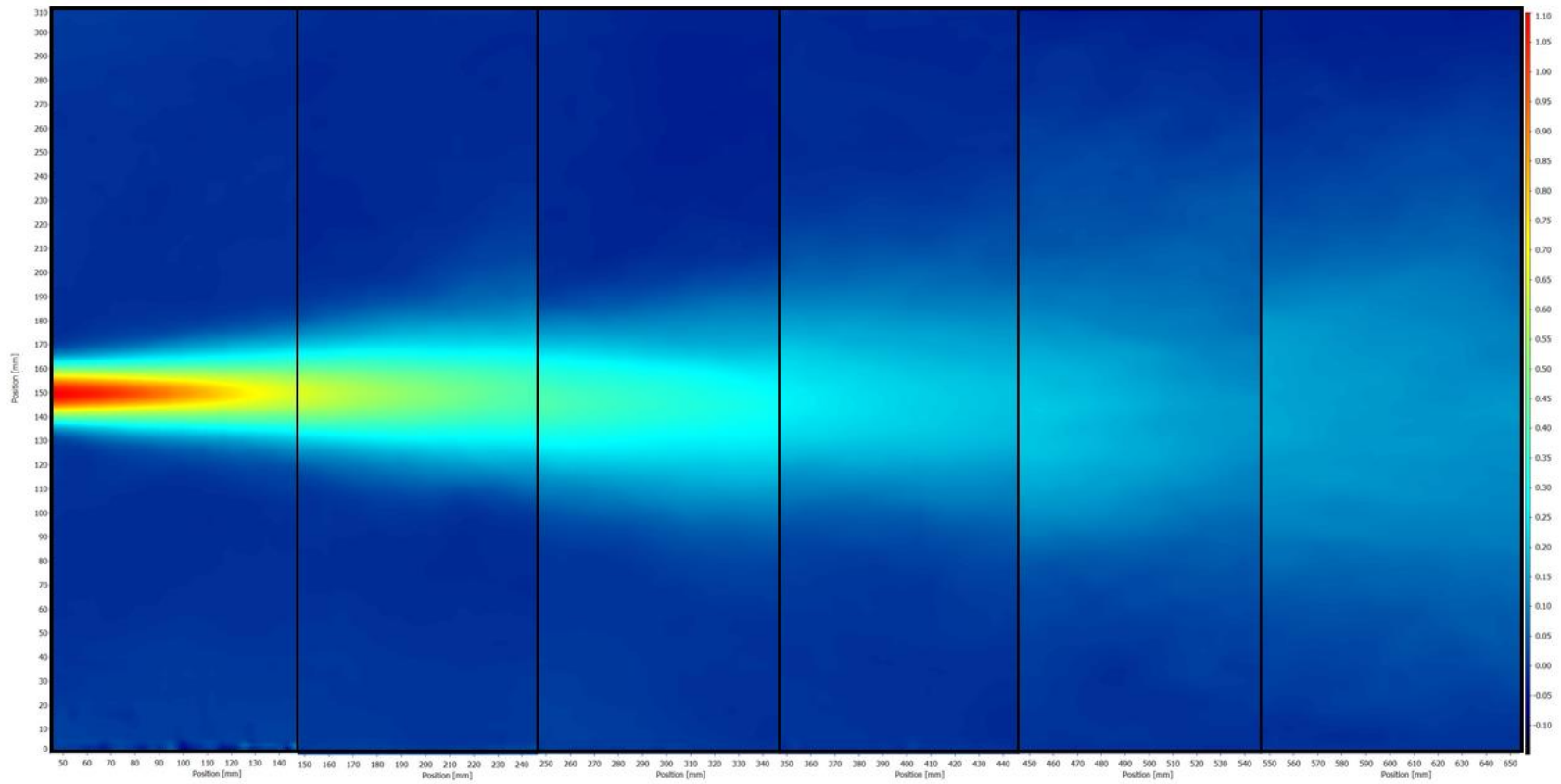


Figure 4-20:  $\langle U \rangle / U_j$  velocity scalar plot for the baseline jet at 20 gpm jet. The x & y-axis are in mm and the color scale ranges from  $-0.1 \leq \langle U \rangle / U_j \leq 1.10$  (blue  $\rightarrow$  red).

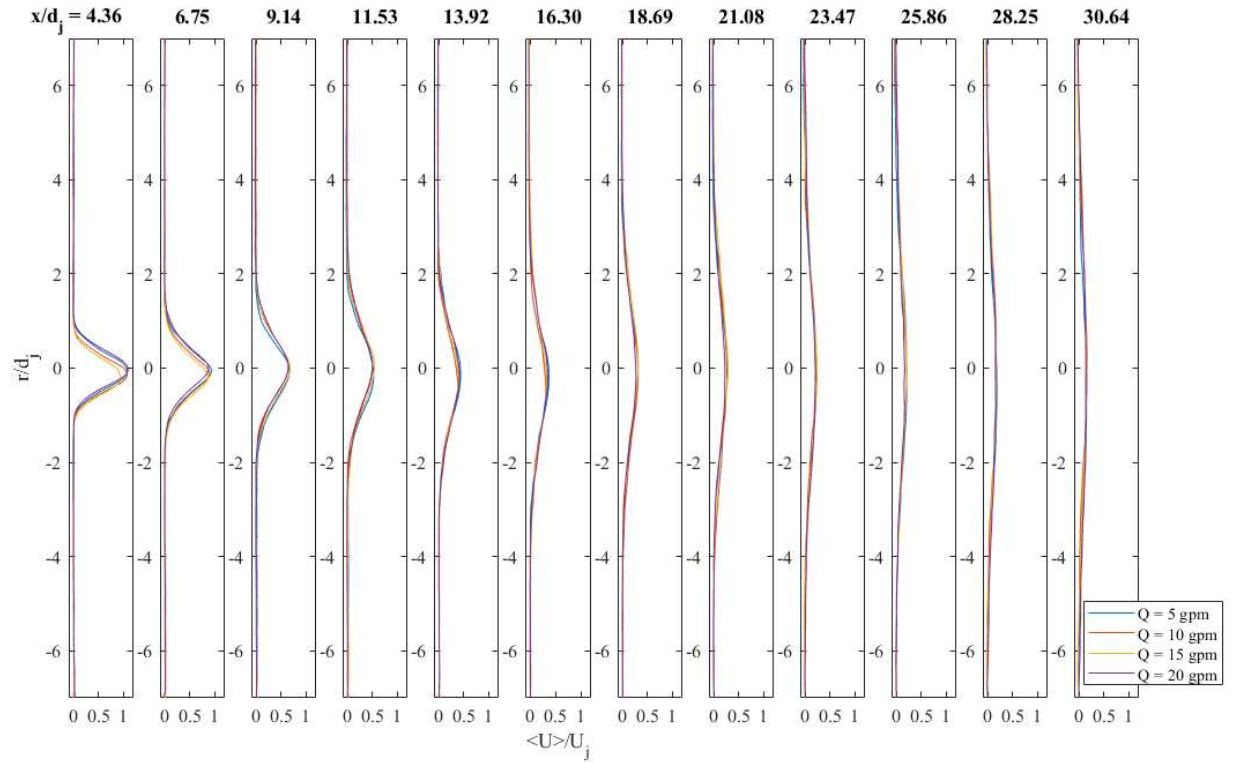


Figure 4-21: Normalized streamwise ( $U$ ) velocity profiles at increasing distances downstream of wall.

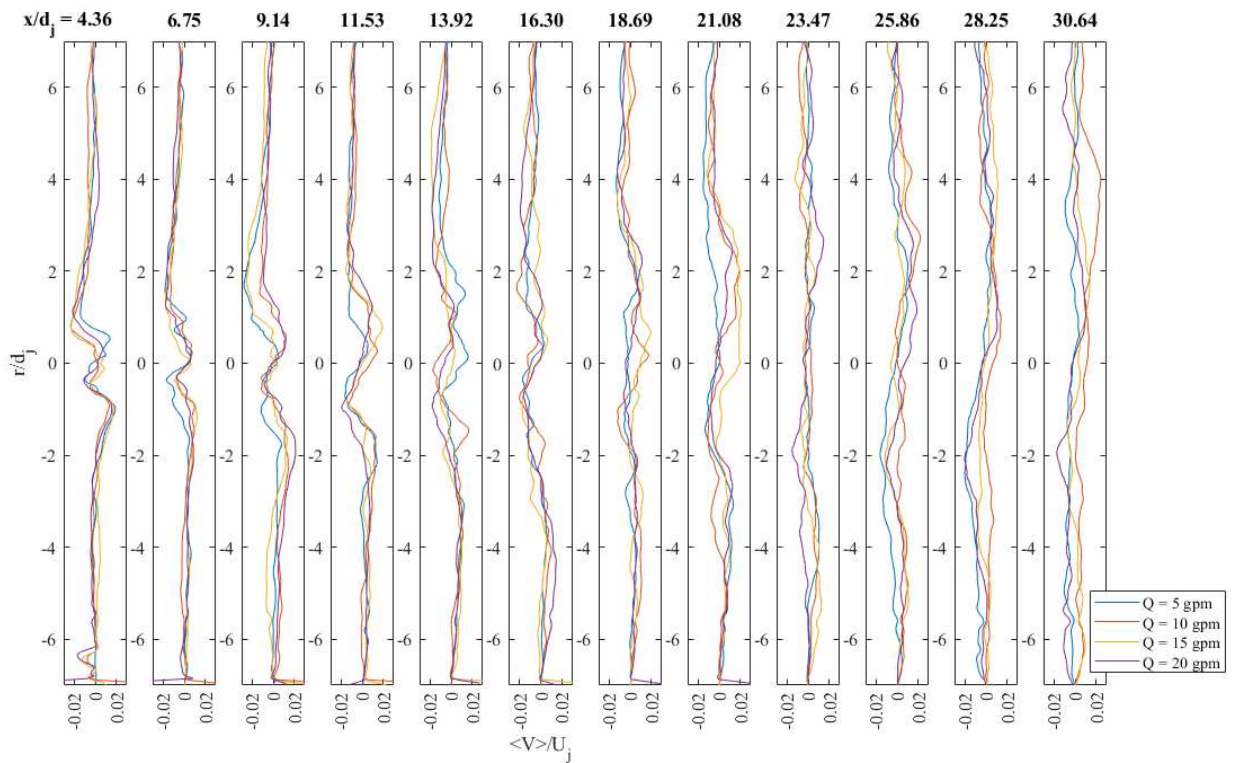


Figure 4-22: Normalized lateral ( $V$ ) velocity profiles at increasing distances downstream of wall.

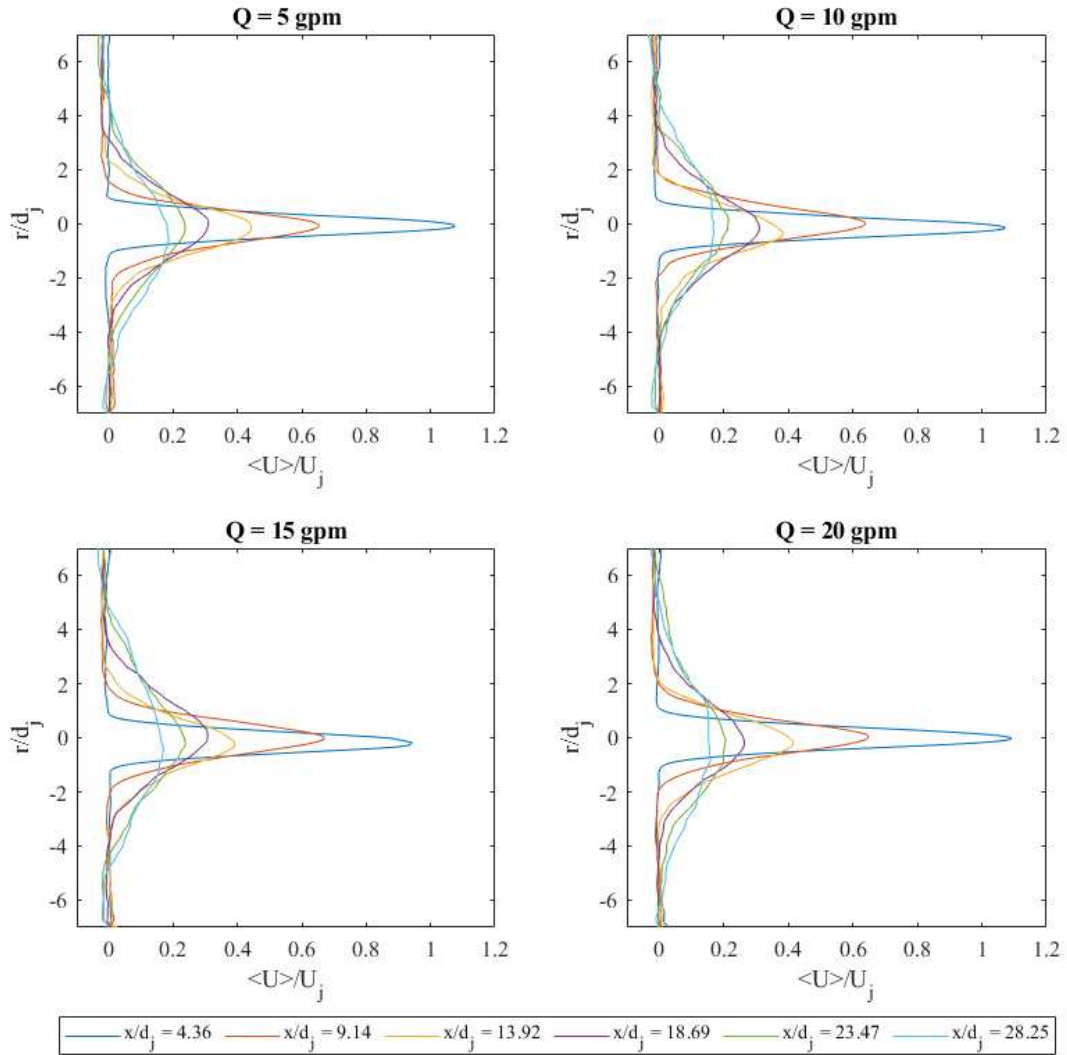


Figure 4-23: Plots of streamwise velocity profiles at select  $x/d_j$  locations.

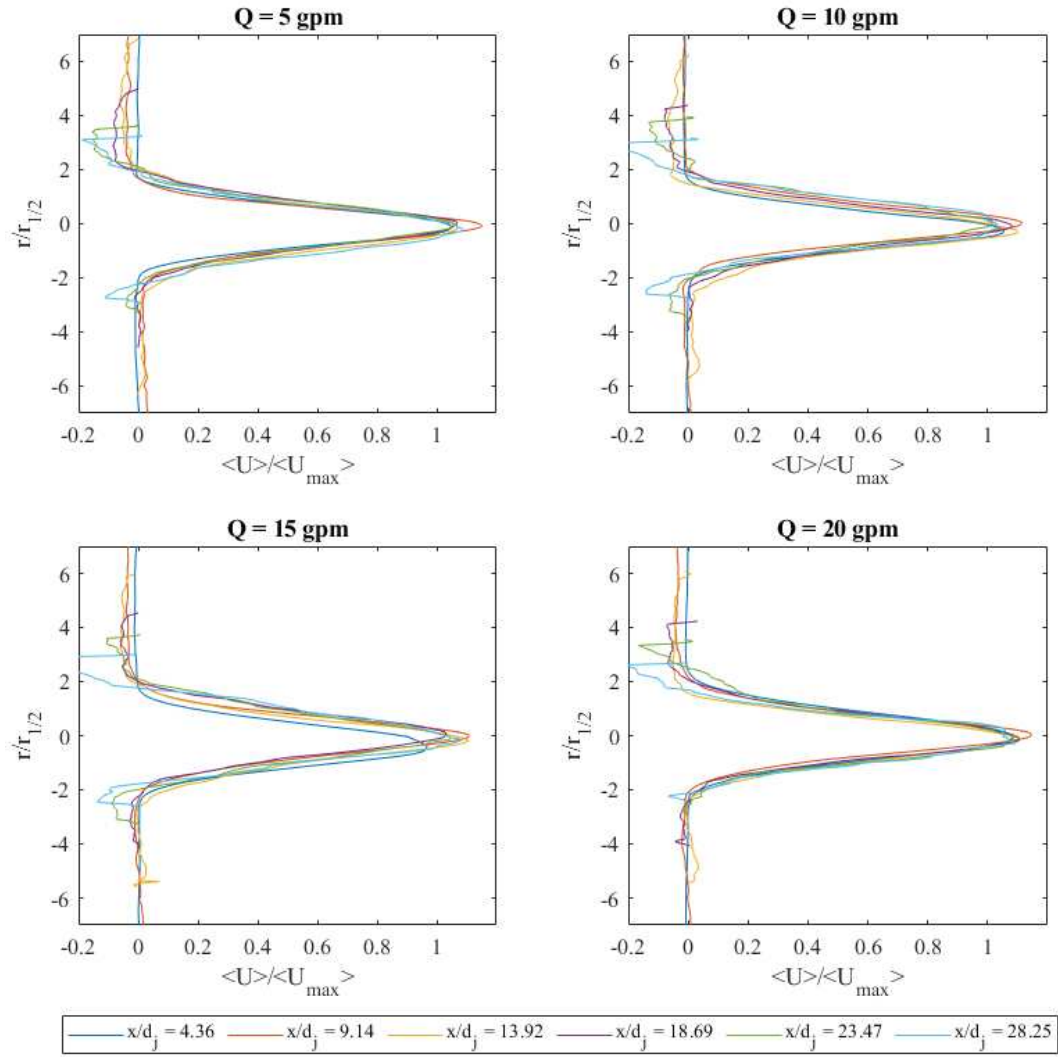


Figure 4-24: Plots of similar streamwise velocity profiles at select  $x/d_j$  locations.

#### 4.3.1.2 Reynolds Stresses

As discussed in Section 2.2.1, a turbulent round jet is assumed to be axisymmetric, therefore only the normal stresses in the streamwise ( $\langle u^2 \rangle$ , Figure 4-25) and lateral ( $\langle v^2 \rangle$ , Figure 4-26) directions along with the shear stress ( $\langle uv \rangle$ , Figure 4-27) are relevant.

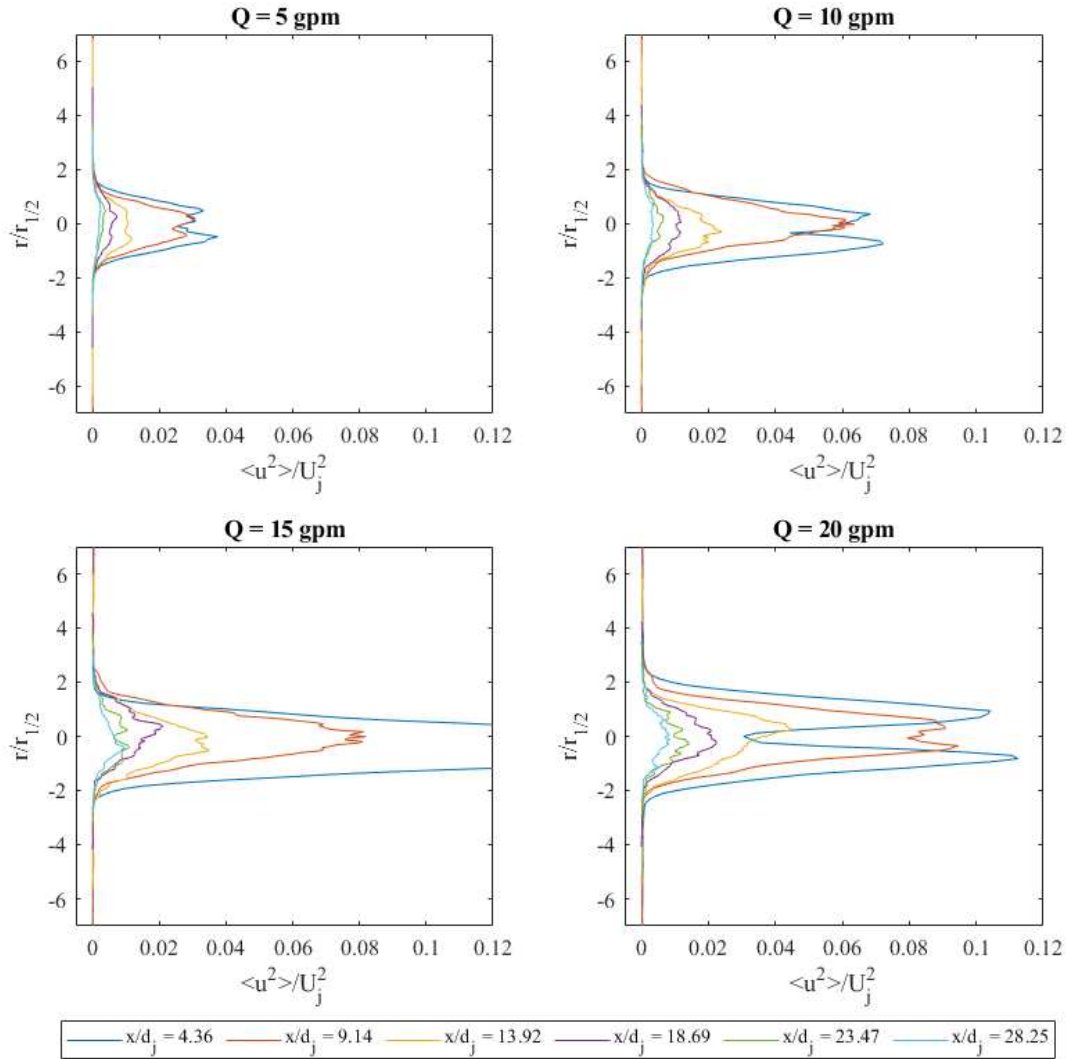


Figure 4-25: Plots of streamwise normal stress profiles at select  $x/d_j$  locations.

In the near region of the jet there are more distinct peaks for  $\langle u^2 \rangle$  and  $\langle v^2 \rangle$  but the further downstream these peaks disappear. Since the turbulent jet in this study is coming from a long pipe, there is a larger initial shear layer resulting in smaller peaks in  $\langle u^2 \rangle$  and  $\langle v^2 \rangle$  (Xu & Antonia 2002). The  $\langle u^2 \rangle$  and  $\langle v^2 \rangle$  for all flow rates (except 15 gpm) increases up to  $x/d_j = 9.14$  and then decreases until about  $x/d_j \sim 20$  where the profiles start to collapse and become self-similar. For the 15 gpm jet, the normal stresses at  $x/d_j = 4.36$  are much larger and do not show distinct peaks indicating an initial shear layer. To investigate this phenomena was beyond the

scope of this study and was therefore ignored since downstream the normal stresses return to the pattern seen in the other jets.

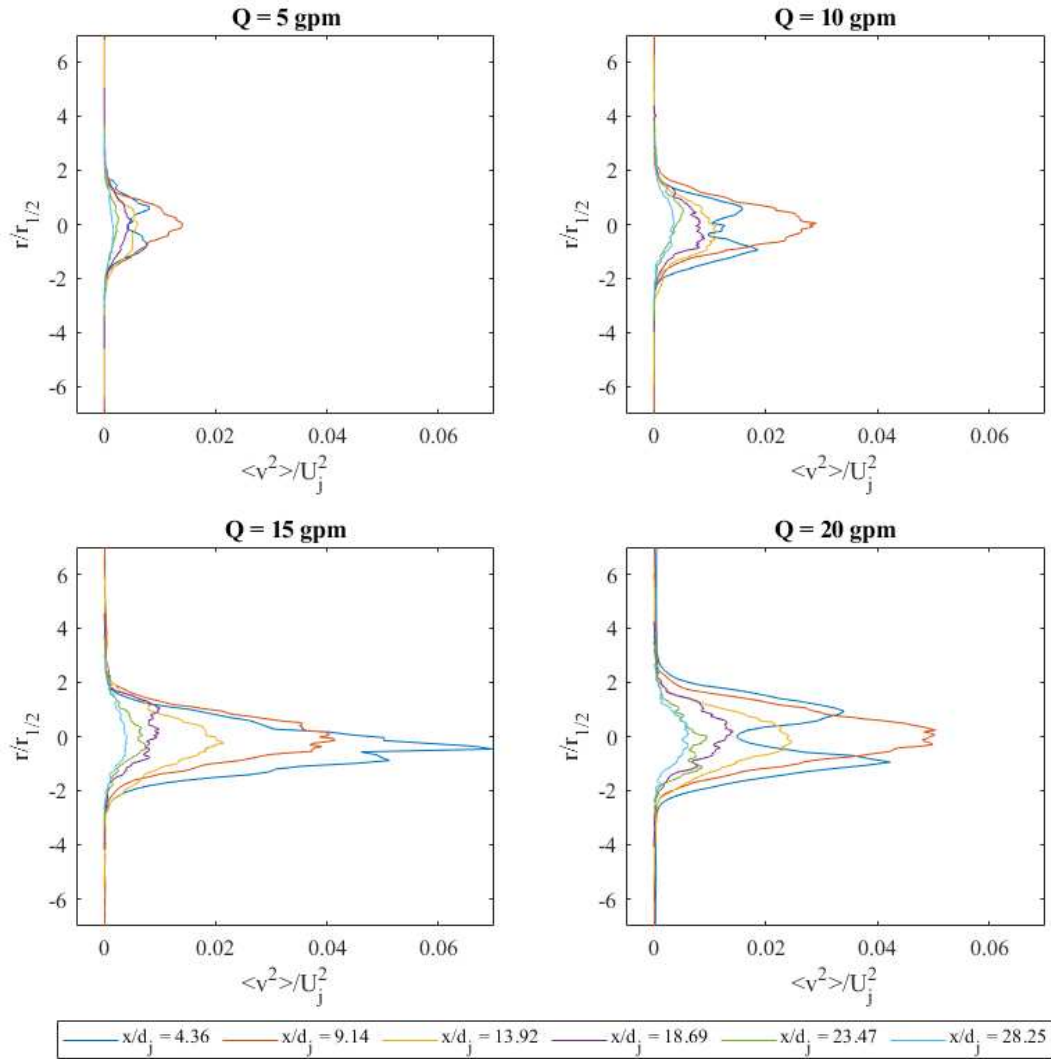


Figure 4-26: Plots of lateral normal stress profiles at select  $x/d_j$  locations.

The shear stress peaks at the edges of the jet (corresponding to the  $\langle V \rangle$  velocities) and are zero at the centerline. It is also noted that as the flow rate (and thus  $Re_j$ ) increases, so do the magnitudes of all the Reynolds stresses.

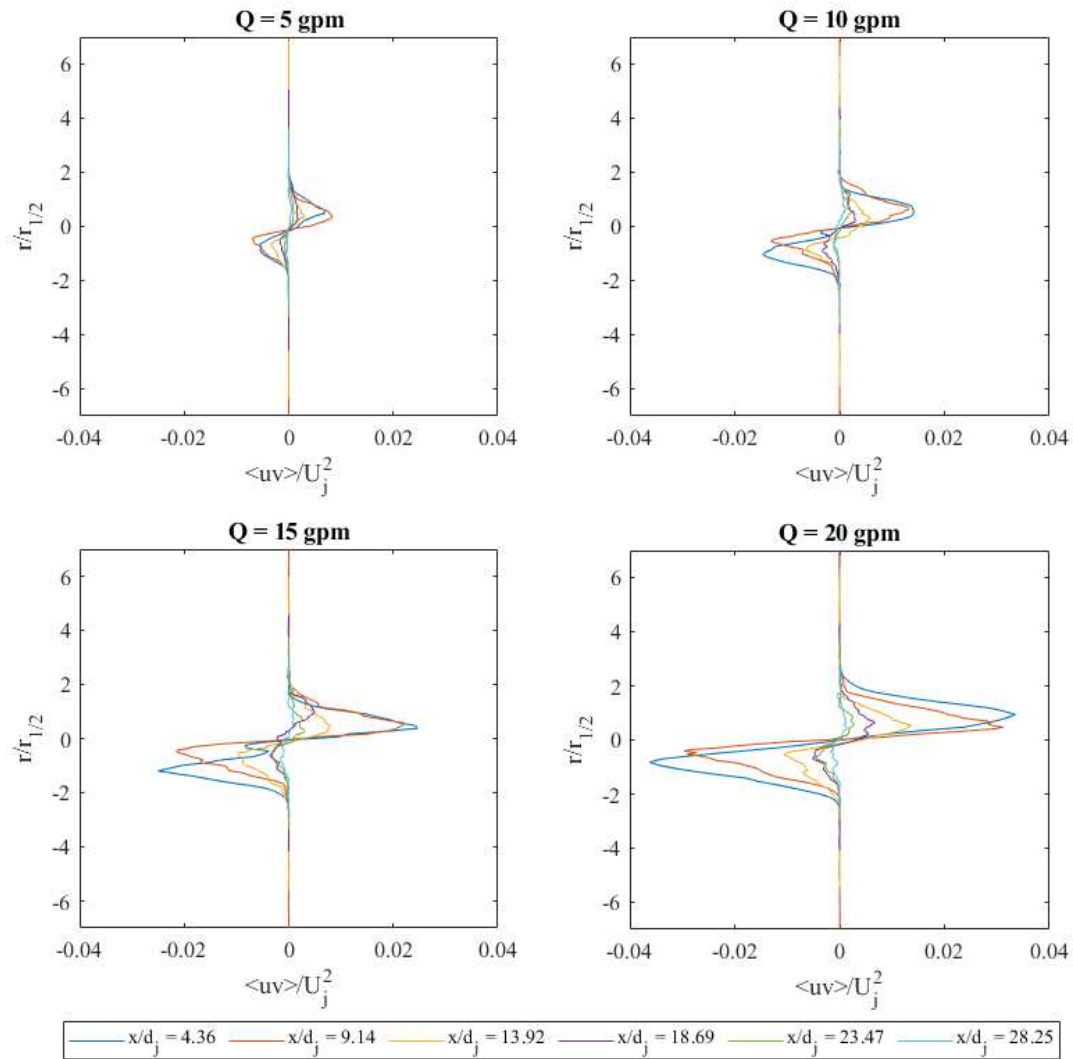


Figure 4-27: Plots of Reynold's shear stress profiles at select  $x/d_j$  locations.

### 4.3.1.3 Turbulence

By definition (see Section 2.2.1) the turbulent kinetic energy ( $k$ ) of a turbulent round jet flow follows the trend of the normal stresses as seen in *Figure 4-28* below.

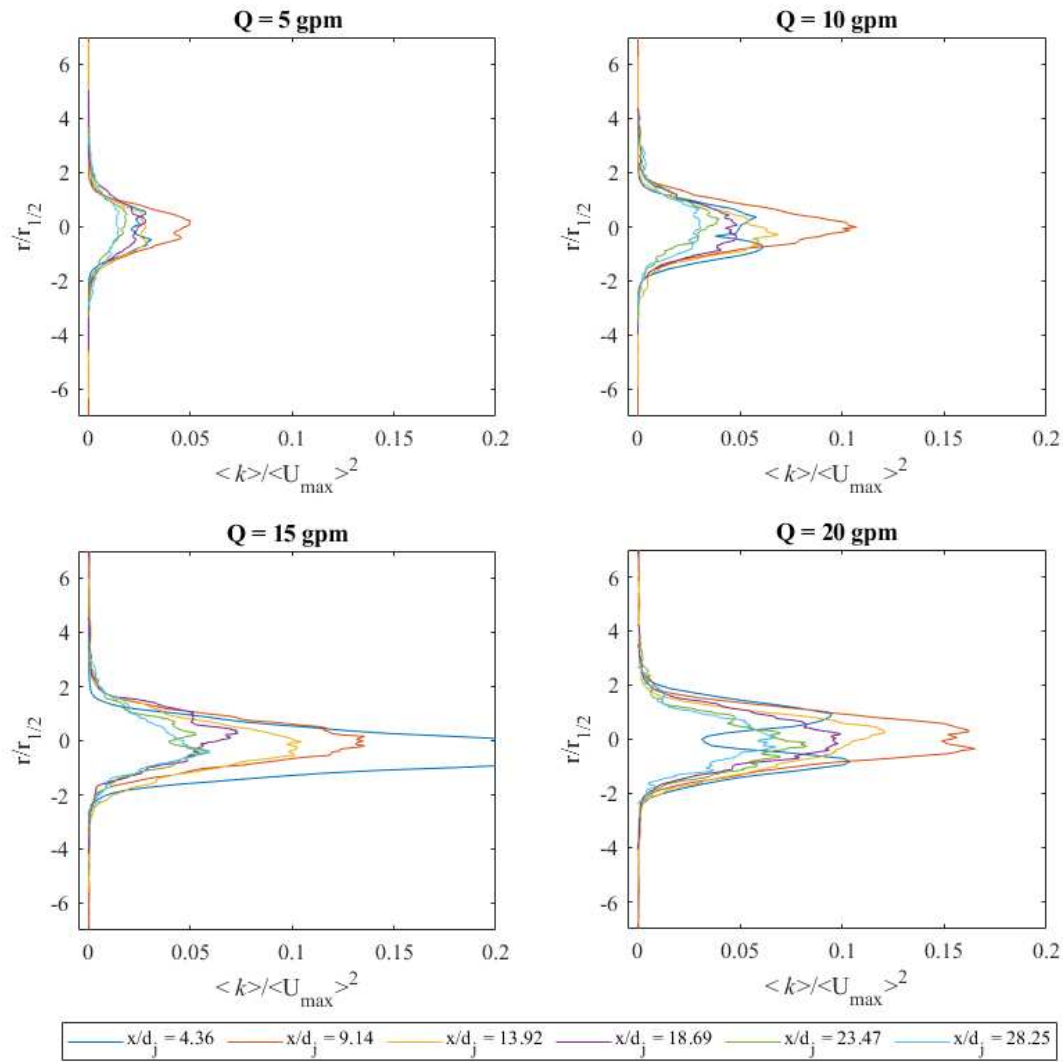


Figure 4-28: Plots of turbulent kinetic energy profiles at select  $x/d_j$  locations.

When looking at the turbulence intensity along the centerline (max), both  $\langle u/U_{max} \rangle$  and  $\langle v/U_{max} \rangle$  increase further downstream until they begin to level off around  $x/d_j = 25$  between 0.25 to 0.35 and 0.2 to 0.3 respectively (Figure 4-29). The  $\langle u/U_{max} \rangle$  is greater than  $\langle v/U_{max} \rangle$  as expected (Xu & Antonia 2002, Mi et al. 2007). The ratio of the lateral ( $v$ ) fluctuations to the streamwise ( $u$ ) fluctuations also start to level off around  $x/d_j = 25$  between  $\sim 0.7$  to 0.9 (Figure 4-30). Since  $\langle v/u \rangle = 1$  signifies isotropic turbulence, the higher  $\langle v/u \rangle$

values, indicative of less anisotropy, is consistent with the study by Xu & Antonia (2002) for a turbulent round jet from a long pipe compared to a smooth contracting nozzle.

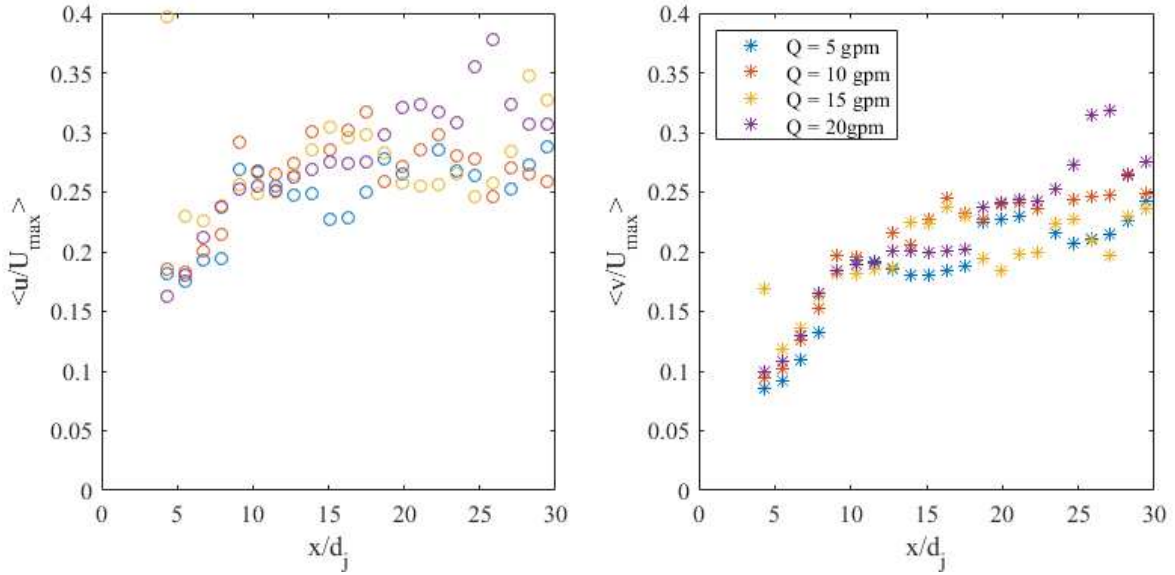


Figure 4-29: Turbulence intensities along the centerline (max).

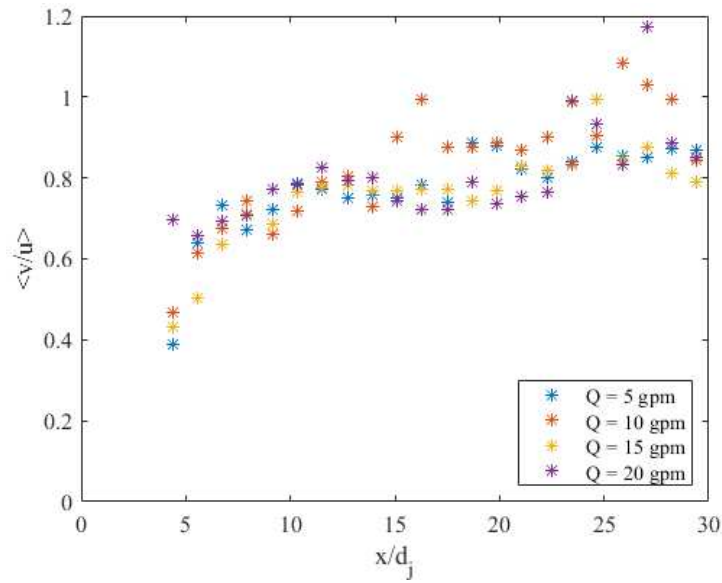
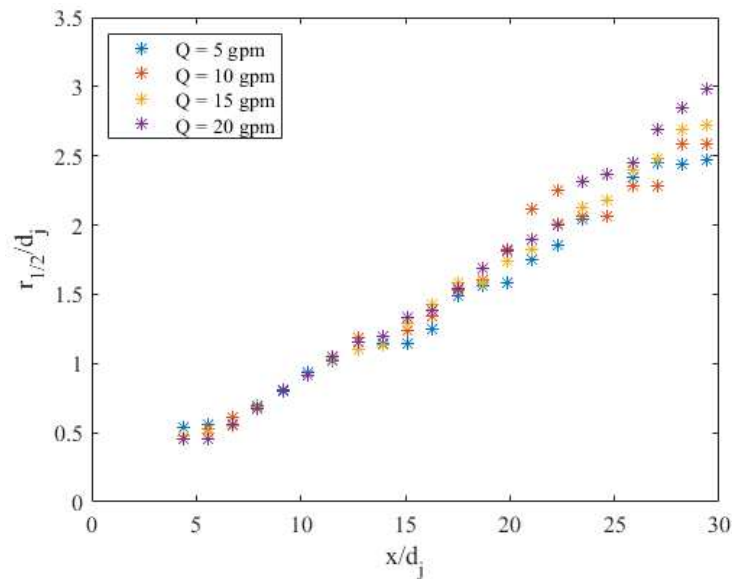


Figure 4-30: Ratio of the turbulent fluctuations along the centerline.

#### 4.3.1.4 Jet Spreading & Decay

The baseline jets spread linearly as seen in *Figure 4-31* below at the following spreading rates ( $S$ ; *Eqn 2-5*): 0.083 (5 gpm), 0.087 (10 gpm), 0.094 (15 gpm), and 0.104 (20 gpm). The spreading rate at 5 gpm is close to what is expected for a jet from a long pipe ( $\sim 0.086$ ; Xu & Antonia 2002), which is lower than for a jet from a smooth contracting nozzle (closer to 0.1; Pope 2000). As the flow rate (i.e.  $Re_j$ ) increased, the spreading rate also increased slightly; a similar trend has been observed previously (Chua & Lua 1998).



*Figure 4-31: The variation in normalized half-width ( $r_{1/2}$ ) along the centerline (max) moving downstream.*

The inverse decay rates for the baseline jets ( $B$ ; *Eqn 2-4*) are 4.575 (5 gpm), 4.580 (10 gpm), 4.333 (15 gpm), and 3.497 (20 gpm) based on the distance downstream being normalized by the diameter of the jet (*Figure 4-32*, left). If the distance downstream is normalized by the effective radius ( $r_e$ ) of the jet, which has been established as a proper variable for normalizing the axial coordinate of jets (Dahm & Dimotakis 1990), then the inverse decay rates for the jets are 7.970 (5 gpm), 7.700 (10 gpm), 7.184 (15 gpm), and 5.837 (20 gpm) (*Figure 4-32*, right).

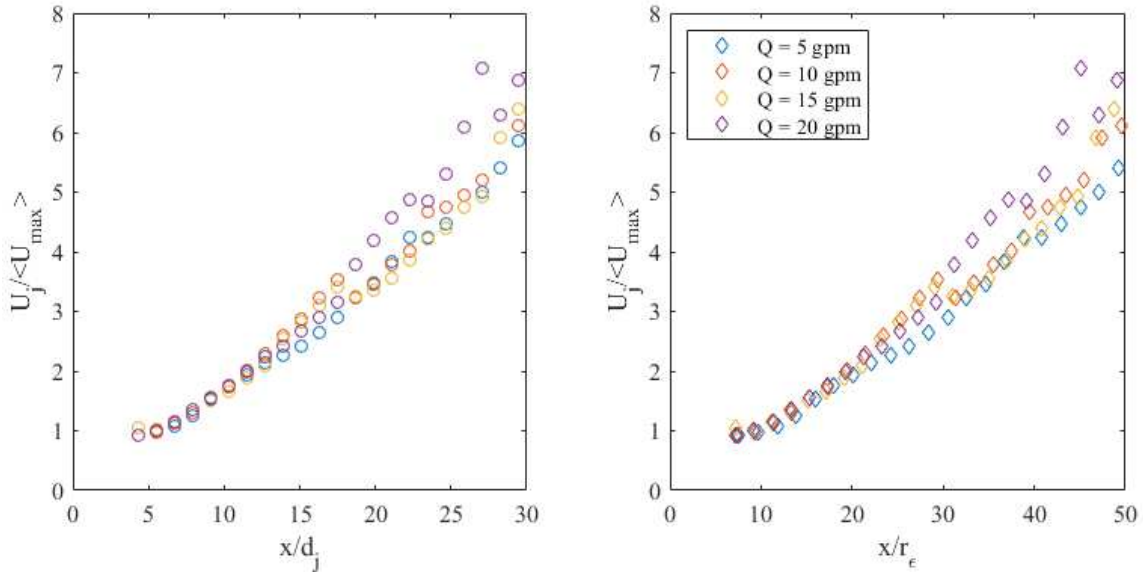


Figure 4-32: The variation in normalized mean velocity along the centerline ( $\max$ ) moving downstream (normalized by the jet diameter [left] and effective radius [right]).

When normalized with the modified effective radius suggested by Pitts & Papadopoulos (1998), which takes into account the initial turbulence intensity of the fully developed pipe flow, there is a clearer spread in the decay rates seen in Figure 4-33 (left).

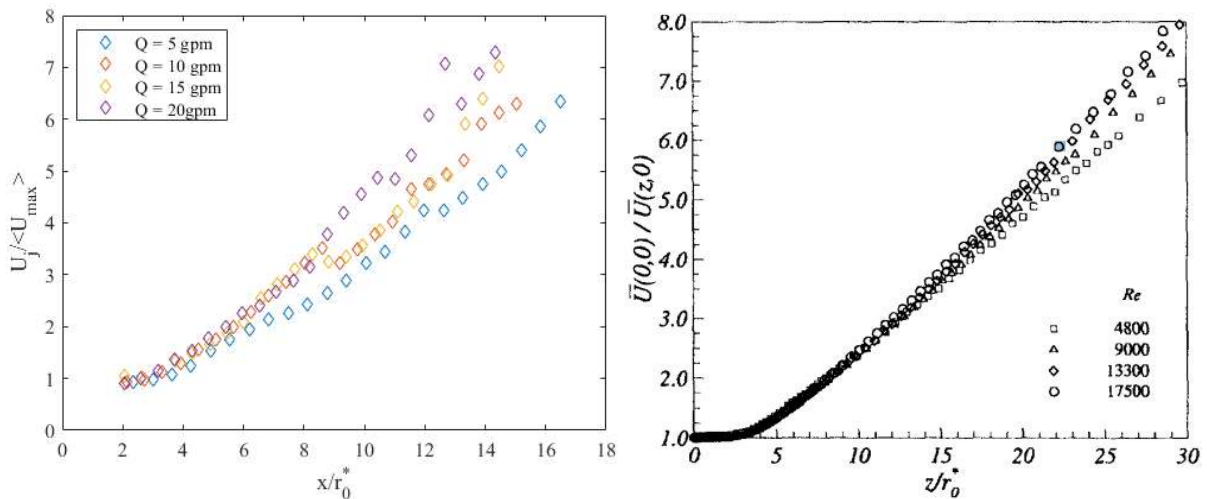


Figure 4-33: The variation in normalized mean velocity along the centerline ( $\max$ ) moving downstream (a modified effective radius): left: this study; right: Papadopoulos & Pitts study (1998).

The increasing decay rate (i.e. inverse slope) as  $Re_j$  increases is consistent with the Pitts & Papadopoulos (1998) study as seen in *Figure 4-33* (right). It is noted, however, that the spread is greater and begins early;  $\sim x/r_0^* = 6$  for the jets in this study compared to  $\sim x/r_0^* = 15$  in the Pitts & Papadopoulos (1998) study. Overall, the  $B$  values are lower than expected for a turbulent round jet from a long pipe ( $\sim 6.5$ ; Xu & Antonia 2002). Not only are they low, but they are lower than  $B$  values for turbulent round jets from a smooth contracting nozzle ( $\sim 5.6-6.0$ ; Pope 2000, Xu & Antonia 2002). However, in a study by Husan and Hussain (1985), a jet with a  $Re_j = 62,000$  and initial conditions being turbulent (such as in a jet from a long pipe) was found to have a decay rate of 0.46, equivalent to  $B = 4.07$ .

As far as the virtual origin of the jets, they are located at  $x_0/d_j = 3.489$  (5 gpm), 2.514 (10 gpm), 3.836 (15 gpm), and 5.264 (20 gpm) based on the distance downstream normalized by the diameter of the jet. The shift of the virtual origin downstream as  $Re_j$  increases has been previously observed (Pitts 1991). However the virtual origins are closer to that of a jet from a smooth contracting nozzle ( $\sim 3.7$ ) than for a jet from a long pipe ( $\sim 2.6$ ) (Xu & Antonia 2002).

#### 4.3.1.5 Mass Flux

The mass flux ( $\dot{m}$ ; normalized by the mass flux of the upstream pipe flow,  $\dot{m}_0$ ) across a vertical profile at increasing distances downstream of the jet shows the entrainment of ambient fluid into the jet flow. The mass flux was calculated from the  $\langle U \rangle$  profile where  $R$  is the location where  $\langle U \rangle$  is about 5% of the max velocity ( $R = r_{0.05\langle U_{max} \rangle}$ ) using equation below.

$$\dot{m} = 2\pi \int_0^R \rho \langle U_{avg} \rangle dr \quad 4-1$$

The rate at which fluid is entrained is represented by the slopes of the best fit lines in *Figure 4-34* (normalized by the  $\dot{m}$  of the jet at  $x/d_j = 2.8$  - the profile just downstream of the bulkhead tank fitting).

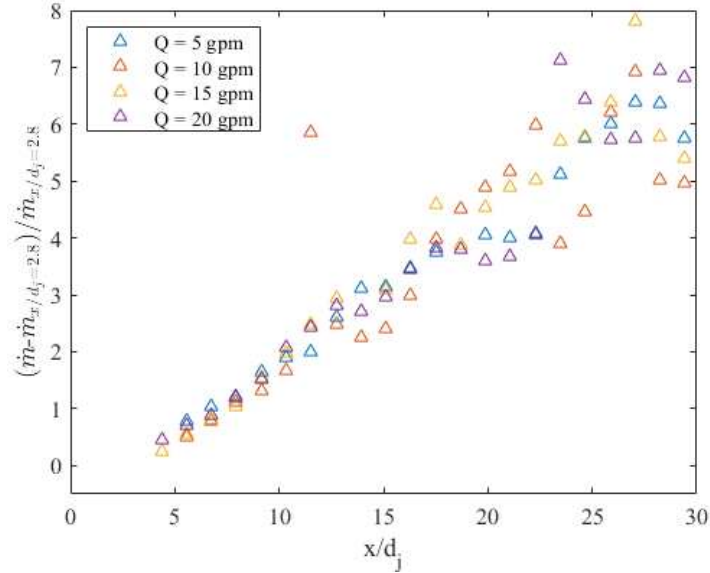


*Figure 4-34: Normalized entrainment downstream of jets.*

The entrainment rates for all four jets are similar;  $\dot{m} = 0.23$  (5 gpm),  $\dot{m} = 0.21$  (10 gpm),  $\dot{m} = 0.24$  (15 gpm), and  $\dot{m} = 0.27$  (20 gpm), yet increasing slightly with the flow rate. The entrainment rates in this study are lower than for a turbulent round jet from a smooth contracting inlet ( $\sim 0.32$ ) shown in *Figure 4-35*. A lower entrainment rate is expected since it has been shown that turbulent round jets from long pipes have a delayed formation of streamwise vortex structures due to the higher initial turbulence, which are instrumental in terms of entrainment and mixing (Xu & Antonia 2002).

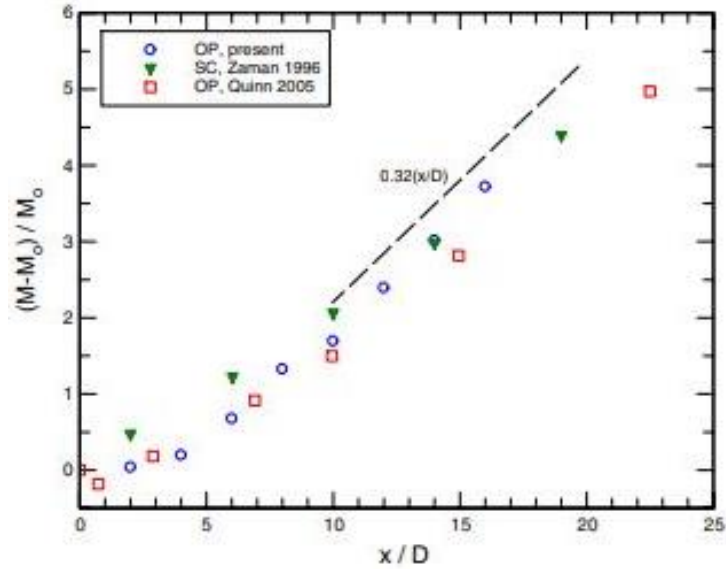


Figure 4-35: Normalized mass flux across vertical profiles downstream of jets for a smooth contracting ( $M =$  mass flux; *Mi et al, 2007*)

#### 4.3.1.6 Momentum

The momentum flux ( $\dot{M}$ ; normalized by the momentum flux of the upstream pipe flow,  $\dot{M}_0$ ) is calculate using *Eqn 4-2* below:

$$\dot{M} = 2\pi \int_0^R \rho \langle U_{avg} \rangle^2 dr. \quad 4-2$$

Normalized by the  $\dot{M}$  of the jet calculated from the profile just downstream of the bulkhead tank fitting (at  $x/d_j = 2.8$ ), *Figure 4-36* shows that the momentum remains relatively constant around 1, demonstrating the conservation of momentum of the jet.

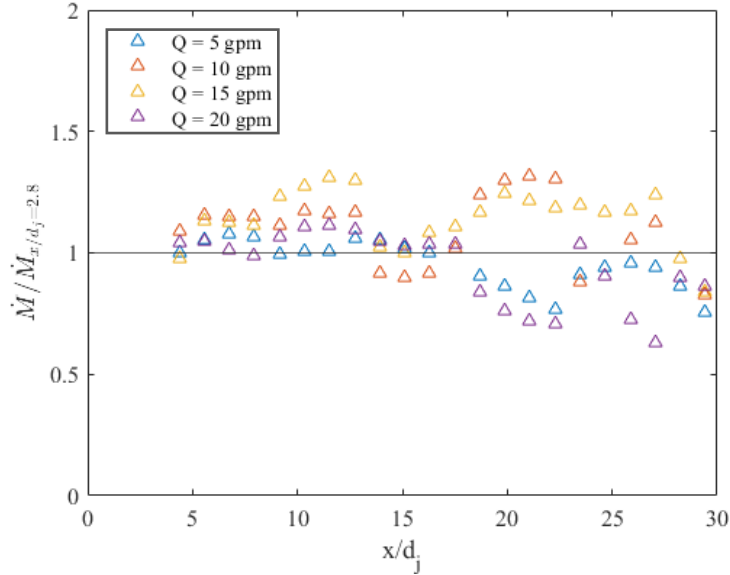


Figure 4-36: Normalized momentum flux across vertical profiles of the jet.

### 4.3.2 Turbulent Round Jet Obstructed by RPM

The same data types presented for the baseline jets were investigated for the flow downstream of the RPM. The data for the various amounts of RPM (defined by  $L$ ) are compared to the equivalent locations of the baseline jets as well as the other amounts of RPM.

#### 4.3.2.1 Velocities

Scalar plots (across multiple windows) of  $\langle U \rangle / U_j$  of the flow downstream of the RPM walls of varying thicknesses ( $L = 100, 150, 200, 250, \& 300$  mm or  $L = 4.78, 7.17, 9.56, 11.94, 14.33d_j$  respectively) at 20 gpm are shown in *Figures 4-37 to 42*. The most prominent difference in the flow field downstream of an RPM wall of thickness  $4.78d_j$  is that the magnitudes are  $\leq 10\%$  of the baseline jet (see *Figure 4-20*). Though there still seems to be remnants of the jet – now a wake.

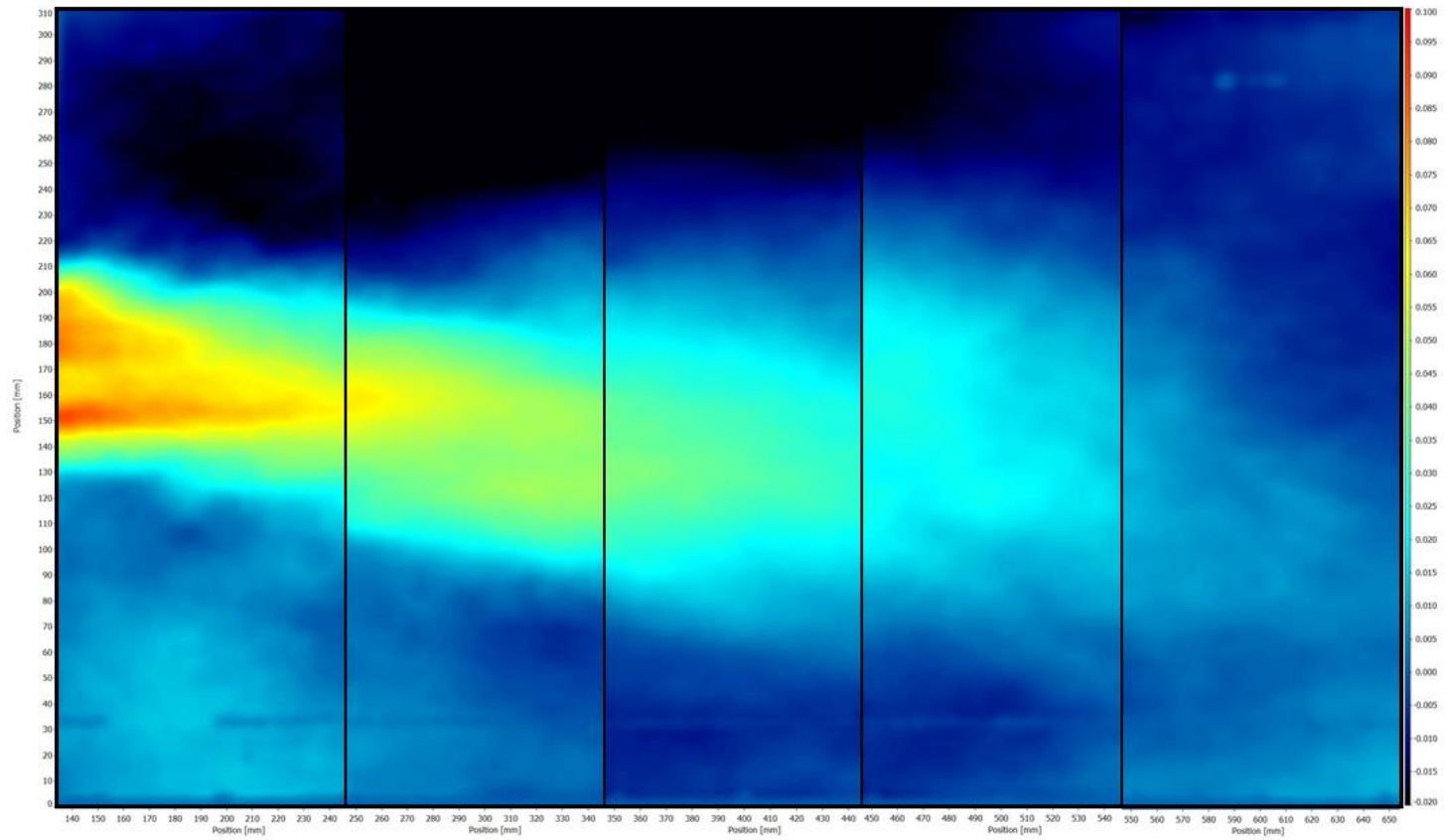


Figure 4-37:  $\langle U \rangle / U_j$  velocity scalar plot for the 20 gpm jet downstream of a RPM wall of thickness  $L = 4.78d_j$ . The x & y-axis are in mm and the color scale ranges from  $-0.020 \leq \langle U \rangle / U_j \leq 0.100$  (blue  $\rightarrow$  red).

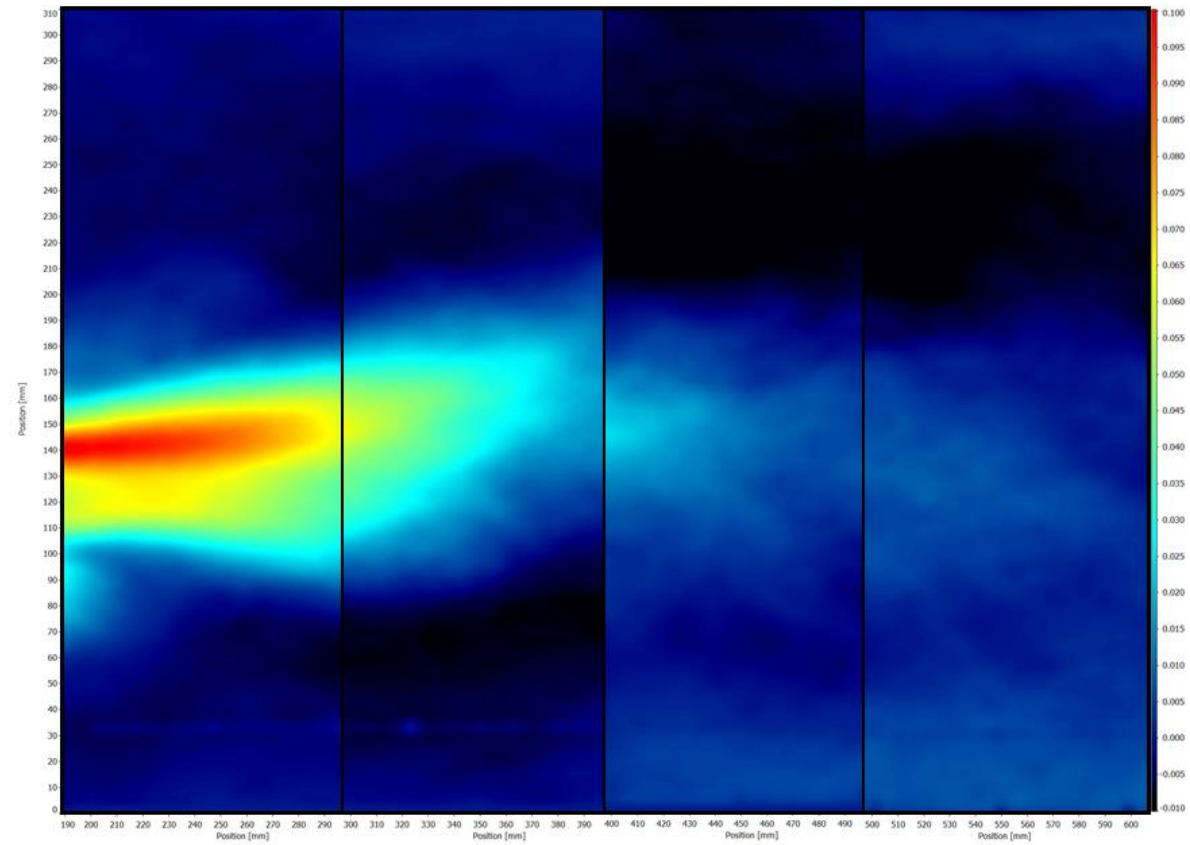


Figure 4-38:  $\langle U \rangle / U_j$  velocity scalar plot for the 20 gpm jet downstream of a RPM wall of thickness  $L = 7.17d_j$ . The x & y-axis are in mm and the color scale ranges from  $-0.020 \leq \langle U \rangle / U_j \leq 0.100$  (blue  $\rightarrow$  red).

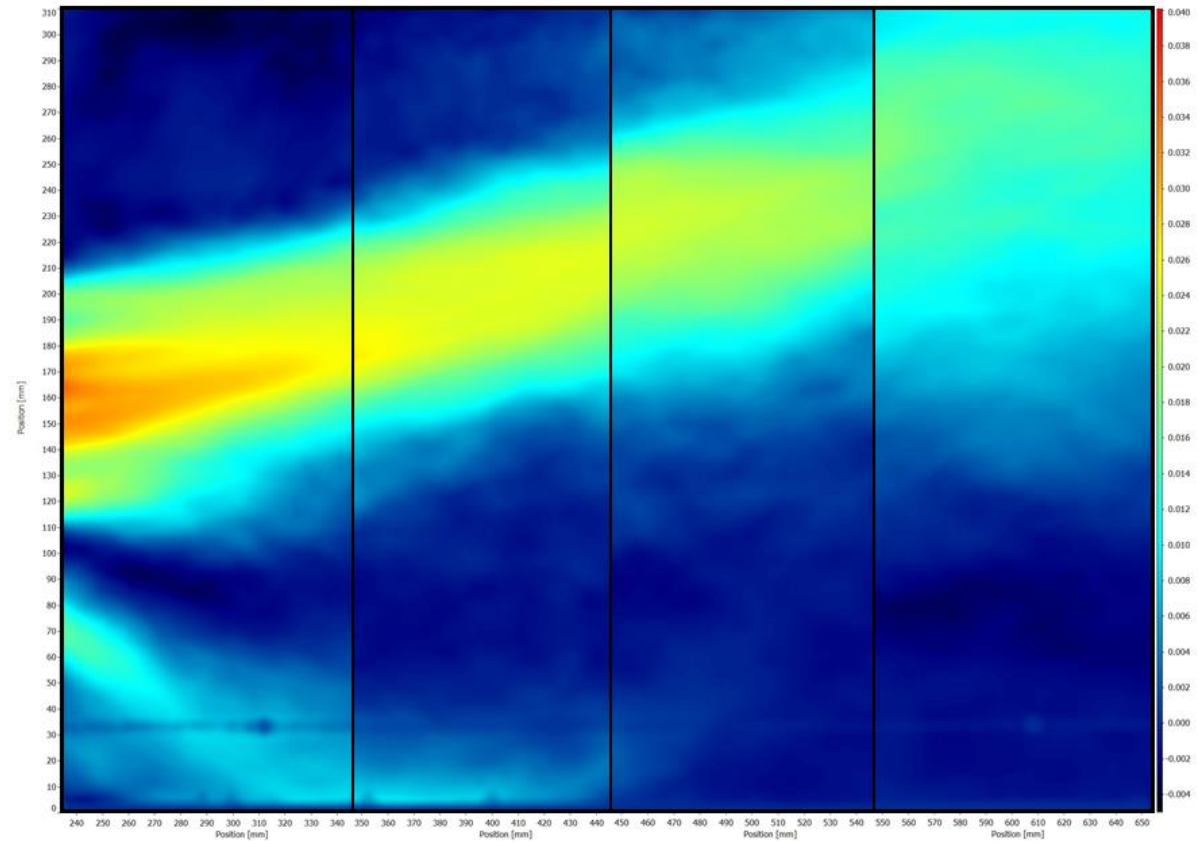


Figure 4-39:  $\langle U \rangle / U_j$  velocity scalar plot for the 20 gpm jet downstream of a RPM wall of thickness  $L = 9.56d_j$ . The x & y-axis are in mm and the color scale ranges from  $-0.005 \leq \langle U \rangle / U_j \leq 0.040$  (blue  $\rightarrow$  red).

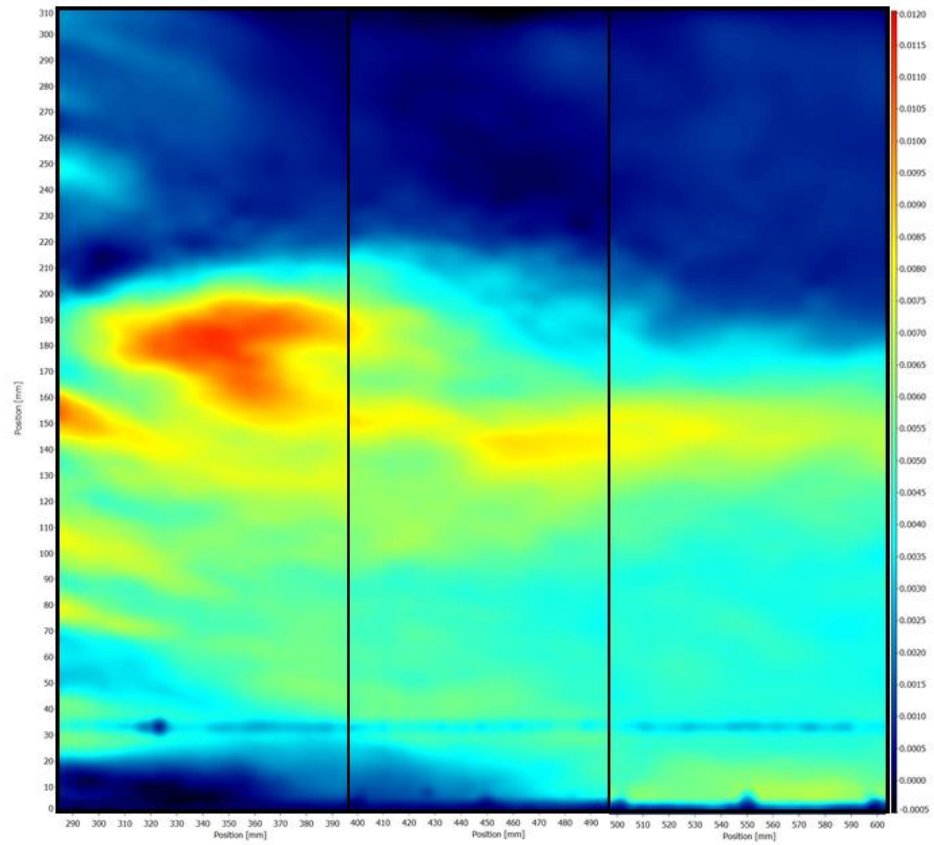


Figure 4-40:  $\langle U \rangle / U_j$  velocity scalar plot for the 20 gpm jet downstream of a RPM wall of thickness  $L = 11.94d_j$ . The x & y-axis are in mm and the color scale ranges from  $-0.005 \leq \langle U \rangle / U_j \leq 0.012$  (blue  $\rightarrow$  red).

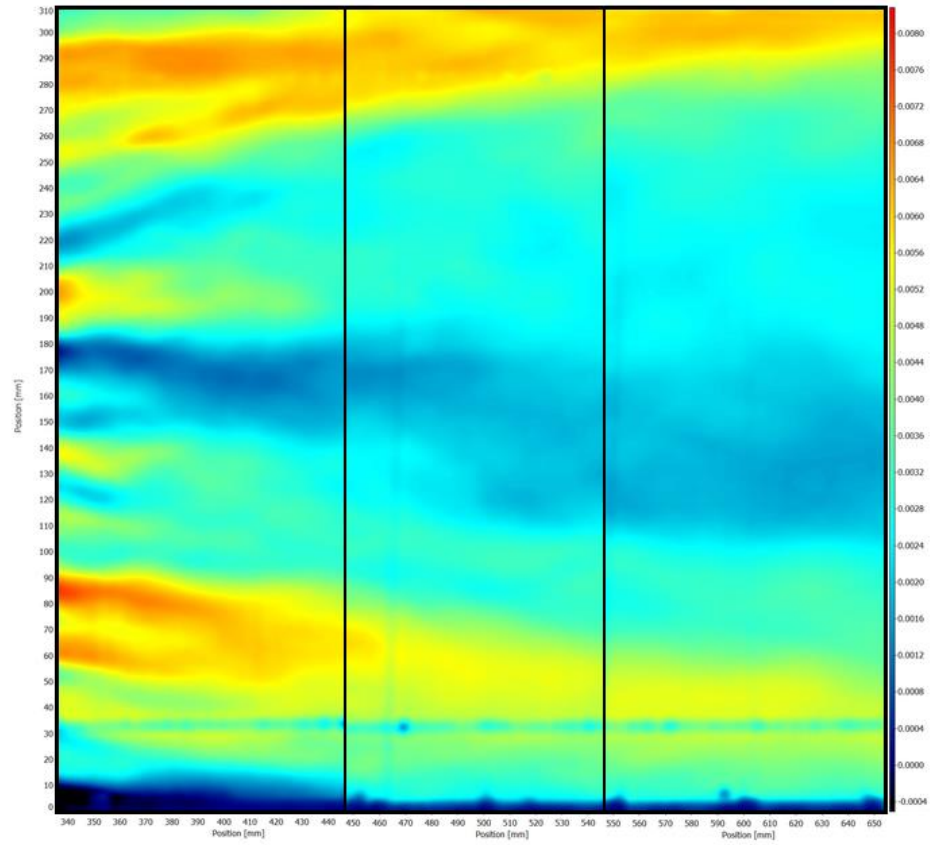


Figure 4-41:  $\langle U \rangle / U_j$  velocity scalar plot for the 20 gpm jet downstream of a RPM wall of thickness  $L = 14.33d_j$ . The x & y-axis are in mm and the color scale ranges from  $-0.0050 \leq \langle U \rangle / U_j \leq 0.0083$  (blue  $\rightarrow$  red).

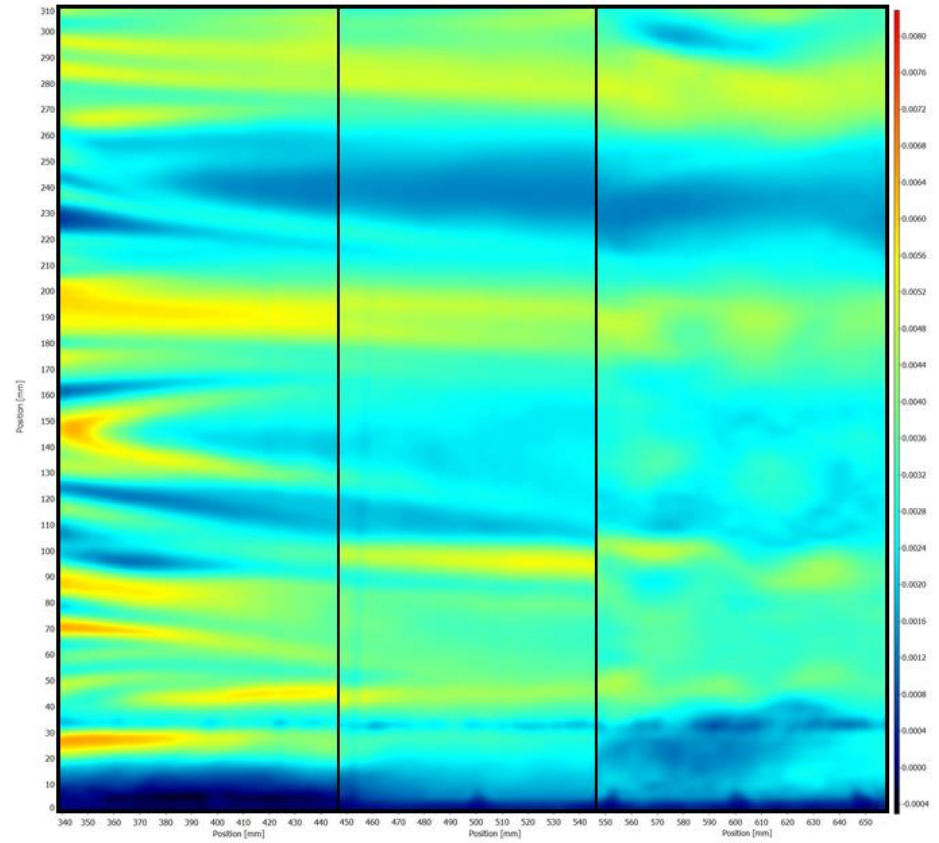


Figure 4-42:  $\langle U \rangle / U_j$  velocity scalar plot of uniform flow at 20 gpm downstream of a RPM wall of thickness  $L = 14.33d_j$ . The x & y-axis are in mm and the color scale ranges from  $-0.0050 \leq \langle U \rangle / U_j \leq 0.0083$  (blue  $\rightarrow$  red).

The wake has visibly spread more however it is no longer symmetric along the centerline but directed downward. There is also some reverse flow near the coupler which could be playing a role in the wake being directed towards the floor of the flume. The flow downstream of an RPM wall of thickness  $7.17d_j$  (*Figure 4-38*) shows a higher maximum velocity as compared to when  $L = 4.78d_j$  (though still  $\leq 10\%$  of the baseline jet) yet has a smaller spread and it seems to decay quicker further downstream. At this thickness, there is an interesting flow dynamic where there appears to be reverse flow above and below the main wake with small bulges of flow along the floor and coupler. Downstream of the RPM wall with  $L = 9.56d_j$  (*Figure 4-39*), the maximum velocity is now less than  $5\%$  of the baseline jet and the spread is larger than when  $L = 4.78d_j$ . The wake is now angled upwards toward the coupler with little reverse flow present. There is also a small ‘off-shoot’ from the main wake just downstream of the RPM directed towards the floor. It is possible that there are more ‘off-shoots’ (for other thicknesses as well) that are simply not in the vertical plane through the centerline (for which the laser sheet illuminates). Once the thickness of RPM reaches  $11.94d_j$  (*Figure 4-40*), the flow downstream looks less like the remnants of a jet and the spread has increased all the more. At this point the velocities are less than about  $1\%$  of the baseline. At  $L = 14.33d_j$  (*Figure 4-41*), the downstream flow no longer resembles a jet, but is more uniform. Nevertheless the flow seems to be split, with minor bulges along the floor and coupler compared to the uniform flow case (with  $L = 14.33d_j$ ; *Figure 4-42*) where the flow is more evenly distributed, though the magnitudes are more or less equivalent, showing that the jet has fully decayed.

The vertical velocity profiles just downstream of the RPM walls (with increasing thickness) are shown in *Figures 4-43 & 44* below. There were no major differences between the average velocity fields between the different flow rates ( $Re_j$ ). For the smallest thickness of RPM ( $L =$

4.78d<sub>j</sub>) the maximum streamwise velocities (for all flow rates) were reduced from  $\langle U_{max} \rangle / U_j = 0.6525 \pm 0.0126$  (baseline jet) to  $0.0624 \pm 0.0028$ , a 90.4% reduction.

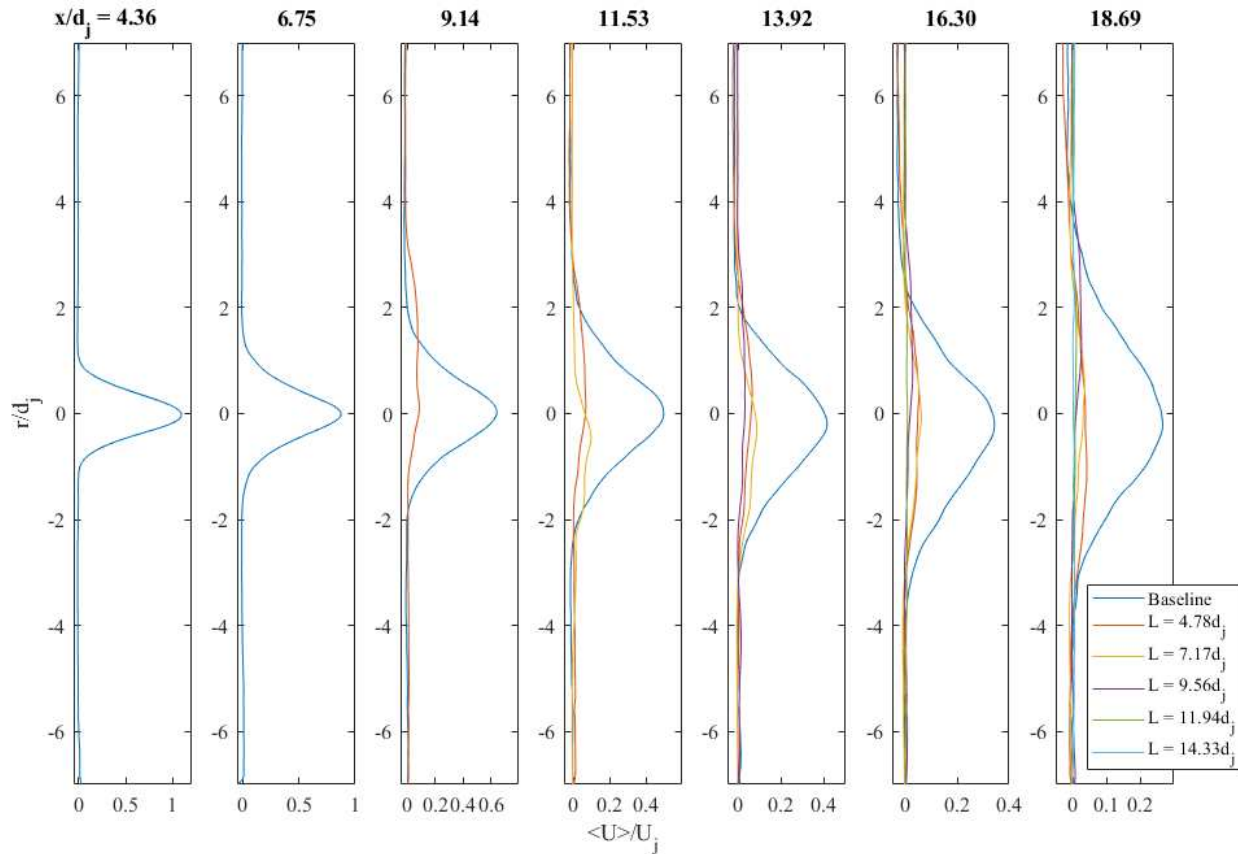


Figure 4-43: Normalized streamwise velocity profiles for  $Q = 20$  gpm. Note the  $\langle U \rangle / U_j$  scales decrease from left to right.

For the increasing thicknesses of RPM ( $L = 7.17, 9.56, 11.94,$  and  $14.33d_j$ ), the  $\langle U_{max} \rangle / U_j$  were reduced by 92.5, 95.2, 97.4, and 97.7% respectively. Similarly, the lateral velocities were reduced substantially. The absolute maximum lateral velocities ( $\langle |V_{max}| \rangle / U_j$ ; averaged for all flow rates) were reduced by 66.5, 67.7, 80.2, 94.3, and 93.2% just downstream of the RPM walls. While there is an increase in the relative reduction of both  $\langle U_{max} \rangle$  and  $\langle |V_{max}| \rangle$  with an increase in the thickness of RPM, it is less so for  $\langle |V_{max}| \rangle$ . Moreover, at the smaller thicknesses ( $L = 4.78d_j$  &  $7.17d_j$ ), there is less impact of the RPM on  $\langle |V_{max}| \rangle$  as compared to when  $L \geq 9.56d_j$ .

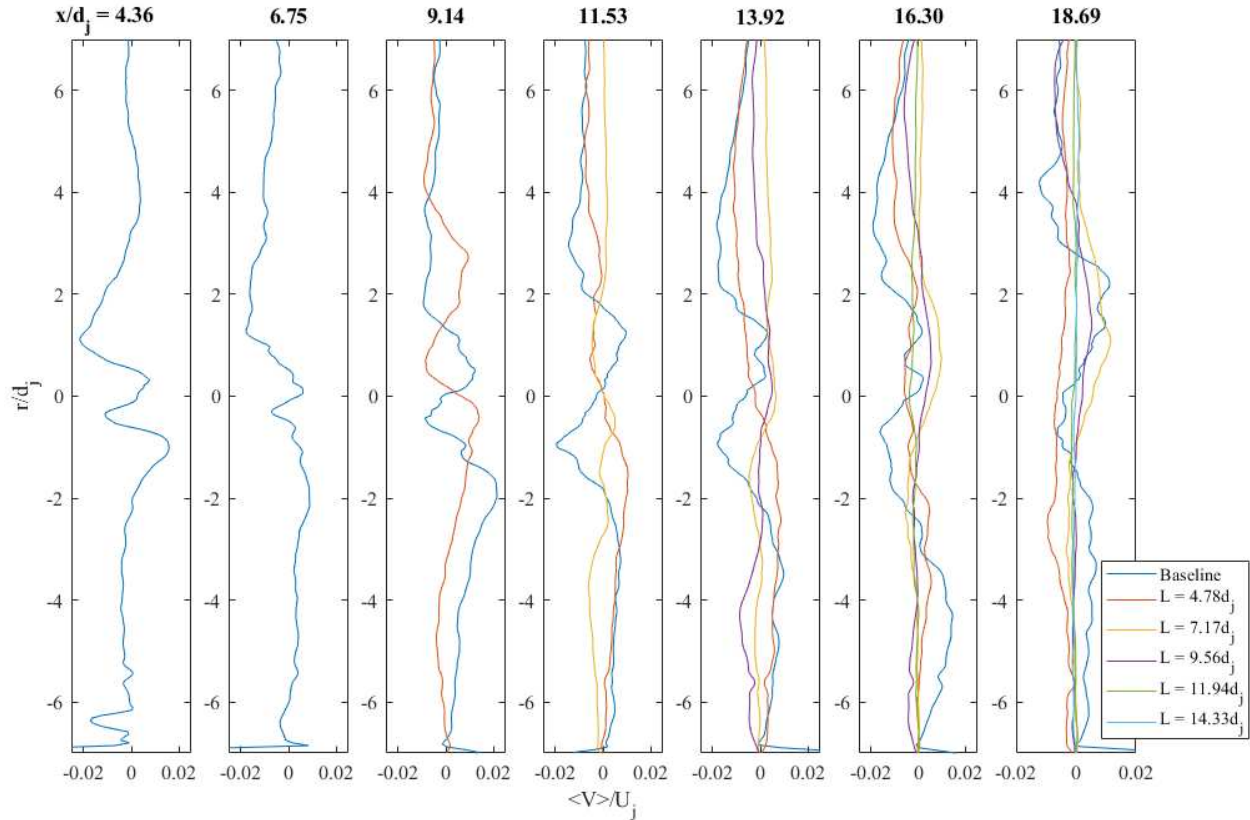


Figure 4-44: Normalized lateral velocity profiles for  $Q = 20$  gpm. Note the  $\langle V \rangle / U_j$  scales decrease from left to right.

Looking at the velocities in Figures 4-43 & 44, it can be seen that the gradients along the vertical direction (i.e.  $d\langle U \rangle / dy$  and  $d\langle V \rangle / dy$ ) are considerably less downstream of the RPM walls compared to the baseline jets. The standard deviation ( $\sigma$ ) of the velocities across the vertical profiles are given in Table 4-5 below. A lesser  $\sigma$  is indicative of smaller velocity gradients along the vertical profiles which is telling of a more uniform flow. For the uniform flow baseline, the  $\sigma_{(U)}$  and  $\sigma_{(V)}$  (normalized by the equivalent  $U_j$ ) are 0.0016 and 0.0002, respectively. On the basis of this data, only after an RPM thickness of  $14.33d_j$  does the flow field downstream achieve uniform flow.

Table 4-5: Normalized standard deviation of velocities across the vertical profiles just downstream of the RPM walls

		<b>L</b>				
<b>Velocity</b>		<b>4.78d<sub>j</sub></b>	<b>7.17d<sub>j</sub></b>	<b>9.56d<sub>j</sub></b>	<b>11.94d<sub>j</sub></b>	<b>14.33d<sub>j</sub></b>
<b><math>\sigma_{\langle u \rangle} / U_j</math></b>	Baseline	0.1615	0.1425	0.1201	0.1069	0.0992
	RPM	0.0250	0.0132	0.0065	0.0026	0.0018
	% reduction	84.5	90.7	94.6	97.6	98.2
<b><math>\sigma_{\langle v \rangle} / U_j</math></b>	Baseline	0.0071	0.0055	0.0052	0.0055	0.0038
	RPM	0.0031	0.0022	0.0013	0.0004	0.0003
	% reduction	56.3	60.0	75.0	92.7	92.1

#### 4.3.2.2 Reynolds Stresses

Analogous to the dramatic reduction of the maximum velocities at each location, the Reynolds stresses (i.e.  $\langle uu \rangle$ ,  $\langle vv \rangle$ , and  $\langle uv \rangle$ ) also decreased significantly as seen in *Table 4-6* below. (For Reynolds stress plots please see *Figures A-38 to 40* in Appendix A). The significant reduction in the Reynolds stresses is to be expected since the length scale of the voids within the RPM walls are small compared to the diameter of the pipe (about an order of magnitude;  $O(1)$ ), let alone the flume ( $\sim O(2)$ ) (Mossa et. al. 2017).

Table 4-6: Percent reduction in maximum Reynolds stresses compared to baseline jet

		<b>L</b>				
<b>Reynold's Stress</b>		<b>4.78d<sub>j</sub></b>	<b>7.17d<sub>j</sub></b>	<b>9.56d<sub>j</sub></b>	<b>11.94d<sub>j</sub></b>	<b>14.33d<sub>j</sub></b>
<b><math>\langle uu \rangle</math></b>		98.7	98.7	99.6	99.9	> 99.9
<b><math>\langle vv \rangle</math></b>		97.8	98.7	99.7	99.9	> 99.9
<b><math>\langle uv \rangle</math></b>		98.7	99.4	99.8	> 99.9	> 99.9

### 4.3.2.3 Turbulence

Following the current pattern, there is also a major reduction in the turbulent kinetic energy ( $k$ ) of the flow downstream of the RPM (for plots of  $\langle k \rangle / U_j^2$  please see *Figure A-41* in Appendix A). There is slight increase in the reduction of  $k$  as  $L$  increases (98.2, 98.8, 99.7, 99.9, and >99.9%), consistent with the Reynolds stresses. When considering the different flow rates, there is a small decrease in the reduction of  $k$  as the flow rate increases for  $L = 4.78d_j$  &  $7.17d_j$  (see *Table 4-7*). The baseline jet, however, showed an increase in  $\langle k \rangle / U_j^2$  as the flow rate increased. That means that there is relatively more energy to be dissipated by the same amount of RPM. Though the differences are minor, it is possible that there may a threshold of how much  $k$  can be dissipated by a certain amount of RPM.

*Table 4-7: Percent reduction in max turbulent kinetic energy by flow rate*

<b><math>Q</math> (gpm)</b>	<b><math>L</math></b>				
	<b><math>4.78d_j</math></b>	<b><math>7.17d_j</math></b>	<b><math>9.56d_j</math></b>	<b><math>11.94d_j</math></b>	<b><math>14.33d_j</math></b>
<b>5</b>	98.5	99.5	99.7	> 99.9	> 99.9
<b>10</b>	98.5	99.1	99.8	> 99.9	> 99.9
<b>15</b>	98.0	99.0	99.8	> 99.9	> 99.9
<b>20</b>	97.7	97.5	99.7	> 99.9	> 99.9

The average turbulent kinetic energy along the vertical profile(s) ( $\langle k_{avg} \rangle$ ) is plotted as the flow moves downstream with respect to the size of the ‘grid’ of the RPM wall ( $M$ ) in *Figure 4-45* (reference *Figure 2-7*). The decrease in  $\langle k_{avg} \rangle / U_j^2$  as  $L$  increases is more evident here. The rate of decay of  $\langle k_{avg} \rangle / U_j^2$  varies until  $L \geq 11.94d_j$  where the decay rate is relatively constant – similar to the decay observed in a grid turbulence. Interestingly, however, the  $\langle k_{avg} \rangle / U_j^2$  seems to remain relatively constant (i.e. no decay) for the uniform flow case.

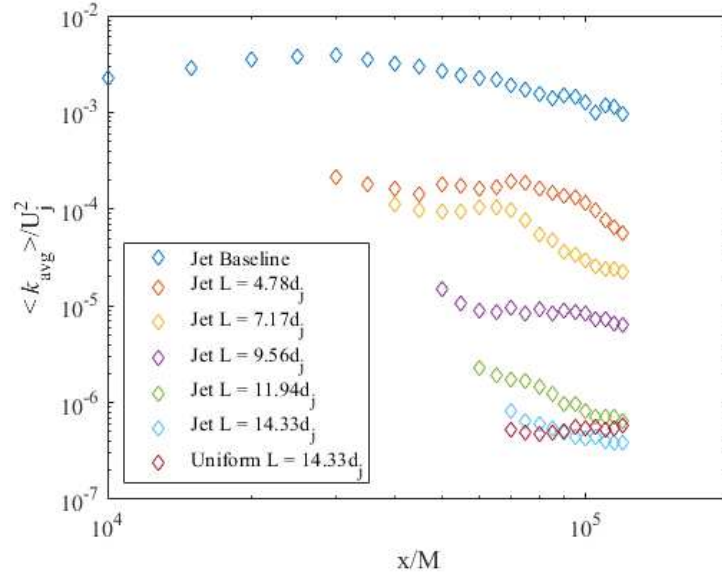


Figure 4-45: Turbulent kinetic energy normalized by  $U_j$  (the initial velocity) for  $Q = 20$  gpm as the distance downstream of the RPM wall increases.

The maximum turbulence intensities ( $\langle u/U_{max} \rangle$  and  $\langle v/U_{max} \rangle$ ) along the vertical profiles downstream of the jet (& RPM walls) for  $Q = 20$  gpm are shown in Figure 4-46 below; a similar pattern is observed for all flow rates.

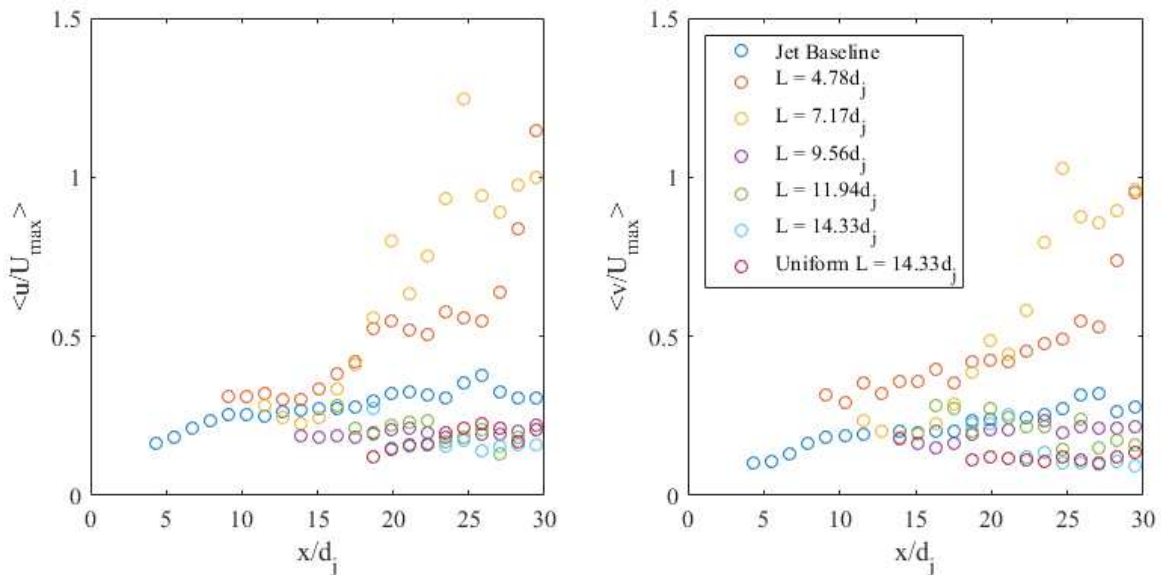
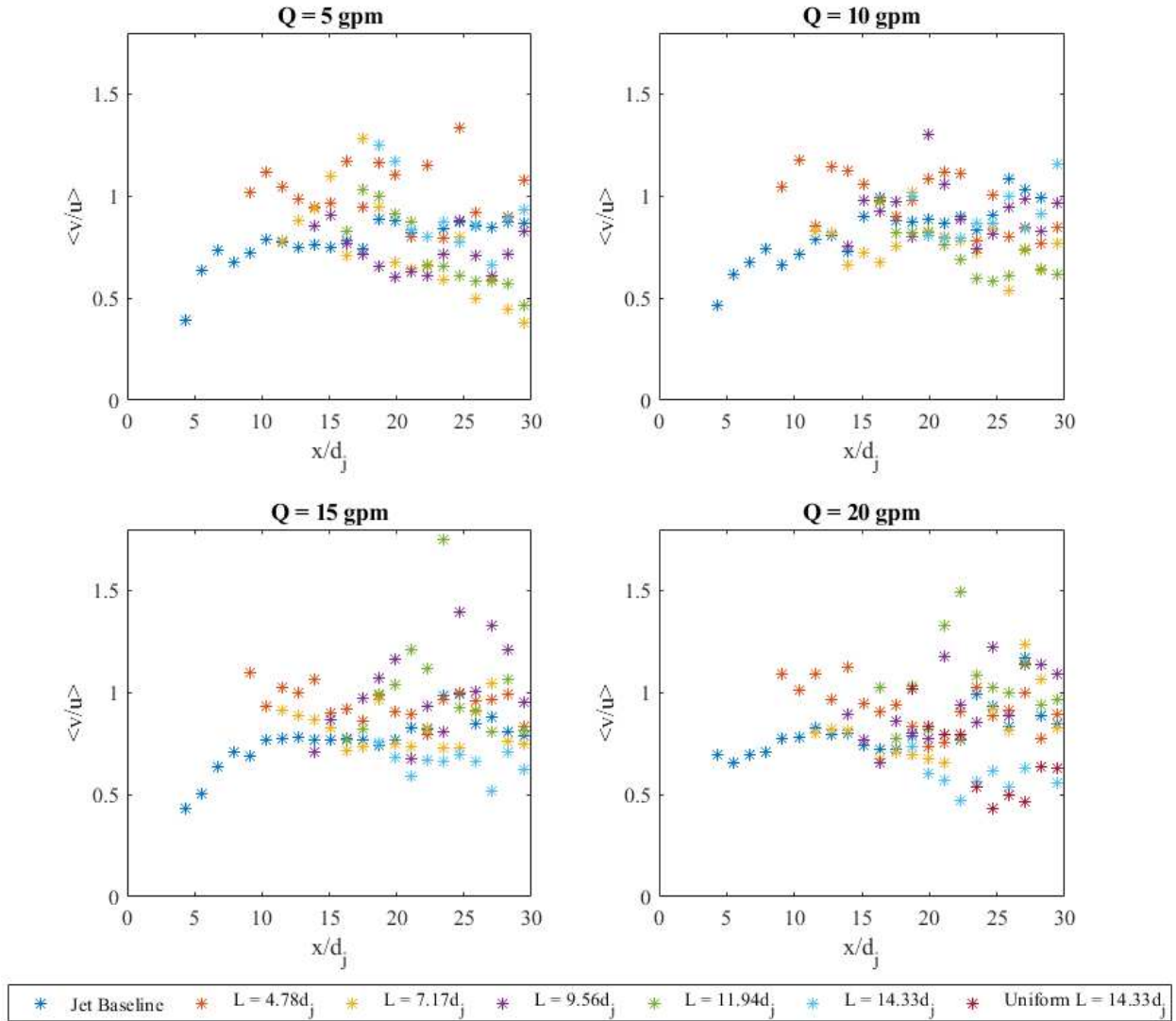


Figure 4-46: Maximum Turbulence intensities for  $Q = 20$  gpm.

Downstream of the smallest thickness of RPM ( $L = 4.78d_j$ ),  $\langle u/U_{max} \rangle$  is slightly higher and follows a similar pattern as the baseline jet until  $x/d_j \approx 15$  when the max relative streamwise fluctuations begin to increase continually, upwards of  $\langle u/U_{max} \rangle \approx 1.15$ . This pattern is also seen at  $L = 7.17d_j$ , but the intensity increases even more so. Once  $L \geq 9.56d_j$ ,  $\langle u/U_{max} \rangle$  becomes slightly less than the baseline jet and remains constant at  $\sim 0.20$  ( $\sim 0.18$  for  $L = 11.94d_j$  and  $\sim 0.16$  for  $L = 14.33d_j$ ). The continually increasing trend for the two smaller thickness of RPM is mimicked by  $\langle v/U_{max} \rangle$ . Also, it should be noted that at the smaller RPM thicknesses,  $\langle v/U_{max} \rangle$  is comparable to  $\langle u/U_{max} \rangle$  (as opposed to being less than  $\langle u/U_{max} \rangle$  in the baseline jet). Another difference is that as  $L$  increases beyond  $7.17d_j$ ,  $\langle v/U_{max} \rangle$  becomes smaller. At  $L = 9.56d_j$ ,  $\langle v/U_{max} \rangle$  is constant after  $x/d_j \approx 18$  at  $\sim 0.22$  which is still slightly higher than  $\langle u/U_{max} \rangle$ . When  $L = 11.94d_j$ ,  $\langle v/U_{max} \rangle$  actually increases initially until  $x/d_j \approx 21$  and then decreases, leveling off  $\sim 0.16$ , which is the same as  $\langle u/U_{max} \rangle$ . And at  $L = 14.33d_j$ ,  $\langle v/U_{max} \rangle$  remains relatively constant at  $\sim 0.10$ , less than  $\langle u/U_{max} \rangle$ .

The ratios of  $u$  and  $v$  along the centerline are show in *Figure 4-47* below. Downstream of the RPM with  $L = 4.78d_j$ , the turbulence is more isotropic ( $\sim 1$ ) at all flow rates. For  $L = 7.17d_j$  at 5 gpm the turbulence is initially more isotropic until  $x/d_j \approx 20$  when the ratio reduces below that of the baseline jet to  $< 0.5$ . For  $Q > 5$  gpm  $\langle v/u \rangle$  is about the same as for the baseline jet. When  $L \geq 9.56d_j$ , there are similar trends depending on the flow rates. For  $Q = 5 - 10$  gpm  $\langle v/u \rangle$  is similar to that of the baseline jet when  $L = 9.56$  &  $14.33d_j$ . Yet, when  $L = 11.94d_j$ ,  $\langle v/u \rangle$  is initially similar but then decreases at  $x/d_j \approx 20$  to  $\sim 0.5$ . For  $Q = 15 - 20$  gpm  $\langle v/u \rangle$  becomes higher than the baseline jet and more isotropic ( $\sim 1$ ) but when  $L = 14.33d_j$  it is lower than the baseline jet at  $\sim 0.6$ .



*Figure 4-47: Ratio of the turbulent fluctuations along the centerline.*

It is noted that there are some differences between the maximum fluctuations and the centerline fluctuations. This can be explained by the non-uniformity of the flow fields. The location  $r$  (or  $y$ ) of the maximum velocity/fluctuations are not necessarily the same at different positions downstream ( $x$ ) for different amounts of RPM, let alone for the same amount of RPM at a different flow rate. The non-uniformity can be seen by looking at the  $\sigma$  of the fluctuations along the vertical profiles (*Figure 4-48*).

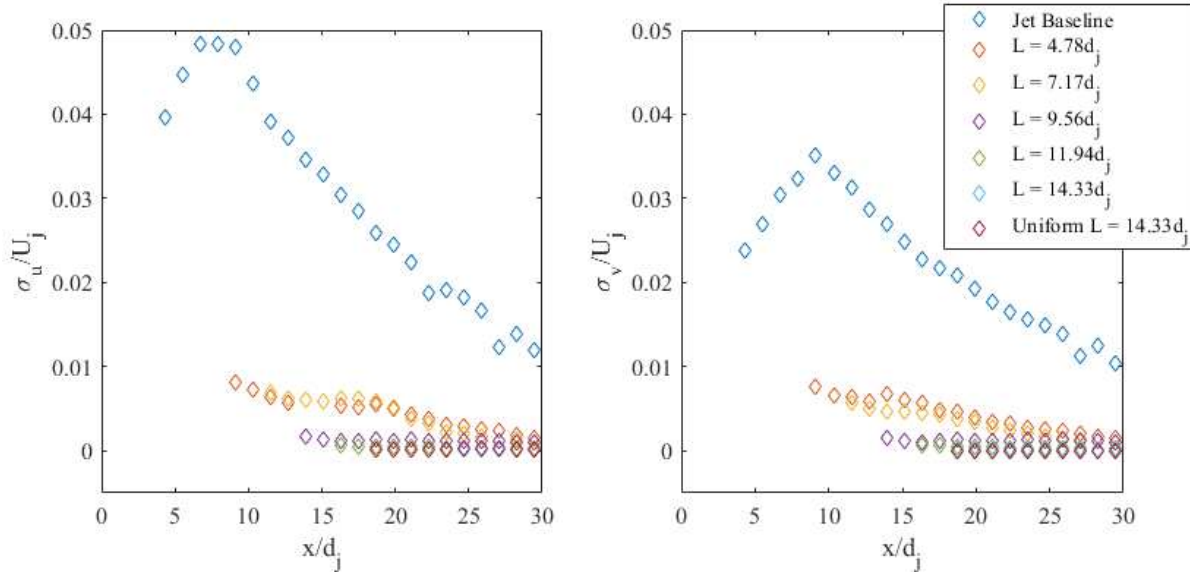


Figure 4-48: The normalized standard deviation of the fluctuations along the vertical profiles for  $Q = 20 \text{ gpm}$ .

Parallel to the velocities, a larger  $\sigma_u$  and/or  $\sigma_v$  is telling of a more non-uniform flow, which is clear for the baseline jet. Again, only downstream of an RPM wall with  $L = 14.33d_j$  are the  $\sigma_u$  &  $\sigma_v$  comparable to the uniform flow baseline. Again, this shows that a uniform flow field downstream of RPM is only achieved at  $L \geq 14.33d_j$ .

#### 4.3.2.4 Jet Spreading and Decay

The normalized half-widths ( $r_{1/2}/d_j$ ) of the flow fields downstream of the RPM walls for each flow rate can be seen in *Figure 4-49* below. The spreading downstream of the various amounts of RPM are similar across all flow rates. For  $L = 4.78d_j$ , the  $r_{1/2}/d_j$  of the flow exiting the RPM is slightly larger than the baseline jets, but then increases at a similar rate as the baseline jet. For  $L = 7.17d_j$ , the spread of the flow exiting the RPM is the same, if not slightly less, compared to the baseline jet until  $x/d_j \approx 20$  when  $r_{1/2}/d_j$  dramatically increases to the full depth of flow ( $H$ ).

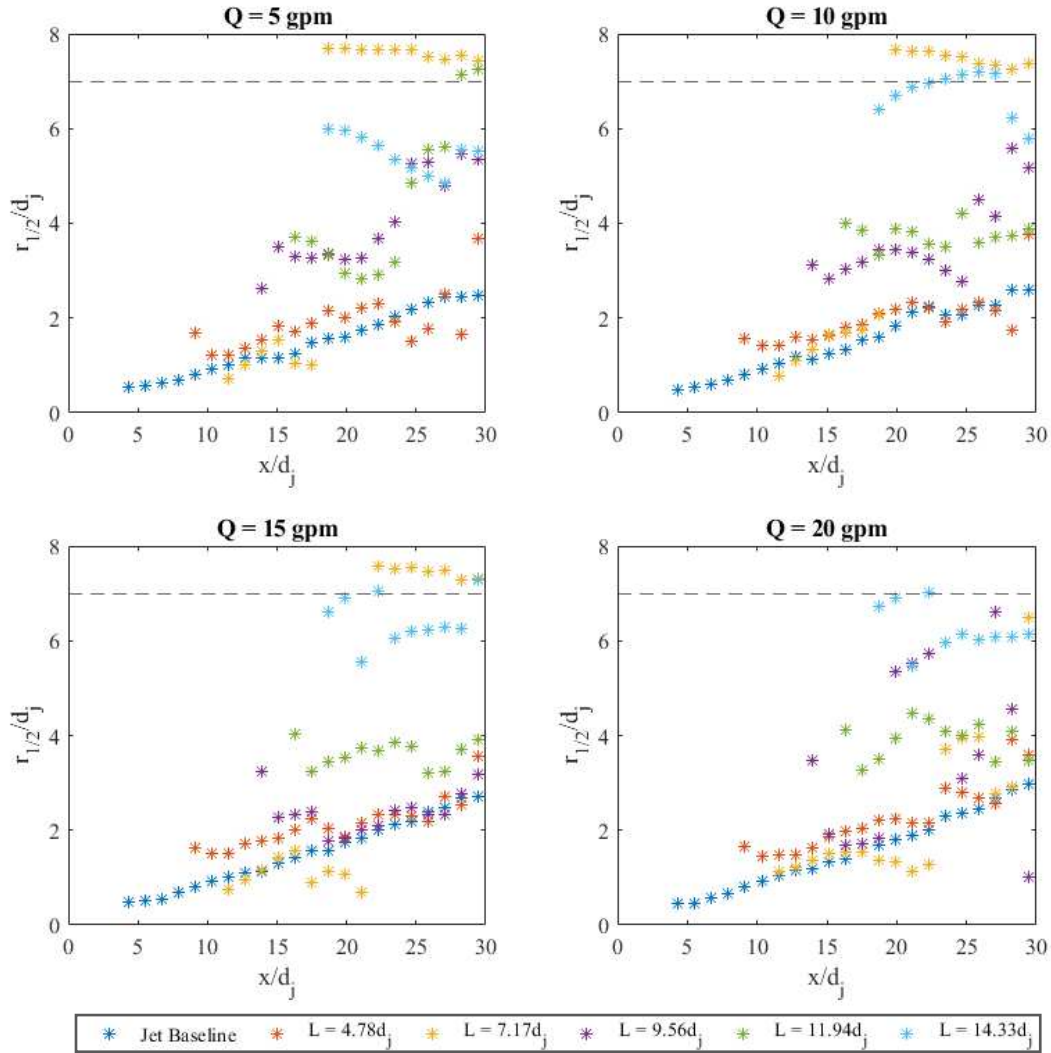


Figure 4-49: The variation in normalized half-width ( $r_{1/2}$  based on  $\frac{1}{2}U_{max}$ ) moving downstream. The dashed line indicates 'fully-spread' based on the width of the flume.

Looking at the velocity scalar plots (Figures 4-37 to 42) it can be seen that there are bulges near the floor and coupler along with areas of reverse flow. It is only when  $L = 7.17d_j$  that this unique flow pattern is observed. The flow field downstream of the RPM wall with  $L = 9.56d_j$  shows the return of the maximum flow near the centerline again. At  $L = 9.56d_j$  the  $r_{1/2}/d_j$  of the flow exiting the RPM is larger than the baseline jets, yet again, continues to spread at a similar rate moving downstream. At  $L = 11.94d_j$ , the  $r_{1/2}/d_j$  of the flow exiting the RPM is

larger than at  $L = 9.56d_j$  and, again, continues to spread at a similar rate moving downstream. Finally, at  $L = 14.33d_j$  the flow exiting the RPM essentially spans the full depth of flow (or nearly so). Understandably, the  $r_{1/2}/d_j$  remains relatively constant moving downstream as it is constrained by the dimensions of the flume (where  $r_{1/2}/d_j \approx (\frac{D}{2})/d_j \approx 7$ ). Although there are slight bulges of flow near the floor and the coupler observed at  $L = 14.33d_j$ , as discussed previously, the  $\sigma$  of the velocities and fluctuations along the vertical profiles are similar to that of the uniform flow case.

The spreading rate within the RPM wall(s) was calculated using the  $r_{1/2}/d_j$  of the flow just downstream of each RPM wall of increasing thickness (see *Figure 4-50*). The overall spreading within the RPM is not constant (linear) as in the baseline jet (with  $S = 0.08-0.10$ ) but quadratic. The best fit polynomial (with an  $R^2 = 0.9153$ ) for this experiment is given as:

$$r_{1/2}/d_j = 0.0432L^2 - 0.2885L + 1.7251. \quad 4-4$$

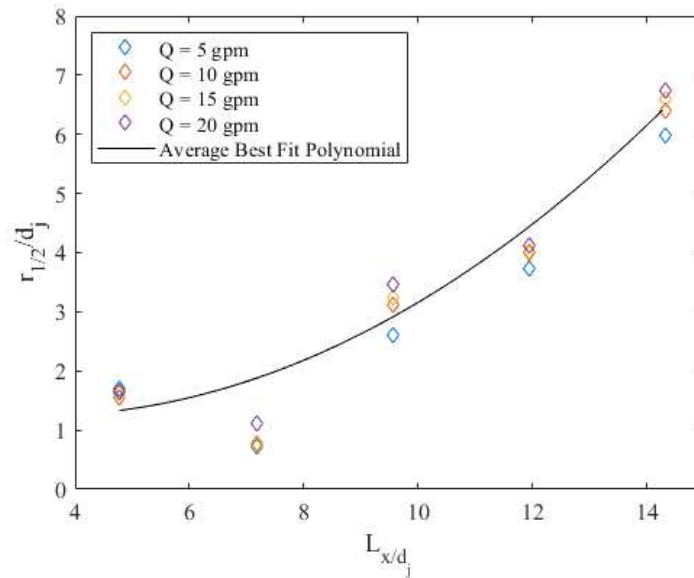


*Figure 4-50: Spreading rate within RPM.*

Also, it appears that the spreading rate increases slightly as the flow rate increases, similar to the baseline jets.

Comparable to the spreading of the jet, the trend in the decay of the initial jet downstream of the RPM is also similar across all flow rates as seen in *Figure 4-51*. The overall trend just downstream of the RPM is that  $U_j/\langle U_{max} \rangle$  is greater as  $L$  increases.

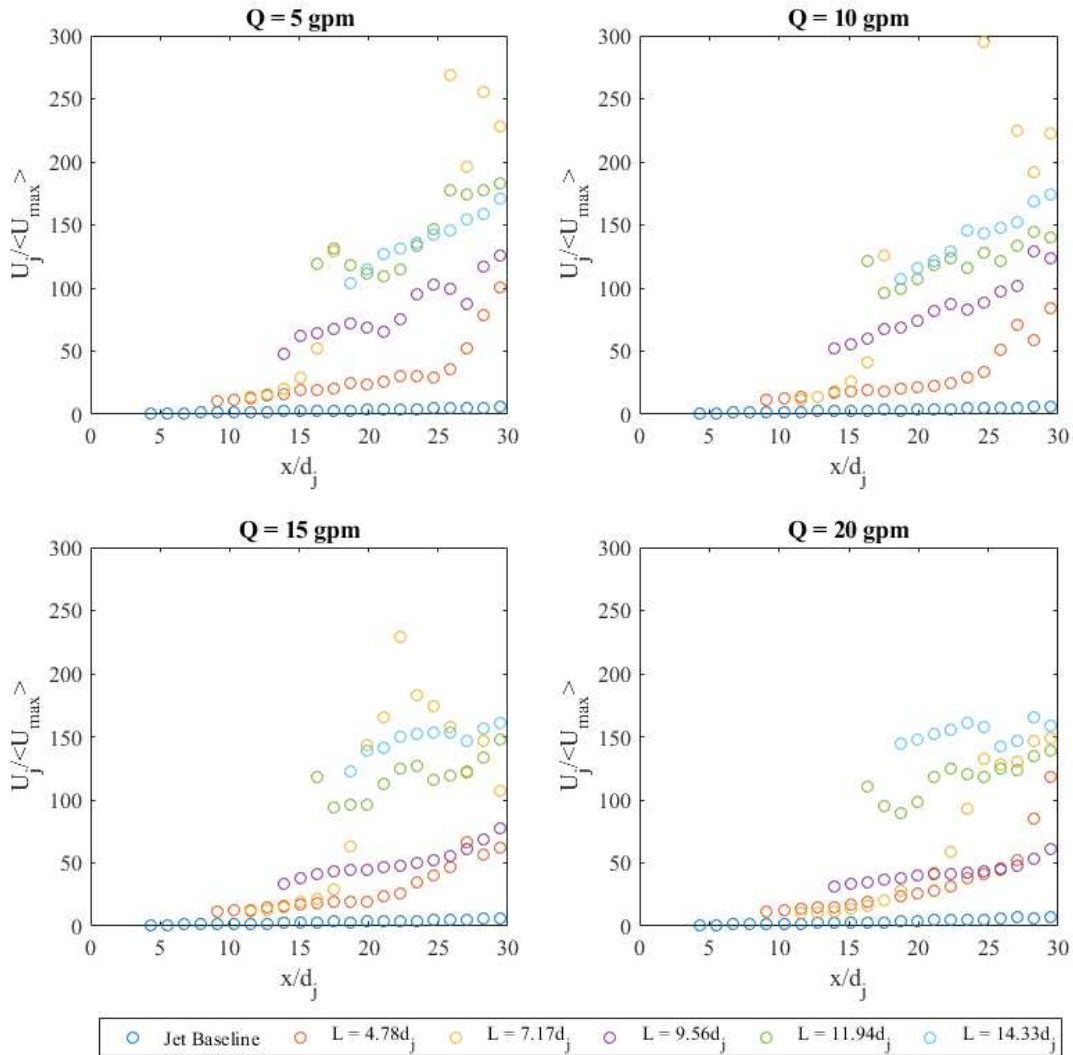


*Figure 4-51: The variation in normalized maximum velocity moving downstream.*

The rate at which  $U_j/\langle U_{max} \rangle$  increases moving further downstream also increases as  $L$  increases. The exception to the overall trend is at  $L = 9.56d_j$ , but as mentioned previously, the flow field at this RPM thickness is different from the others (see *Figure 4-38*). The inverse decay rate within the RPM wall was calculated using the  $U_j/\langle U_{max} \rangle$  of the flow just downstream of each thickness

of RPM (see *Figure 4-52*). Looking at the flow rates, in general, the inverse decay rate decreases as the flow rate increases, again, similar to the baseline jets. Even so the overall decay within the RPM is not constant (linear) as for the baseline jets (with  $B = 3.5-4.6$ ) but exponential with the best fit curve (with an  $R^2 = 0.9047$ ) for this experiment given below:

$$U_j / \langle U_{max} \rangle = 2.3578e^{0.2911L} \quad 4-5$$

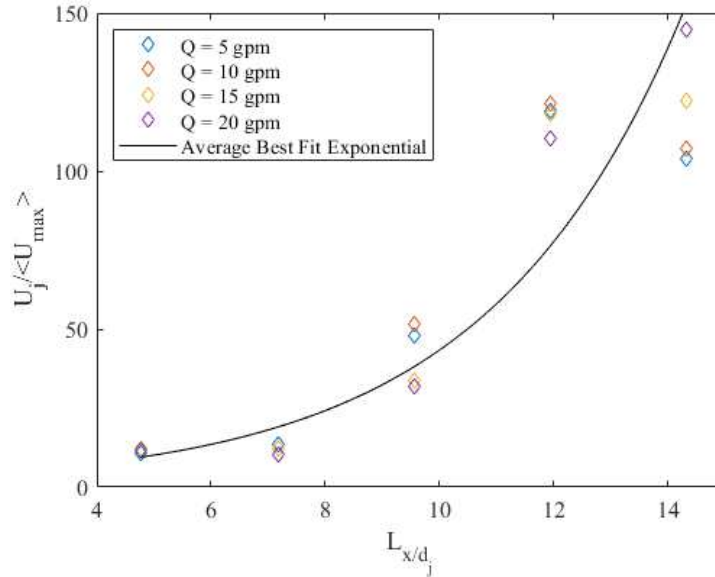


*Figure 4-52: Inverse Decay Rate within RPM.*

#### 4.3.2.5 Mass Flux

In a free jet, the strong shear layers at the edge of the jet produce vortices that entrain quiescent fluid into the flow of the jet. This is described by the entrainment rate of the jet which increases linearly as the axial distance from the jet origin increases. The entrainment rate of the flow downstream of the RPM is essentially nil as seen in *Figure 4-53*. Although there seems to be a negative entrainment at  $L = 7.17d_j$ , this can be explained by the reverse flow patterns observed in the flow fields (*Figure 4-38*).

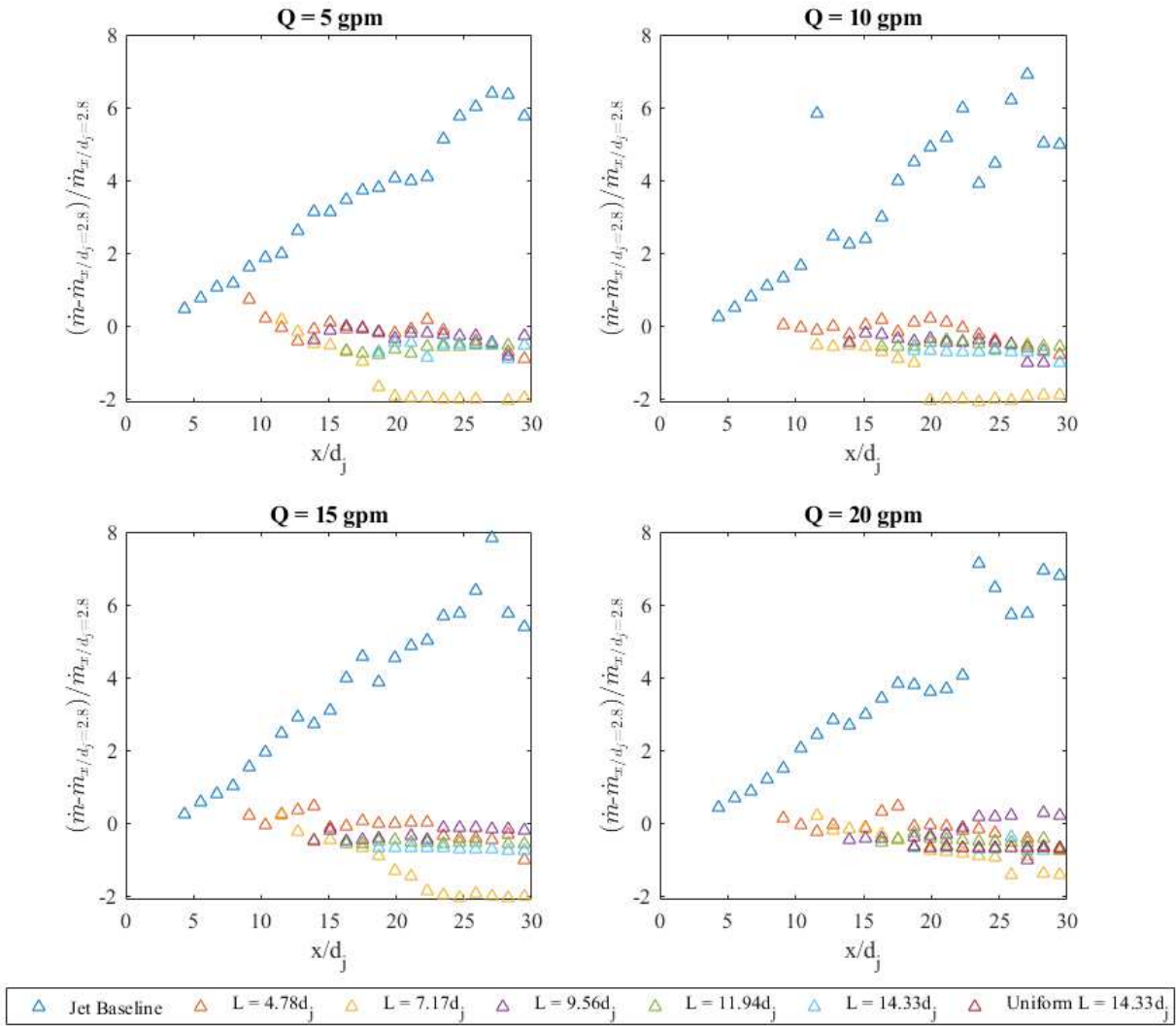
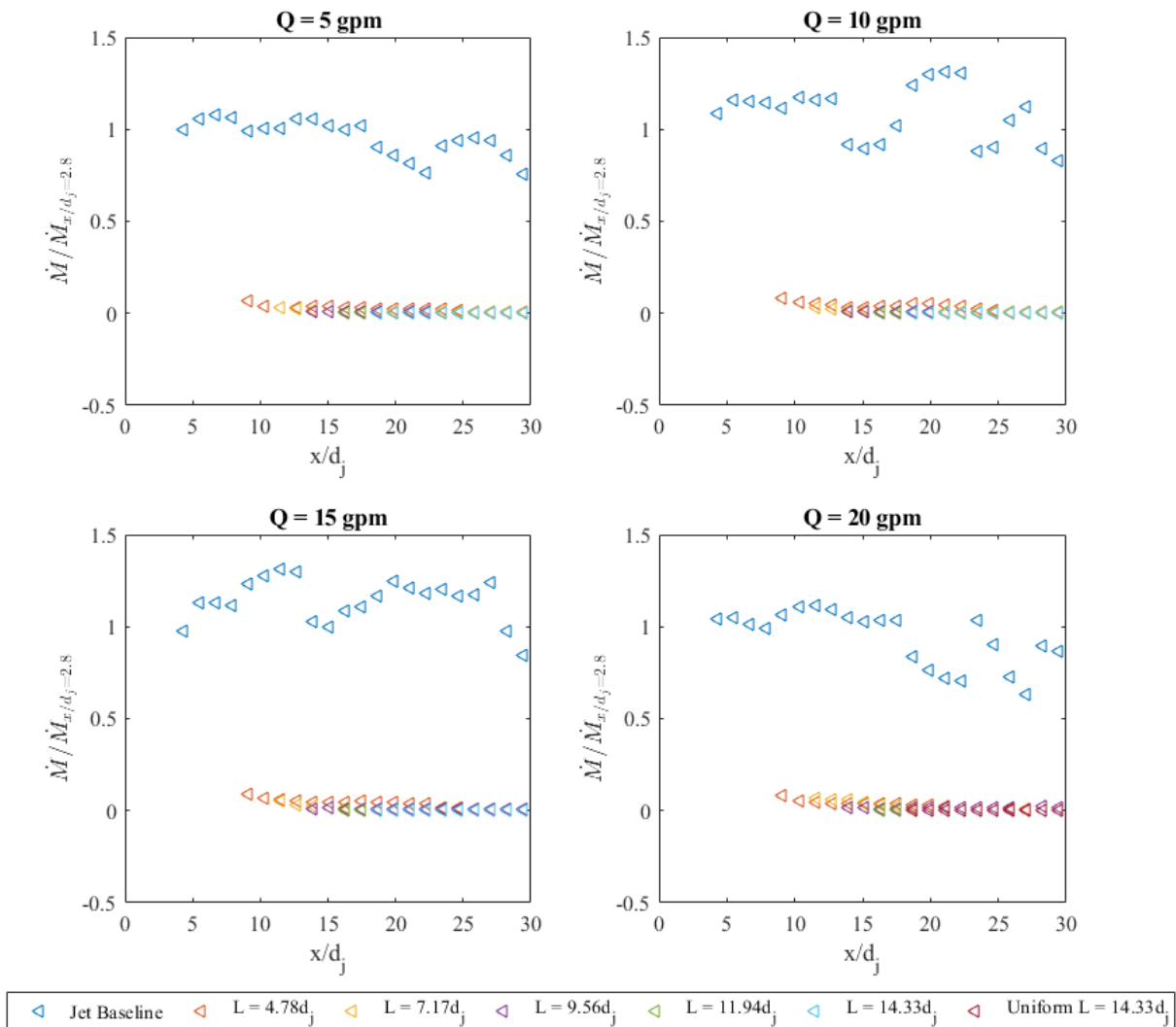


Figure 4-53: Normalized entrainment downstream of jets.

The jets entering RPM have spread and slowed extensively by the time the flow exits the RPM and the Reynolds stresses have been reduced by  $\geq 98\%$  with even the smallest amount of RPM. This significant reduction in shear stress is linked to the lack of entrainment of fluid (Dahm & Dimotakis 2012) that is a characteristic of jet flow. This loss of entrainment supports that the flow downstream of RPM (in any amount) is no longer a ‘jet’ flow.

### 4.3.2.6 Momentum Flux

While momentum is maintained in a free jet, it is clear that the momentum of a jet is not preserved when obstructed by an obstacle (Mossa et. al. 2017). This is definitely the case for the jets encountering RPM as shown in *Figure 4-54* below. Since momentum must be conserved, the difference in the momentum flux is a result of the resistance to the flow referred to as the bulk drag, which is a complex combination of skin (friction) and form (pressure) drag (discussed in Section 2-3).



*Figure 4-54: Normalized momentum flux across vertical profiles of the jet.*

### 4.3.2.7 Coefficient of Drag

The bulk coefficient of drag ( $C_D$ ) associated with the RPM is calculated using *Eqn 4-6* below that was derived by Mossa & De Serio (2017) for an obstructed jet where  $A(x) = \pi R^2$ .

$$\dot{M}(x) = \dot{M}_0 \exp\left(-\frac{1}{2}C_D A(x)x\right) \quad 4-6$$

Though *Eqn 4-6* was developed for a different scenario, where the jet encounters a cross-flow and the obstruction is a 2D organized array of cylinders, the equation was considered appropriate given the exponential decay of the maximum streamwise velocity through RPM determined in the previous section. Using *Eqn 4-6* to calculate the values of  $C_D$  for this experiment, however, resulted in unrealistically high values ( $O(3)$ ) (*Figure 4-55*).

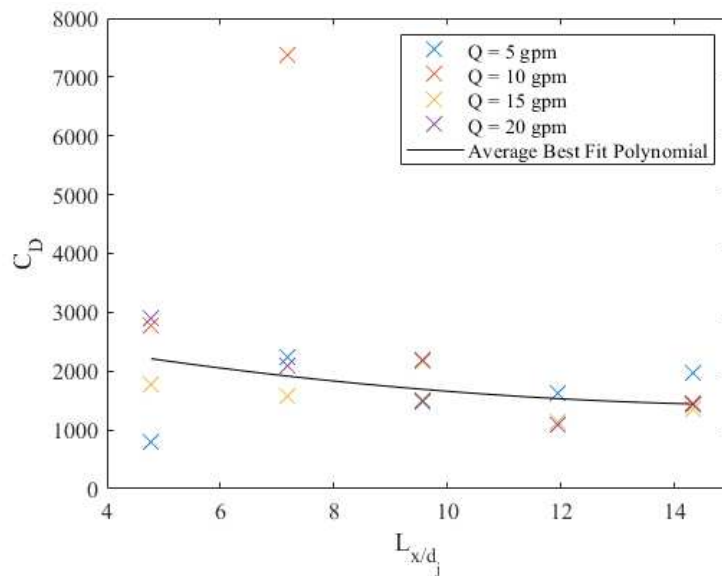


*Figure 4-55: Drag coefficients ( $C_D$ ) versus amount of RPM ( $L$ ; in terms of  $x/d_j$ ).*

The  $\dot{M}$  was calculated under the assumption that the flow downstream of the RPM remained axisymmetric, however it is evident from *Figures 4-37* to *42* that the flow is clearly not symmetric about the centerline in the vertical direction and therefore it is likely that the flow is not symmetric in the radial direction(s). This could have led to an underestimation in  $\dot{M}$ .

Despite the large values, the trend in  $C_D$  was analyzed. At first glance, there seems to be a weak (negative) second order relationship between  $C_D$  and the amount of RPM ( $L$ ) ( $C_D \sim L^2$ , with an  $R^2 \sim 0.7$  if  $C_D(10 \text{ gpm})$  at  $L = 7.17d_j$  is considered an outlier). Comparing flow rates, there is a larger range of  $C_D$  when  $L \leq 7.17d_j$ . To further investigate this,  $C_D$  was compared to the jet Reynolds numbers ( $Re_j$ ). From *Figure 4-56*, a non-monotonic relationship is observed for  $L = 4.78$  &  $7.17d_j$ . However at  $L = 9.56d_j$  it is shown that  $C_D$  generally increases as  $Re_j$  increases, but when  $L \geq 11.94d_j$   $C_D$  tends to decrease as  $Re_j$  increases with larger amounts of RPM.

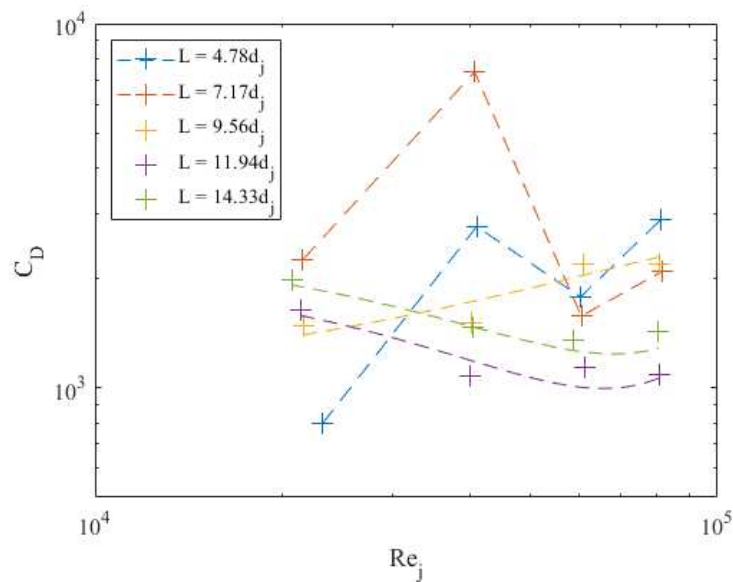


*Figure 4-56: Drag coefficients ( $C_D$ ) versus amount of jet Reynolds's number ( $Re_j$ ).*

The variety of trends was interesting but not necessarily explainable based on the  $Re_j$  as all jets are considered wholly turbulent ( $Re_j > 10,000$ ; Pope 2000). Since the flow downstream of the RPM seems to no longer resemble a jet flow, the particle Reynolds numbers ( $Re_{dp}$ ; Eqn 2-37) of the flow within the RPM was examined.  $Re_{dp}$  was calculated using the  $\langle U_{avg} \rangle$  just downstream of the RPM walls with the equivalent particle diameter ( $d_p$ ; Eqn 2-28) calculated from the void fraction ( $\varepsilon$ ) and specific particle surface area ( $a_p$ ) provided by the manufacturer of the RPM used

in this study. Comparing  $Re_{dp}$  to  $L$ , seen in *Figure 4-57*, the flow within the RPM can be classified by regime via the  $Re_{crit}$  values for flows interacting with obstacles discussed in Section 2.3.

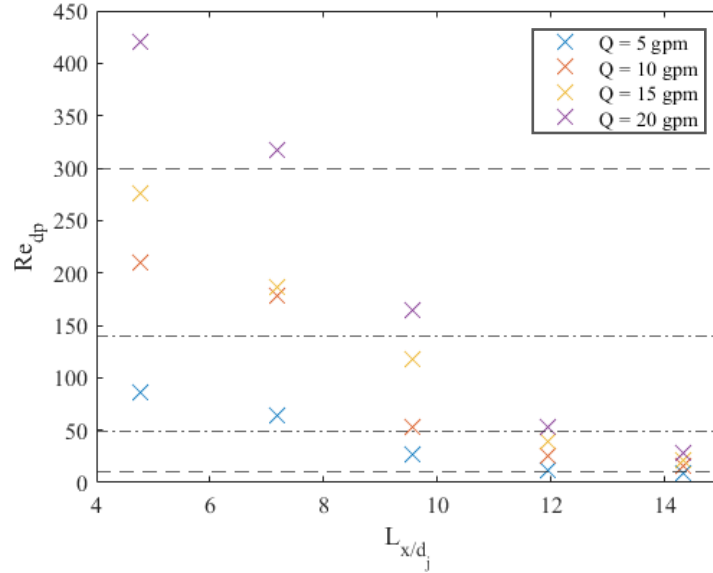


*Figure 4-57: The particle Reynold's number compared to the amount of RPM ( $L$ ). The dashed line [--] indicates laminar ( $Re_{dp} < 10$ ), transitional ( $10 < Re_{dp} < 300$ ) and turbulent ( $Re_{dp} > 300$ ) flow in a packed bed. The dashed-dotted line [- ·] indicates the  $Re_{crit}$  values of different wake regimes for flow around an infinitely long cylinder: Laminar Steady Regime ( $Re_{crit} < 49$ ), Vortex Shedding Laminar Regime ( $49 < Re_{crit} < \sim 140$ ), and the Wake Transition Regime ( $Re_{crit} > \sim 140$ ).*

On the basis of packed bed theory, for the most part, the flow within the RPM (for  $L \leq 14.33d_j$  at least) would be considered transitional ( $10 < Re_{dp} < 300$ ). Even for transitional flows, studies of various RPM geometries have demonstrated that the Ergun Equation (*Eqn 2-48*; a second-order monotonic relationship) has shown to be a good fit to predict the pressure drop (Nemec & Levec 2005). However, using the  $Re_{crit}$  values from the theory of uniform flow around an infinitely long cylinder (which is the simplest case), the flows could be considered to be within three different regimes: the Laminar Steady Regime ( $Re_{crit} < 49$ ), the Vortex

Shedding Laminar Regime ( $49 < Re_{crit} < \sim 140$ ), and the Wake Transition Regime ( $Re_{crit} > \sim 140 - 190$ ).

Looking at the  $Re_{dp}$  values, when  $L \geq 11.94d_j$  all flow rates could be considered to be in the Laminar Steady Regime. Recalling *Figure 2-8* in Section 2.3.1.2, in this regime the  $-C_{PB}$  decreases as  $Re$  increases, which is the trend observed in this data. Also, the decrease in  $C_D$  at higher  $Re$  is consistent with findings by Tanino & Nepf (2008) of drag from a uniform flow through a random array of cylinders. For jet flow obstructed by RPM, the flow downstream of the RPM becomes more uniform at  $L \geq 11.94d_j$ . It is also noted that  $C_D$  is consistently higher for  $L = 14.33d_j$  versus  $11.94d_j$  (see *Figure 4-56*). Once the flow is nearly uniform, it would be expected that the drag would increase proportionately with the amount ( $L$ ) of RPM (*Eqn 2-48*). When there is an RPM thickness of  $L = 9.56d_j$ , the flow within the RPM reaches  $Re_{dp}$  values (seen in *Figure 4-57*) that span the Vortex Shedding Laminar Regime of flow around an infinitely long cylinder. In this regime,  $-C_{PB}$  begins to increase as  $Re$  increases (refer to *Figure 2-8*). This supports the increase in  $C_D$  with an increase in flow rate for  $L = 9.56d_j$ . At  $L = 4.78$  &  $7.17d_j$ , the  $Re_{dp}$  values fall into the Vortex Shedding and Wake Transition regimes. For both cases  $C_D$  initially increases (consistent with the Vortex Shedding Regime), but then decreases (moves into the Wake Transition Regime) and then increases again. As discussed in Section 2.3.1.2, flow in the Vortex Shedding Regime is still relatively two-dimensional (2D) but as it moves into the Wake Transition Regime (at some point between  $Re = 140$  and  $194$ ) it becomes three-dimensional (3D). Correspondingly, there is a slight decrease in  $C_D$  followed by a slight increase when the wake transitions from a Mode A to Mode B instability. Once  $Re = 260$  there is a supercritical bifurcation leading to increasing 3D disorder and as  $Re$  continues to increase  $C_D$  will begin to decrease again (refer to *Figure 2-8*).

If  $C_D$  is plotted against  $Re_{dp}$  for the different scenarios in this study, the same relationship trend that is well established for uniform flow around an infinitely long cylinder is also observed for jet flow through RPM shown in *Figure 4-58* below.

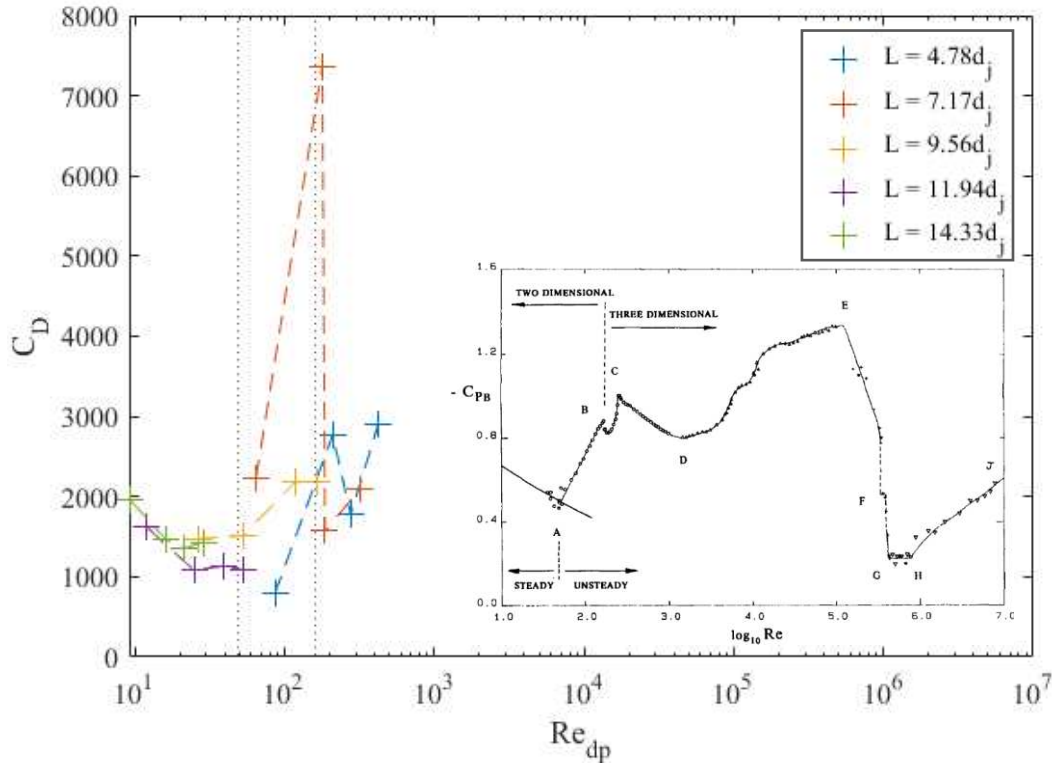


*Figure 4-58: Drag coefficients ( $C_D$ ) versus amount of particle Reynolds number ( $Re_{dp}$ ) with the plot of base suction coefficients ( $-C_{PB}$ ) versus Reynolds numbers ( $Re$ ) (Williamson 1996).*

The main difference is that the  $Re_{dp,crit}$  for the transition between the 2<sup>nd</sup> and 3<sup>rd</sup> regimes is delayed and seems to occur closer to  $Re_{dp} \approx 180 - 210$ , followed by a dip in  $C_D$  between  $Re_{dp} \approx 200 - 350$ . Since the trend is followed relatively closely, it is plausible that the dynamics of the jet flow within and/or downstream of RPM would exhibit some of the characteristics of these flow regimes. Further investigation into the wake-vortex dynamics would provide insight.

## 4.4 Conclusions

This study investigated a turbulent round jet flow from a long pipe through a wall of highly porous material (e.g. RPM). The results of this laboratory-scale study established, from a fundamental perspective, that a wall of RPM is able to effectively kill a jet flow by increasing the spreading rate ( $S_{RPM} \sim L^2$ ) and, more importantly, increasing the rate of decay exponentially. An RPM wall that is  $\sim 5$  times the diameter of the pipe ( $L \approx 5d$ ) reduces the maximum velocity and the Reynolds stresses by over 90%, essentially killing the jet's momentum, though the flow downstream of the RPM wall is still not uniform. Even with a relatively small amount of RPM, a significant improvement in the hydraulic disinfection efficiency of a contact tank would be achieved through the reduction of short-circuiting. For the flow downstream of RPM to be uniform – allowing for the highest efficiency possible for a particular system – the thickness of the RPM wall would need to be  $\geq 15d$ . While the flow rate does influence the spreading and decay rates induced by the RPM, they are small. The coefficients of drag for flow through RPM in this study, while unreasonably large ( $O(3)$ ), were highly variable with respect to the local Reynolds number of the flow within the RPM (i.e.  $Re_{dp}$ ). The  $Re_{dp}$  is dependent on the amount of RPM mainly due to the spreading which increases the area through which there is flow. From the continuity principle, the larger cross-sectional area where there is flow results in lower velocities. Therefore using enough RPM to fully spread the jet across the cross-section of a tank (and not much more) would lead to less drag induced by the wake downstream of the RPM.

The relationships established in this study are helpful in order to better determine the amount of RPM necessary to achieve the highest hydraulic disinfection efficiency possible of a particular contact system. However, there are more variables that could impact jet flows through RPM that

were not addressed in this study. For instance, it is still unknown whether the size of the flume (translating to the relative length scale of a tank/basin;  $D$ ) had any impact. The effect of the size of the tank, however, is likely to be small given the study by Kattnig & Venayagamoorthy (2015) where the width of the inlet box showed little impact on the baffling factor ( $BF$ ). Other variables including the diameter of the jet and the various aspects of the RPM (which are many; refer to Section 2.1) that were held constant in this study but would likely vary from system to system, are more likely to influence the flow dynamics. For instance, 1” special RPM has a higher packing factor meaning that more individual pieces fit in the same volume. So even though this size has a relatively similar porosity to the 2” RPM used in this study it would have a lower permeability, which would have a greater impact on its ability to slow the jet flow (Yakkatelli et. al. 2010).

Although there is more to investigate and analyze, the results of this study provide a baseline fundamental understanding of flow of a turbulent round jet from a long pipe (commonly seen in disinfection contact tanks) through RPM – a highly porous material. The knowledge gained will help inform best practices for the innovative application of RPM to improve the hydraulic disinfection efficiency in SWTSSs.

## CHAPTER 5

### 5 EFFICIENCY GAIN AND ENERGY LOSS<sup>1</sup>

#### 5.1 Introduction

In the United States, close to 21 million people rely on public water systems that have violated health-based quality standards as stipulated by the Safe Drinking Water Act (SDWA); 21% were related to the surface and ground water treatment rules (including *Cryptosporidium*, *Giardia lamblia*, and viruses), 37% were from Total Coliform, 36% from disinfection byproducts (DBPs), etc. (Allaire et al. 2018). Moreover, small systems in rural areas have had the largest number of violations (Allaire et al. 2018). From these data it could be said that the majority of SDWA violations are related to the disinfection stage in small water treatment systems (SWTSs).

There are multiple methods to eliminate pathogens from drinking water including chemical disinfection processes such as chlorination, chloramination, and ozone treatment, as well as physical removal processes such as the use of membranes (Crittenden et al. 2012). Chemical disinfection, specifically chlorination, is still the most widely used method of disinfection in the United States and around the world (Crittenden et al. 2012). When using chemicals for disinfection (or other water treatment processes including coagulation), the chemical must be dispersed uniformly across the cross-section of the tank (or pipe). Effective mixing is necessary

---

<sup>1</sup> The research presented in this chapter is a modified version that has been published as original research in the *Journal of American Water Works Association - Water Science* (August 2021) under the title “Random packing material in disinfection contactors: Effects on baffling and energy loss” by J. L. Baker, S. K. Venayagamoorthy, & S. K. De Long. Background information and literature relevant to this chapter are presented again so that the chapter may be read as a stand-alone work.

to ensure that all the water receives its proportionate share of the disinfectant as it continuously flows through a system. Since continuous-flow systems have a non-ideal flow pattern (as compared to continuously stirred tank reactors [CSTRs], etc.), simply injecting a disinfectant inline is often not sufficient (Crittenden et al., 2012).

In addition to mixing, the time in which the water remains in the treatment system, or residence time, after a disinfectant is injected is just as important (Crittenden et al. 2012). The time requirement is based upon the chemical reaction rate of the particular disinfectant used and the particular microorganisms present in the water that require inactivation (Crittenden et al. 2012). Most drinking water treatment systems include a “contact” basin (disinfection contactor) that is designed to retain the water long enough to meet the required “*CT*”--- the designated parameter to ensure microbial inactivation (United States Environmental Protection Agency [USEPA] 2003).  $CT = CT_{10}$  where  $C$  is the residual chlorine concentration (mg/L) and  $T_{10}$  is the time for the concentration of the tracer at the outlet to reach 10% of the inlet concentration ( $C_0$ ) (USEPA 2003).

The baffling factor ( $BF$ ) is the designated parameter used by USEPA to quantify the hydraulic disinfection efficiency of a particular system. Conceptually, the  $BF$  is a non-dimensional indicator of short-circuiting of the flow through the tank (Wilson & Venayagamoorthy 2010) and is defined as the ratio of  $T_{10}$  to the theoretical detention time (TDT) of that system ( $BF = T_{10}/TDT$ ). As a normalized value,  $BF$ s can range from 0 to 1, where 1 designates ideal plug flow conditions and anything less than 1 indicates impaired hydraulic efficiency (e.g.,  $BF = 0.5$  is considered average and a  $BF$  of 0.1 is considered very poor) (USEPA 2003). Another parameter often used to evaluate hydraulic disinfection efficiency internationally is called the Morrill index ( $MI$ ). In contrast to the  $BF$ , the  $MI$  is used as a numerical evaluation of diffusion (or mixing);

defined as the ratio of  $T_{90}$  (i.e. the dimensionless time required for 90% of the inlet concentration to reach the outlet) to  $T_{10}$  ( $MI = T_{90}/T_{10}$ ) (Wilson & Venayagamoorthy 2010).  $MI = 1$  is indicative of ideal plug flow, but  $MI < 2$  is considered to be an effective design (USEPA, 1991). The  $BF$  and  $MI$  together give a more holistic insight into the extent of short circuiting ( $BF$ ) and mixing ( $MI$ ). There are various models used to analyze disinfection contactors such as tank-in-series and the dispersed-flow model, but these are not relevant to the present context.

While there are multiple designs of disinfection contactors used in SWTSs, non-pressurized plastic water storage tanks (e.g. cylindrical tanks) are an option (CDPHE 2014). In an international context, cylindrical tanks are often used simultaneously as disinfection contactors and storage tanks. The benefits of these cylindrical tanks are the low cost, relatively small footprint, and easy maintenance. However, these cylindrical tanks suffer greatly from short-circuiting and large dead zones due to the jet of water from the inlet pipe into the ambient tank. The presence of short-circuiting and dead zones is hydraulically inefficient as not all of the available volume in the tank is being used (Barnett et al. 2014). This means, on the one hand, some water is not remaining within the system to achieve ideal disinfection (i.e., very low  $BF$ ) based on the flow rate and dimensions of the tank used. On the other hand, studies have shown that there is often a loss of disinfection residual with an increased production of DBPs where water is stagnant (i.e. in dead zones) (Chen et al. 2020). The combined short-circuiting and dead zones prevent thorough mixing (i.e. high  $MI$ ) as a result of the highly non-uniform flow within the tank itself.

With aging infrastructure, decreasing source water quality, and limited financial resources, there is a need for innovative yet cost-effective technologies to improve drinking water treatment – particularly for SWTS. A cost-effective and innovative technology to improve the hydraulic

disinfection efficiency in SWTSSs, proposed in the *Baffling Factor Guidance Manual* (CDPHE 2014), was the use of random packing material (RPM). RPM come in many designs (and materials), but the basic design idea consists of a relatively high porosity (60 - 98%) while maintaining a high surface area. A laboratory-scale study by Barnett et al. (2014), filled a cylindrical tank with RPM and determined the *BF*. The greatest improvement was seen when the tank was 100% full by volume of RPM, reaching near plug flow conditions (Barnett et al. 2014), which is ideal for chemical disinfection purposes in terms of microbe inactivation as well as reduction of disinfection byproducts (DBPs) (Wilson & Venayagamoorthy 2010). However, since the inlet was at the bottom of the tank and the RPM used was made of polypropylene, when the tank was only partially full (25 and 50%), the RPM floated and therefore did not disperse the jet as soon as it entered the tank.

In another laboratory-scale study by Kattnig and Venayagamoorthy (2015), RPM was used to create “porous walls” located at the inlet and turns in a baffled tank. Results of this study indicated a 35-62% improvement in the hydraulic disinfection efficiency in terms of *BF* (Kattnig 2014). On the basis of these results, if the RPM were secured at the inlet of a cylindrical tank, similar to the baffled tank study, it is likely that the results would differ from the Barnett et al. (2014) study. Thus, it was hypothesized that securing the RPM near the inlet would achieve a sufficient efficiency gain without the tank needing to be 100% filled with RPM.

While the presence of RPM has been shown to improve the hydraulic efficiency of disinfection contactors, there are a couple of practical concerns for adoption in practice: (1) biofilm growth and (2) the head loss (or pressure drop) associated with the use of RPM. The concern of biofilm growth on RPM, due to the quality of water entering a disinfection contactor, was investigated in a recent study by Baker et al. (2020). The results of this study showed no excessive biofilm

growth but the head loss has yet to be examined. It is well known that flow through RPM experiences a drop in pressure ( $\Delta P$ ) caused by frictional and form drag. The main focus for the improvement in RPM has been (and continues to be) on reducing the  $\Delta P$  because of the associated operational costs (McNult 1988). At this time, the  $\Delta P$  models, empirical studies, and specifications reported by RPM manufacturers only concern the current applications that involve countercurrent two-phase (uniform) flow. The single-phase flow of a turbulent jet entering into a disinfectant contactor (ambient) will likely behave differently, producing a unique  $\Delta P$ , thus requiring an empirical study investigating this phenomenon.

The purpose of this study is two-fold: (1) to determine the  $BF$  of flow through a cylindrical tank with varying amounts of RPM that is secured in the critical location(s) (i.e. at the inlet and outlet) and (2) to compare the  $BF$  with the energy requirement (in terms of head loss or bulk  $\Delta P$ ) through RPM. The results will give insight into the optimal amount and configuration of RPM to achieve the greatest improvement in  $BF$  with the minimal added energy costs.

## 5.2 Materials and Methods

### 5.2.1 Experimental configuration

A laboratory-scale (55 gal) tank with open access at the top of the tank was used to more easily vary and secure the configurations of 2" spherical RPM (Polypropylene (PP) NSF-61 certified with 93.5% void space (or porosity;  $\epsilon$ ) (Raschig USA, Inc., Arlington, TX; RTJ 2020) for this study. Three-quarter-inch bulkhead tank fittings were used for the inlet/outlets, one near the bottom of the tank and the other near the top, on diametrically opposite ends ( $180^\circ$  apart). The RPM were held in place using polyvinyl chloride-coated galvanized steel wire cloth with a 304

stainless-steel wire (10-gauge) woven through the mesh and routing eyebolts (304 stainless steel) secured in the tank wall. A dosing pump (LMI Milton Roy, 1.0GPH 110PSI 120VAC 50/60Hz 1.4A; model #: P151-392BI; Ivyland, PA) was connected just upstream of a static mixer to conduct step-dose tracer tests using a highly concentrated NaCl solution (according to the “Standard operating procedure for conductivity analysis of small public water disinfection systems”; Wilson 2011) to determine the *BF*. Photographs of both the bottom inlet – top outlet (BI/TO) and top inlet - bottom outlet (TI/BO) experimental setups can be seen in *Figure 5-1*.

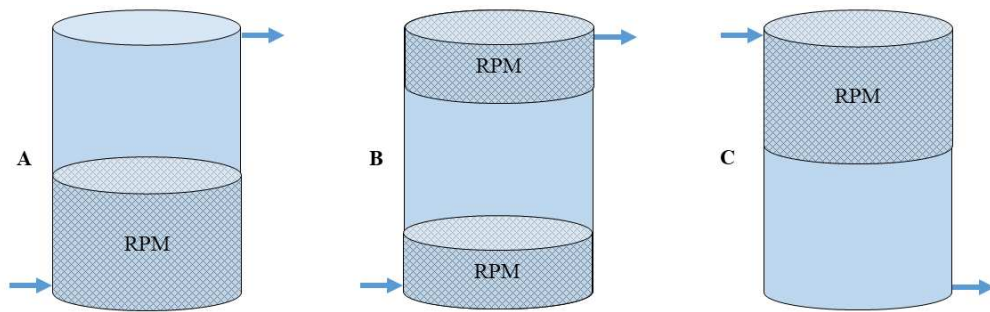


*Figure 5-1: Schematic of experimental set-up for an energy loss versus baffling efficiency gain study: A = BI/TO, B = BI/TO Split, C = TI/BO. Arrows indicate direction of inlet/outlet flow.*

Pressure taps were installed just upstream of the inlet and just downstream of the outlet to allow for the measurement of the bulk  $\Delta P$  through the tank using an ExTech Heavy Duty Differential Pressure Manometer (ExTech, model #: 407910; Nashua, NH). Outflow was diverted downstream of the outlet pressure tap to a flow-through device that held the conductivity probe (YSI Professional Plus - Pro Plus Handheld [Model # 6050000] with a Pro 30 cable [Serial# 14G100085], YSI Inc., Yellow Springs, OH) to obtain instantaneous readings. Treated water was pumped from storage tanks using a submersible pump (Dayton, 1/3 hp, cast iron, 120VAC; model #: 4HU68; West Carrollton) and flow rates varied using a DART Variable AC Voltage Supply (10 max. amps, 120VAC input/output; model #: 55AC10E; Zionsville, IN). Five flow rates (*Q*) were selected within the allowable range of the submersible pump and the tank seal (due to being a pressurized system) (see *Table 5-1*).

Table 5-1: Experimental Flow Rates

<i>Q</i> (gpm)	<i>Re<sub>jet</sub></i>	<i>Re<sub>tank</sub></i>
5	13,800	650
7.5	20,700	970
10	27,700	1,290
12.5	34,600	1,620
15	41,500	1,940

\*Note: 1. Italics indicate flow rates only performed for BI/TO 25, 50, and 100% filled  
 2. Reynolds number values based on average water temperature during trials (15.8 °C)

The Jet Reynolds number ( $Re_{jet} = ud/v$  where  $u$  is the velocity of the jet,  $d$  the diameter of the jet and  $v$  the kinematic viscosity of water) of the inlet for each flow rate along with the Reynolds number within the tank ( $Re_{tank} = UD/v$  where  $U$  is the superficial velocity (assuming uniform flow),  $D$  the diameter of the tank) are also given. All jets from the inflow are considered to be wholly turbulent jets ( $Re_{jet} > 10,000$ ; Pope, 2000) while flows within the tank are considered to be laminar ( $Re < 2,300$ ; White, 2003). These  $Re_{jet}$  values are representative of approximately half of the possible  $Re_{jet}$  values found in SWTSSs (see Table 5-2).

Table 5-2: Estimated Jet Reynolds number ( $Re_{jet}$ ) values of SWTSSs

Nominal Inlet dimensions	<i>Q</i> (gpm)				
	10	20	30	40	50
1"	28,200	56,400	84,700	112,900	141,100
1 ¼"	21,300	42,700	64,100	85,400	106,800
1 ½"	18,300	36,500	54,800	73,000	19,300
2"	14,200	28,400	42,600	56,700	70,900
2 ½"	11,900	23,700	35,600	47,500	59,400
3"	9,500	19,100	28,600	38,200	47,700
3 ½"	8,200	16,500	24,700	33,000	41,200
4"	7,300	14,500	21,800	29,100	36,300
5"	5,800	11,600	17,400	23,200	28,900
6"	4,800	9,600	14,400	19,300	24,100

\*Note: 1. blue shading indicates  $Re_{jet}$  values represented through this laboratory-scale study  
 2. Reynolds number values based on average water temperature during trials (15.8°C)

Because of the sensitivity of the conductivity meter (with an average fluctuation in conductivity readings of 5.4%), tracer tests were repeated until three trials resulted in matching residence time distribution (RTD) curves for each experimental scenario (a total of 138 trials). The conductivity meter and digital manometer used were independently verified to be within 1.9% and 9.0% error margins respectively.

Multiple scenarios and configurations were investigated to establish the relationship of BF gain and the associated energy loss to the amount of RPM (%RPM to the total volume of the tank).

Initially, RPM was secured at the inlet at %RPM = 25%, 50%, 75%, 90%, and 100% full with a BI/TO configuration (*Figure 5-2*).

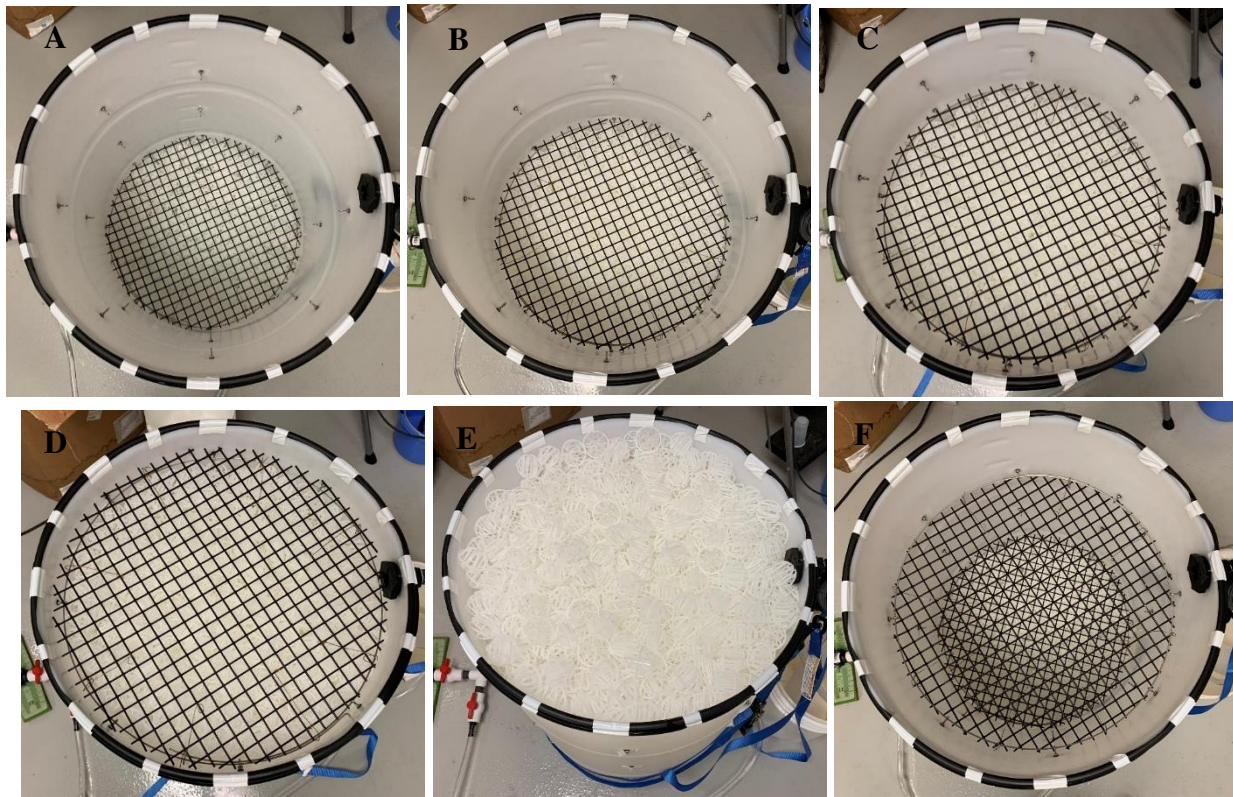


*Figure 5-2: Photographs of 55-gallon tank (BI/TO) filled with 2" spherical RPM; A = 25%, B = 50%, C = 75%, D = 90%, E = 100%, F = 25/25% (before RPM filled near outlet)*

Then, a split configuration was considered in which RPM was secured at the inlet (25%) and outlet (25%). This was done to study the effect of the sharp outlet, further investigating the importance of location in addition to the %RPM. Finally, RPM was secured at inlet (50%) but with a TI/BO configuration in order to investigate the gravitational effects. The baselines for this study were taken of the BI/TO and TI/BO systems with no RPM present.

### 5.2.2 Data analysis

The global minimum baseline conductivity of the industrial water, i.e. before any dosing of tracer (concentrated NaCl solution;  $86.4 \pm 7.6 \mu\text{S}/\text{cm}$ ), was subtracted from the conductivity data values. These data values were then normalized using the global maximum (inlet) conductivity data ( $C_0$ ;  $124.9 \pm 22.8 \mu\text{S}/\text{cm}$ ). Time data values ( $t$ ) were normalized with the  $TDT$  of the flow through the tank. Normalized conductivity ( $C/C_0$ ) was plotted against the normalized time ( $t/TDT$ ) to create RTD curves, smoothed using a Savitzky-Golay smoothing filter (with order = 4 and frame length = 21; Press & Teukolsky 1990) in MATLAB. The  $BF$  was determined by linear interpolation of the normalized data in which  $C/C_0$  reached 0.1 and continued to increase. Bulk  $\Delta P$  data of the empty tank (baseline) was fit to a 2<sup>nd</sup>-order polynomial. The bulk  $\Delta P$  data was then normalized using the equivalent bulk  $\Delta P$  of the baseline ( $\Delta P/\Delta P_{\text{baseline}}$ ). The  $BF$  and  $\Delta P$  data were analyzed by multiple  $t$ -tests (two-tailed, two-sample with uneven variance) at a significance level of  $p < 0.05$ . Additionally, the RTD curves were analyzed by two-sample Kolmogorov-Smirnov tests at a significance level of 5% ( $\alpha = 0.05$ ) - the null hypothesis being that the RTD curves are from the same continuous distribution.

## 5.3 Results & Discussion

### 5.3.1 Efficiency

Without any RPM, the baseline efficiency of the 55-gal tank is considered to be poor with a  $BF$  of approximately  $0.08 \pm 0.01$  to  $0.15 \pm 0.04$  (USEPA 2003; see *Figure 5-3*). When the %RPM = 25%, the  $BF$  increased to  $0.53 \pm 0.04$  at 15 gpm up to  $0.77 \pm 0.04$  at 5 gpm; or average to good efficiency (USEPA 2003). The greatest improvement in  $BF$  occurring at the lowest flow rate is inconsistent with the results of the Barnett et al. study (2014). This suggests that the location of the RPM within a tank matters. Increasing the %RPM to 50%, the  $BF$  followed a similar trend except at the higher flow rates the  $BF$  increased again to about  $0.63 \pm 0.01$ .

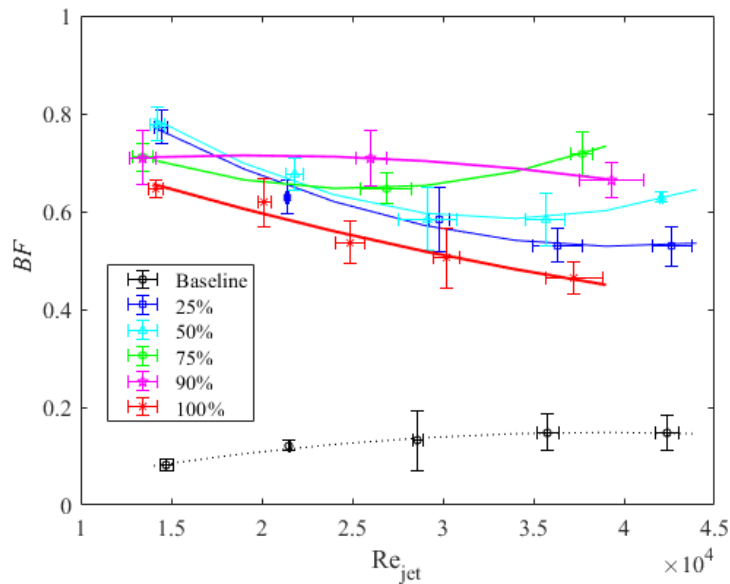


*Figure 5-3: Graph of  $BF$  of varying %RPM as a function of turbulent jet Reynolds number ( $Re_{jet}$ ) for the BI/TO configurations.*

When %RPM = 75%, the  $BF$  followed a similar pattern to 50% but ranging from  $0.65 \pm 0.03$  to  $0.72 \pm 0.05$ . When %RPM = 90%, the  $BF$  ranged from  $0.67 \pm 0.04$  to  $0.71 \pm 0.06$  but did not follow any pattern similar to other fill amounts. However, at %RPM = 100% the  $BF$ s followed the trend of %RPM=25% yet were consistently lower ranging from  $0.46 \pm 0.03$  to  $0.65 \pm 0.02$ . On the basis

of these results, the maximum  $BF$  achievable using RPM for this particular tank/system is about  $0.78 \pm 0.03$ . Furthermore, the possible efficiency gain was more variable at higher flow rates (or  $Re_{jet}$ ) than at the lower ones. It is more evident from *Figure 5-4*, showing the  $BF$  as a function of %RPM for different flow rates, that the greatest possible improvement for higher flow rates was achieved when the %RPM was greater than 50% but less than 100%.

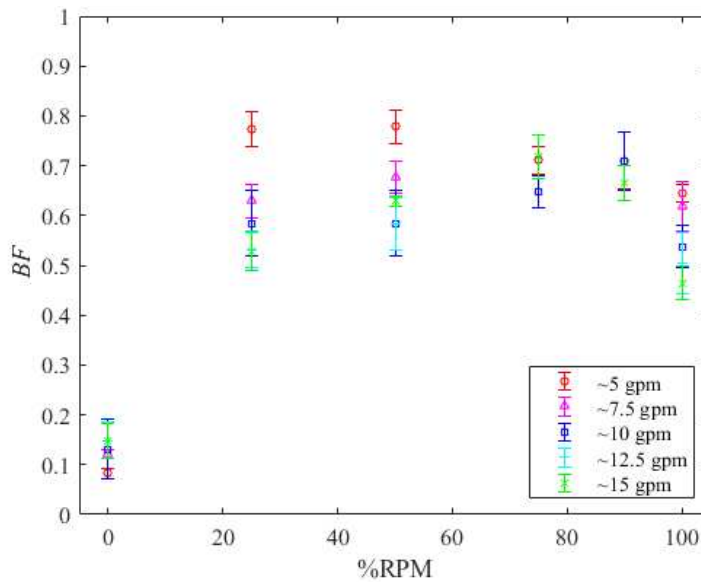


*Figure 5-4: Graph of  $BF$  of various flow rates as a function of % RPM for the BI/TO configurations.*

The change in the shape of the RTD curves for three of the different flow rates as seen in *Figures 5-5 to 7*, demonstrates the reduced short-circuiting and dead zones due to the presence of RPM secured near the inlet of the BI/TO configuration. The shift and sharp turn in the RTD curves closer to  $t/TDT = 1$  at all flow rates is indicative of the reduced short-circuiting from the jet at the inlet of the tank; thus flow is not leaving the system as quickly (Teixeira & Siqueira 2008). This could be explained by the RPM spreading the turbulent jet and the increased hydrodynamic dispersion of flow through porous media (Puyguiraud et al. 2021). In addition, the quicker transition to  $C/C_0 = 1$  just past  $t/TDT = 1$  represents the diminished dead zones present

(resulting in a lower  $MI$ ); therefore flow is not lingering within the tank longer than expected (Teixeira & Siqueira 2008).

When comparing flow rates, the shape of the RTD curves at 5 gpm more closely resemble the ‘plug flow’ curve than the RTD curves at 10-15 gpm. This highlights that the presence of RPM secured near the inlet, in any amount, has the greatest impact at lower flow rates (or  $Re_{jet}$ ) due to significant increases in hydrodynamic dispersion. However, the amount of RPM did not seem to significantly alter the shape of the curves with the same flow rate, except when  $\%RPM = 100\%$ .

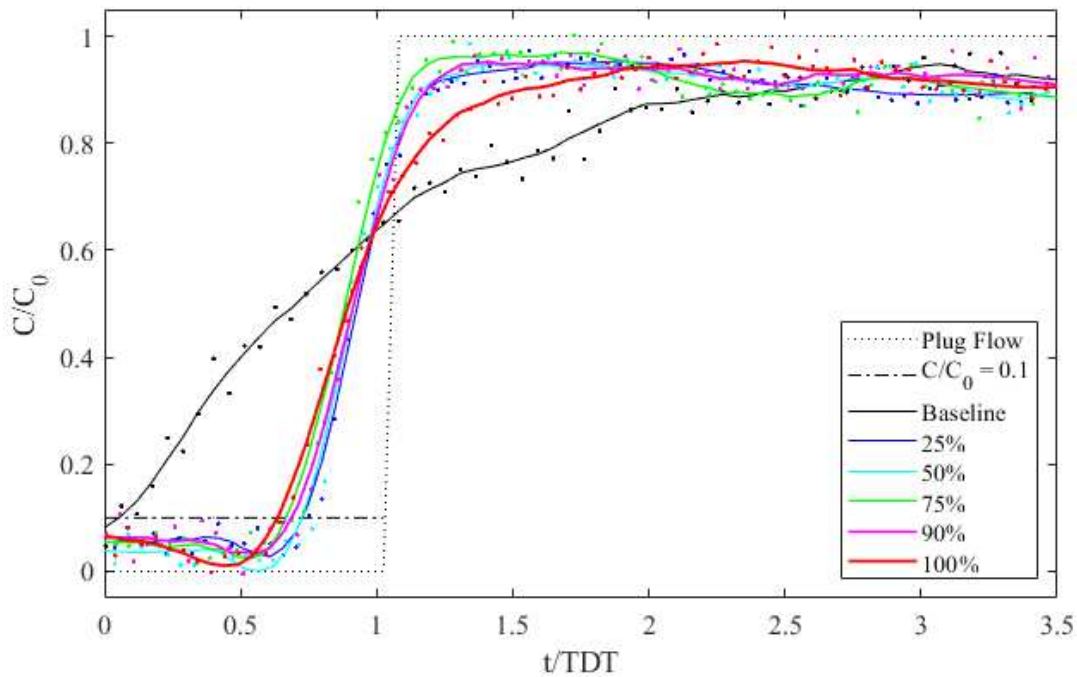


Figure 5-5: Average RTD curves of various  $\%RPM$  for 5 gpm ( $Re_{jet} = \sim 13,800$ ) for the BI/TO configurations.

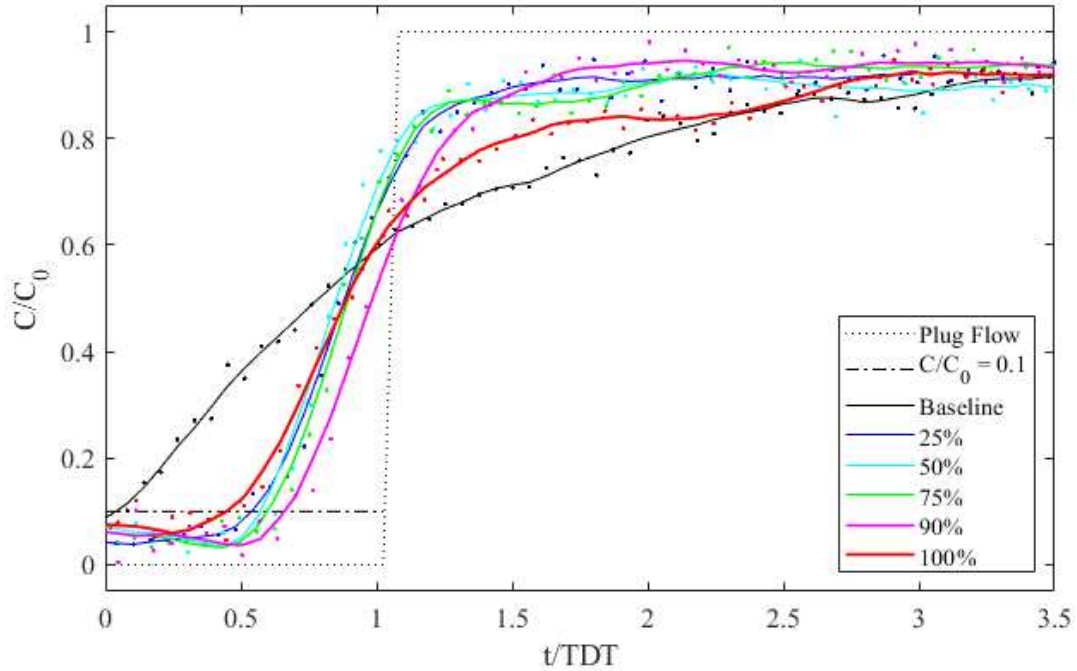


Figure 5-6: Average RTD curves of various %RPM for 10 gpm ( $Re_{jet} = \sim 27,700$ ) for the BI/TO configurations.

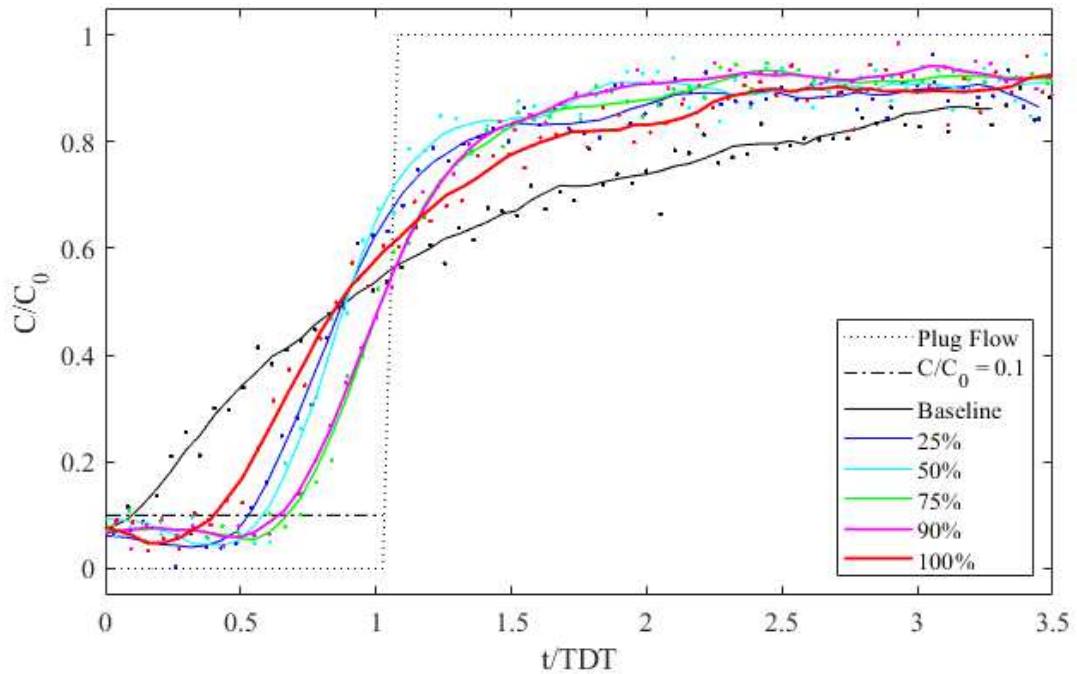


Figure 5-7: Average RTD curves of various %RPM for 15 gpm ( $Re_{jet} = \sim 41,500$ ) for the BI/TO configurations.

While a similar shift leading up to  $t/TDT = 1$  is observed at all %RPM, when %RPM = 100% the RTD curves at every flow rate reach  $C/C_0 = 1$  more gradually, more similarly to the

baseline (no RPM). This indicates a greater occurrence of dead zones than when the %RPM < 100%. The variable changes on the leading and tail-ends of the RTD curves (*Figures 5-5 to 7*) show that both short-circuiting (*BF*) and re-circulation (or dead zones; *MI*) are not always linked and may need to be addressed separately.

The change in the shape of the RTD curves to more closely resembling a step function is similar to the Barnett et al. (2014) study. When comparing analogous studies (i.e. 50% filled with 2” RPM in a 50-gal tank at 5 & 10 gpm) it is evident that securing the RPM near the inlet resulted in a steeper RTD curve, closer to plug flow than when not secured (Barnett et al. 2014). The improvement in *BF* is consistent. When securing the (50%) RPM near the inlet, a *BF* of  $0.77 \pm 0.04$  at 5 gpm was achieved versus 0.46 when not secured (Barnett et al. 2014). This indicates that there was a greater improvement within the specific system when the RPM was secured in a critical location. A similar pattern is seen for similar studies when 25% filled with RPM. The statistical analysis reveals that the improvement in hydraulic efficiency in term of *BF* and a more uniform flow by securing RPM near the inlet (in any amount) is significant (See *Table 5-3*). Also, consistent with the visual analysis of the RTD curves, the amount of RPM becomes significant as the flow rate (or  $Re_{jet}$ ) increases, i.e. the higher the flow rate, the greater the difference in *BF* based on %RPM. The statistical analysis of the RTD curves shows a higher rate of significant difference between the curves and also supports that the curves are more similar at the lowest flow rate.

Table 5-3: P-value results of t-test for baffling factor and Kolmogorov-Smirnov test for RTD curves\* for the BI/TO configurations.

Q	%RPM	25%		50%		75%		90%		100%	
		$p_t$	$p_{ks}$								
5 gpm	Base-line	0.000	0.019	0.000	0.002	0.000	0.019	0.000	0.002	0.000	0.110
	25%			0.677	0.160	0.117	0.160	0.356	0.007	0.058	0.540
	50%					0.087	0.110	0.249	0.031	0.046	0.160
	75%							0.513	0.012	0.606	0.160
	90%									0.283	0.074
7.5 gpm	Base-line	0.000	0.000	0.000	0.000					0.000	0.000
	25%			0.097	0.000					0.402	0.046
	50%									0.509	0.000
10 gpm	Base-line	0.000	0.000	0.001	0.000	0.000	0.000	0.000	0.000	0.000	0.072
	25%			0.855	0.000	0.062	0.000	0.012	0.000	0.117	0.028
	50%					0.161	0.000	0.130	0.000	0.523	0.017
	75%							0.828	0.127	0.014	0.000
	90%									0.001	0.000
12.5 gpm	Base-line	0.000	0.000	0.000	0.000					0.000	0.010
	25%			0.048	0.006					0.373	0.000
	50%									0.042	0.028
15 gpm	Base-line	0.000	0.017	0.000	0.000	0.000	0.000	0.000	0.000	0.000	0.046
	25%			0.017	0.003	0.000	0.000	0.006	0.000	0.299	0.111
	50%					0.005	0.002	0.246	0.000	0.003	0.072
	75%							0.014	0.589	0.000	0.006
	90%									0.001	0.000

Note: green shading indicates significant difference with a p-value < 0.05 for the t-tests and yellow shading represents a rejection of the null hypothesis of the Kolmogorov-Smirnov tests at  $\alpha = 0.05$ .

\*See Appendix B for other Kolmogorov-Smirnov test results (h and ks-stat).

### 5.3.2 Configuration

To better understand why the *BF* decreased when %RPM = 100%, the RPM near the outlet was considered to be a potential factor. To confirm this, the tank was 25% filled with RPM secured

near the inlet and 25% secured near the outlet (%RPM = 25/25%), a total of 50% filled. Since the %RPM = 100% and 25/25% were the only scenarios in which RPM was near the outlet, this configuration gives insight into the exit effects of this particular tank/system. A slight decrease in  $BF$  when %RPM = 25/25% is seen in *Figure 5-8* as compared with the  $BF$  when the %RPM = 50% all secured near the inlet. This shift is similar to the decrease in  $BF$  observed when %RPM = 100%.

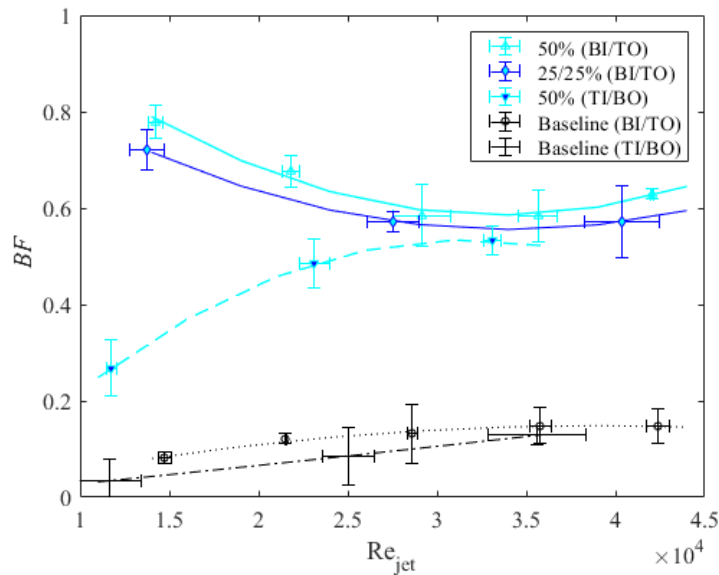


*Figure 5-8: Graph of  $BF$  compared with various  $Re_{jet}$ 's of different configurations of %RPM = 50%; secured near inlet (50% BI/TO), split between inlet & outlet (25/25% BI/TO), and reverse direction (50% TI/BO)*

In the BI/TO configuration, the majority of the momentum of the flow is in the upward vertical direction. However, the outlet is on the upper side of the tank. This arrangement requires the flow to not only converge but to turn. In an empty tank, the effect of the sharp outlet would lead to a convergence of flow ‘up-stream’ of the outlet. Whilst the presence of RPM is beneficial for spreading the incoming jet, it seems to work against the flow converging and turning at the outlet. The presence of RPM increases tortuosity, or the length of the pathlines of the flow, which impedes the flow’s ability to converge smoothly. This is consistent with the argument that the RPM increases the hydrodynamic dispersion. The RPM creates pseudo-dead zones as seen by

the more gradual transition to reach  $C/C_0 = 1$  when the %RPM = 25/25% (similar to %RPM = 100%), which is not seen when %RPM = 50% (Figure 5-9), nor for any scenario with %RPM < 100% (Figures 5-5 to 7) in which the RPM is not near the outlet. Despite the difference in RTD curves, there is not a significant difference in the resultant  $BF$  between %RPM = 50% and 25/25%. This, again, supports addressing short-circuiting and dead zones separately as  $BF$  is not sufficient to evaluate the internal hydraulics holistically. Assessing the RTD curve from a tracer test on a particular system, from which various hydraulic efficiency indexes (e.g.  $MI$ , dispersion  $[\sigma^2]$ , etc.) can be determined (Teixeira & Siqueira 2008; Wilson and Venayagamoorthy 2010), is a better method of evaluation than simply considering the  $BF$ . This is especially true when the  $BF$  is credited on the basis of certain design aspects of a system (USEPA 2003).

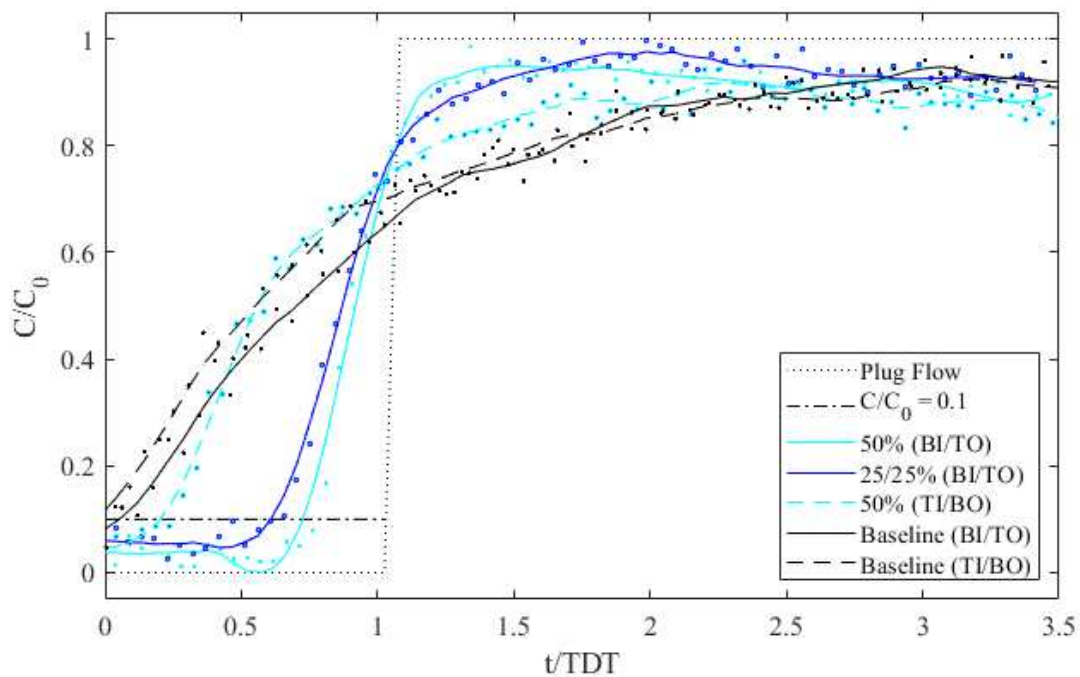


Figure 5-9: Average RTD curve of different configurations of %RPM = 50% at ~5 gpm ( $Re_{jet} = \sim 13,800$ ); secured near inlet [50% (BI/TO)], split between inlet & outlet [25/25% (BI/TO)], and reverse direction [50% (TI/BO)].

Changing the direction of the flow changes the potential energy of the systems which could possibly impact the overall energy requirements ( $\Delta P$ ) and the efficiency ( $BF$ ). The results of

%RPM = 50% (TI/BO) configuration deviate from the general trend in  $BF$  for the other %RPM = 50% scenarios (see *Figure 5-8*). The difference is most evident at the lowest flow rate (or  $Re_{jet}$ ), which is consistent with the statistical analysis results shown in *Table 5-4*. Similarly to the 25/25% split scenario, a shift on the leading end of the RTD curve as well as a more gradual transition to  $C/C_0 = 1$  is observed, yet to a greater extent is seen in *Figure 5-9*.

*Table 5-4: P-value results of t-test for baffling factor and Kolmogorov-Smirnov test for RTD curves\* of different %RPM = 50% configurations.*

Q	%RPM	Baseline (TI/BO)		50% (BI/TO)		25/25% (BI/TO)		50% (TI/BO)	
		$p_t$	$p_{ks}$	$p_t$	$p_{ks}$	$p_t$	$p_{ks}$	$p_t$	$p_{ks}$
5 gpm	Baseline (BI/TO)	0.005	0.048	0.000	0.002	0.000	0.031		
	50% (BI/TO)					0.184	0.004	0.001	0.000
	25/25% (BI/TO)							0.001	0.000
	50% (TI/BO)	0.006	0.3116						
10 gpm	Baseline (BI/TO)	0.221	0.1327	0.001	0.000	0.000	0.000		
	50% (BI/TO)					0.927		0.506	0.179
	25/25% (BI/TO)							0.403	0.002
	50% (TI/BO)	0.006	0.019						
15 gpm	Baseline (BI/TO)	0.028	0.996	0.000	0.000	0.001	0.016		
	50% (BI/TO)					0.092	0.133	0.014	0.002
	25/25% (BI/TO)							0.699	0.226
	50% (TI/BO)	0.000	0.048						

*Note: green shading indicates significant difference with a p-value < 0.05 for the t-tests and yellow shading represents a rejection of the null hypothesis of the Kolmogorov-Smirnov tests at  $\alpha = 0.05$ .*

*\*See Supplemental Information for other Kolmogorov –Smirnov test results (h and ks-stat).*

In the TI/BO configuration, the majority of momentum of the flow is in the downward vertical direction compared to the BI/TO where it is in the upward vertical direction. Moreover, the total available energy head is higher in the TI/BO than in the BI/TO configuration as a result of the increase in potential energy (PE) as result of the higher elevation of the inlet. While the increase in PE increases the momentum of the mean flow in the TI/BO configuration, the opposite situation occurs for the BI/TO configuration. When comparing the baselines of the BI/TO versus

TI/BO scenarios, the  $BF$ s are significantly lower across the flow rates tested. Additionally, the results of %RPM = 50% (TI/BO) are less hydraulically efficient than %RPM = 50% (BI/TO) as seen in *Figure 5-9*. The lower  $BF$  values in the TI/BO configuration are consistent with a greater momentum leading to a smaller overall possible effect RPM has in improving the hydraulic disinfection efficiency as discussed previously. The difference in the RTD curves of the 50% (BI/TO) and 50% (TI/BO) scenarios is statistically significant at the lowest flow rate, but less so at the higher flow rates. Therefore the results of this study seem to suggest there is a threshold as to when the difference in PE has a significant impact on the hydraulic disinfection efficiency for this system when  $Re_{tank} < \sim 1,290$  ( $Re_{jet} < \sim 27,700$ ).

### 5.3.3 Energy Loss

The bulk  $\Delta P$  followed a 2<sup>nd</sup> order relationship in every scenario tested as seen in *Figure 5-10*.

This was expected on the basis of the knowledge of Darcy-Weisbach's head loss ( $h_L$ ) relationship (where  $\gamma$  is the specific weight,  $f$  is Darcy-Weisbach's friction factor,  $g$  is gravity, and  $L$  &  $D$  are the height and diameter of the tank, respectively):

$$h_L = \frac{\Delta P}{\gamma} = f \left( \frac{L}{D} \right) \frac{8}{g} \left( \frac{Q}{\varepsilon \pi D^2} \right)^2 \quad 5-1$$

Similarly, the Ergun equation, which is commonly used to predict pressure loss in packed bed theory, demonstrates a 2<sup>nd</sup> order relationship (where  $\mu$  the dynamic viscosity of water and  $d_p$  the particle equivalent diameter of the RPM):

$$\frac{\Delta P}{L} = 150 \frac{U \mu (1-\varepsilon)^2}{d_p^2 \varepsilon^3} + 1.75 \frac{U^2 (1-\varepsilon)}{d_p \varepsilon^3} \quad 5-2$$

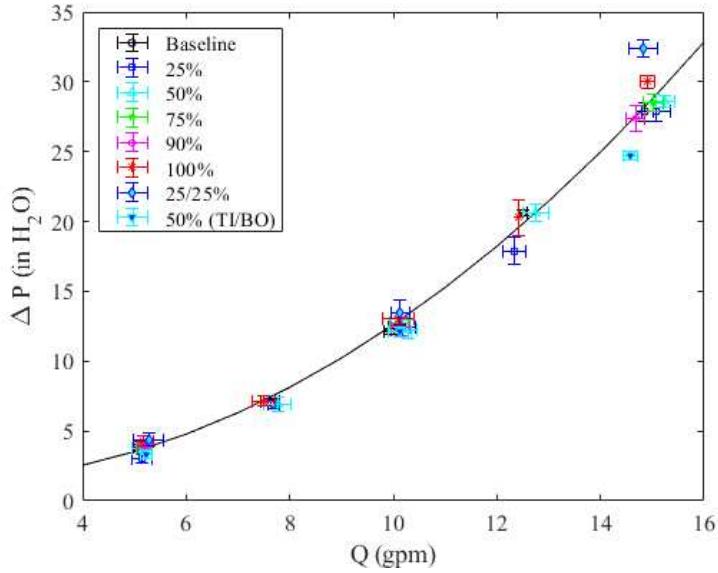


Figure 5-10: Graph of  $\Delta P$  of all experimental scenarios compared to  $Q$

It is also evident that there is little change in the bulk  $\Delta P$  as the fill amount of RPM increases, seen by the nearly horizontal trends when comparing bulk  $\Delta P$  with % RPM (see Figure 5-11).

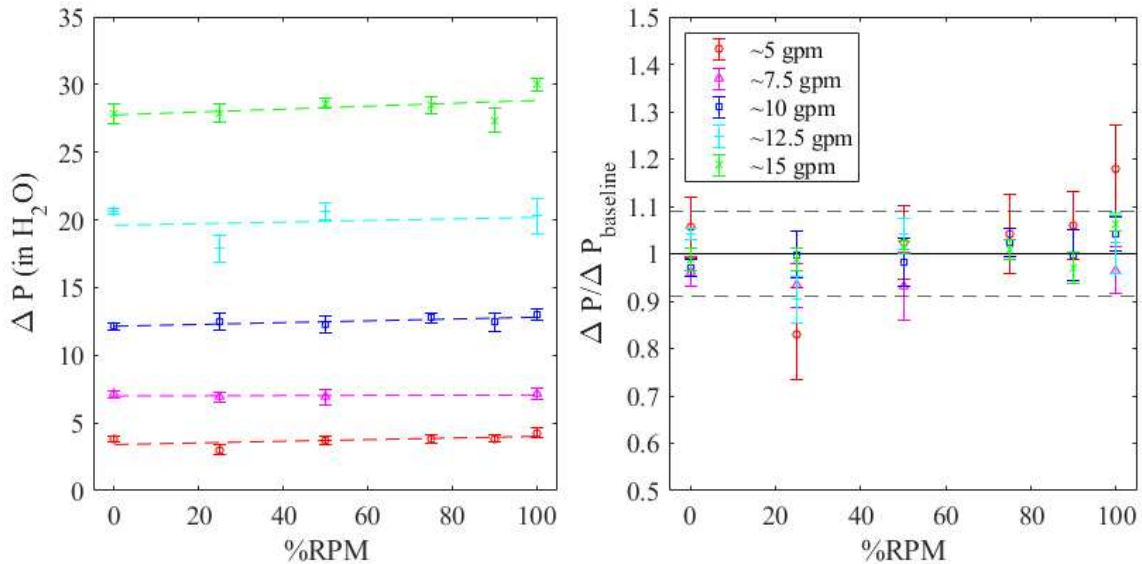


Figure 5-11: Graph of  $\Delta P$  (left) and normalized  $\Delta P$  (right; dashed lines on indicate accuracy bounds of digital manometer) from various flow rates through varying fill amounts of RPM

When comparing the  $\Delta P / \Delta P_{\text{baseline}}$  with the %RPM, the greatest variation from the  $\Delta P_{\text{baseline}}$  occurred at the lowest flow rate (5 gpm; see Figure 5-11). However, majority of the  $\Delta P / \Delta P_{\text{baseline}}$  values remain within the accuracy limit of the digital manometer used. This is consistent with the

statistical analysis in which the majority of scenarios did not see a significant change in the bulk  $\Delta P$ , nor was there a distinguishable pattern in significance (See *Table 5-5*). Thus, there is not enough evidence that the presence of RPM increased the energy requirements for this tank/system. This finding, however, was not consistent with the hypothesis that the more RPM present, the more bulk  $\Delta P$  or head loss the system would experience.

*Table 5-5: P-value results of t-test for  $\Delta P/P_{baseline}$  for all configurations.*

Q	25% (BI/TO)	50% (BI/TO)	75% (BI/TO)	90% (BI/TO)	100% (BI/TO)	25/25% (BI/TO)	50% (TI/BO)
5 gpm	0.015	0.491	0.297	0.604	0.032	0.190	0.000
7.5 gpm	0.072	0.013			0.279		
10 gpm	0.423	0.060	0.362	0.723	0.353	0.125	0.187
12.5 gpm	0.025	0.067			0.969		
15 gpm	0.064	0.064	0.306	0.796	0.002	0.010	0.007

*Note: green shading indicates significant difference with a p-value < 0.05*

The hypothesis was that the substantial increase in surface area would result in a greater resistance the flow would need to overcome. However, assuming the RPM is successful in spreading the turbulent jet from the inlet, then the velocities within the tank would be relatively low, indicated by the laminar flow at each flow rate tested (see *Table 5-1*). When considering Darcy-Weisbach’s head loss relationship, with low velocities (laminar flow), the head loss due to friction (associated with the high surface area of the RPM) would be small. Since the bulk  $\Delta P$  did not significantly change, it can be concluded that the local losses due to the sharp inlet and outlet to the tank are greater than any head losses due to friction caused by the presence of RPM.

The tank filled with RPM could also be treated as a packed bed. From this perspective, the values of Re for a packed bed ( $Re_{dp}$ ) range between ~3-10, where  $Re_{dp} < 10$  is considered to be laminar (Ziolkowska & Ziolkowska 1988). In packed bed theory, it is argued that when  $Re_{dp} <$

10, the wall friction is dominant (Baker 2011). The lack of significant change in bulk  $\Delta P$  in this study is consistent with wall friction being dominant.

The lack of significant change in head loss could also be explained by the reduced short circuiting. A turbulent jet entering an ambient (in this case the disinfection contactor) experiences high levels of shear, resulting in energy loss (Pope 2000). It is plausible that any added head loss due to friction by the presence of RPM was offset by the reduction of head loss due to the high shear between the turbulent jet from the inlet and laminar flow within the disinfection contactor.

## 5.4 Conclusions

This study showed that by securing RPM near the inlet of a cylindrical tank (disinfection contactor), in any amount, will result in significant improvements in the hydraulic efficiency in terms of  $BF$ . The greatest impact of RPM is seen at lower flow rates and the %RPM is significant at higher flow rates. It is noted, however, that the inlet/outlet configuration (direction of flow) does affect the highest  $BF$  possible, even when using RPM, within a system.

Remarkably, the presence of RPM adds no significant head loss, equating to no additional operational costs.

While this laboratory-scale study demonstrated the hydraulic conditions in cylindrical disinfection contactors, a scaling study would be necessary to model the higher  $Re_{jet}$  values seen in SWTSSs. Ultimately, with the aim of promoting the adoption of RPM in drinking water disinfection treatment, a pilot scale study using finished water that has gone through the entire conventional treatment process is crucial. Such a study would provide confidence in the

innovative use of RPM to improve hydraulic disinfection efficiency of SWTSs from a holistic (microbiological, chemical, and energy) perspective.

Having investigated and tentatively concluded the concerns related to potential for increased biofilm formation (Baker et al. 2020) as well as the potential concerns regarding energy requirements, we are nearer to the adoption of RPM to improve the hydraulic disinfection efficiency in terms of *BF*. The acceptance of the innovative use of RPM has the potential to significantly help SWTSs, which account for the majority of health-based water quality violations, to meet SDWA standards. Ultimately, the use of RPM in drinking water disinfection could be a valuable tool in providing safe drinking water to communities in the US and beyond.

## CHAPTER 6

### 6 POTENTIAL BIOFILM GROWTH<sup>2</sup>

#### 6.1 Introduction

In the US, and around the world, we are faced with aging infrastructure, decreasing source water quality, and limited financial resources, which pose a challenge in providing safe drinking water. In 2015, close to 21 million people in the US relied on community water systems that violated health-based quality standards as stipulated by the Safe Drinking Water Act (SDWA) (Allaire et al. 2018). Of the different violations, 37% were from Total Coliform and 36% from disinfection byproducts (DPBs). Additionally, the highest prevalence of violations occurred in small systems in rural areas (Allaire et al. 2018). On the national scale, the majority of SDWA violations are related to the disinfection stage in small drinking water treatment systems.

The most common method of drinking water disinfection worldwide is chlorination. The Environmental Protection Agency's (EPA) standard parameter for microbiological inactivation of drinking water is the "CT" (min-mg/L), which is defined as the product of the residual chlorine concentration (mg/L) and the characteristic time that the chlorine is in contact with the water (minutes). The characteristic time used in the US, as stipulated by the EPA, is 'T<sub>10</sub>', which

---

<sup>2</sup> The research presented in this chapter has been published as original research in the *Journal of American Water Works Association - Water Science* (June 2020) under the title "Random packing material in disinfection contactors: Effects on final drinking water quality" by J. L. Baker, S. K. De Long, & S. K. Venayagamoorthy. Background information and literature relevant to this chapter are presented again so that the chapter may be read as a stand-alone work.

is defined as the time for 10% of the inlet concentration to be observed at the outlet (USEPA 2003).

The hydraulic disinfection efficiency of a particular system is measured in terms of the baffling factor (*BF*). The *BF* is defined as the ratio of  $T_{10}$  to the theoretical detention time (TDT) of that system and is a numerical indicator of short-circuiting and consequential re-circulation or 'dead' zones (Wilson & Venayagamoorthy 2010). A *BF* of 1 indicates ideal plug flow conditions, whereas a *BF* less than 1 indicates the presence of short-circuiting and dead zones, or impaired hydraulic efficiency (e.g., *BF* = 0.5 is considered average and a *BF* of 0.1 is considered very poor) (USEPA 2003). In terms of health, economics, and the environment, increasing the *BF* (or  $T_{10}$ ) of a system is more favorable than increasing the concentration of chlorine used to meet the required *CT*. However, in small systems, that often use non-pressurized concrete or plastic tanks as chlorine contactors, a *BF* greater than 0.5 is difficult to achieve (CDPHE 2014).

The *Baffling Factor Guidance Manual* proposed multiple simple and cost-effective modifications and innovative technologies to improve the *BF* of contact basins for small drinking water systems (CDPHE 2014). One of the innovative technologies proposed was the use of random packing material (RPM). RPM is commonly used in different types of engineering systems including, but not limited to chemical distillation (Hanley 2011), aeration columns for volatile organic compound removal (Kavanaugh & Trussell 1980), and trickling filters for wastewater treatment (Richards & Reinhart 1986). In all of these contexts, there is two-phase flow through the RPM as opposed to single-phase flow, as would be the case in a contact basin or tank. There are many different designs of RPM, but the basic design principles include a relatively high porosity (60% or greater) and high surface area. RPM are constructed from different materials, some of which are National Sanitation Foundation Standard 61 certified, and

therefore, safe for use in drinking water systems (NSF 2016). Recently, a lab-scale study was conducted demonstrating that filling a cylindrical tank with RPM created near plug flow conditions ( $BF \sim 0.9$ ) (Barnett et al. 2014), which are ideal for chemical disinfection purposes in terms of microbe inactivation as well as reduction of disinfection byproducts (DBPs) (Wilson & Venayagamoorthy 2010).

However, the fact that water entering a chlorine contact system still contains bacteria posed a potential concern for the practical use of RPM in this context. Since RPM is designed to have a large surface area, the concern is that biofilms may grow on the RPM (an aspect that is exploited in trickling filters); biofilm growth could potentially have a negative impact on the produced water quality due to biofilm sloughing. Moreover, the presence of the exopolysaccharides in biofilms provide a partial protection against disinfection and often harbor bacterial species that are more resistant to chlorine such as *Pseudomonas aeruginosa*, an opportunistic pathogen. (Vander Wende et al. 1989). An excessive presence of biofilms would potentially be counterproductive to the disinfection process and negatively affect the produced bulk water quality. This study sought to address this concern. Since biofilms are ubiquitous throughout water treatment and distribution systems (Hou et al. 2018), and yet the final water is typically still safe for consumption at the tap due to the chlorine residual, we hypothesized that biofilms: (1) would likely form, but (2) would not negatively affect the biological quality of the water produced. Addressing this concern supports the continued investigation of RPM use in chlorine contact systems to improve the hydraulic disinfection efficiency for small drinking water treatment systems.

## 6.2 Materials and Methods

### 6.2.1 Experimental configuration

In order to mimic the bacteriological quality of the water entering a chlorine contact system, a raw water source from College Lake in Fort Collins, Colorado (1 gpm) was split with industrial treated water in the Environmental Fluid Mechanics Laboratory at Colorado State University (CSU) (4 gpm). This influent was then filtered to 100 microns, and then to 50 microns, using household filters (ECP50-10 Pleated Cellulose/Polyester 50 micron Filter Cartridge (Pentek, Inc., Upper Saddle River, NJ) and 100 Micron Rating Filter String and Blanket Wound Cartridge Mfr. Model #8R20A (Parker Hannifin Corp., Cleveland, OH)), which were periodically checked and replaced when necessary. A 55-gallon cylindrical tank (inlet at the bottom and outlet at the top) was filled with 2" spherical RPM (Polypropylene (PP) NSF-61 certified with 90% void fraction (Raschig USA, INC., Arlington, TX)). At 5 gpm, this contact system has a *BF* of 0.94 (Barnett et al. 2014) providing 10 minutes of retention (or contact) time. According to the EPA's standards, 10 minutes is sufficient for log-4 removal of bacteria and log-3 removal of viruses (USEPA 2003). The chlorine dosage was set to 2 mg/L, and chlorine was continuously injected inline just upstream of a static mixer before the inlet of the RPM-filled tank. The experiment was operated at ambient room temperature. A schematic of the experimental set-up can be seen in *Figure 6-1*.

The rapid direct microscopic counts (DMC) was considered to assess the microbial quality of a sample, but DMC only uses a very small sample volume (~0.01 mL) (Jay, et al. 2005). Since the expected CFU of the outflow (and RPM) samples was on the order of  $10^0$  per mL, DMC was not considered an appropriate method. Adenosine Triphosphate (ATP) has been used to measure the

amount of biofilm formation in water treatment systems (Hallam, et al. 2001), however, a study by Yaginun, et al. (2014) showed that individual cells of the same species have diverse levels of ATP. Since the level of ATP has been shown to be linked to the energy level in a cell and therefore variable, it was determined to not be the best method for this study. Therefore, Heterotrophic Plate Counts (HPC) and *P. aeruginosa* counts were conducted. HPC is a broad category of bacteria often used as an indicator of the effectiveness of water treatment processes, or as an indirect indication of pathogen removal (WHO 2003). *P. aeruginosa* are commonly found in biofilms and are typically used as indicators of biofilm presence in pools and spas (Mena & Gerba 2009).

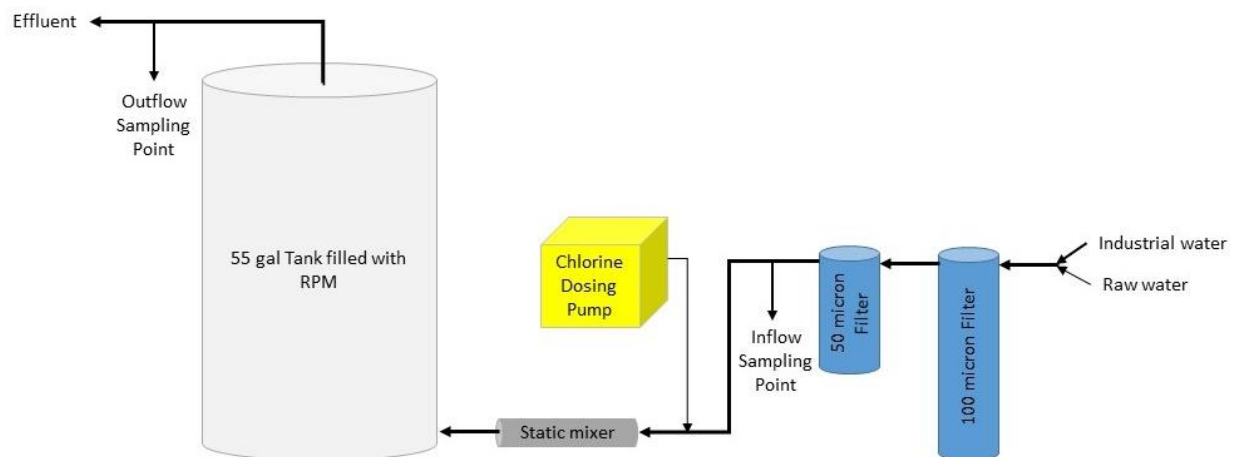


Figure 6-1: Experimental Set-up Schematic

### 6.2.2 Sample collection

A baseline was conducted by taking samples of inflow and outflow from the experimental set-up without RPM in the tank, along with samples of new RPM that had not been in the system. These baseline data were important since neither the system set-up nor the RPM were sterile at the beginning of the study. After the baseline was conducted, the 55-gallon tank was filled with RPM and the system was run continuously. Samples were collected twice a week over the course

of 64 days. Sterile water sample jars (120-mL) containing sodium thiosulfate to neutralize unreacted chlorine (or chlorine residual) were used to collect bulk water samples. For each sampling session, multiple 100-mL bulk water samples were taken first of the inflow and then of the outflow. Next, the entire system was shut down and the top of the tank was removed in order to access the RPM. Using gloves, six RPM were selected at random and each placed in a mason jar (previously sterilized by autoclaving) with 150 mL phosphate buffered solution (PBS) (Kobayashi et al. 2008). Due to the 6 inch diameter access point at the top of the 55 gallon tank used, only RPM within the top ¼ of the tank were selected in order to limit the disturbance of the RPM. Excessive movement could have led to undesired mechanical removal of any potential biofilm from the RPM surface(s). The top of the tank was replaced and the system was started up again according to the experimental configuration described above. The samples were immediately taken to the lab to be processed.

### 6.2.3 Removal of biofilm cells from RPM

Biofilm cells were removed from the RPM surface via sonication (Gagnon & Slawson 1999). All sonication was conducted in a biosafety cabinet due to the possibility of aerosolization of *P. aeruginosa*, which are considered Biosafety Level 2 organisms (FDA/CDC 2019). A 150E Sonic Dismembrator (Fisher Scientific International, Inc., Pittsburg, PA) with a 4C15 convertor and probe (Branson Ultrasonics, Danbury, CT) was used with an operating frequency of 40 kHz and set at 50% amplitude. The sonication probe was placed through the center of the RPM centered in the jar so as to not be in contact with the jar itself (*Figure 6-2*). A sonication protocol was tested for 0.5, 1, 2, and 5 minutes to determine the optimal time for removal of biofilm from the RPM. From the trial, 2 minutes was determined to be sufficient, and therefore, each RPM sample was sonicated for 2 minutes in PBS prior to membrane filtration.

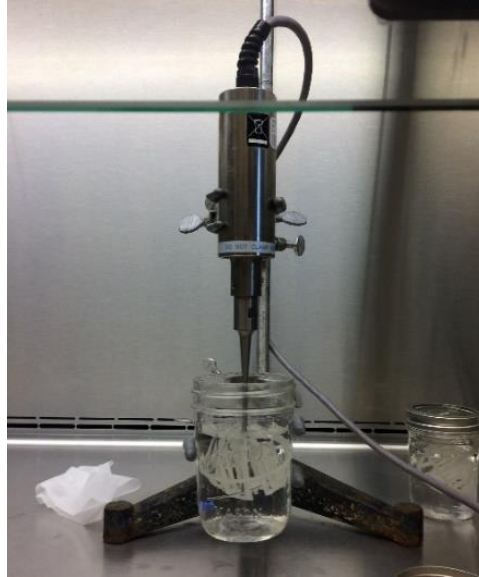


Figure 6-2: Photograph of Sonication Set-up for RPM samples

#### 6.2.4 Sample processing

HPC plates (BD Difco™ m-HPC Agar, REF 275220 (Fisher Scientific International, Inc., Pittsburg, PA)), PIA plates (BD Difco™ *Pseudomonas* Isolation Agar, REF 292710 (Fisher Scientific International, Inc., Pittsburg, PA)), and PBS (Standard Method 9050 C (**Standard Methods** 2017)) were prepared by the Environmental Health Services laboratory at CSU. For each sample run, dilutions were performed (estimated based on expected colony forming units for each sample type) for plate readings. For consistency, all samples were filtered through Fisherbrand™ Water-Testing Membrane Filters (Mixed Ester Cellulose, 0.45µm pore size, Cat # 09719555 (Fisher Scientific International, Inc., Pittsburg, PA)) (Allen et al. 2004) using the Standard Method 9215 D for HPC test and Standard Method 9213 E (with the exception of PIA agar instead of M-PA agar) for the *P. aeruginosa* test (**Standard Methods** 2017). Filter membranes for each sample type were placed on HPC plates and PIA plates (in triplicate) with one control (PBS) for HPC and PIA each. Plates were incubated at 35°C for 48 hours. Each plate was counted for colony forming units (CFU) and the data recorded. For *P. aeruginosa* counts,

only the green fluorescent colonies were counted under ultraviolet (UV) light (380nm) (King et al. 1954; WHO 2004).

### 6.2.5 Data analysis

All plate counts were converted to the CFU/mL. CFU counts for RPM were converted from CFU/RPM to CFU/mL based upon the volumetric dimensions of the RPM themselves to be comparable to bulk water counts. One RPM unit occupies a volume of 68 mL (4.19 in<sup>2</sup>) resulting in a conversion factor of 0.0146. The data were analyzed by multiple *t*-tests using Microsoft Excel at a significance level of  $p < 0.05$ .

## 6.3 Results & Discussion

### 6.3.1 HPC results

The countable HPC data are plotted on a logarithmic scale shown in *Figure 6-3*. Average inflow HPC counts were relatively stable on the order of  $10^3$  CFU/mL, which is above the EPA's recommended standard of 500CFU/mL (USEPA 2019) and typical of surface water that has gone through the coagulation, flocculation, sedimentation, and filtration steps of a conventional drinking water treatment system (Hou et al. 2018). Average HPC counts were also relatively stable over time for outflow and RPM ranging on the order of  $10^0 - 10^1$  CFU/mL and  $10^{-1} - 10^1$  CFU/mL respectively. Both the outflow and RPM values were well below the EPA's recommendation.

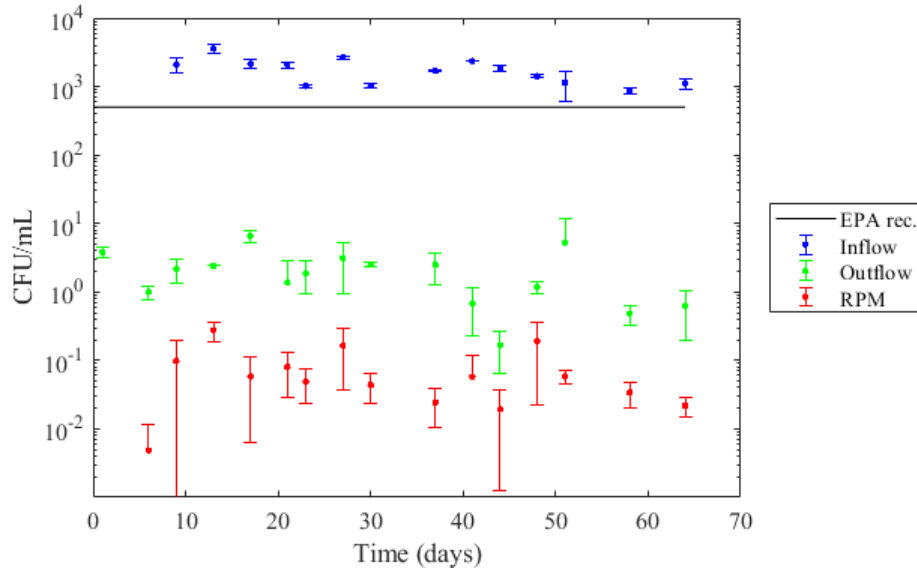


Figure 6-3: Average heterotrophic plate counts (HPC) with standard deviation error bars for bulk water inflow and outflow and randomly selected RPM surface

### 6.3.2 Pseudomonas results

The countable *P. aeruginosa* data are plotted on a logarithmic scale shown in Figure 6-4.

Compared to HPC, average inflow *P. aeruginosa* counts decreased over time, starting on the order of  $10^3$  CFU/mL and decreasing to  $10^1$  CFU/mL. Similarly, average outflow *P. aeruginosa* counts also decreased over time from the order of  $10^1$  to  $10^{-1}$  CFU/mL. However, similar to HPC, *P. aeruginosa* counts from the RPM were relatively stable ranging on the order of  $10^0$  –  $10^1$  CFU/mL. It should be noted that there is no EPA recommendation for *P. aeruginosa* for drinking water, but it was monitored here due to the focus on biofilm formation.

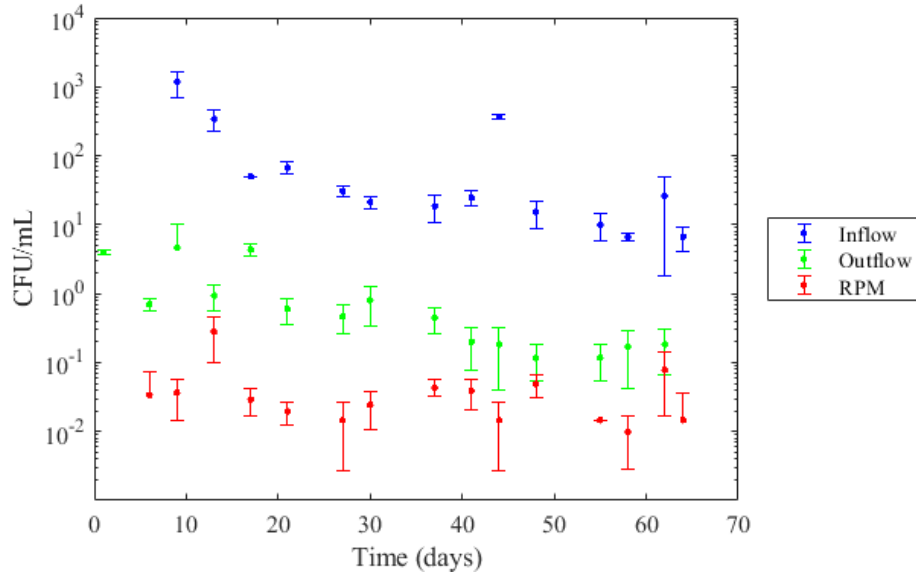


Figure 6-4: Average *Pseudomonas* plate counts (PIA) with standard deviation error bars for bulk water inflow and outflow and randomly selected RPM surface

### 6.3.3 Inactivation results

The *t*-tests showed that the chlorination treatment was effective in that there was a significant difference in HPC and *P. aeruginosa* counts between inflow and outflow (*p*-values < 0.05) over the entire 64-day study. Percent inactivation ranged from 99.54-99.99% for HPC and from 91.33-99.95% for *P. aeruginosa* as seen in Figure 4. The median percent removal for HPC was 99.9% (log-3 removal) and 99.0% (log-2 removal) for *P. aeruginosa* as seen in Figure 6-5.

There are a few anomalous *P. aeruginosa* data points, however only one (inactivation of 91%) is statistically an outlier using the Interquartile Rule for Outliers (See Table 6-1). There was no correlation between the outflow outlier and the inflow (e.g. no spike in *P. aeruginosa* counts), and thus, the reason for the lower inactivation is unknown. Given that *P. aeruginosa* is not a regulated parameter for drinking water and inactivation was still above 90% (log-1 removal), the authors do not consider this data point a major cause for concern.

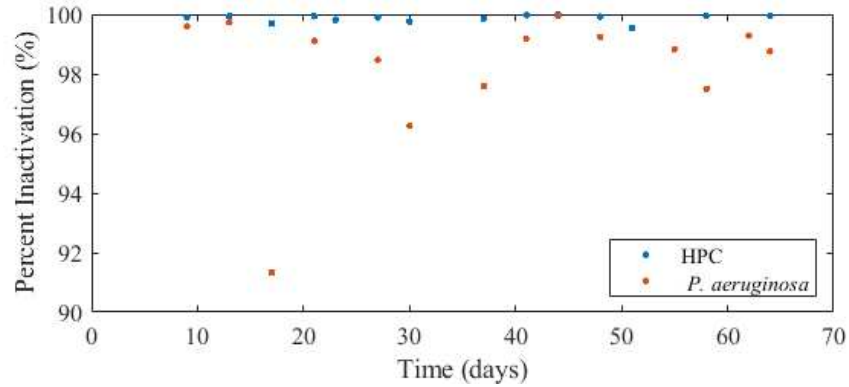


Figure 6-5: Percent of inactivation of heterotrophic and *Pseudomonas* bacteria based upon average counts

Table 6-1: Percent Inactivation and Outlier Results

Day of Experiment	HPC		PIA	
	Percent Inactivation	Outlier	Percent Inactivation	Outlier
0 (Baseline)	99.93%	FALSE	99.15%	FALSE
9	99.90%	FALSE	99.61%	FALSE
13	99.93%	FALSE	99.73%	FALSE
17	99.69%	TRUE	91.33%	TRUE
21	99.93%	FALSE	99.11%	FALSE
23	99.82%	FALSE	N/A	N/A
27	99.88%	FALSE	98.48%	FALSE
30	99.76%	FALSE	96.25%	FALSE
37	99.85%	FALSE	97.59%	FALSE
41	99.97%	FALSE	99.19%	FALSE
44	99.99%	FALSE	99.95%	FALSE
48	99.92%	FALSE	99.24%	FALSE
51	99.54%	TRUE	N/A	N/A
55	N/A	N/A	98.83%	FALSE
58	99.94%	FALSE	97.50%	FALSE
62	N/A	N/A	99.29%	FALSE
64	99.94%	FALSE	98.75%	FALSE

\*Note: Data that were either too numerous to count (TNTC) or did not pass quality control are not reported.

#### 6.3.4 Visual results

Some residue was visible on the membrane filters from the sonicated RPM samples towards the end of the experiment seen in *Figure 6-6*. However, no residue was visible on filters from bulk water samples. According to the manufacturer, scaling of the RPM is inevitable and primarily depends on the water quality, including the amount of calcium, iron, magnesium, etc. (RTJ 2019).

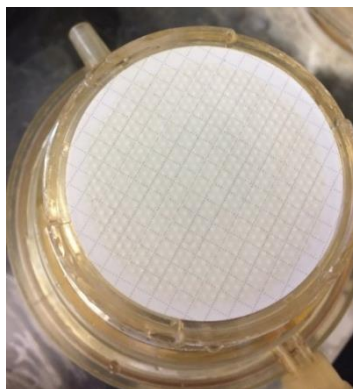


*Figure 6-6: Photograph of residue on membrane filter from a sonicated RPM sample towards the end of the study*

Additionally, random rust-colored discoloration of the RPM was observed (*Figure 6-7*).

Considering the rust color, the discoloration was most likely the result of iron reacting with the chlorine residual. In a conventional drinking water treatment plant, a surface water source would first go through coagulation, flocculation, and sedimentation before filtration, thereby removing a greater amount of in/organic compounds. Since the water used in this study was only filtered in order to mimic the biological quality of water entering a chlorine contact tank, any discoloration due to chemical reactions may not be representative of a real system. The measurement and determination of any non-biological fouling was beyond the scope of this research due to the quality of the water used. A pilot or case study using an influent that has gone through the entire conventional treatment process would be needed to investigate this further.



Figure 6-7: Before (left) and after (right) photographs of 2" RPM used in experiment

### 6.3.5 Statistical analysis results

In order to evaluate the potential biofilm growth over long-term operation, it was important to look for changes over time. The null hypothesis being no change in the difference between the inflow and outflow over time. The results of the *t*-tests can be found in *Table 6-2* (HPC) and *Table 6-3* (PIA). As compared to the baseline (new RPM), the statistical analysis indicated that there was no significant growth of biofilm on the RPM over the course of the 64-day study (*p*-values > 0.05). The fact that biofilms are ubiquitous throughout water treatment systems yet biofilm growth was not statistically significant herein was an interesting finding. The added turbulence caused by the presence of RPM may have helped prevent significant biofilm growth on the RPM. Further studies would be needed to investigate the mitigation of biofilm growth (e.g., by varying turbulence and shear forces). Additionally, over the course of 64 days there was no significant difference of HPC and *P. aeruginosa* in the inflow (*p*-values > 0.05) nor the outflow (*p*-values > 0.05). The treatment system can therefore be considered to be at a steady state throughout the study.

Table 6-2: Median HPC counts (CFU/mL) and t-test results <sup>a</sup>

Day of Experiment	Inflow		Outflow		RPM		Overall Treatment
	MEDIAN	t-test <sup>b</sup>	MEDIAN	t-test <sup>b</sup>	MEDIAN	t-test <sup>b</sup>	t-test <sup>c</sup>
0 (Baseline)	1010	1.000	0.4	1.000	0.07	1.000	0.004
1	N/A	N/A	3.4	0.026	N/A	N/A	N/A
6	N/A	N/A	9	0.128	0	0.382	N/A
9	2300	0.075	1.9	0.610	0.04	0.446	0.014
13	3600	0.116	2.4	N/A	0.28	0.606	N/A
17	2260	0.015	6.3	0.027	0.03	0.418	0.005
21	2120	0.006	0.4	0.372	0.08	0.433	0.003
23	1030	0.764	1.9	0.448	0.06	0.411	0.001
27	2590	0.001	1.8	0.801	0.13	0.501	0.000
30	1010	0.719	2.6	0.832	0.03	0.407	0.001
37	1680	0.028	1.9	0.874	0.01	0.394	0.000
41	2370	0.008	0.65	0.083	0.03	0.418	0.000
44	1910	0.011	0.15	0.065	0.01	0.391	0.003
48	1410	0.054	1.3	0.152	0.09	0.528	0.001
51	830	0.713	0.7	0.642	0.06	0.418	0.046
58	890	0.535	0.4	0.082	0.04	0.401	0.003
64	1090	0.494	0.63	0.085	0.02	0.393	0.035

<sup>a</sup> Data that were either too numerous to count (TNTC) or did not pass quality control are not reported; green shading indicates significant difference with a p-value < 0.05

<sup>b</sup> Two Sample assuming Unequal Variances

<sup>c</sup> Paired Two Sample for Means

Since there was no significant difference in the inflow nor outflow over the course of the study, it can be inferred that there was no significant change in the difference between the inflow and outflow over the 64-day period. No significant change of bacteriological quality in the difference between the inflow and outflow suggests that the authors cannot reject the null hypothesis. Failure to reject the null hypothesis submits that there was no reduction in disinfection due to the long-term presence of RPM in the laboratory-scale chlorine contact tank.

Table 6-3: Median PIA counts (CFU/mL) and t-test results <sup>a</sup>

Day of Experiment	Inflow		Outflow		RPM		Overall Treatment
	MEDIAN	t-test <sup>b</sup>	MEDIAN	t-test <sup>b</sup>	MEDIAN	t-test <sup>b</sup>	t-test <sup>c</sup>
0 (Baseline)	35.33	1.000	0.23	1.000	0.03	1.000	0.024
1	N/A	N/A	3.95	0.013	N/A	N/A	N/A
6	N/A	N/A	0.6	0.722	0.15	1.000	N/A
9	1350	0.081	1	0.442	0.04	0.930	0.038
13	340	0.219	1.1	0.938	0.36	0.193	0.100
17	50	0.350	4.6	0.015	0.03	0.649	0.000
21	60	0.101	0.6	0.602	0.01	0.101	0.010
27	28	0.598	0.5	0.457	0.01	0.134	0.007
30	22	0.263	0.7	0.882	0.01	0.438	0.009
37	20	0.213	0.4	0.441	0.04	0.387	0.045
41	24	0.353	0.2	0.268	0.04	0.751	0.013
44	364	0.000	0.2	0.259	0.01	0.134	0.001
48	18	0.158	0.1	0.232	0.04	0.379	0.044
55	12	0.111	0.1	0.232	0.01	0.057	0.041
58	6	0.099	0.2	0.252	0.01	0.024	0.005
62	12	0.608	0.1	0.260	0.06	0.418	0.134
64	6	0.095	0.05	0.218	0	0.313	0.034

<sup>a</sup> Data that were either too numerous to count (TNTC) or did not pass quality control are not reported; green shading indicates significant difference with a p-value < 0.05

<sup>b</sup> Two Sample assuming Unequal Variances

<sup>c</sup> Paired Two Sample for Means

## 6.4 Conclusions

The results of this study show that biofilm growth on the surface of RPM over 64 days in a lab-scale chlorine contact system could be considered negligible, and the presence of RPM does not negatively impact the bacteriological quality of the water produced. While viable but not culturable (VBNC) bacteria should also be considered (Chen et al. 2018), the authors conclude that biofilm growth on RPM in chlorine contact systems should not be a major concern, and the

hypothesis that chlorine residual would protect the final water produced held true at the laboratory-scale.

A pilot scale study using finished water that has gone through the entire conventional treatment process (coagulation, flocculation, sedimentation, and sand filtration) is the next step in order to promote the adoption of the use of RPM in drinking water disinfection treatment from a bacteriological perspective. Visualization using a Scanning Electron Microscope could be conducted as an additional method check for growth of biofilms on the RPM in future studies. Further, while the biological analyses used herein focused on culturable bacteria, it is suggested that VBNC bacteria also be examined. Other methods recommended to monitor for biofilm growth on the RPM include ATP analyses or molecular methods targeting DNA or RNA.

Other aspects of the use of RPM in contact basins including energy requirements (in terms of pumping) as well as the chemical aspects including the formation of DPBs require further investigation. With practical concerns related to potential for increased biofilm formation addressed, we are one step closer to the adoption of the innovative use of RPM to improve the hydraulic disinfection efficiency in terms of *BF*. The adoption of use of RPM has the potential to significantly aid small water systems, which account for the majority of health-based water quality violations, to meet SDWA standards. Ultimately, the use of RPM in drinking water disinfection could help provide safe drinking water to communities throughout the US and beyond.

## CHAPTER 7

### 7 SUMMARY & CONCLUSIONS

#### 7.1 Summary of Investigation

In this dissertation, an in-depth investigation of how the innovative application of RPM to improve the hydraulic disinfection efficiency of SWTSs was carried out via multiple laboratory-scale physical experiments. A diverse selection of measurement tools (of varying complexity) were used to collect data. The main results of the research are presented in chapters 4, 5, and 6, respectively.

In Chapter 4, a turbulent round jet flow (from a long pipe) encountering a wall ('bed') of RPM in a flume was examined using PIV. The variables investigated were the volumetric flow rate ( $Q = 5\text{-}20$  gpm) and the thickness of the RPM wall ( $L = 100 - 300\text{mm}$ ). A statistical analysis was conducted to determine the appropriate methodology of data collection with the PIV system available for use in the EFML, verified by LDA. Jets into an ambient (i.e. no RPM) were used to validate and provided a baseline. The captured velocity fields of the jets (with and without RPM) were used to determine the spreading and decay rates of the jet flow. The captured velocity fields of the flow downstream of the RPM walls were also used to determine the coefficients of drag and characterize the flow (wake) downstream of the RPM.

In Chapter 5, a 55-gal tank was filled with RPM secured in critical locations to investigate the effects on the gain in efficiency (i.e.  $BF$ ) and energy loss (i.e. head loss). Step-dose tracer tests were conducted to determine the  $BF$  and the head loss was measured using a digital manometer (in terms of bulk  $\Delta P$ ). The relative amount of RPM (25-100% filled) and the volumetric flow

rate ( $Q = 5-15$  gpm) were varied. Different configurations were also studied, including reversing the direction of flow and securing RPM near the outlet, totaling 138 trials run. The relationships between the amount of RPM, flow rate, and configuration to the increase in  $BF$  and the effect on head loss were analyzed.

In Chapter 6, a longer-term study was conducted over a 64-day period looking at the bacteriological quality of the ‘final’ water and the presence of biofilm on the surfaces of RPM in a laboratory-scale chlorine contactor. Irrigation water was mixed with industrial water and then filtered to 50 microns to mimic the bacteriological water quality of water that would be entering a disinfection contactor. The flow was dosed with chlorine (with a residual concentration of  $\sim 2$  mg/L). Water samples (influent & effluent) along with RPM samples were taken bi-weekly and assessed by HPC and PIA plate counts. The ‘final’ bacteriological water quality and the growth of biofilm on the surfaces of RPM (or lack thereof) over the course of the 64-day study were discussed in detail.

## 7.2 Conclusions and Key Findings

The following is a brief description of the main outcomes of the research presented in this dissertation:

- Turbulent jet flow from a long pipe can be ‘killed’ by obstructing its path with a highly porous material, such as RPM. Jet flow encountering RPM will decay exponentially and spread non-linearly ( $S_{RPM} \sim L^2$ ). The impact of RPM at killing a jet is high such that a thickness of RPM that is  $\sim 5$  times the diameter of the inlet pipe ( $d$ ) will reduce the maximum velocity and the Reynolds stress by more than 90% which translates to a

significant improvement of the hydraulic disinfection efficiency of a contact tank. To achieve a uniform flow downstream of an RPM wall, the thickness of the RPM wall would need to be  $\geq 15d$ . The flowrate does effect the spreading and decay rates induced by the RPM, but not significantly. The coefficients of drag for the jet flow through RPM in this study, however, are dependent on flow rate. The relationship between  $C_D$  and  $Re_{dp}$  show different regimes of flow that mimic the regimes of a uniform flow around an infinitely long cylinder. This discovery provides (potential) insight into the flow (wake-vortex) dynamics within and/or downstream of RPM to be investigated further.

- The most pressing practical concerns for the application of RPM to improve the hydraulic disinfection efficiency of SWTSs were the added head loss and potential for excessive biofilm growth. On the basis of the efficiency gain vs. energy loss study, the head loss associated with securing RPM in a tank was negligible and so no additional operational (i.e. pumping) costs are anticipated. As for the biofilm concern, it was demonstrated that the chlorine residual present in the water entering a contact tank was sufficient to prevent any significant growth of biofilm on the surfaces of RPM in a laboratory-scale chlorine contact tank. The lack of substantial biofilm throughout this study suggests that the potential for excessive biofilm growth on RPM in chlorine contact systems should not be considered a barrier for adopting the application of RPM as a viable technology to help improve the hydraulic disinfection efficiency of SWTSs.

- *Best Practice Guidelines*

*Contact System Assessment:* Before implementing the innovative use of RPM to improve the hydraulic disinfection efficiency of a SWTS, a holistic evaluation of the design/configuration of the disinfection contact system is recommended. If possible, a

tracer study would provide a baseline understanding of the current disinfection hydraulic efficiency of the particular system. A tracer study, while insightful, is not absolutely necessary. The studies presented in this research suggest that there are 3 key features of the system that should be considered in this assessment:

- 1) *Dimensions.* The necessary dimensions include the diameter of the inlet pipe ( $d$ ) and the cross-sectional area ( $A$ ) of the tank/basin over which the jet would need to spread in order to achieve uniform flow.
- 2) *The critical location(s) to secure the RPM within a tank.* RPM is best secured near the inlet. Based on the type/design of the tank/basin (i.e. cylindrical, rectangular, baffled, etc.) there may be other critical locations where RPM could be helpful (i.e. anywhere where flow separation or undesired flow contraction, and therefore acceleration, might occur). It is recommended to avoid securing RPM near a sharp outlet as the presence of RPM is counteractive to the necessary contraction of flow at this location.
- 3) *The operating range of flow rates of the SWTS.* While the effect of flow rate on the potential improvement in  $BF$  is small, depending on the desired efficiency goal it should be taken into account. From the range of volumetric flow rate(s) ( $Q$ ) and the diameter of the inlet pipe, the velocity(s) ( $U_j$ ) and Reynolds number(s) ( $Re_j$ ) of the resulting jet(s) should be calculated. At higher flow rates is when the amount of RPM becomes significant – i.e. more RPM will further improve the hydraulic disinfection efficiency. To be conservative, it is recommended that the highest flow rate be the basis for determining the (possible) desired efficiency goal.

*Determining the amount of RPM:* Once the evaluation of the disinfection contact system is complete, then the appropriate amount of RPM to achieve the improvement goal can be determined. Three levels of improvement are suggested based on the desired efficiency goal determined from the contact system assessment.

- a) *Minimal RPM Recommendation.* The minimum amount of RPM recommended is based on the thickness ( $L$ ) downstream of the jet (in the direction of mean momentum) such that  $L \approx 5d$ . Based on the laboratory-scale studies conducted, a  $\geq 90\%$  reduction in velocity and a  $\geq 250\%$  increase in  $BF$  would be expected.
- b) *Intermediate RPM Recommendation.* If this  $L \approx 5d$  is not sufficient to achieve the desired efficiency goal, then the next level would be  $L \approx 15d$ , which would expect to reduce the velocity by  $\geq 98\%$  and improve the  $BF$  by  $\geq 300\%$ .
- c) *Maximum RPM Recommendation.* The maximum amount of RPM recommended would be  $L \approx D$  where  $D$  is the relevant length scale (i.e. diameter or width) of the contact tank/basin which is equivalent to the max spread of the jet possible. At  $L \approx D$ , it is expect that the  $BF$  increase by  $\geq 350\%$ . It is not recommend that  $L > D$  as no further improvement in the hydraulic disinfection efficiency would be significant.

Once the thickness ( $L$ ) is decided, the volume of RPM can be determined based on the dimensions of the disinfection contact tank/basin.

*Securing RPM in a disinfection contactor:* The RPM should be secured in the critical location(s) determined through the contact system assessment using NSF-61 certified materials. How this is accomplished will depend of the particular system, yet it should be done in a manner where the RPM is easily accessible. This is important as the RPM will need to be checked and (likely) replaced periodically.

*Maintenance of RPM within SWTs:* In terms of maintenance, while an excessive growth of biofilm should not be considered a barrier to using RPM in disinfection contactors, since there was some discoloration and non-biological fouling towards the end of the biofilm study, it is recommended that the RPM be replaced and/or cleaned periodically. After the RPM is first implemented, it is suggested that the RPM be visually inspected after 3 months. If there is little to no build-up, and the final water quality has not diminished, then check again after another 3 months. Repeat this process until if/when any fouling becomes significant and/or the final water quality has diminished (for no other known reason). At this point it is advised that the RPM be replaced with new and/or clean RPM. How often RPM would need to be replaced will depend on the RPM used (material in particular) as well as the quality of water which can vary from one SWTs to another – even seasonally.

### 7.3 Suggestions for Future Research

The research presented in this dissertation address the practical biological and energy concerns surrounding the innovative use of RPM in disinfection contactors as well as provides fundamental insights into the spreading of a turbulent round jet through a highly porous material such as RPM. These results provide a basis for the adoption of the innovative use of RPM to improve the hydraulic disinfection efficiency of SWTs. Given the limitations of this study, several directions of future research are suggested below:

- Investigate variables that were fixed in this study in order to show scalability of the non-dimensional relations demonstrated in this dissertation research. This includes the

diameter of the jet as well as the RPM which is available in various types and sizes - differing in porosity, geometry, permeability, etc.

- In order to demonstrate proof of concept of the innovative use of RPM in a disinfection contact basin, a pilot and/or case study is necessary, requiring a utility partner. A utility partner would provide finished water that has gone through all the conventional treatment steps upstream of disinfection as well as afford an opportunity to scale to an intermediate size [~1000-2000 gallon tank(s)] as a pilot study. This study would entail comparing two identical disinfection contact tanks in parallel; one tank as is and one tank with the recommended amount of RPM secured in the critical location(s). Prior to running the pilot study, tracer tests should be conducted to determine the *BF* along with the bulk pressure drop measured for the modified and un-modified tanks. Finished water would be diverted from a live system, before the disinfection inject point, to the two parallel tanks. The diverted water should be dosed with the appropriate disinfectant concentration upstream of a static mixer before the water splits to flow through the two separate contact tanks. The final water from each contactor would then be monitored for an extended duration of time according to the required biological and chemical SDWA parameters. By comparing the drinking water parameters from the disinfection contactor with an enhanced *BF* using RPM to the un-enhanced contactor, the full effects of improving the hydraulic disinfection efficiency on the overall disinfection treatment process would be observed. A case study would involve modifying an actual disinfection contactor of a SWTS by securing the recommended amount of RPM in the critical location(s) and monitoring final water quality and operating (i.e. pumping) costs over a longer period of time. Not only would a case study demonstrate the innovative application of RPM to enhance the hydraulic disinfection

efficiency, but lessons learned would provide valuable information to include in the Best Practice Guidelines with respect to the implementation process.

- Upon further analysis of the results from the turbulent round jet flow through RPM study, it is plausible that the necessary input parameters for a CFD simulation using a  $k - \epsilon$  turbulence model could be determined (an example of an open source calculator of necessary parameter inputs for CFD programs, such as *Fluent* and/or *Flow3D*: <https://www.cfd-online.com/Tools/turbulence.php>). Assuming that the flow is fully spread over the cross-sectional area of a tank, simply defining a new ‘inlet’ at the exit of the RPM and inputting the aforementioned parameters, allows for a relatively simple way to model the flow in CFD. The results of the efficiency gain and energy loss study could be used to validate such a CFD model.
- Investigate different materials that RPM could be made of that would benefit the water treatment process – such as impregnating with silver nano-particles, since silver is a well-documented antimicrobial, and/or looking at adsorption to address other drinking water quality parameters such as pharmaceuticals and personal care products (PPCPs), etc.

## REFERENCES

- Abdel-Rahman, A. A., Chakroun, W., & Al-Fahed, S. F. (1997) LDA measurements in the turbulent round jet. *Mechanics Research Communications*. 24(3), 277-288.
- Abdel-Rahman, A. (2010). A Review of Effects of Initial and Boundary Conditions on Turbulent Jets. *WSEAS Transactions on Fluid Mechanics*. 4(5), 257-275.
- Aberle, J.; Rennie, C. D.; Admiraal, D. M.; & Muste, M. (2017). Experimental Hydraulics: Methods, Instrumentation, Data Processing and Management Vol. 2. *International Association for Hydro-Environment Engineering and Research*. CRC Press Taylor & Francis Group, London, UK.
- Adrian, R.J. & Westerweel, J. (2010) Particle Image Velocimetry. Cambridge University Press.
- Aleyasin, S. S., Tachie, M. F., & Koupriyanov, M. (2017). PIV Measurements in the Near and Intermediate Field Regions of Jets from Eight Different Nozzle Geometries. *Flow, Turbulence and Combustion*. 99, 329-351. DOI 10.1007/s10494-017-9820-3.
- Allaire, M., Wu, H., & Lall, U. (2018). National trends in drinking water quality violations. *Proceedings of the National Academy of Sciences of the United States of America*. 115(9), 2078-2083. <https://doi.org/10.1073/pnas.1719805115>.
- Allen, M. J., Edberg, S. C, & Reasoner, D. J. (2004). Heterotrophic plate count bacteria – what is their significance in drinking water?. *International Journal of Food Microbiology*. 92, 265-274.
- Aris, R. (1957). On shape factors for irregular particles – I: The steady state problem. Diffusion and reaction. *Chemical Engineering Science*. 6(6), 262-268.
- Astarita, T. (2007) Analysis of weighting windows for image deformation methods in PIV. *Experiments in Fluids*. 43(6), 859-872.
- Atkinson C., Buchmann, N.A., Amili, O., & Soria, J. (2014) On the appropriate filtering of PIV measurements of turbulent shear flows. *Experiments in Fluids*. 55(1), 1654. doi:10.1007/s00348-013-1654-8.
- Baker, M. J. (2011). *CFD simulation of flow through packed beds using the finite volume technique*. PhD Dissertation, Department of Engineering, University of Exeter, Exeter, UK.
- Baker, J. L., De Long, S. K., & Venayagamoorthy, S. K. (2020). Random packing material in disinfection contactors: Effects on final drinking water quality. *AWWA Water Science*. e1187. <http://doi.org/10.1002/aws2.1187>.

- Baker, J. L., Venayagamoorthy, S. K., & De Long, S. K. (2021). Random packing material in disinfection contactors: Effects on baffling and energy loss. *AWWA Water Science*. e1231. <https://doi.org/10.1002/aws2.1231>.
- Barnett, T.C. (2013). *Flow Dynamics and Scalar Transport in Drinking Water Contact Tanks*. Master's Thesis, Department of Civil and Environmental Engineering, Colorado State University, Fort Collins, Colorado, USA.
- Barnett, T. C.; Kattinig, J. J.; Venayagamoorthy, S. K.; & Whittaker, G. (2014). Improving the Hydraulics of Drinking Water Contact Tanks Using Random Packing Material. *Journal AWWA*, 106(2), 98-104. <https://doi.org/10.5942/jawwa.2014.106.0005>.
- Barnett, T. C. & Venayagamoorthy, S. K. (2014). Laminar and turbulent regime changes in drinking water contact tanks. *Journal AWWA*. 106(12), 561-568.
- Bird, R. B.; Stewart, W.E.; & Lightfoot, E.N. (1960). *Transport phenomena*. Wiley. 33, 34.
- Blake, F.C. (1922). The resistance of packing to fluid flow. *Transactions of American Institute of Chemical Engineers*. 14, 415-421.
- Brinkman, H.C. (1947). A calculation of viscous force exerted by a flowing fluid on a dense swarm of particles. *Applied Sciences Research*. 1, 27-33.
- Burke, S.P. & Plummer, W.B. (1928). ?? *Industrial Engineering Chemistry*. 20(11), 1125-1127.
- Cameron, S.M. (2011) PIV algorithms for open-channel turbulence research: Accuracy, resolution and limitations. *Journal of Hydro-environmental Resources*. 5(4), 247-262.
- Cannon, M. R. (1952). United States Patent Office, 2,602,651, Packing Material, Patented July 8, 1952.
- Capone, A., Soldati, A., & Romano, G. P. (2013). Mixing and entrainment in the near field of turbulent round jets. *Experiments in Fluids*. 54, 1434. <https://doi.org/10.1007/s00348-012-1434-x>.
- Carlston, J. S. (2015). *Impact of Geometric Design of Hydraulic Contact Tanks on Residence Time Distribution*. Master's Thesis, Department of Civil and Environmental Engineering, Colorado State University, Fort Collins, CO.
- Carman, P.C. (1937). Fluid flow through a granular bed. *Transactions of the Institution of Chemical Engineers*. 15, 150-156. London, UK.
- CDC, 2009. *Disinfection By-products (DBPs)*. [www.cdc.gov/biomonitoring/pdf/THM-DBP\\_FactSheet.pdf](http://www.cdc.gov/biomonitoring/pdf/THM-DBP_FactSheet.pdf) (accessed January 30, 2018).
- CDPHE. (2014). *Baffling Factor Guidance Manual – Determining Disinfection Capability and Baffling Factors for Various Types of Tanks at Small Public Water Systems*. Denver, CO:

- Colorado Department of Public Health and Environment. <https://www.colorado.gov/pacific/sites/default/files/CDPHE%20Baffling%20Factor%20Guidance%20Manual.pdf>.
- Cengel, Y.A. & Cimbala, J.M. (2006). *Fluid Mechanics; Fundamentals and Applications*. McGraw Hill.
- Chen, S.; Li, X.; Wang, Y.; Zeng, J.; Ye, C.; Li, X.; Guo, L.; Zhang, S.; & Yu, X. (2018). Induction of *Escherichia coli* into a VBNC state through chlorination/chloramination and differences in characteristics of the bacterium between states. *Water Research*. 142, 279-288. Elsevier Ltd. Kidlington, UK.
- Choo, Y. J. & Song, C. (2010) PIV measurements of turbulent jet and pool mixing produced by a steam jet discharge in a subcooled water pool. *Nuclear Engineering and Design*. 240, 2215-2224.
- Choi, Y.S.; Kim, S.J.; & Kim, D. (2008). A semi-empirical correlation for pressure drop in packed beds of spherical particles. *Transport in Porous Media*. 35, 36, 38, 178. Springer Nature, Switzerland.
- Christensen, B.E.; Trønnes, H. N.; Vollan, K., Smidsrød, O.; & Bakke, R. (1990). Biofilm removal by low concentration of hydrogen peroxide. *The Journal of Bioadhesion and Biofilm Research*. 2, 165-175.
- Chua, L. P. & Lua, A. C. (1998). Measurements of a confined jet. *Physics of Fluids*. 10, 3137-3144. <https://doi.org/10.1063/1.869841>.
- Comte-Bellot, G. & Corrsin, S. (1966). The use of a contraction to improve the isotropy of grid-generated turbulence. *Journal of Fluid Mechanics*. 25, 657-682.
- Coulson, J. M. & Richardson, J. F. (1976). *Chemical Engineering. Vol. 2, Unit Operations*. Pergamon Press. Oxford, UK.
- Crittenden, J. C.; Trussell, R. R.; Hand, D. W.; Howe, K. J.; & Tchobanoglous, G. (2012). *Water treatment principles and design 3<sup>rd</sup> Ed*. MWC, John Wiley & Sons, Inc. Hoboken, NJ.
- Dahm, W. A. & Dimotakis, P. E. (1990). Mixing at Large Schmidt Number in the Self-Similar Far Field of Turbulent Jets. *Journal of Fluid Mechanics*. 217, 299-330.  
doi: 10.1017/S002211209000073
- Darcy, H. (1856). Determination des lois d'écoulement de l'eau travers le sable. *In Les Fontaines Publiques de la Ville de Dijon*. 85, 590-594.
- Dullen, F. A. L. (1992). *Porous Media: Fluid Transport and Pore Structure*. Academic Press Inc.
- Engel, V.; Stichlmair, J.; & Giepel, W. (2001). Fluid Dynamics of Packings for Gas-Liquid Contactors. *Chemical Engineering & Technology*. 24(5), 459-462.

- Ergun, S. (1952). Flow through packed columns. *Chemical Engineering Progress*. 48, 89.
- FDA/CDC (September 19, 2019). *Antimicrobial Resistance Bank: Pseudomonas Aeruginosa*. Retrieved from <https://www.cdc.gov/drugresistance/pdf/0440-pseudomonas-aeruginosa.pdf>
- Fielder, H. E.; El-Hak, M. G.; Pollard, A.; & Bonnet (Eds.), J. P. (1998). *Control of free turbulent shear flows, In Flow Control: Fundamentals and Practices*. 335-429. Springer-Verlag, Germany.
- Flemming H. C.; Wingender J.; and Szewzyk U. (eds). (2011). Microbial Biofouling: Unsolved Problems, Insufficient Approaches, and Possible Solutions. Biofilm Highlights. *Springer Series on Biofilms*. 5, 81-109. Springer, Berlin, Heidelberg
- Gagnon, G. A. & Slawson, R. M. (1999). An efficient biofilm removal method for bacterial cells exposed to drinking water. *Journal of Microbiological Methods*. 34, 203-214. Elsevier B.V. Amsterdam, Netherlands.
- Gerrard, J. H. (1966). The mechanism of the formation region of vortices behind bluff bodies. *Journal of Fluid Mechanics*. 25(2), 401-413.
- Hallam, N. B., West, J. R., Forster, C. F., & Simms, J. (2001). The Potential for Biofilm Growth in Water Distribution Systems. *Water Research*. 35(17), 4063-4071. Elsevier Science Ltd., Great Britain.
- Handley, D. & Heggs, P.J. (1968). Momentum and heat transfer in regularly shaped packing. *Transactions of the Institution of Chemical Engineers*. 46, 251-264. London, UK.
- Hanley, B. (2011). On Packed Column Hydraulics. *American Institute of Chemical Engineers Journal*. 58(6), 1671.
- Harshit, Pugh, J. E., Klema, M, & Venayagamoorthy, S. K. (2021). *Enabling Particle Image Velocimetry in open channel flows by directing laser sheet through the free surface* [Unpublished Manuscript]. Department of Civil & Environmental Engineering, Colorado State University.
- Hicks, R.E. (1970). Pressure drop in packed beds of spheres. *Industrial and Engineering Chemistry Fundamentals*. 9, 500-502. ACS Publications.
- hiimtia (2012). Presentation 4 - Microbio Slide 37. Retrieved from SlideShare website: <https://www.slideshare.net/hiimtia/presentation4-microbio> (accessed Feb. 10, 2018)
- Hou, L.; Zhou, Q.; Wu, Q.; Gu, Q.; Sun, M.; & Zhang, J. (2018). Spatiotemporal changes in bacterial community and microbial activity in a full-scale drinking water treatment plant. *Science of the Total Environment*. 625, 449-459. Elsevier B.V. Amsterdam, Netherlands.

- Hasan, M. A. Z. & Hussain, A. K. M. F. (1985). The self-excited axisymmetric jet. *Journal of Fluid Mechanics*. 115(59).
- Hussien, H. J.; Capp, S.; & Georger, W. K. (1994). Velocity measurements in a high-Reynolds-number, momentum-conserving, axisymmetric, turbulent jet. *Journal of Fluid Mechanics*. 258, 31-35.
- Jackson, C. P. (1987). A finite-element study of the onset of vortex shedding in flow past variously shaped bodies. *Journal of Fluid Mechanics*. 182, 23-45.
- Jay, J. M., Loessner, M. J., & Golden, D. A. (2005). Culture, Microscopic, and Sampling Methods. *Modern Food Microbiology (7<sup>th</sup> ed)*. 217-240. Springer US. Boston, MA.
- Kattnig, J. J. (2014). *Use of Innovative Techniques to Optimize the Residence Time Distribution of Drinking Water Contact tanks*. Master's Thesis, Department of Civil and Environmental Engineering, Colorado State University, Fort Collins, Colorado, USA.
- Kattnig, J. J. & Venayagamoorthy, S. K., 2015. A Hybrid Approach for Increasing Baffling Factors in Contact Tanks. *Journal AWWA*. 107(12), e702-711.  
<https://doi.org/10.5942/jawwa.2015.107.0164>.
- Kavanaugh, M. C. & Trussell, R. R. (1980). Design of Aeration Towers to Strip Volatile Contaminants from Drinking Water. *Journal AWWA*. 72(12), 684.
- Kilb, B.; Lange, B.; Schaule, G.; Flemming, H. C.; & Wingender, J., 2003. Contamination of drinking water by coliforms from biofilms grown on rubber-coated valves. *International Journal of Hygiene and Environmental Health*. 206(6), 563-573.
- King, E. O; Ward, M. K.; & Raney, D. E. (1954). Two simple media for the demonstration of pyocyanin and fluorescein. *Journal of Laboratory and Clinical Medicine*. 44(2), 301-307.
- Klema, M. R.; Pirzado, A. G.; Venayagamoorthy, S. K.; & Gates, T. K. (2020). Analysis of acoustic Doppler current profiler mean velocity measurements in shallow flows. *Flow Measurement and Instrumentation*. 74, 101755.  
<https://doi.org/10.1016/j.flowmeasinst.2020.101755>.
- Kobayashi, H., Oethinger, M., Tuohy, M. J., Procop, G. W., & Bauer, T. W. (2008). *Journal of Clinical Orthopaedics and Related Research*. 467, 1360-1364. Springer US. Boston, MA.
- Kozeny, G. & Sitzber, J. (1927). Ober kapillare Leitung das Wassers im Boden. *Akad. Wiss, Wein, Math-naturw Kl*. 136, 271.
- LaVision (2019). *Pressure from PIV*. LaVision Inc. Ypsilanti, MI, USA.
- Lecordier, B. & Westerweel, J. (2004) The EUROPIV Synthetic Image Generator (S.I.G.). In: Particle Image Velocimetry: Recent Improvements. Proceedings of the EUROPIV 2

- Workshop, 31. March 31–1 April 2003, Zaragoza, Spain. Berlin, Germany. Springer-Verlag.
- Leva, M. (1959). *Fluidisation*. McGraw-Hill Book Company, New York.
- Liao, B. & Chen, S. (2015) Experimental study of flow past obstacles by PIV. *Procedia Engineering* (ICFM7). 126, 537-541.
- Liao, X., Chen, C., Wang, Z., Chang, C. H., Zhang, X., & Xie, S. (2015). Bacterial community change through drinking water treatment processes. *International Journal of Environmental Science and Technology*. 12, 1867-1874.
- MacDonald, T. F.; El-Sayer, M. S.; Mow, K.; & Dullen, F. A. L. (1979). Flow through porous media: The ergun equation revisited. *Industrial and Engineering Chemistry Fundamentals*. 18, 199-208.
- Mena, K. D. & Gerba, C. P. (2009). Risk Assessment of *Pseudomonas aeruginosa* in Water. *Reviews of Environmental Contamination and Toxicology*. 201, 71-115. Springer US. Boston, MA.
- McKeon, B.J., Comte-Bellot, G., Foss, J.F., et al. (2007) Velocity, vorticity, and Mach number. In: Tropea, C., Yarin, A.L., & Foss, J.F. (eds.) Springer Handbook of Experimental Fluid Mechanics. Berlin, Springer-Verlag. 215-472.
- McNulty, K. J. (1988). United States Patent Office, 4,731,205, *Random Packing for Fluid Contact Devices and Method of Preparing said Packing*. Patented March 15, 1988.
- Mena, K. D. & Gerba, C. P. (2009). Risk Assessment of *Pseudomonas aeruginosa* in Water. *Reviews of Environmental Contamination and Toxicology*. 201, 71-115. Springer US. Boston, MA.
- Mi, J., Kalt, P., Nathan, G. J., & Wong, C. Y. (2007). PIV measurements of a turbulent jet issuing from round sharp-edged plate. *Experiments in Fluids*. 42, 625-637. DOI 10.1007/s00348-007-0271-9
- Mohamed, M. S. & LaRue, J. C. (1990). The decay power law in grid-generated turbulence. *Journal of Fluid Mechanics*. 219, 195-214.
- Mossa, M., Meftah, M. B., De Serio, F., & Nepf, H. M. (2017). How vegetation in flows modifies the turbulent mixing and spreading of jets. *Scientific Reports*. 7, 6586. <https://www.nature.com/articles/s41598-017-05881-1>.
- Mudgal, B. V. & Pani, B. S. (1998). Flow around obstacles in plane turbulent wall jets. *Journal of Wind Engineering and Industrial Aerodynamics*. 73, 193-213.
- Mungal, M. G. & Hollingsworth, D. (1989). Organized motion in a very high Reynolds number jet. *Physics of Fluids A 1*, 1615-1623. *Scientific Reports*. 7, 6587. <http://dx.doi.org/10.1038/s41598-017-05881-1>.

- Muste, M, Aberle, J., Rennie, C. D., & Admiraal, D. M. (2017) Methods, Instrumentation, Data Processing and Management, Volume II: Instrumentation and Measurement. *CRC Press*, Taylor & Francis Group.
- National Research Council (US) Safe Drinking Water Committee (NRCSDWC). (1980). *II The Disinfection of Drinking Water, In Drinking Water and Health: Vol. 2*. Washington (DC): National Academies Press (US). < <https://www.ncbi.nlm.nih.gov/books/NBK234590/>> (accessed October 8, 2019).
- Nemec, D. & Levec, J. (2005). Flow through packed bed reactors: 1. Single-phase flow. *Chemical Engineering Science*. 60, 6947-6957. Elsevier B.V. Amsterdam, Netherlands.
- Nogueira, J., Lecuona, A., & Rodriguez, P.A. (1999) Local field correction PIV: On the increase of accuracy of digital PIV systems. *Experiments in Fluids*. 27(2), 107-116.
- NSF, 2016. (September 19, 2019). NSF/ANSI/CAN 61. Retrieved from [http://www.nsf.org.cn/en/our-services/service-by-industry/water\\_and\\_wastewater/municipal-water-treatment/nsf-ansi-standard-61](http://www.nsf.org.cn/en/our-services/service-by-industry/water_and_wastewater/municipal-water-treatment/nsf-ansi-standard-61)
- Panchapakesan, N. R. & Lumley, J. L. (1993a). Turbulence measurements in axisymmetric jets of air and helium. Part 1. Air jet. *Journal of Fluid Mechanics*. 246, 197-223.
- Papadopoulos, G. & Pitts, W. M. (1998). Scaling the Near-Field Centerline Mixing Behavior of Axisymmetric Turbulent Jets. *AIAA Journal*. 36(9), 1635-1642.
- Perderson, K. (1990). Biofilm development on stainless steel and PVC in drinking water. *Water Resources*. 24(2), 239-243. Elsevier science Ltd. Great Britain.
- Perry, R. H.; Green, D. W. (1984). *Perry's Chemical Engineers' Handbook* (6th ed.). McGraw-Hill. ISBN 978-0-07-049479-4.
- Pitts, W. M. (1991). Reynolds Number Effects on the Mixing Behavior of Axisymmetric Turbulent Jets, *Experiments in Fluids*. 11, 135-141.
- Plessis, P. J. D. & Woudberg, S. (2008). Pore-scale derivation of the ergun equation to enhance its adaptability and generalization. *Chemical Engineering Sciences*. 63, 2576-2586.
- Pope, S. B. (2000). *Turbulent Flows*. Cambridge University Press. Cambridge, UK.
- Raffel, M., Willert, C., Werely, S., & Kompenhans, J. (2007) Particle Image Velocimetry: A Practical Guide. Berlin, Springer-Verlag.
- Raschig Jaeger Technologies (RJT) (December 17, 2020). *Jaeger Tri-Paks / Hacketten: Product Bulletin 600*. Raschig GmbH – Jaeger Products, Inc. Retrieved from <http://www.raschig.de/editor/assets/RaschigRings/Literature%20-%20Random%20Packings/Info%20RASCHIG-JAEGER%20Tripacks-Hacketten-600.pdf>

- Richards, T. & Reinhart, D. (1986). Evaluation of Plastic Media in Trickling Filters. *Journal of Water Pollution Control Federation*. 58(7), 774.
- Richardson, J. F. & Zaki, W. N. (1954). *Transactions of the Institution of Chemical Engineers*. 32-35. London, UK.
- Rodriguez, I.; Lehmkuhl, O.; Chiva, J.; Borrel, R.; & Oliva, A. (2015). On the flow past a circular cylinder from critical to super-critical Reynolds numbers: Wake topology and vortex shedding. *International Journal of Heat and Fluid Flow*. 55, 91-103.
- Rogallo, R. S. (1981). Numerical experiments in homogeneous turbulence. Technical Report TM81315, NASA.
- Rogers, M. M. & Moin, P. (1987). The structure of the vorticity field in homogeneous turbulent flows. *Journal of Fluid Mechanics*. 176, 33-66.
- Roshko, A. (1961). Experiments on the flow past a circular cylinder at very high Reynolds numbers. *Journal of Fluid Mechanics*. 10, 345-356.
- Rumpf, H. & Gupte, A.R. (1971). *Chemie Ingenieur Technik*. 43, 367. WILEY-VCH Verlag GmbH & Co. KGaA, Weinheim, Germany.
- Sartory, D. P. (2004). Heterotrophic plate count monitoring of treated drinking water in the UK: a useful operational tool. *International Journal of Food Microbiology*. 92, 297-306.
- Scarano, F. & Riethmuller, M.L. (2000) Advances in iterative multigrid PIV image processing. *Experiments in Fluids*. 29(7), S51–S60.
- Sciacchitano, A. & Wieneke, B. (2016). PIV uncertainty propagation. *Measurement Science and Technology*. 27:084006. <http://dx.doi.org/10.1088/0957-0233/27/8/084006>.
- Schwartz, T.; Hoffman, S.; & Obst, U. (1998). Formation and bacterial composition of young, natural biofilms obtained from public bank-filled drinking water systems. *Water Resources*. 32(9), 2787-2797. Elsevier science Ltd. Great Britain.
- Sissom, L. E. & Pitts, D. R. (1972). *Elements of Transport Phenomena*. McGraw-Hill, Kogakush, Japan.
- Sousa, J. M. M. (2001) Turbulent flow around a surface-mounted obstacle using 2D-3C PIV. 4<sup>th</sup> International Symposium on PIV. Paper 1044. Göttingen, Germany.
- Standard Methods** (2017). *Standard Methods for the Examination of Water and Wastewater* (23<sup>rd</sup> ed.). APHA, AWWA, and WEF, Washington.
- Stanislas, M.; Okamoto, K.; Kähler, C.; & Westerweel, J. (2008). Main results of the third international PIV challenge. *Experiments in Fluids*. 45, 27-71.

- Stichlmair, J.; Bravo, J. L.; & Fair, J. R. (1989). General model for prediction of pressure drop and capacity of countercurrent gas/liquid packed columns. *Gas Separation & Purification*. 3, 19-28. Butterworth & Co Ltd. London, UK.
- Stoodley, P.; Sauer, K.; Davies, D. G.; & Costerton, J. W. (2002). Biofilms as Complex Differentiated Communities. *Annual Review of Microbiology*. 56(1), 187-209.
- Strigle, R. F. (1994). *Packed Tower Design and Applications: Random and Structured Packings*. Gulf Publishing Company. Houston, TX.
- Tanino, Y & Nepf, H. M. (2008). Laboratory Investigation of Mean Drag in a Random Array of Rigid, Emergent Cylinders. *Journal of Hydraulic Engineering*. 134(1), 34-41. [https://doi.org/10.1061/\(ASCE\)0733-9429\(2008\)134:1\(34\)](https://doi.org/10.1061/(ASCE)0733-9429(2008)134:1(34)).
- Taylor, G. (1938). The spectrum of turbulence. Proceedings of the Royal Society London. Series A-Mathematical and Physical Sciences. *The Royal Society*. 164, 476-490. doi:10.1098/rspa.1938.0032.
- Tavoularis, S. & Corrsin, S. (1981). Experiments in nearly homogeneous turbulent shear flow with a uniform mean temperature gradient. Part 1. *Journal of Fluid Mechanics*. 104, 311-347.
- Teixeira, E. & Siqueira, R. (2008). Performance Assessment of Hydraulic Efficiency Indexes. *Journal of Environmental Engineering*. 134 (10), 851-859. [https://doi.org/10.1061/\(ASCE\)0733-9372\(2008\)134:10\(851\)](https://doi.org/10.1061/(ASCE)0733-9372(2008)134:10(851)).
- USEPA (1998). *Revisions to Primacy Requirements*. EPA 63 FR 23362, Office of Water, Washington, DC.
- USEPA (1999). *Disinfection profiling and benchmarking guidance manual*. EPA 815-R-99-013, Office of Water, Washington, D.C.
- USEPA (2000). *Wastewater Technology Fact Sheet: Trickling Filters*. EPA 823-F-00-014, Office of Water, Washington.
- USEPA (2002). *EPA Air Pollution Control Cost Manual*. EPA 452-B-02-001, Office of Water, Washington. <https://www3.epa.gov/ttn/ecas/docs/cs5-2ch1.pdf>
- USEPA (2003). *LT1ESWTR Disinfection Profiling and Benchmarking Technical Guidance Manual*. EPA 816-R-03-004, Office of Water, Washington, DC.
- USEPA (2004). *Understanding the Safe Drinking Water Act*. EPA 816-F-04-030, Office of Water, Washington, DC.
- USEPA (2009). *National Primary Drinking Water Regulations*. EPA 816-F-09-004, Office of Water, Washington, DC.

- USEPA (2011). *National Characteristics of Drinking Water Systems Serving 10,000 or Fewer People*. EPA 816-R-10-022, Office of Water, Washington.
- USEPA (2019). *Drinking Water Treatability Database: Aeration and Air Stripping*. <https://iaspub.epa.gov/tdb/pages/treatment/treatmentOverview.do?treatmentProcessId=-346223903>. (accessed October 9, 2019).
- USEPA (September 11, 2019). National Primary Drinking Water Regulations. Office of Water, Washington. Retrieved from <https://www.epa.gov/ground-water-and-drinking-water/national-primary-drinking-water-regulations>
- Vander Wende, E., Characklis, W. G., & Smith, D. B. (1989). Biofilms and Bacterial Drinking Water Quality. *Water Research*. 23(10), 1313-1322.
- Van Dyke, M. (1982). *An Album of Fluid Motion*. Stanford, CA: Parabolic Press.
- Westerweel, J., Dabiri, D., & Gharib, M. (1997) The effect of a discrete window offset on the accuracy of cross-correlation analysis of digital PIV recordings. *Experiments in Fluids*. 23(1), 20-28.
- Westerweel, J., Elsinga, G.E., & Adrian, R.J. (2013) Particle image velocimetry for complex and turbulent flows. *Annual Review of Fluid Mechanics*. 45, 409-436.
- White, F. (2003). *Fluid Mechanics*. McGraw Hill.
- WHO (2003). *Heterotrophic Plate Counts and Drinking-water Safety: The Significance of HPCs for Water Quality and Human Health*. IWA Publishing. London, UK.
- WHO (2004). 11. Microbial fact sheets. *Guidelines for Drinking-water Quality (3<sup>rd</sup> ed), Volume 1 Recommendations*. Geneva, Switzerland.
- Williamson, C. H. K. (1996). Vortex dynamics in the cylinder wake. *Journal of Fluid Mechanics*. 28, 477-539.
- Williamson, C.H. K. (1996). Three-dimensional wake transition. *Journal of Fluid Mechanics*. 328, 345-407.
- Wilson, B. M. & Smith, B. L. (2013). Uncertainty on PIV mean and fluctuating velocity due to bias and random errors. *Measurement Science Technology*. 24, 035302. doi:10.1088/0957-0233/24/3/035302.
- Wilson, J.M. & Venayagamoorthy, S. K. (2010). Evaluation of Hydraulic Efficiency of Disinfection Systems Based on Residence Time Distribution Curves. *Environmental Science & Technology*. 44, 9377-9382. <https://doi.org/10.1021/es102861g>.
- Wilson, J. M. (2011). *Evaluation of Flow and Scalar Transport Characteristics of Small Public Drinking Water Disinfection System using Computational Fluid Dynamics*. Master's

Thesis, Department of Civil and Environmental Engineering, Colorado State University, Fort Collins, CO.

- Wingender, J. & Flemming, H. (2011). Biofilms in drinking water and their role as reservoirs for pathogens. *International Journal of Hygiene and Environmental Health*. 214, 417-423.
- Xu, G. & Antonia, R. A. (2002). Effect of different initial conditions on a turbulent round free jet. *Experiments in Fluids*. 33, 677-683. <http://dx.doi.org/10.1088/0957-0233/27/8/084006>.
- Yaginuma, H., Kawai, S., Tabata, K. V., Tomiyama, K., Kakizuka, A., Komatsuzaki, T., Noji, H., & Imamura, H. (2014). Diversity in ATP concentrations in a single bacterial cell population revealed by quantitative single-cell imaging. *Scientific Reports*. 4, 6522.
- Yakkatelli, R., Wu, Q., & Fleischer, A. S. (2010). A visualization study of the flow dynamics of a single round jet impinging on porous media. *Experimental Thermal and Fluid Science*. 34:1008-1015. <http://dx.doi.org/10.1016/j.expthermflusci.2010.03.004>.
- Zhang, Z. (2010) LDA Application Methods. Laser Doppler anemometry for fluid dynamics. *Experimental Fluid Mechanics*, Springer-Verlag, Berlin, Heidelberg. 272. ISBN: 978-3-642-13513-2. doi:10.1007/978-3-642-13514-9\_16.
- Ziolkowska, I. & Ziolkowska, D. (1988). Fluid flow inside packed beds. *Chemical Engineering Process*. 23, 137 – 164. [https://doi.org/10.1016/0255-2701\(88\)80012-6](https://doi.org/10.1016/0255-2701(88)80012-6).

## APPENDIX A

Supplemental Materials for Turbulent Round Jet from a Pipe through RPM Study

*Table A-1: PIV data collection parameters for the Baseline Jet*

Q (gpm)	PIV Window (x in mm)	Max Expected velocity (m/s)	Pulse/Frame Type	Frequency (Hz)	Dt ( $\mu$ s)	# of images processed consecutively	Time Interval (s)	# of cycles	Total # of images	Overall Time Period (min)
20	50-150	4.3	TP/DF	400	300	200	0.50	7	1400	2.86
	150-250	2.7	TP/DF	400	500	200	0.50	7	1400	2.86
	250-350	1.8	TP/DF	400	700	200	0.50	7	1400	2.86
	350-450	1.2	TP/DF	400	1100	200	0.50	7	1400	2.86
	450-550	1.0	SP/SF	800	300	200	0.25	7	1400	1.43
	550-650	0.8	SP/SF	600	300	200	0.33	7	1400	1.44
15	50-150	3.1	TP/DF	400	500	200	0.50	7	1400	2.86
	150-250	2.0	TP/DF	400	700	200	0.50	7	1400	2.86
	250-350	1.3	TP/DF	400	1100	200	0.50	7	1400	2.86
	350-450	0.9	SP/SF	600	300	200	0.33	7	1400	1.44
	450-550	0.7	SP/SF	500	300	200	0.40	8	1600	1.69
	550-650	0.6	SP/SF	400	300	200	0.50	9	1800	1.94
10	50-150	2.1	TP/DF	400	700	200	0.50	7	1400	2.86
	150-250	1.4	TP/DF	400	1100	200	0.50	7	1400	2.86
	250-350	0.9	SP/SF	600	300	200	0.33	7	1400	1.44
	350-450	0.6	SP/SF	400	300	200	0.50	9	1800	1.94
	450-550	0.5	SP/SF	400	300	200	0.50	9	1800	1.94
	550-650	0.4	SP/SF	300	300	200	0.67	10	2000	2.21
5	50-150	1.1	SP/SF	800	300	200	0.25	7	1400	1.43
	150-250	0.7	SP/SF	500	300	200	0.40	8	1600	1.69
	250-350	0.5	SP/SF	400	300	200	0.50	9	1800	1.94
	350-450	0.3	SP/SF	200	300	200	1.0	12	2400	2.77
	450-550	0.2	SP/SF	200	300	200	1.0	12	2400	2.77
	550-650	0.2	SP/SF	200	300	200	1.0	12	2400	2.77

Table A-2: PIV data collection parameters for  $L = 100$  mm

Q (gpm)	PIV Window (x in mm)	Max Expected velocity (m/s)	Pulse/Frame Type	Frequency (Hz)	Dt ( $\mu$ s)	# of images processed consecutively	Time Interval (s)	# of cycles	Total # of images	Overall Time Period (min)
20	150-250	0.7	SP/SF	500	300	200	0.40	8	1600	1.69
	250-350	0.4	SP/SF	300	300	200	0.67	10	2000	2.77
	350-450	0.3	SP/SF	200	300	200	1.0	12	2400	2.77
	450-550	0.2	SP/SF	200	300	200	1.0	12	2400	2.77
	550-650	0.1	SP/SF	200	300	200	1.0	12	2400	2.77
15	150-250	0.5	SP/SF	400	300	200	0.50	9	1800	1.94
	250-350	0.3	SP/SF	200	300	200	1.0	12	2400	2.77
	350-450	0.2	SP/SF	200	300	200	1.0	12	2400	2.77
	450-550	0.1	SP/SF	200	300	200	1.0	12	2400	2.77
	550-650	< 0.1	SP/SF	200	300	200	1.0	12	2400	2.77
10	150-250	0.3	SP/SF	300	300	200	0.67	10	2000	2.21
	250-350	0.2	SP/SF	200	300	200	1.0	12	2400	2.77
	350-450	0.1	SP/SF	200	300	200	1.0	12	2400	2.77
	450-550	< 0.1	SP/SF	200	300	200	1.0	12	2400	2.77
	550-650	< 0.1	SP/SF	200	300	200	1.0	12	2400	2.77
5	150-250	0.1	SP/SF	200	300	200	1.0	12	2400	2.77
	250-350	< 0.1	SP/SF	200	300	200	1.0	12	2400	2.77
	350-450	< 0.1	SP/SF	200	300	200	1.0	12	2400	2.77
	450-550	< 0.1	SP/SF	200	300	200	1.0	12	2400	2.77
	550-650	< 0.1	SP/SF	200	300	200	1.0	12	2400	2.77

Table A-3: PIV data collection parameters for  $L = 150$  mm

Q (gpm)	PIV Window (x in mm)	Max Expected velocity (m/s)	Pulse/Frame Type	Frequency (Hz)	Dt ( $\mu$ s)	# of images processed consecutively	Time Interval (s)	# of cycles	Total # of images	Overall Time Period (min)
20	200-300	0.2	SP/SF	200	300	200	1.0	12	2400	2.77
	300-400	0.1	SP/SF	200	300	200	1.0	12	2400	2.77
	400-500	< 0.1	SP/SF	200	300	200	1.0	12	2400	2.77
	500-600	< 0.1	SP/SF	200	300	200	1.0	12	2400	2.77
15	200-300	0.1	SP/SF	200	300	200	1.0	12	2400	2.77
	300-400	< 0.1	SP/SF	200	300	200	1.0	12	2400	2.77
	400-500	< 0.1	SP/SF	200	300	200	1.0	12	2400	2.77
	500-600	< 0.1	SP/SF	200	300	200	1.0	12	2400	2.77
10	200-300	< 0.1	SP/SF	200	300	200	1.0	12	2400	2.77
	300-400	< 0.1	SP/SF	200	300	200	1.0	12	2400	2.77
	400-500	< 0.1	SP/SF	200	300	200	1.0	12	2400	2.77
	500-600	< 0.1	SP/SF	200	300	200	1.0	12	2400	2.77
5	200-300	< 0.1	SP/SF	200	300	200	1.0	12	2400	2.77
	300-400	< 0.1	SP/SF	200	300	200	1.0	12	2400	2.77
	400-500	< 0.1	SP/SF	200	300	200	1.0	12	2400	2.77
	500-600	< 0.1	SP/SF	200	300	200	1.0	12	2400	2.77

Table A-4: PIV data collection parameters for  $L = 200$  mm

Q (gpm)	PIV Window (x in mm)	Max Expected velocity (m/s)	Pulse/Frame Type	Frequency (Hz)	Dt ( $\mu$ s)	# of images processed consecutively	Time Interval (s)	# of cycles	Total # of images	Overall Time Period (min)
20	250-350	< 0.1	SP/SF	200	300	200	1.0	12	2400	2.77
	350-450	< 0.1	SP/SF	200	300	200	1.0	12	2400	2.77
	450-550	< 0.1	SP/SF	200	300	200	1.0	12	2400	2.77
15	250-350	< 0.1	SP/SF	200	300	200	1.0	12	2400	2.77
	350-450	< 0.1	SP/SF	200	300	200	1.0	12	2400	2.77
	450-550	< 0.1	SP/SF	200	300	200	1.0	12	2400	2.77
10	250-350	< 0.1	SP/SF	200	300	200	1.0	12	2400	2.77
	350-450	< 0.1	SP/SF	200	300	200	1.0	12	2400	2.77
	450-550	< 0.1	SP/SF	200	300	200	1.0	12	2400	2.77
5	250-350	< 0.1	SP/SF	200	300	200	1.0	12	2400	2.77
	350-450	< 0.1	SP/SF	200	300	200	1.0	12	2400	2.77
	450-550	< 0.1	SP/SF	200	300	200	1.0	12	2400	2.77

Table A-5: PIV data collection parameters for  $L = 250$  mm

Q (gpm)	PIV Window (x in mm)	Max Expected velocity (m/s)	Pulse/Frame Type	Frequency (Hz)	Dt ( $\mu$ s)	# of images processed consecutively	Time Interval (s)	# of cycles	Total # of images	Overall Time Period (min)
20	300-400	< 0.1	SP/SF	200	300	200	1.0	12	2400	2.77
	400-500	< 0.1	SP/SF	200	300	200	1.0	12	2400	2.77
	500-600	< 0.1	SP/SF	200	300	200	1.0	12	2400	2.77
15	300-400	< 0.1	SP/SF	200	300	200	1.0	12	2400	2.77
	400-500	< 0.1	SP/SF	200	300	200	1.0	12	2400	2.77
	500-600	< 0.1	SP/SF	200	300	200	1.0	12	2400	2.77
10	300-400	< 0.1	SP/SF	200	300	200	1.0	12	2400	2.77
	400-500	< 0.1	SP/SF	200	300	200	1.0	12	2400	2.77
	500-600	< 0.1	SP/SF	200	300	200	1.0	12	2400	2.77
5	300-400	< 0.1	SP/SF	200	300	200	1.0	12	2400	2.77
	400-500	< 0.1	SP/SF	200	300	200	1.0	12	2400	2.77
	500-600	< 0.1	SP/SF	200	300	200	1.0	12	2400	2.77

Table A-6: PIV data collection parameters for  $L = 300$  mm

Q (gpm)	PIV Window (x in mm)	Max Expected velocity (m/s)	Pulse/Frame Type	Frequency (Hz)	Dt ( $\mu$ s)	# of images processed consecutively	Time Interval (s)	# of cycles	Total # of images	Overall Time Period (min)
20	350-450	< 0.1	SP/SF	200	300	200	1.0	12	2400	2.77
	450-550	< 0.1	SP/SF	200	300	200	1.0	12	2400	2.77
15	350-450	< 0.1	SP/SF	200	300	200	1.0	12	2400	2.77
	450-550	< 0.1	SP/SF	200	300	200	1.0	12	2400	2.77
10	350-450	< 0.1	SP/SF	200	300	200	1.0	12	2400	2.77
	450-550	< 0.1	SP/SF	200	300	200	1.0	12	2400	2.77
5	350-450	< 0.1	SP/SF	200	300	200	1.0	12	2400	2.77
	450-550	< 0.1	SP/SF	200	300	200	1.0	12	2400	2.77

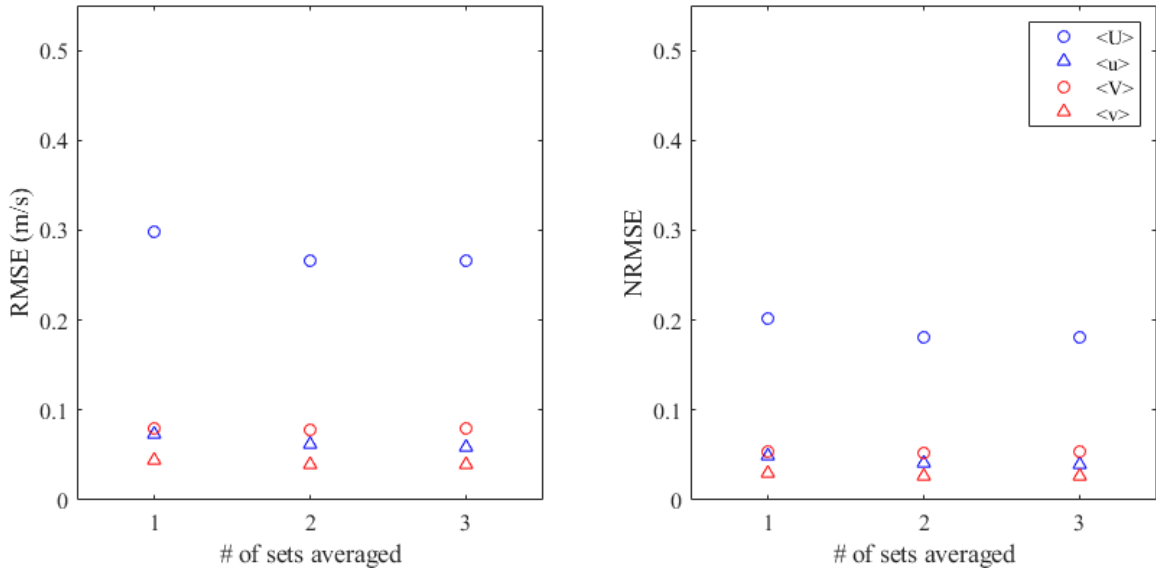


Figure A-1: RMSE and NRMSE for 3 sets of 1000 images averaged compared to the LDA measurements along the vertical profile at  $x = 98$  mm.

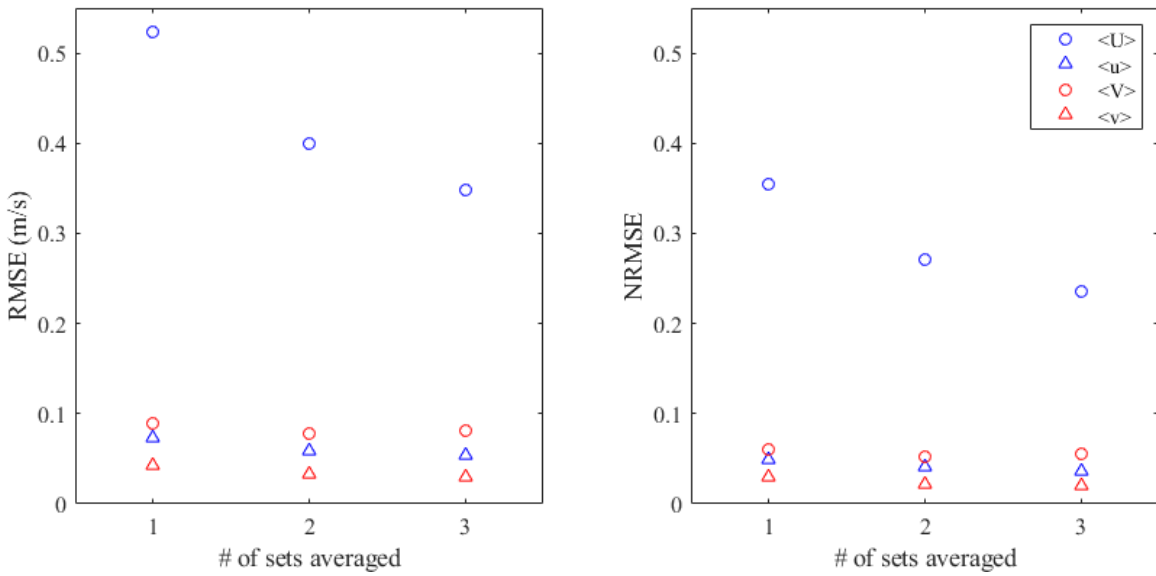


Figure A-2: RMSE and NRMSE for 3 sets of 1200 images averaged compared to the LDA measurements along the vertical profile at  $x = 98$  mm.

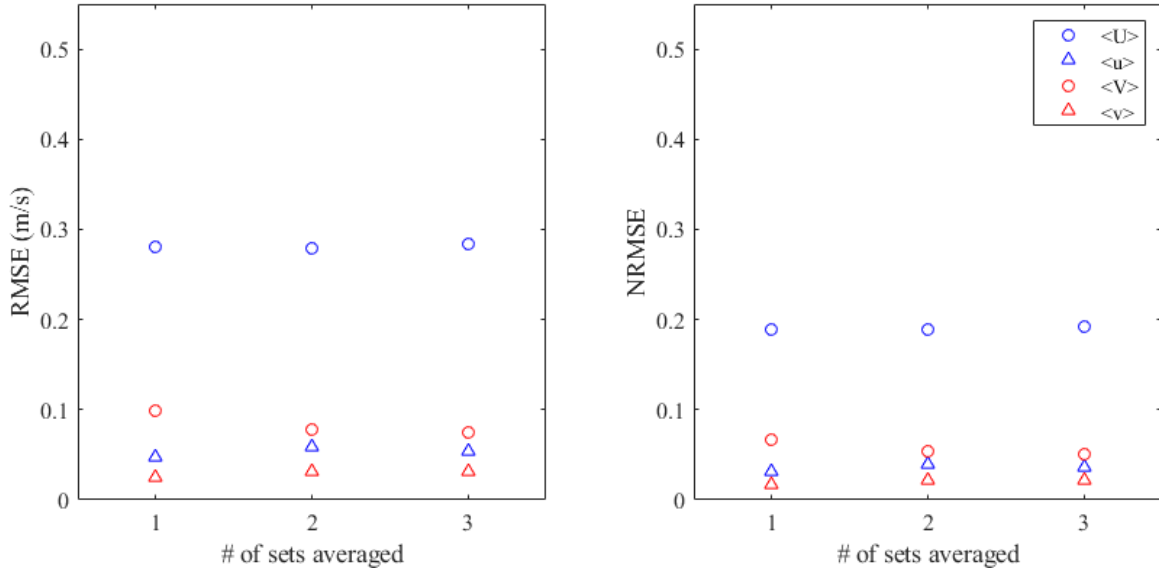


Figure A-3: RMSE and NRMSE for 3 sets of 1400 images averaged compared to the LDA measurements along the vertical profile at  $x = 98$  mm.

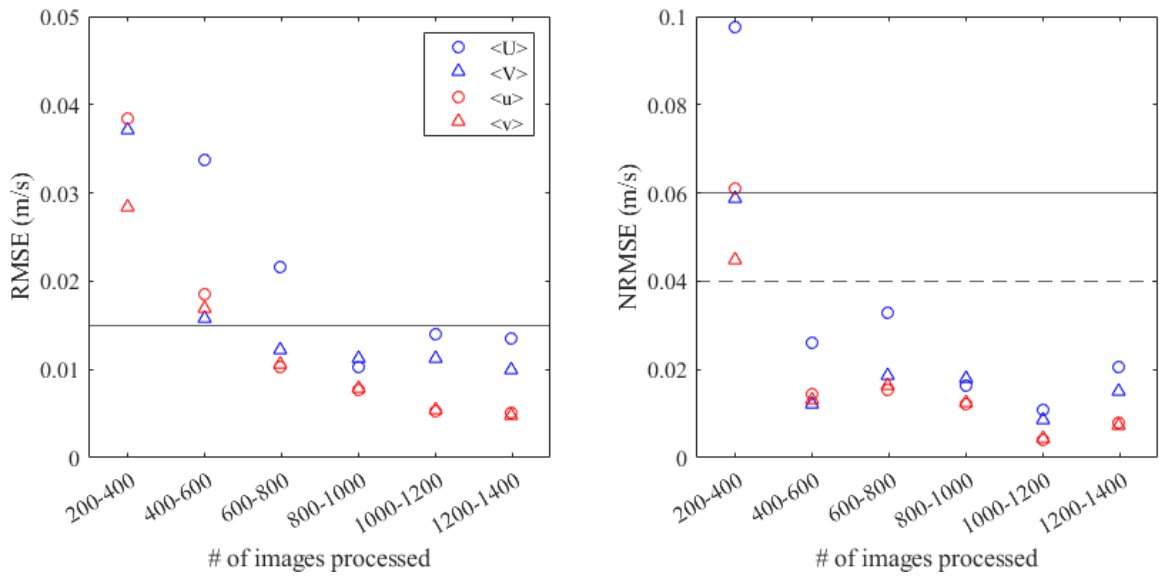


Figure A-4: RMSE and NRMSE between an increasing number of images (vector fields) of PIV measurements along the vertical profile for TP/DF at 400 Hz &  $DT = 500\mu s$ .

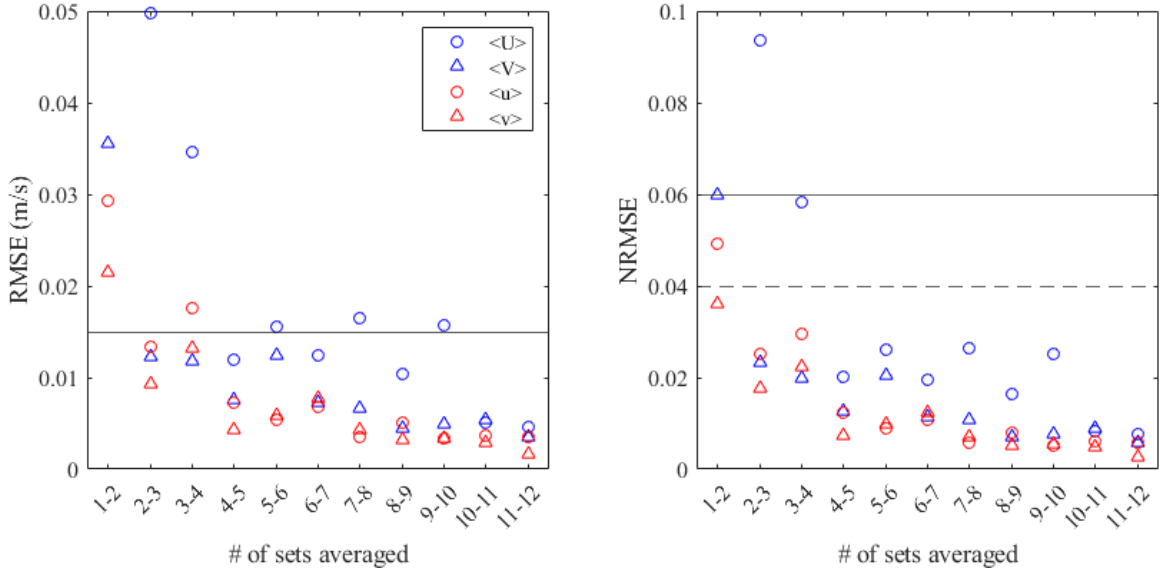


Figure A-5: RMSE and NRMSE between increasing number of sets of 200 images averaged of PIV measurements along the vertical profile for TP/DF at 400 Hz & DT = 500 $\mu$ s.

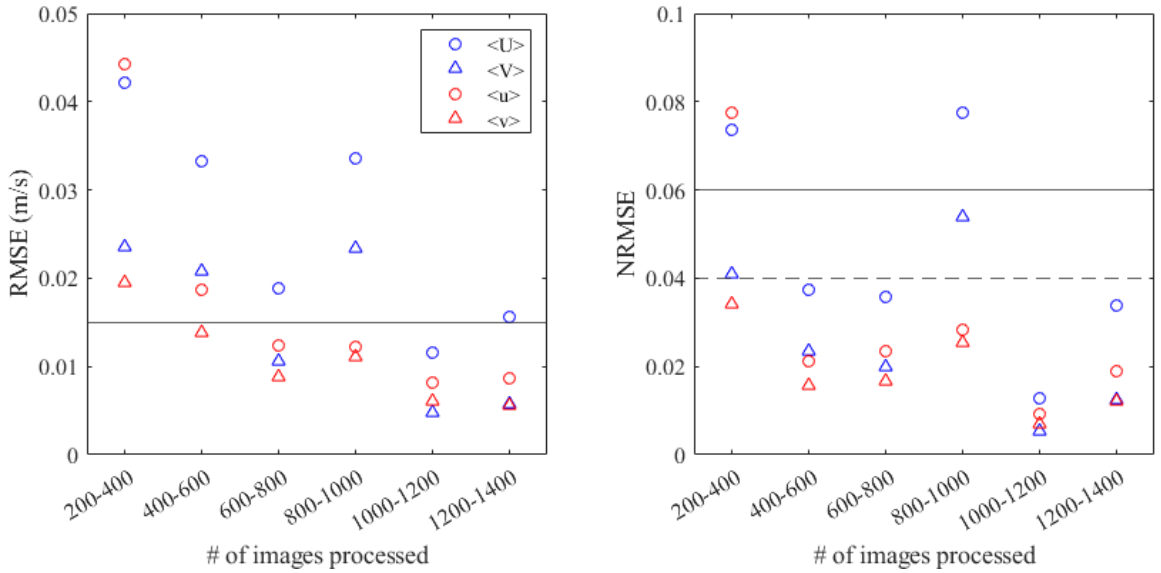


Figure A-6: RMSE and NRMSE between increasing number of images (vector fields) of PIV measurements along the vertical profile for TP/DF at 400 Hz & DT = 700 $\mu$ s.

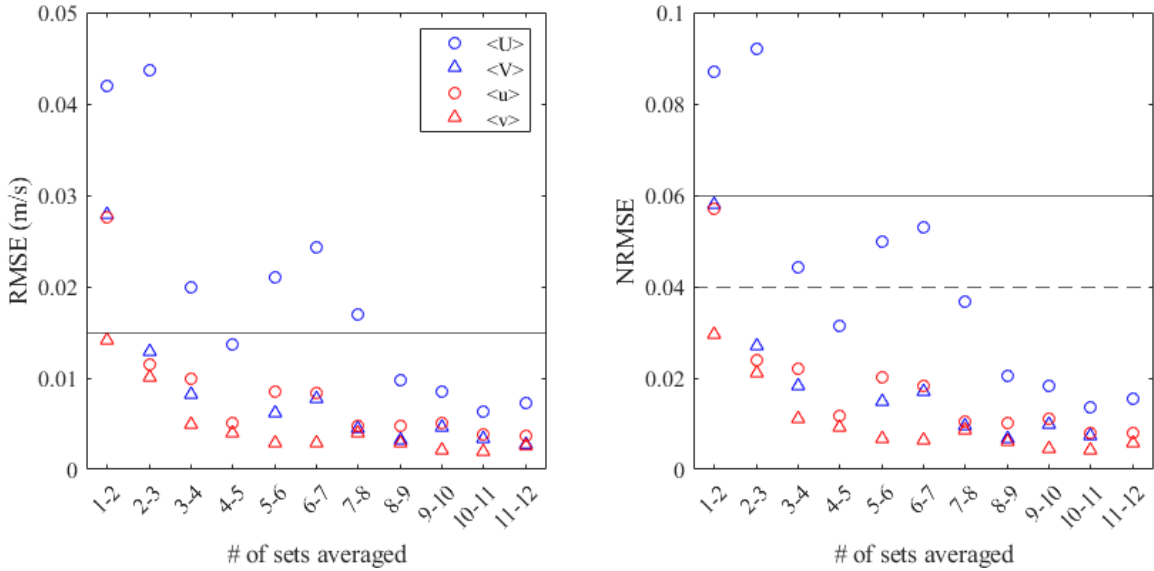


Figure A-7: RMSE and NRMSE between increasing number of sets of 200 images averaged of PIV measurements along the vertical profile for TP/DF at 400 Hz & DT = 700us.

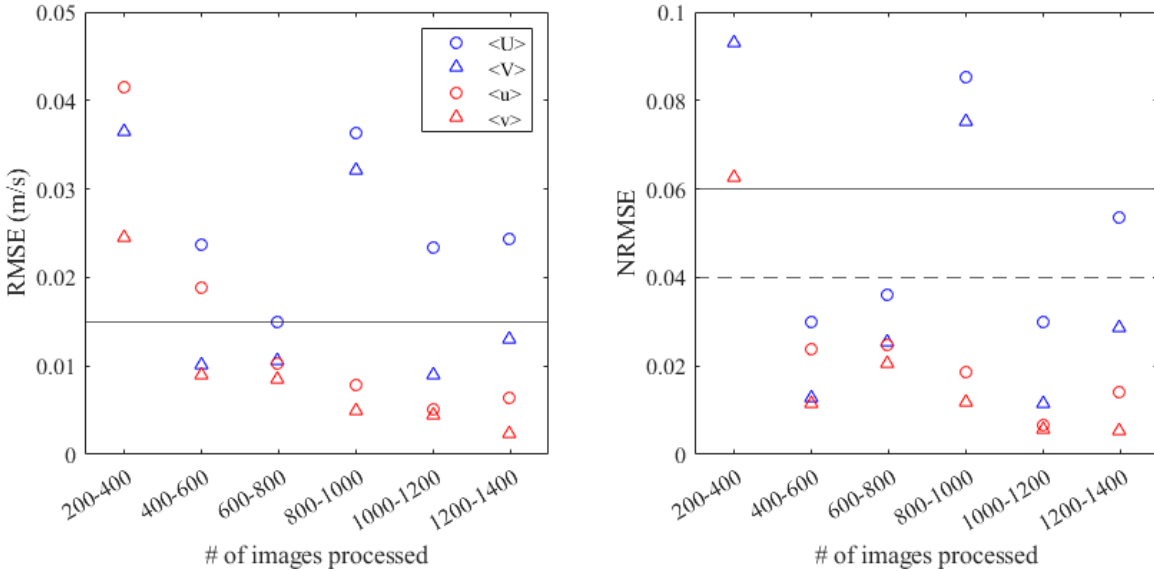


Figure A-8: RMSE and NRMSE between an increasing number of images (vector fields) of PIV measurements along the vertical profile for TP/DF at 400 Hz & DT = 1100us.

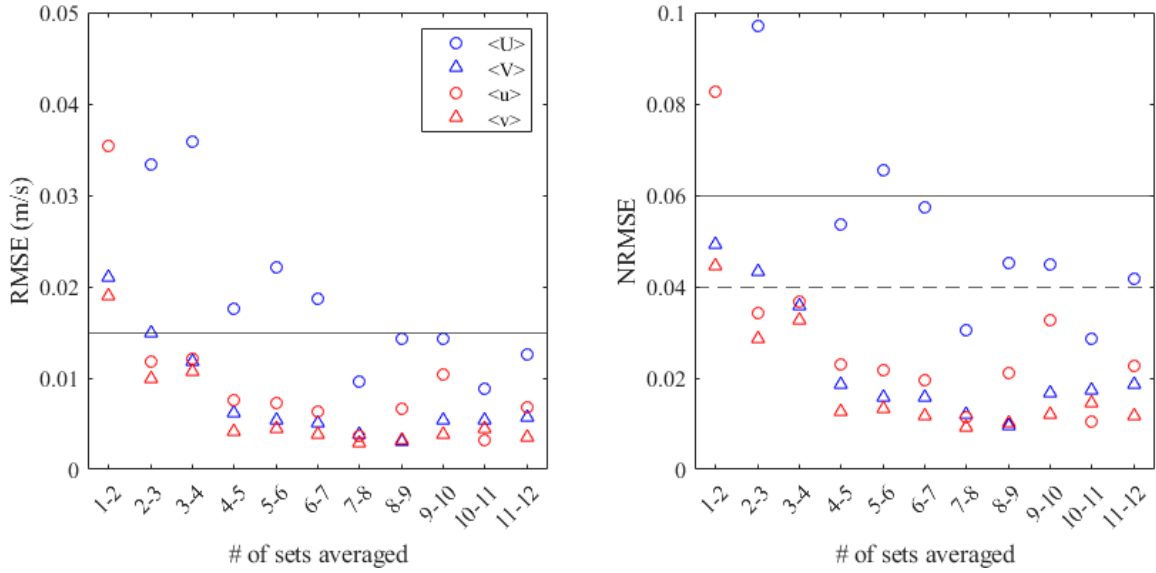


Figure A-9: RMSE and NRMSE between increasing number of sets of 200 images averaged of PIV measurements along the vertical profile for TP/DF at 400 Hz & DT = 1100us.

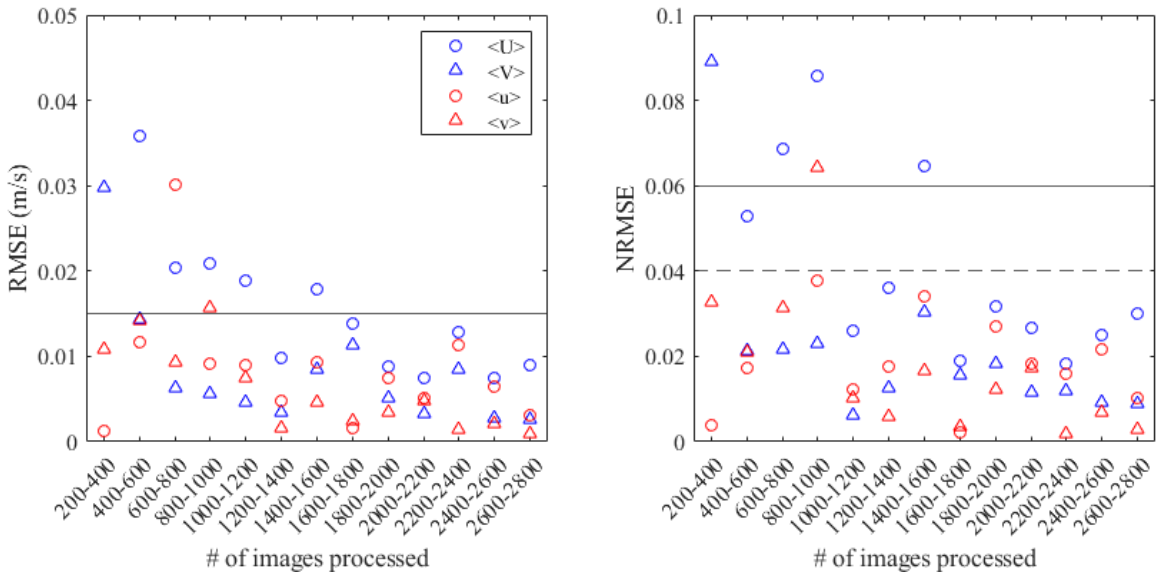


Figure A-10: RMSE and NRMSE between an increasing number of images of PIV measurements along the vertical profile for SP/SF at 800 Hz & DT = 300us.

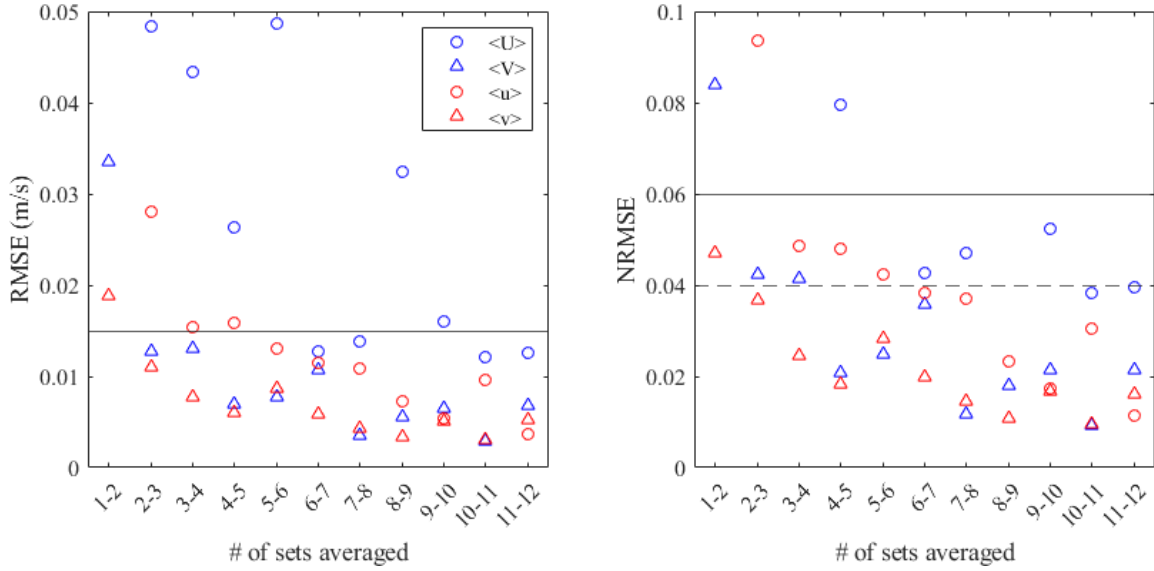


Figure A-11: RMSE and NRMSE between increasing number of sets of 200 images averaged of PIV measurements along the vertical profile for SP/SF at 800 Hz & DT = 300us.

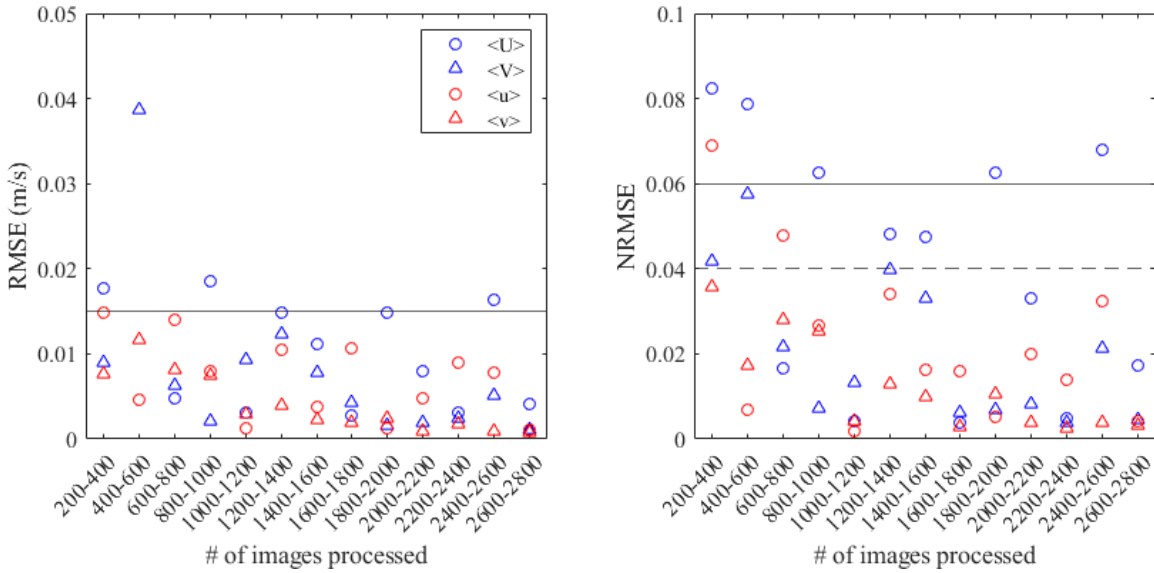


Figure A-12: RMSE and NRMSE between an increasing number of images of PIV measurements along the vertical profile for SP/SF at 600 Hz & DT = 300us.

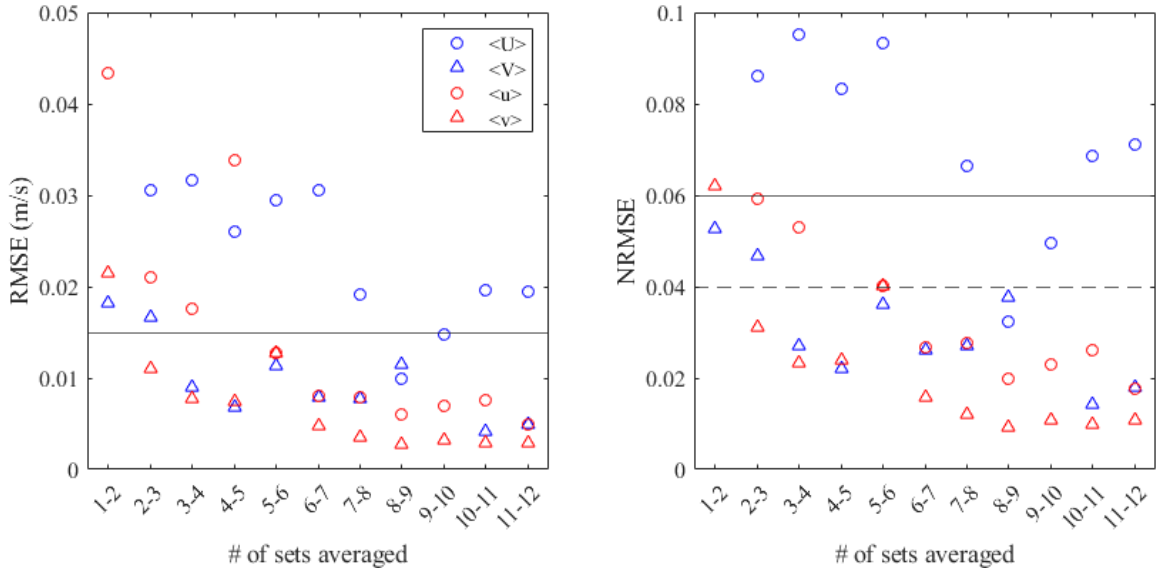


Figure A-13: RMSE and NRMSE between increasing number of sets of 200 images averaged of PIV measurements along the vertical profile for SP/SF at 600 Hz & DT = 300us.

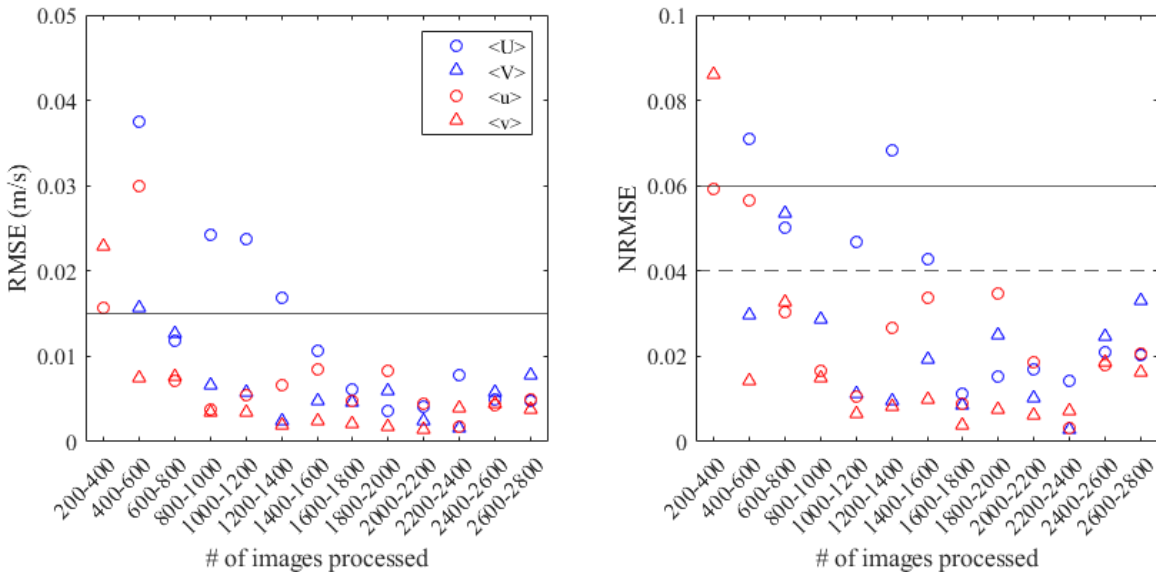


Figure A-14: RMSE and NRMSE between an increasing number of images of PIV measurements along the vertical profile for SP/SF at 500 Hz & DT = 300us.

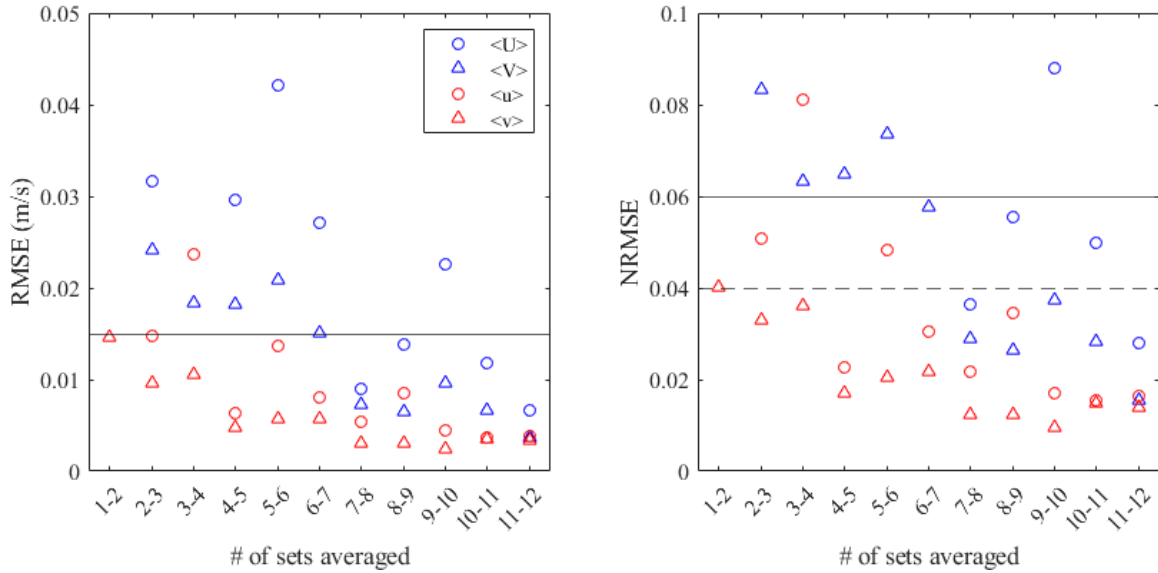


Figure A-15: RMSE and NRMSE between increasing number of sets of 200 images averaged of PIV measurements along the vertical profile for SP/SF at 500 Hz & DT = 300us.

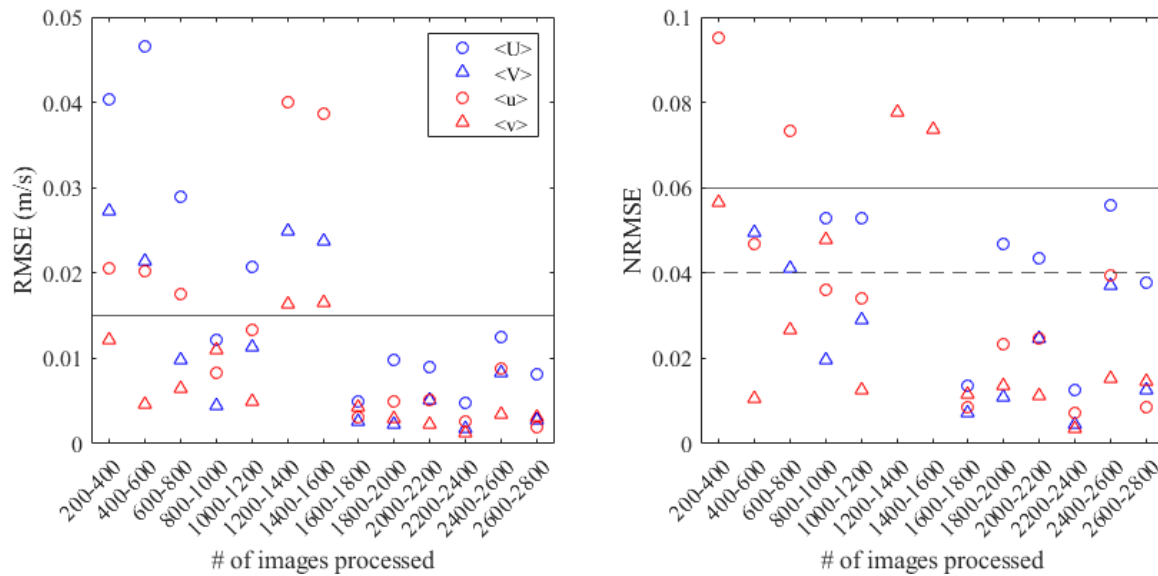


Figure A-16: RMSE and NRMSE between an increasing number of images of PIV measurements along the vertical profile for SP/SF at 400 Hz & DT = 300us.

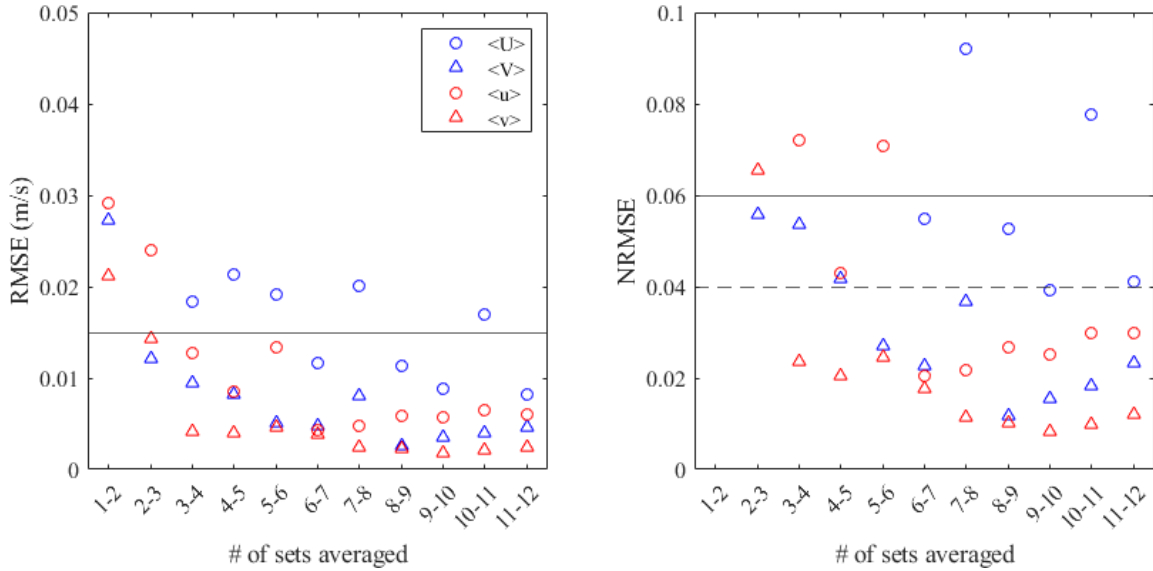


Figure A-17: RMSE and NRMSE between increasing number of sets of 200 images averaged of PIV measurements along the vertical profile for SP/SF at 400 Hz & DT = 300us.

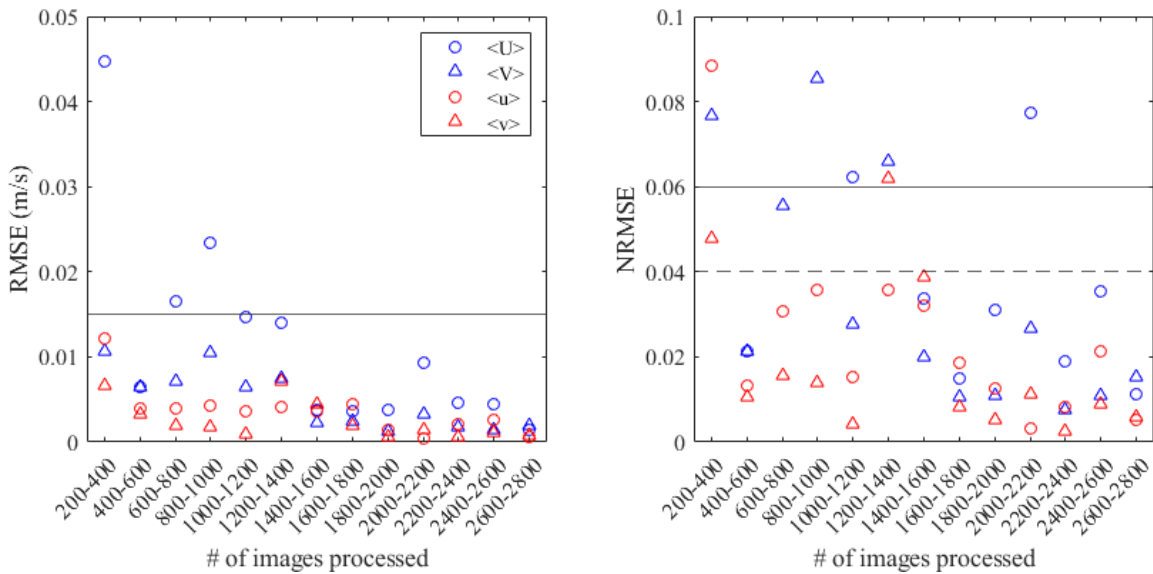


Figure A-18: RMSE and NRMSE between an increasing number of images of PIV measurements along the vertical profile for SP/SF at 300 Hz & DT = 300us.

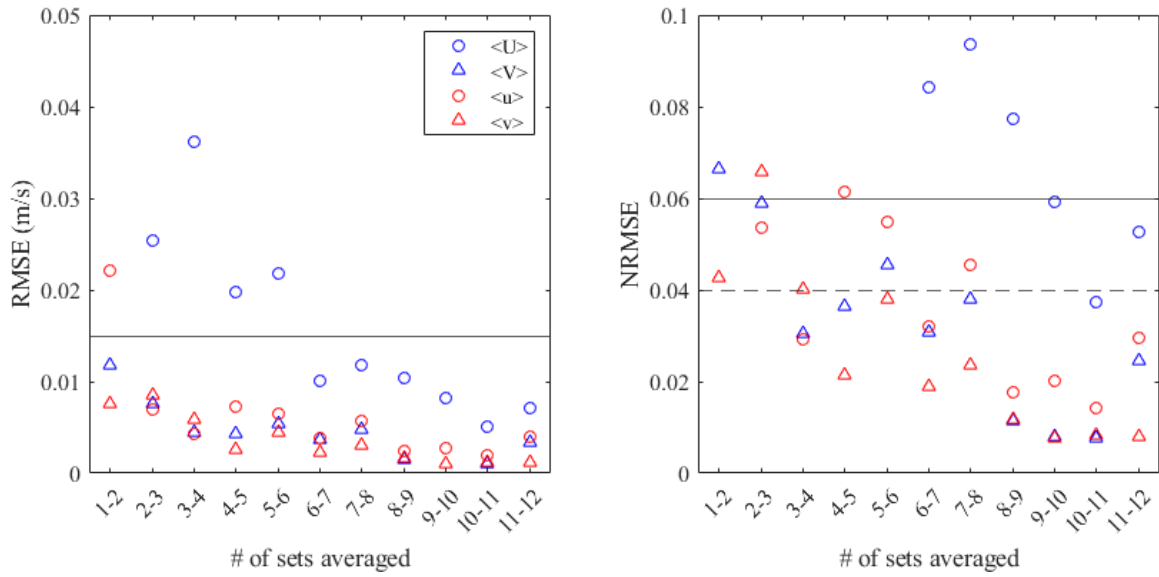


Figure A-19: RMSE and NRMSE between increasing number of sets of 200 images averaged of PIV measurements along the vertical profile for SP/SF at 300 Hz & DT = 300us.

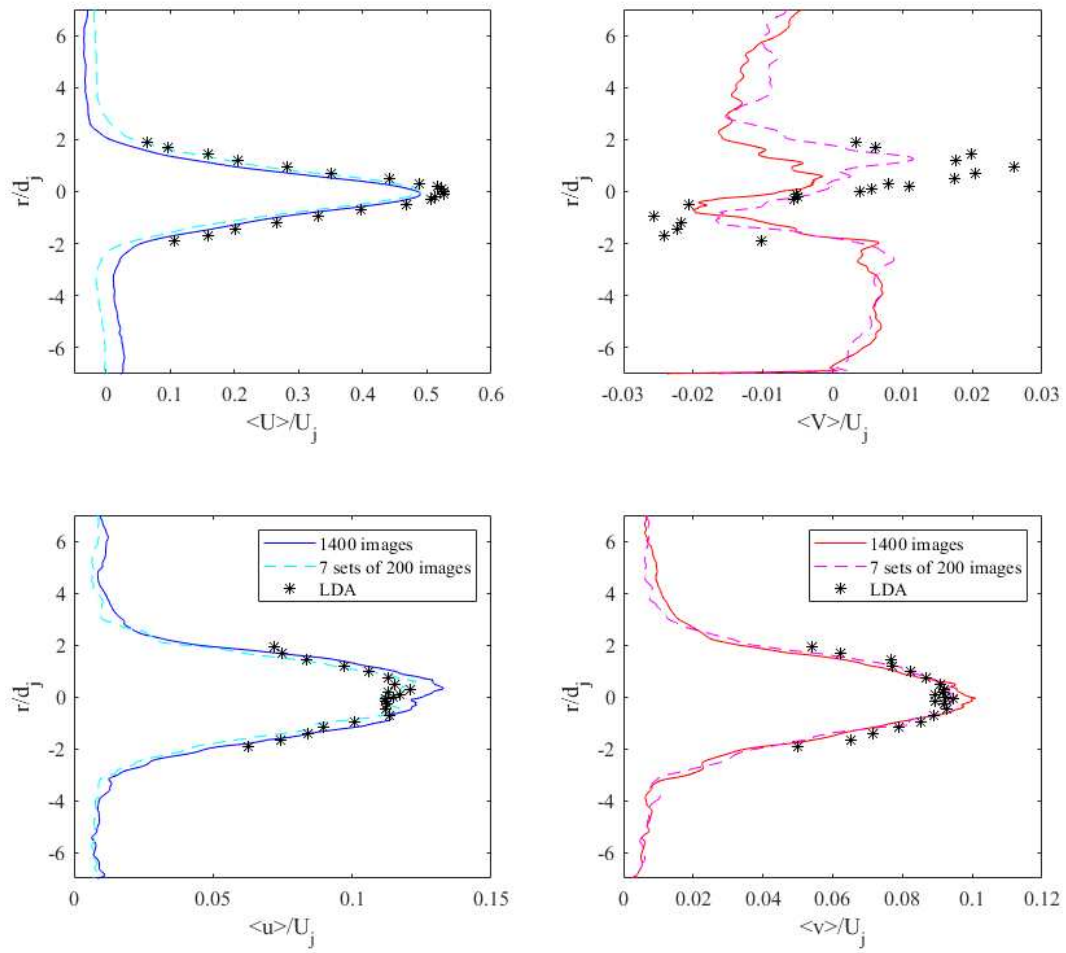


Figure A-20: Average streamwise and vertical velocity profiles for consecutive images and sets of 200 images of PIV and LDA measurements along the vertical profile for TP/DF at 400 Hz &  $DT = 500\mu s$ .

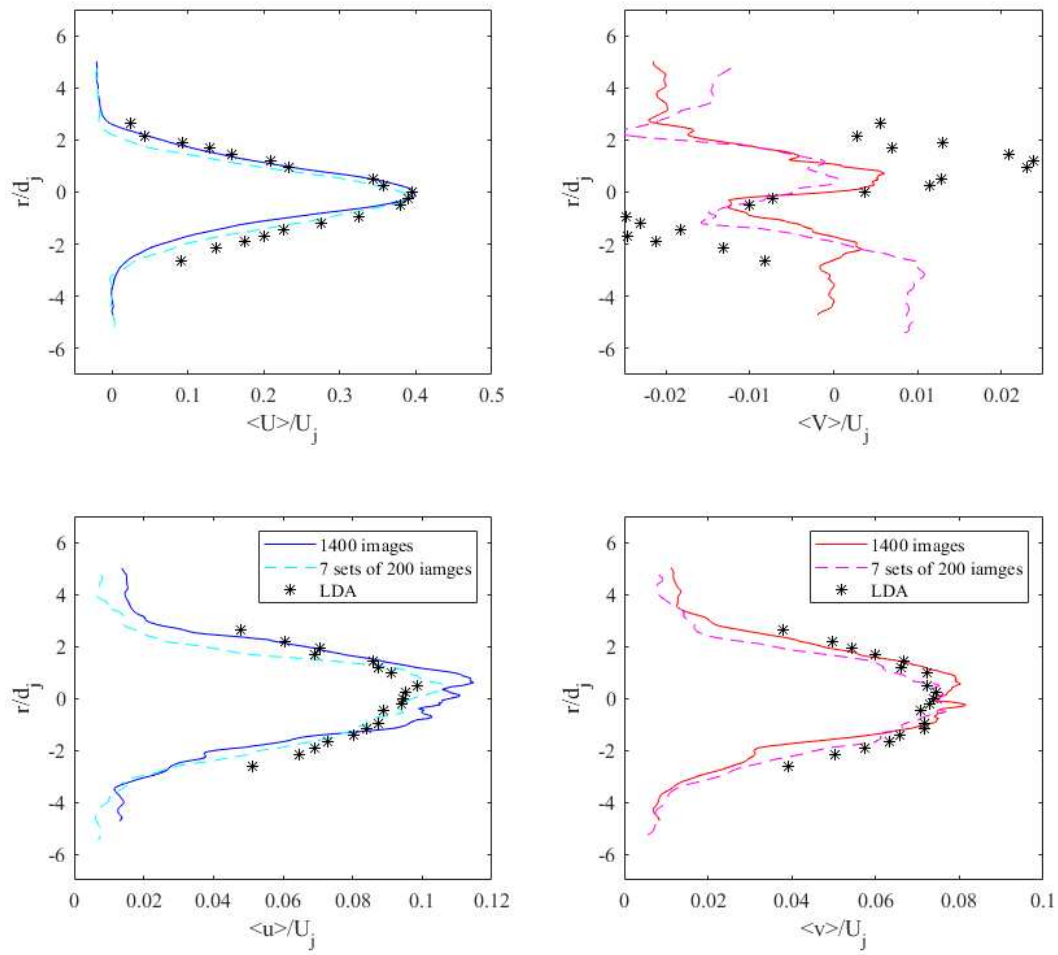


Figure A-21: Average streamwise and vertical velocity profiles for consecutive images and sets of 200 images of PIV and LDA measurements along the vertical profile for TP/DF at 400 Hz &  $DT = 700\mu s$ .

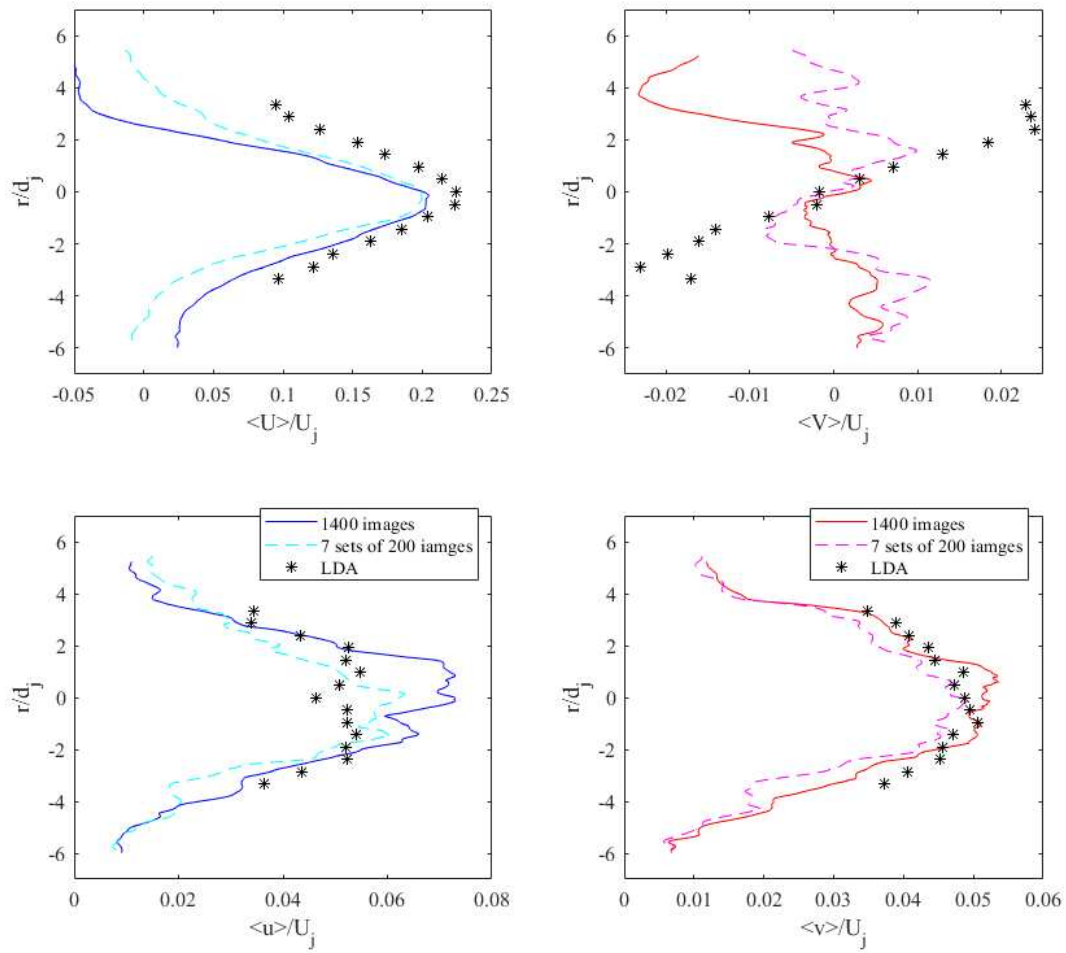


Figure A-22: Average streamwise and vertical velocity profiles for consecutive images and sets of 200 images of PIV and LDA measurements along the vertical profile for TP/DF at 400 Hz &  $DT = 1100\mu s$ .

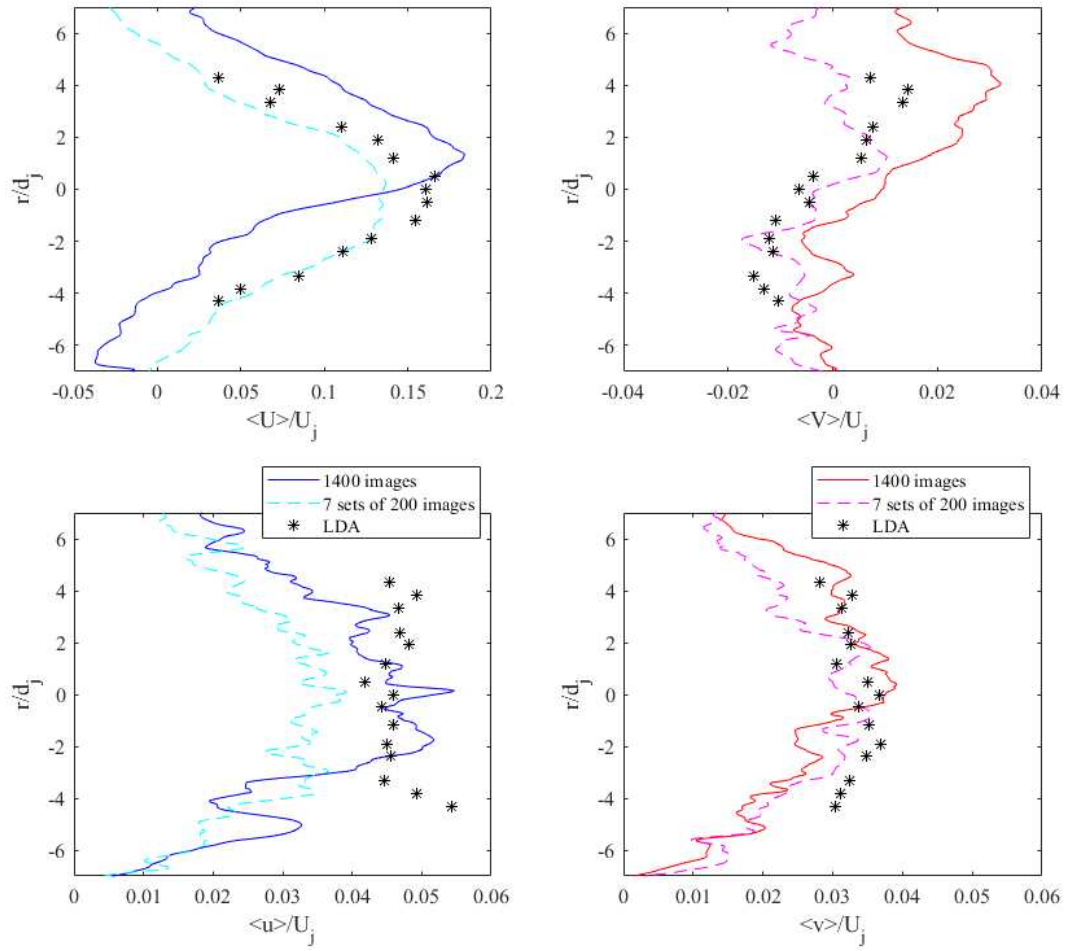


Figure A-23: Average streamwise and vertical velocity profiles for consecutive images and sets of 200 images of PIV and LDA measurements along the vertical profile for SP/SF at 600 Hz &  $DT = 300\mu s$ .

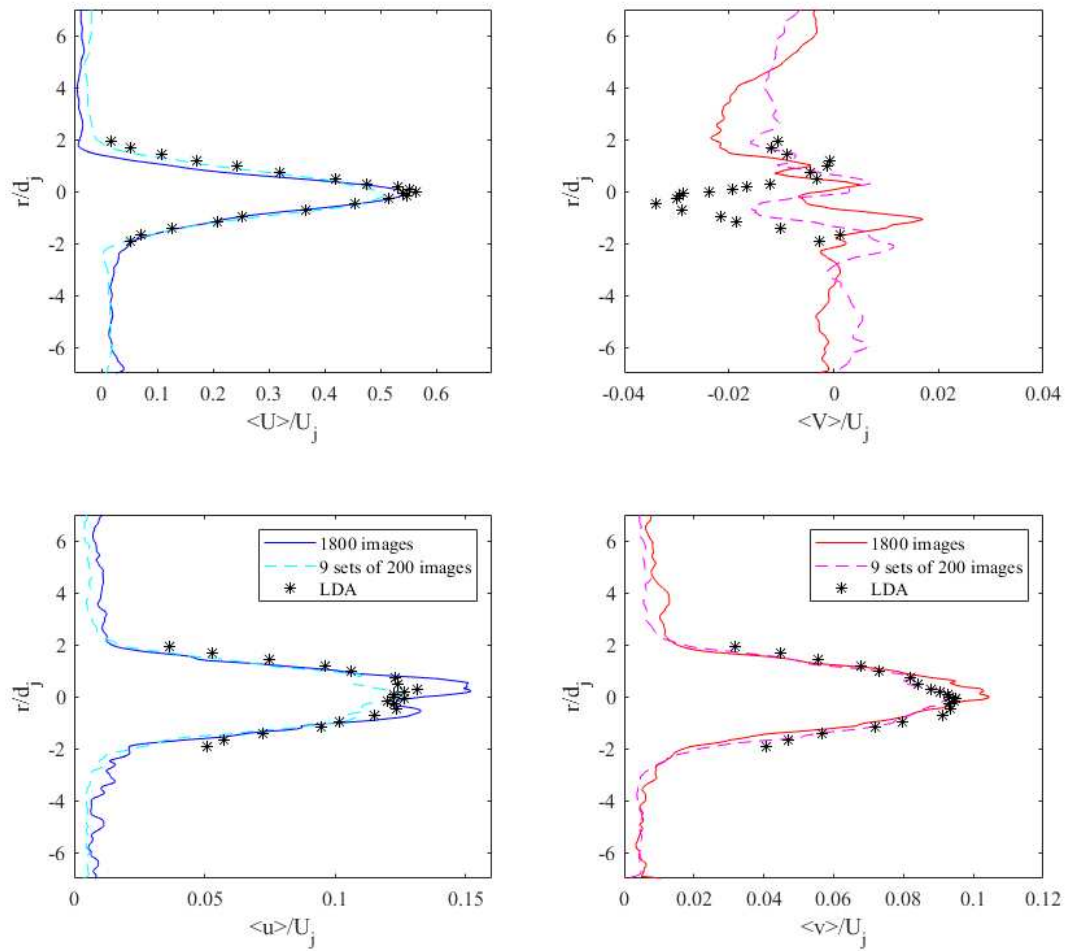


Figure A-24: Average streamwise and vertical velocity profiles for consecutive images and sets of 200 images of PIV and LDA measurements along the vertical profile for SP/SF at 500 Hz &  $DT = 300\mu s$ .

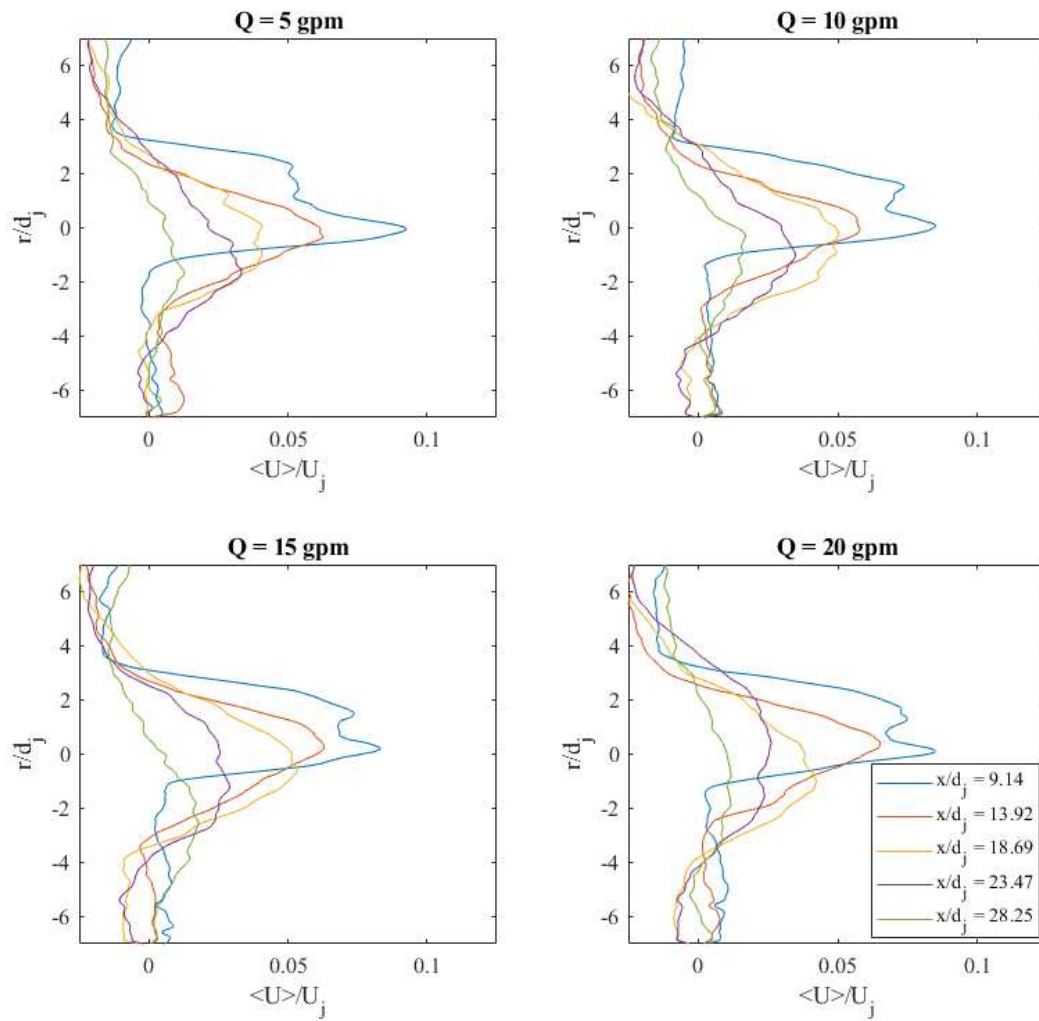


Figure A-25: Streamwise velocity profiles downstream of RPM wall with  $L = 4.78d_j$ .

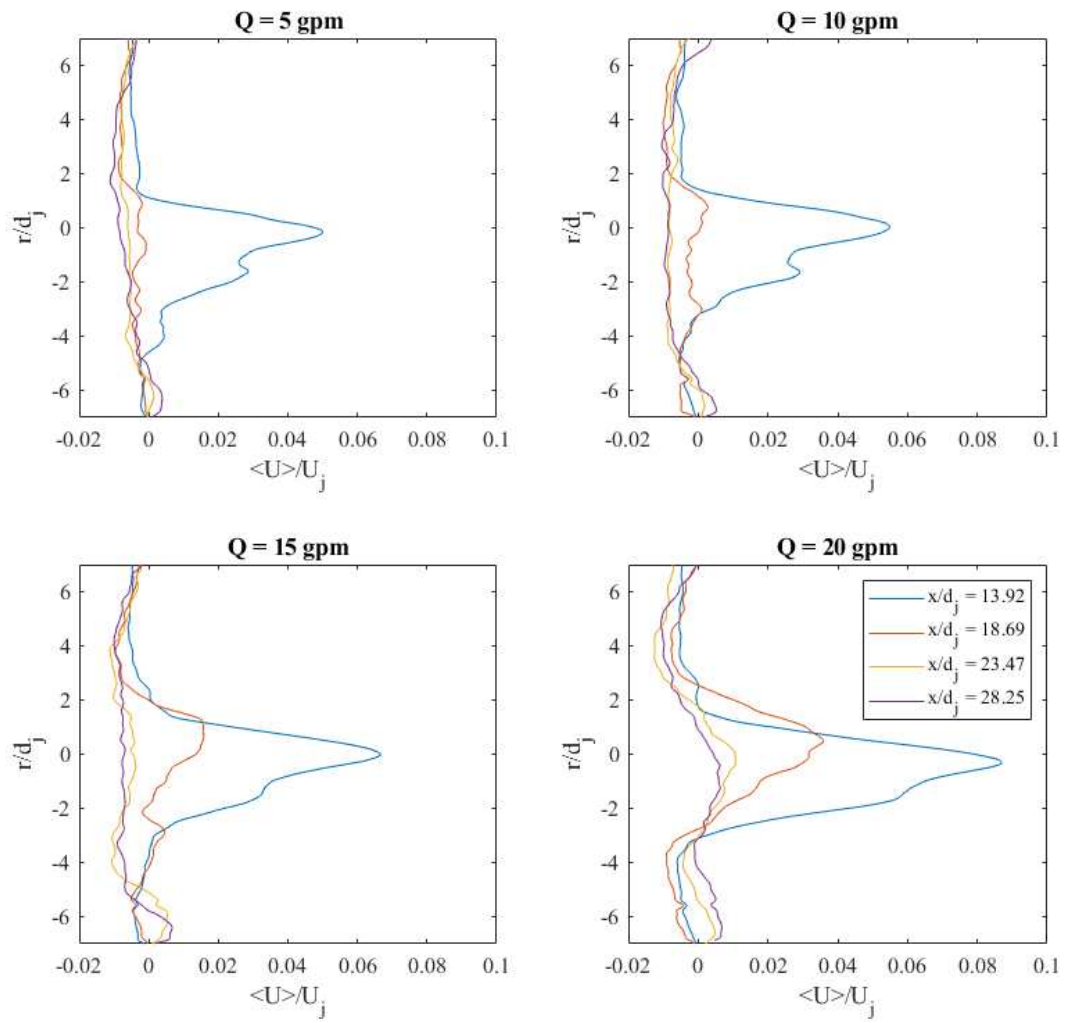


Figure A-26: Streamwise velocity profiles downstream of RPM wall with  $L = 7.17d_j$ .

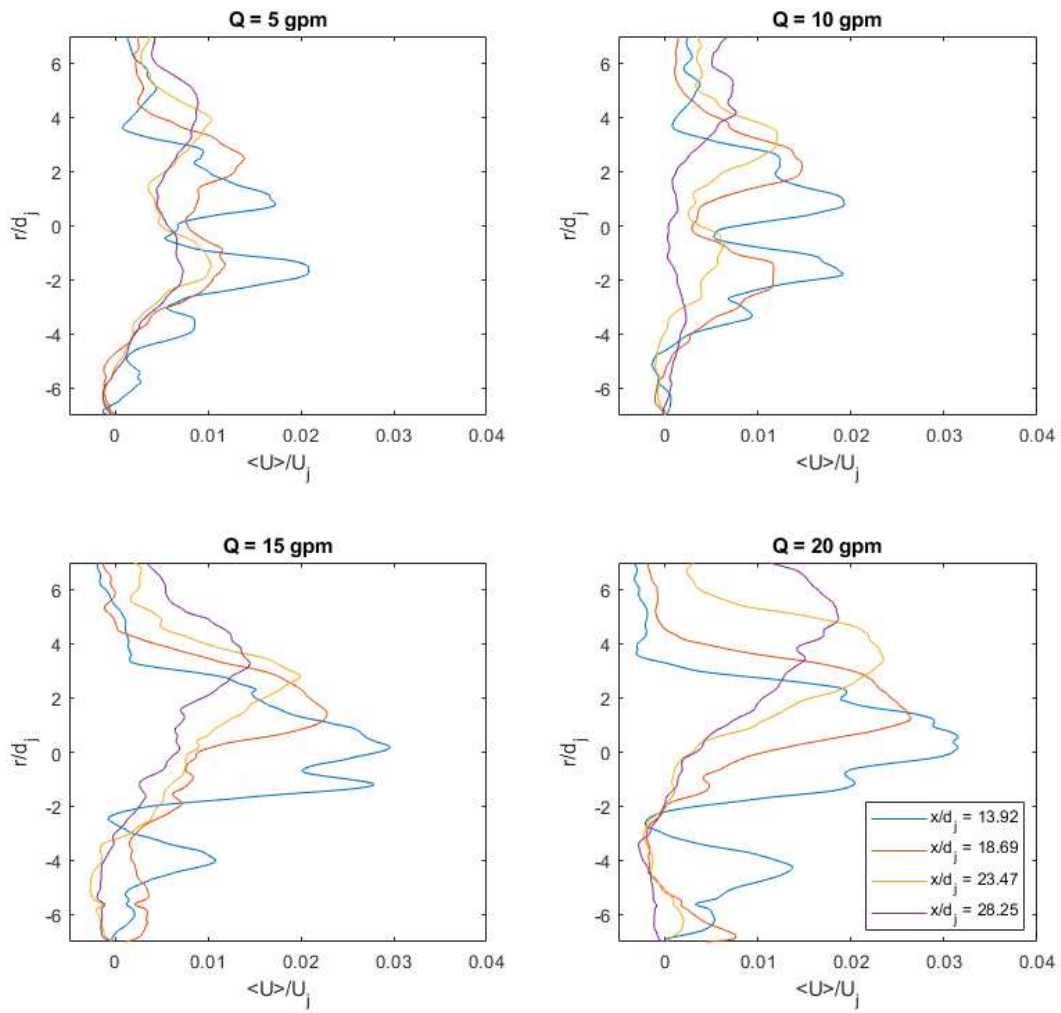


Figure A-27: Streamwise velocity profiles downstream of RPM wall with  $L = 9.56d_j$ .

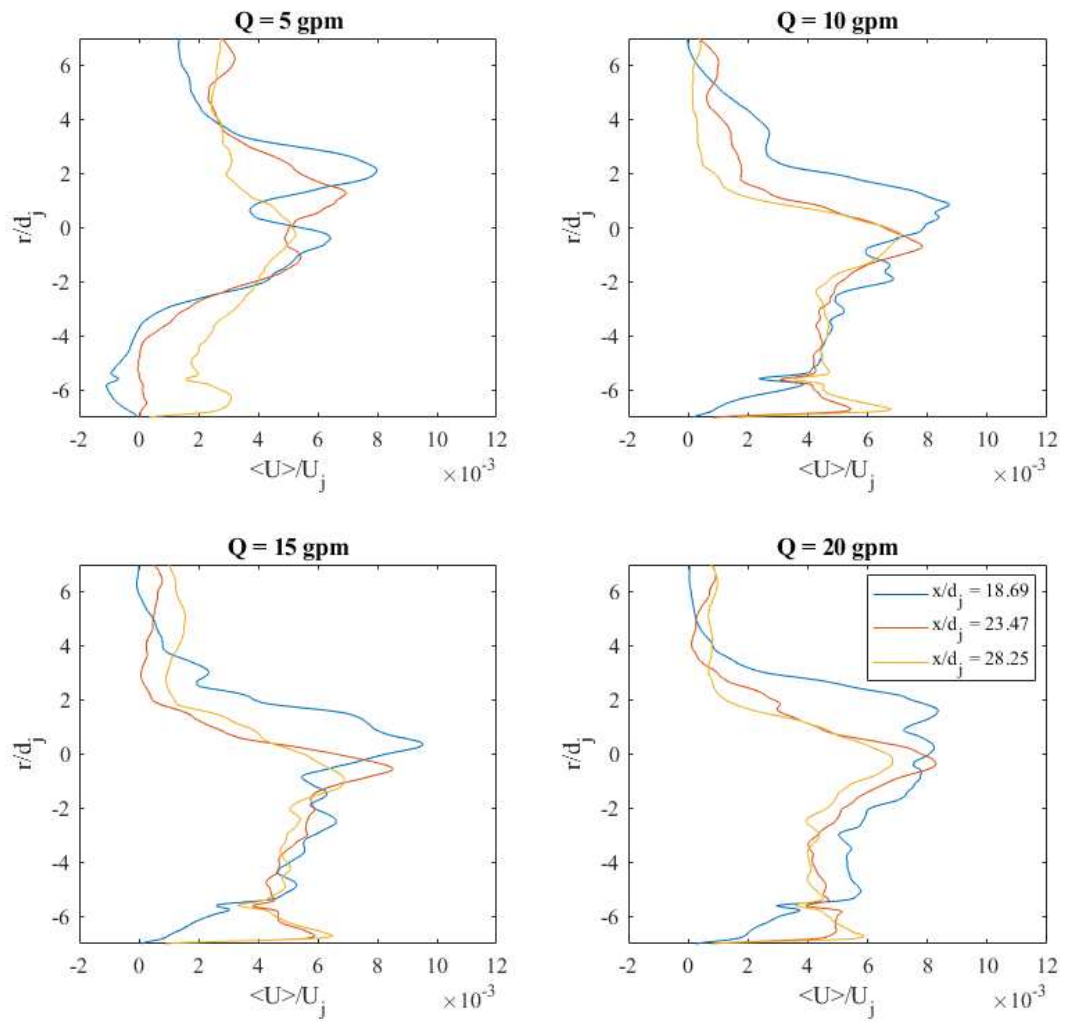


Figure A-28: Streamwise velocity profiles downstream of RPM wall with  $L = 11.94d_j$ .

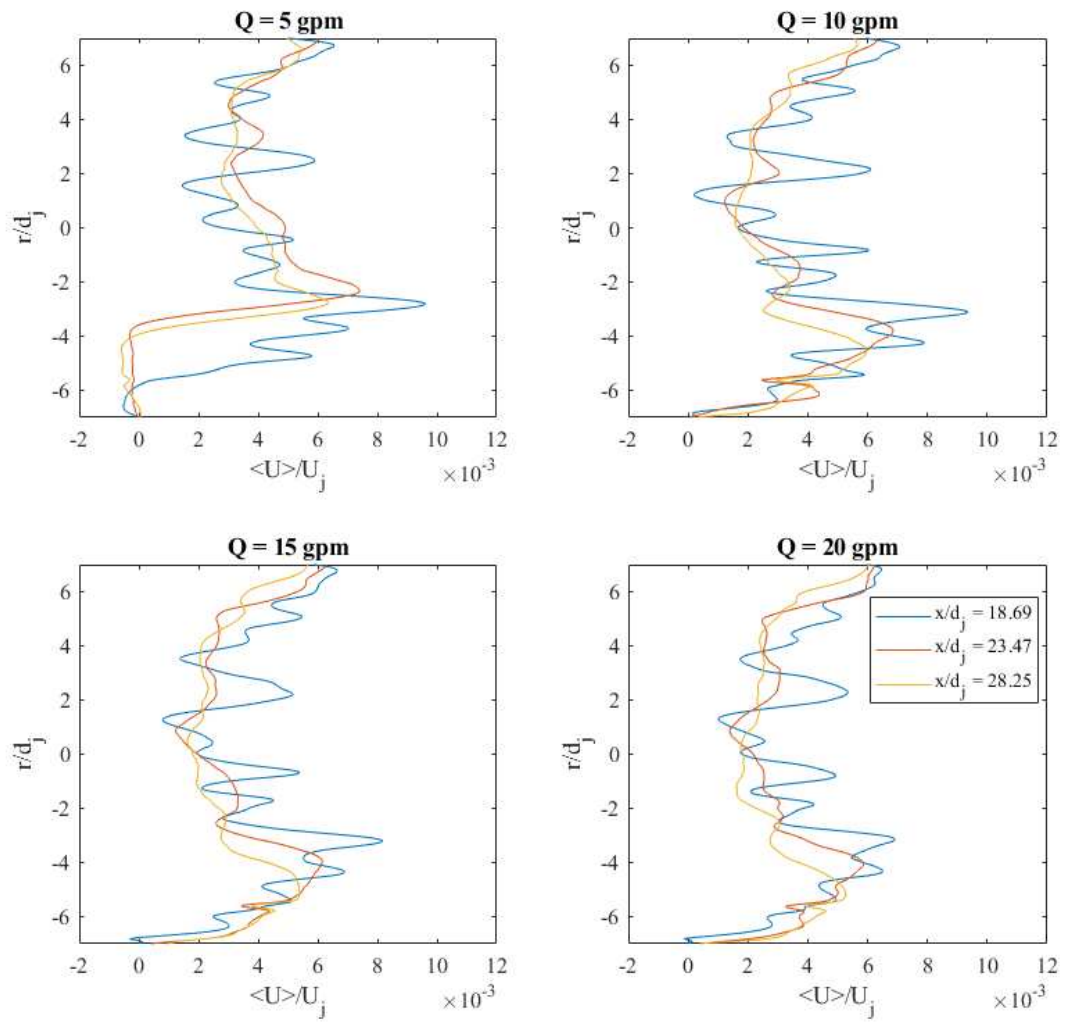


Figure A-29: Streamwise velocity profiles downstream of RPM wall with  $L = 14.33d_j$ .

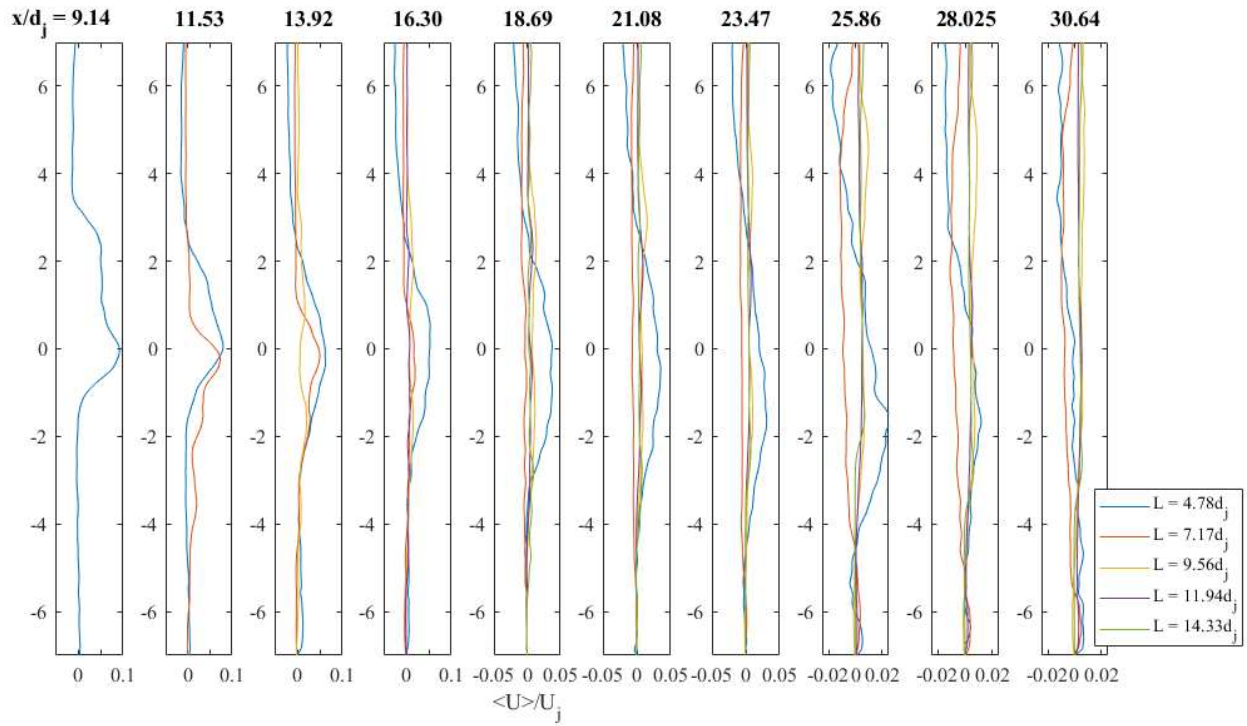


Figure A-30: Streamwise Velocities downstream of various RPM walls at 5 gpm.

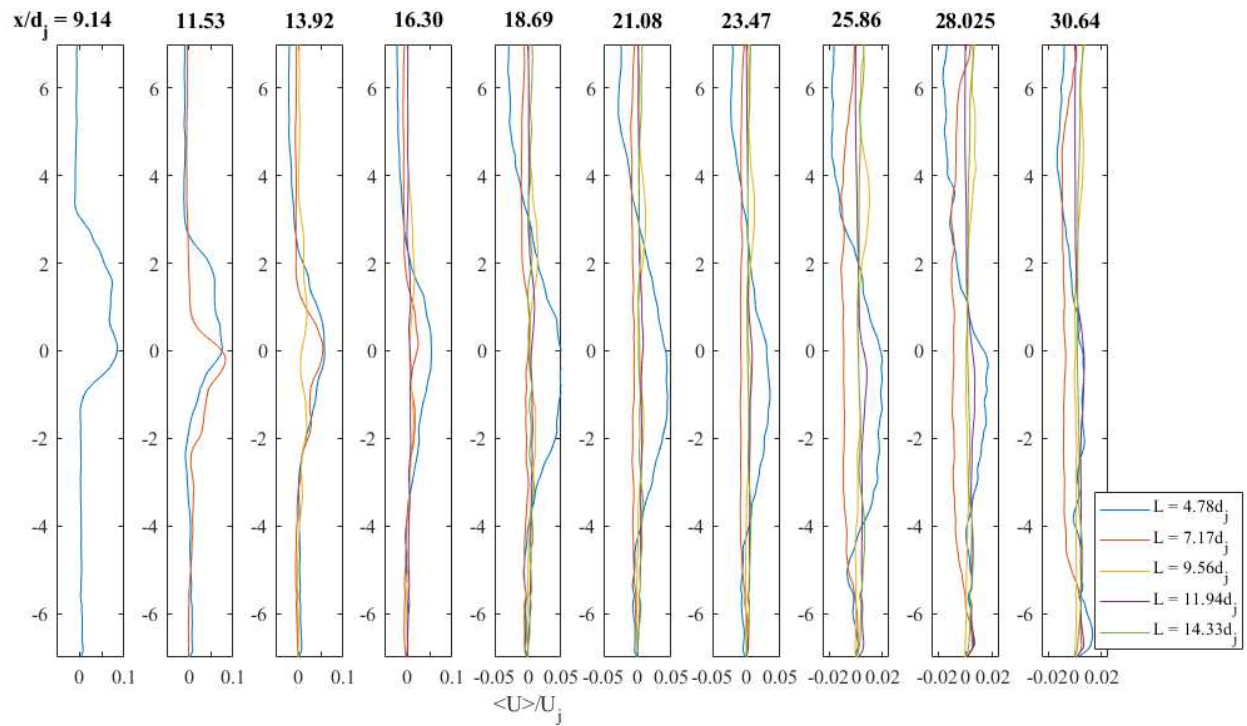


Figure A-31: Streamwise Velocities downstream of various RPM walls at 10 gpm.

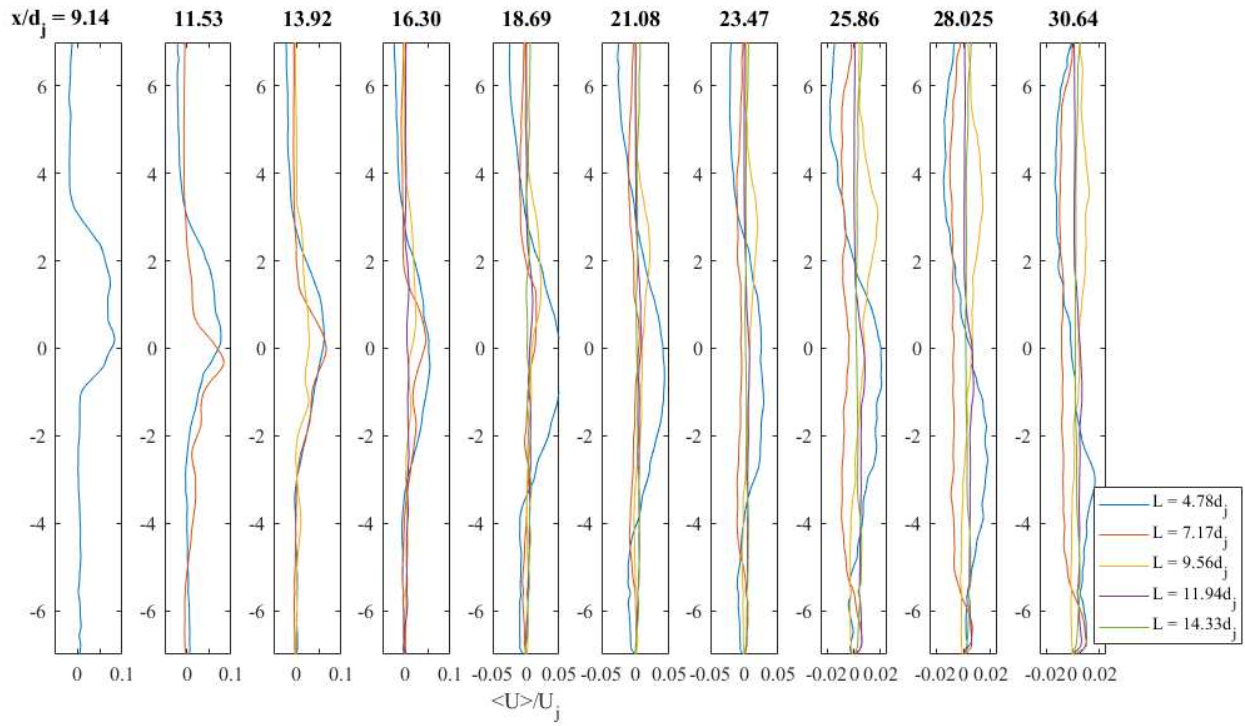


Figure A-32: Streamwise Velocities downstream of various RPM walls at 15 gpm.

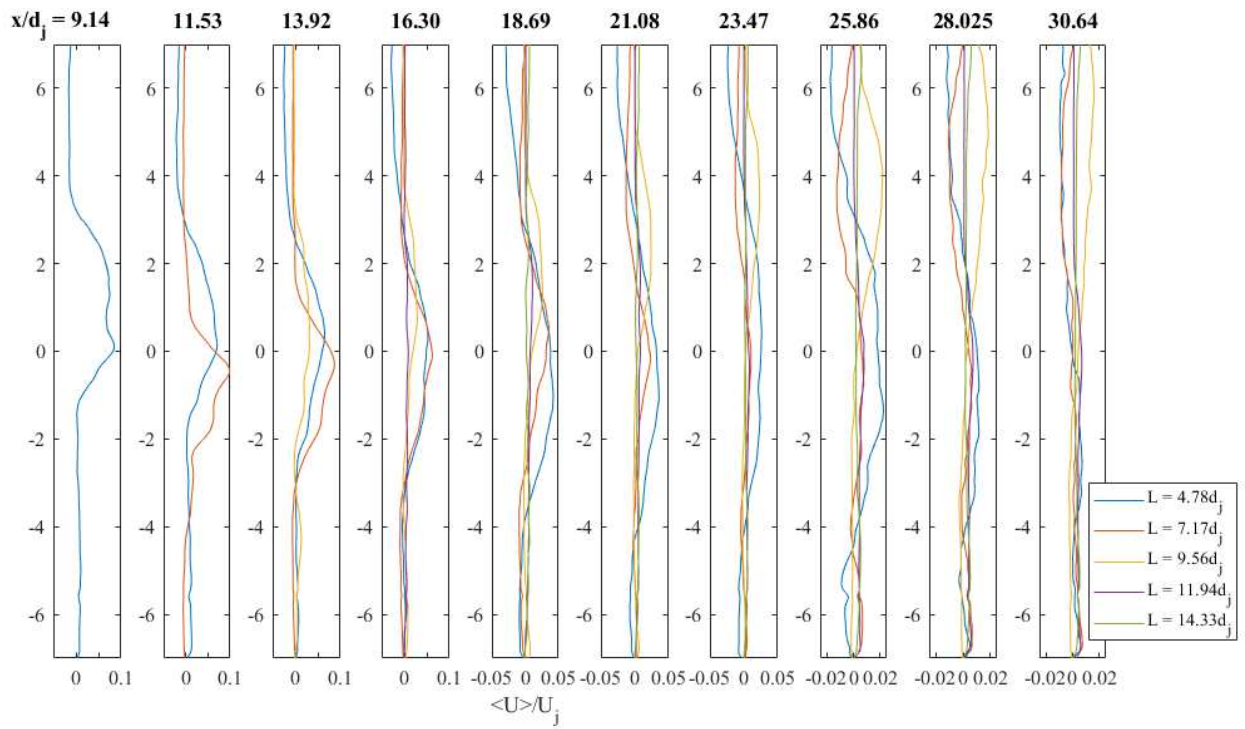


Figure A-33: Streamwise Velocities downstream of various RPM walls at 20 gpm.

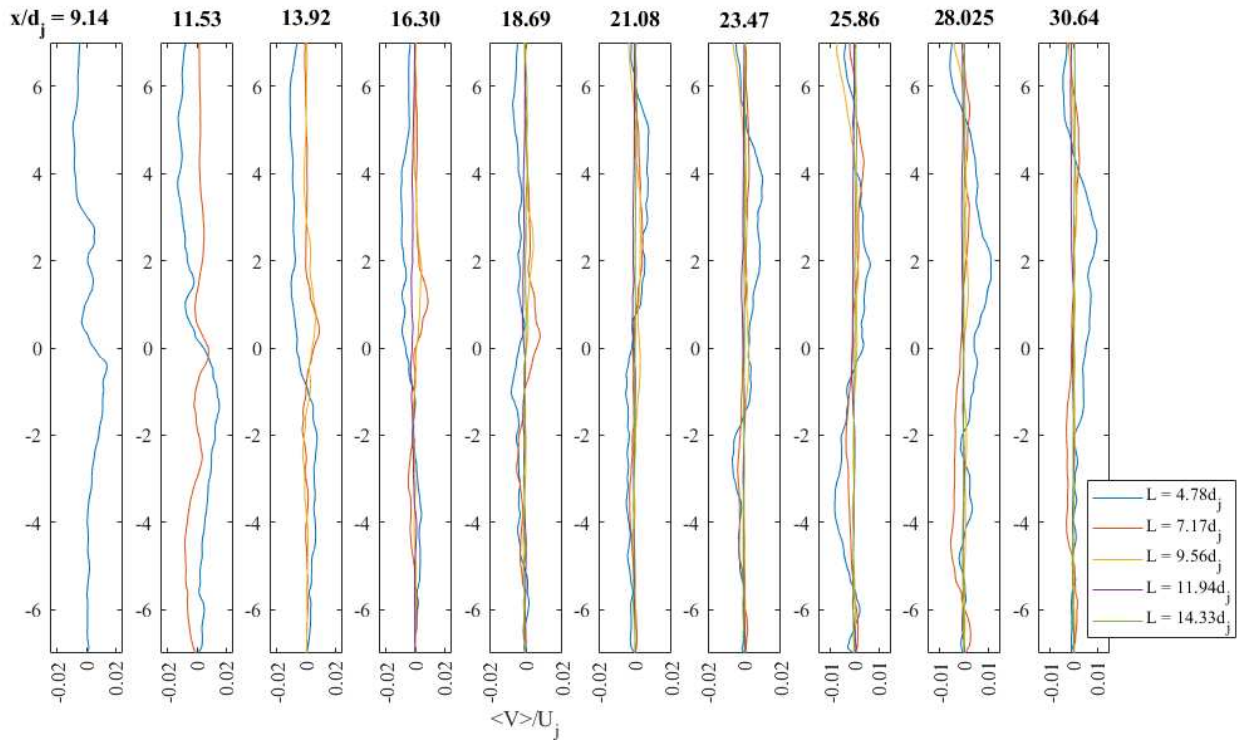


Figure A-34: Lateral Velocities downstream of various RPM walls at 5 gpm.

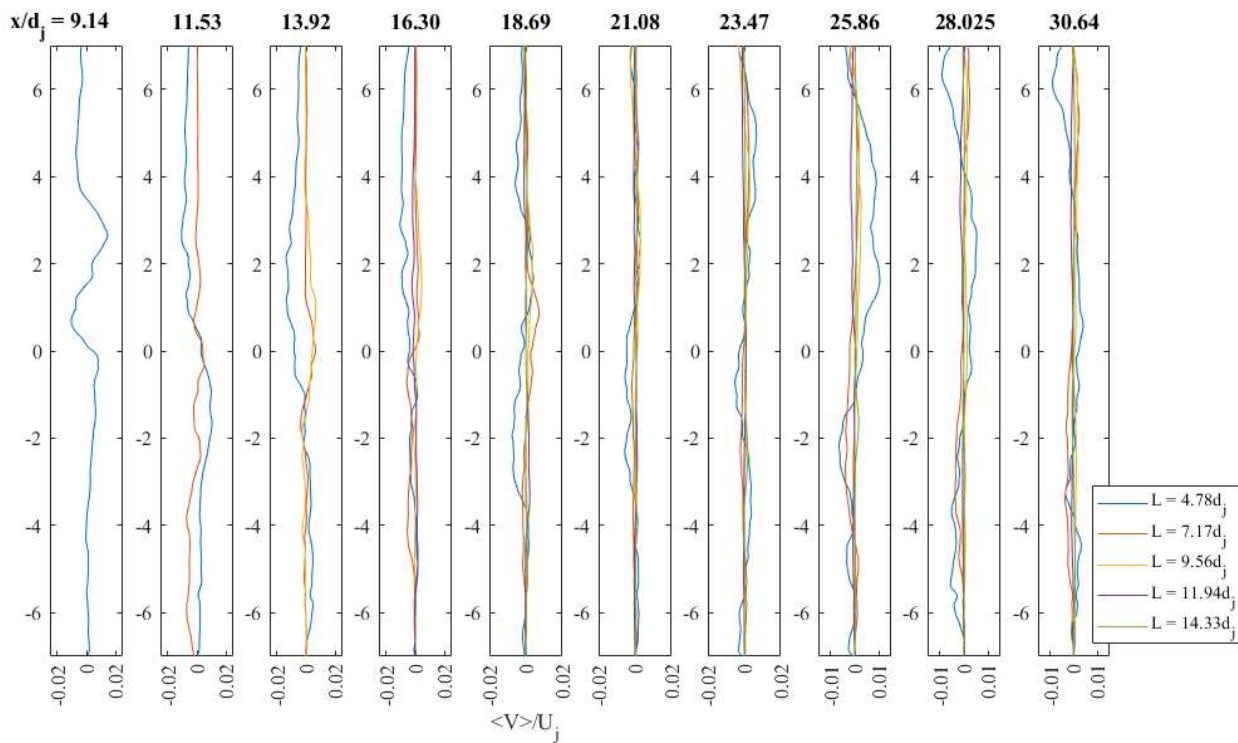


Figure A-35: Lateral Velocities downstream of various RPM walls at 10 gpm.

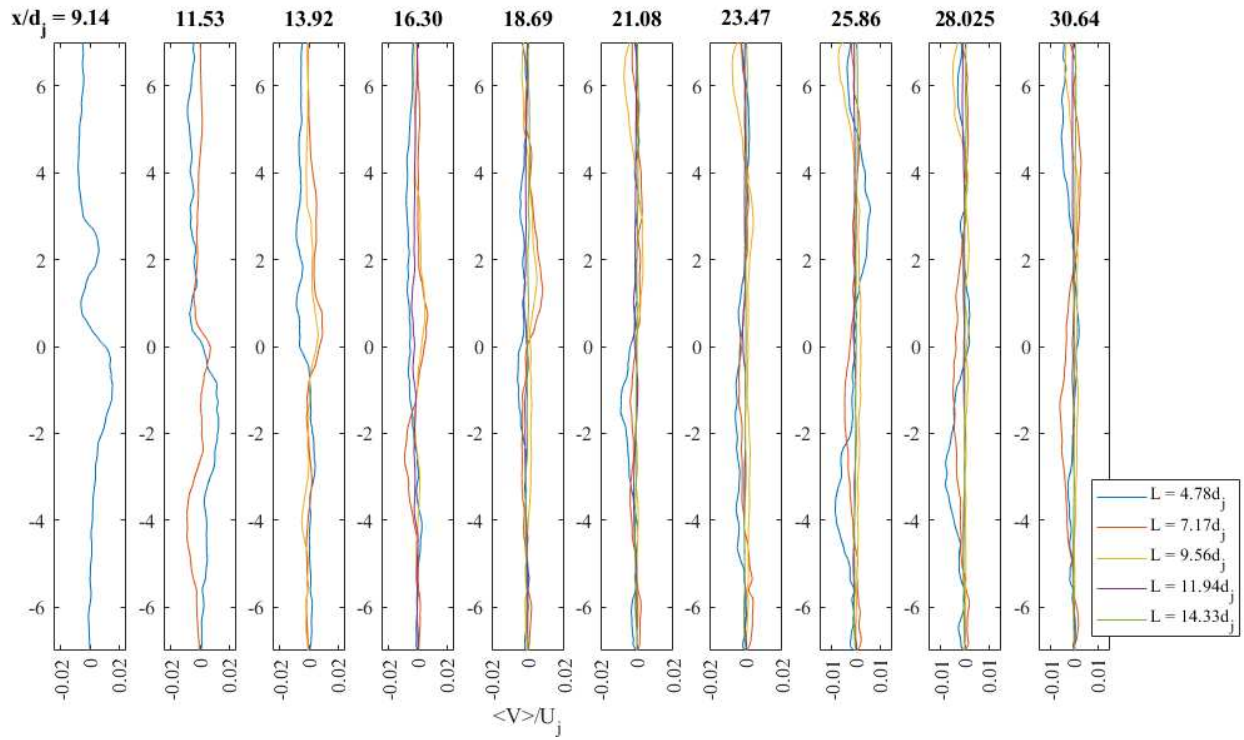


Figure A-36: Lateral Velocities downstream of various RPM walls at 15 gpm.

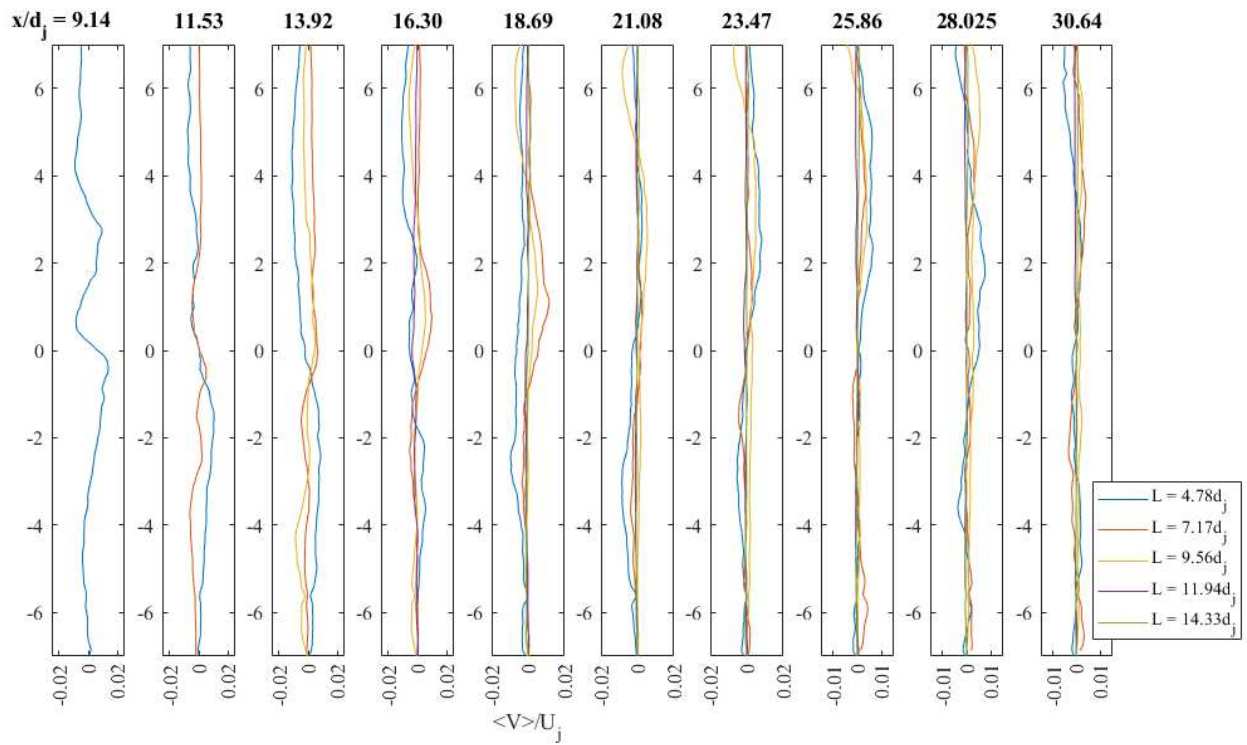


Figure A-37: Lateral Velocities downstream of various RPM walls at 20 gpm.

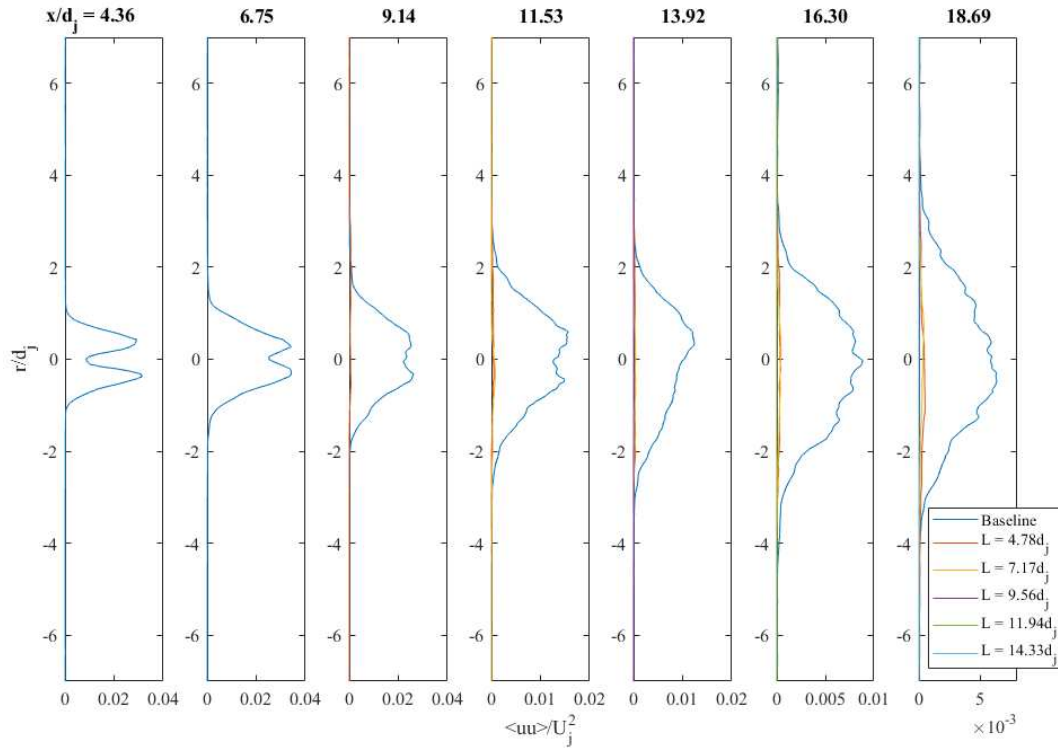


Figure A-38: Normalized streamwise normal stresses for  $Q = 20$  gpm. Note the  $\langle uu \rangle / U_j^2$  scales decrease from left to right.

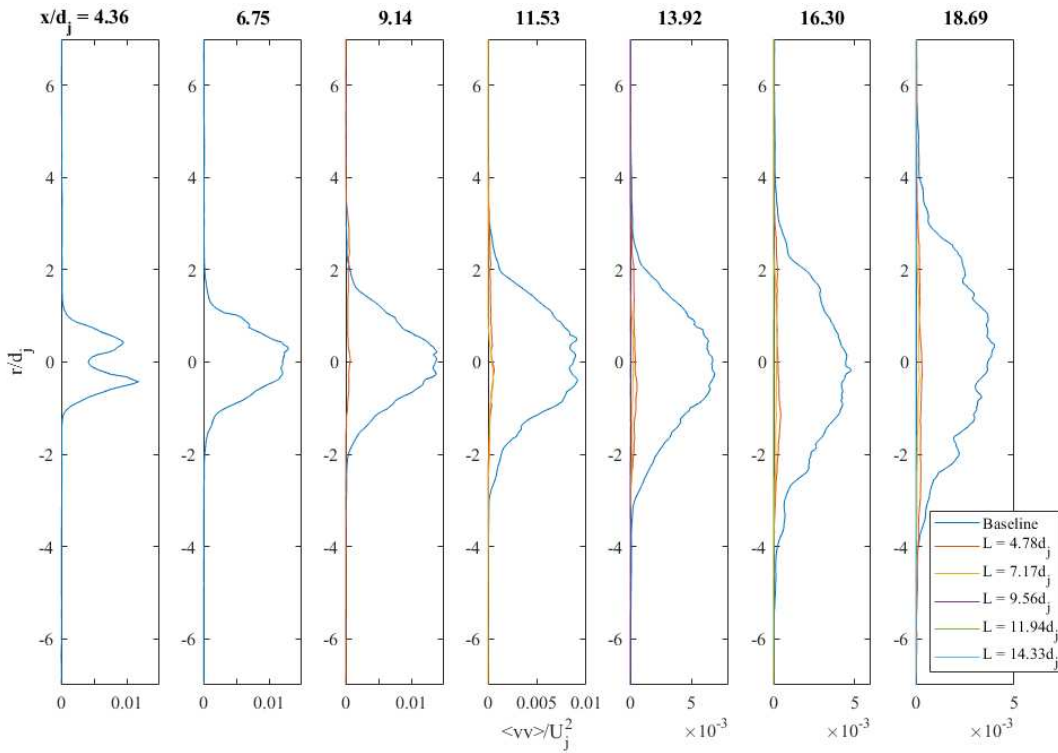


Figure A-39: Normalized lateral normal stresses for  $Q = 20$  gpm. Note the  $\langle vv \rangle / U_j^2$  scales decrease from left to right.

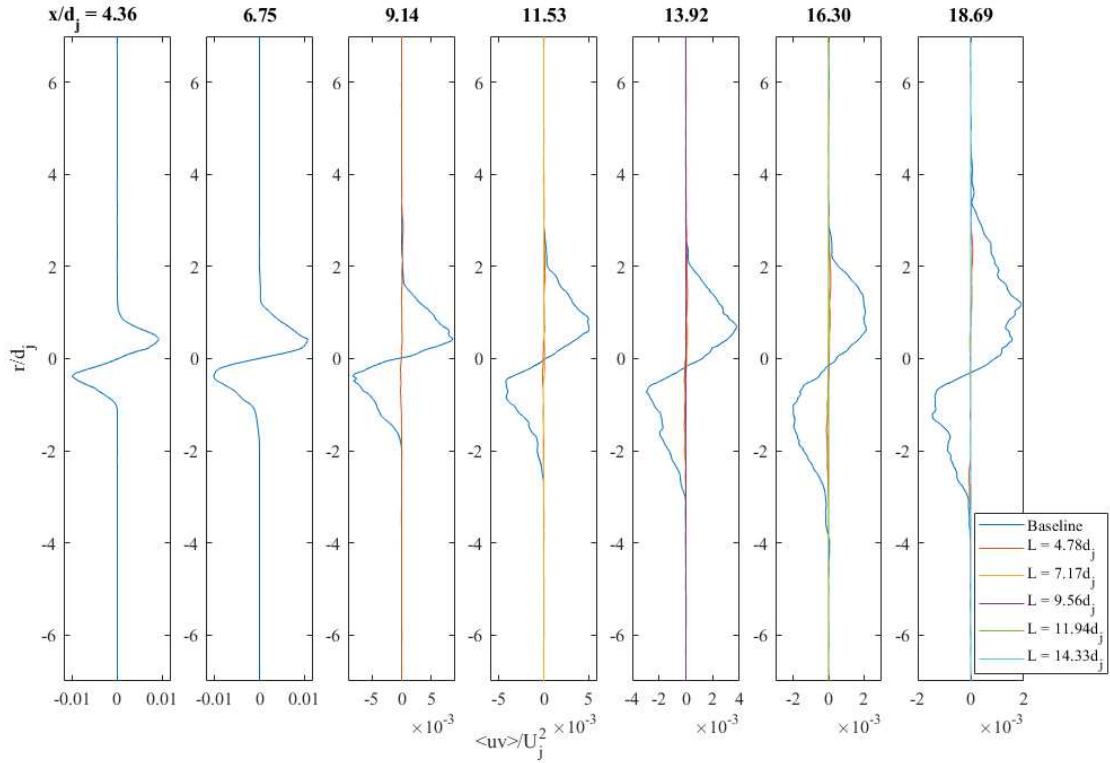


Figure A-40: Normalized Reynolds shear stresses for  $Q = 20$  gpm. Note the  $\langle uv \rangle / U_j^2$  scales decrease from left to right.

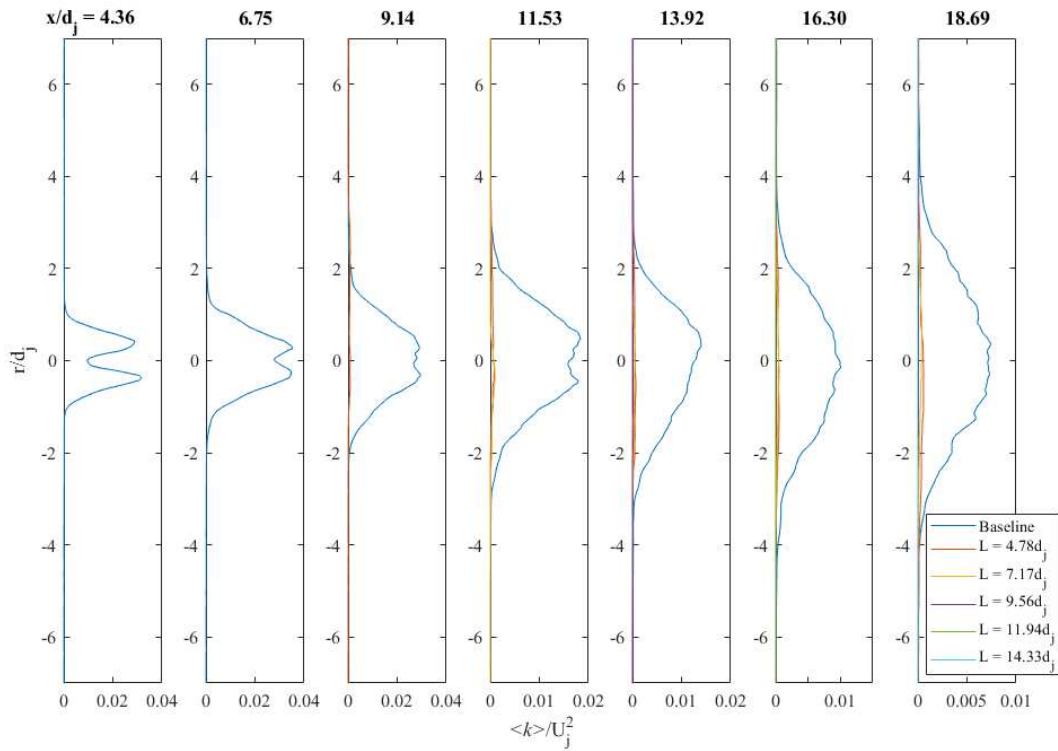


Figure A-41: Normalized turbulent kinetic energy for  $Q = 20$  gpm. Note the  $\langle k \rangle / U_j^2$  scales decrease from left to right.

## APPENDIX B

### Supplemental Materials for Efficiency Gain and Energy Loss Study

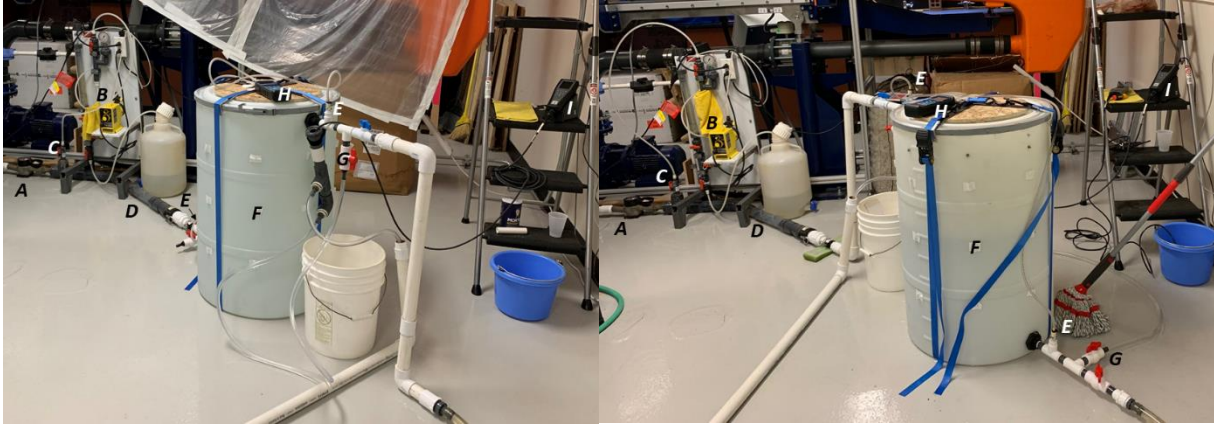


Figure B-1: Experimental set-up for an energy loss versus baffling efficiency gain study (BI/TO left; TI/BO right); A = flow meter, B = dosing pump, C = dosing injection point, D = static mixer, E = pressure tap, F = 55-gallon tank, G = tracer sampling point, H = digital manometer, I = conductivity meter

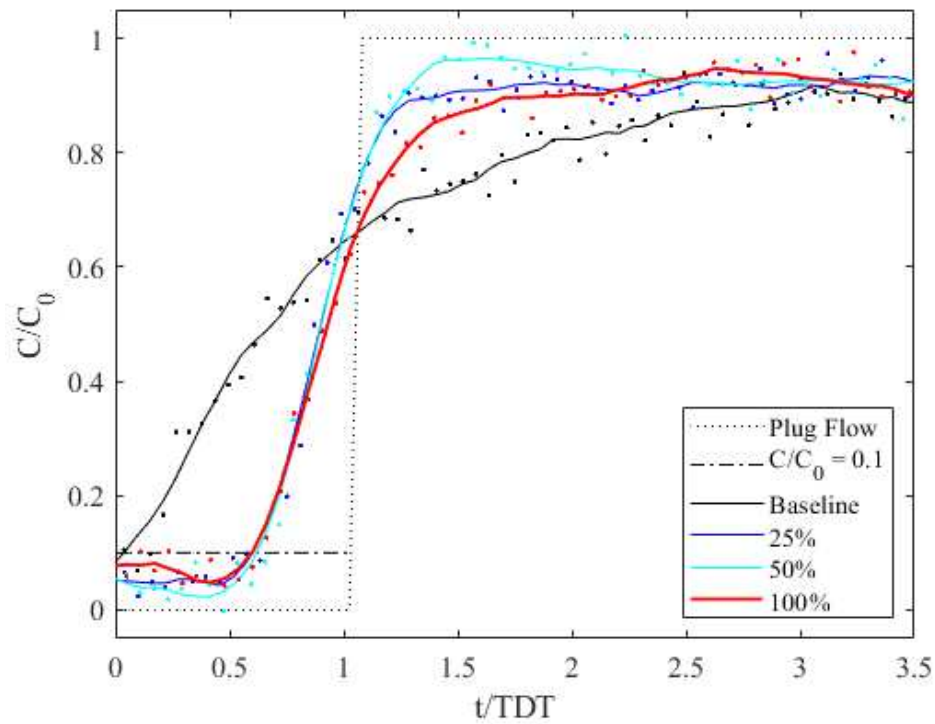


Figure B-2: Average RTD curves of various %RPM for 5 gpm ( $Re_{jet} = \sim 20,700$ ) for the BI/TO configurations.

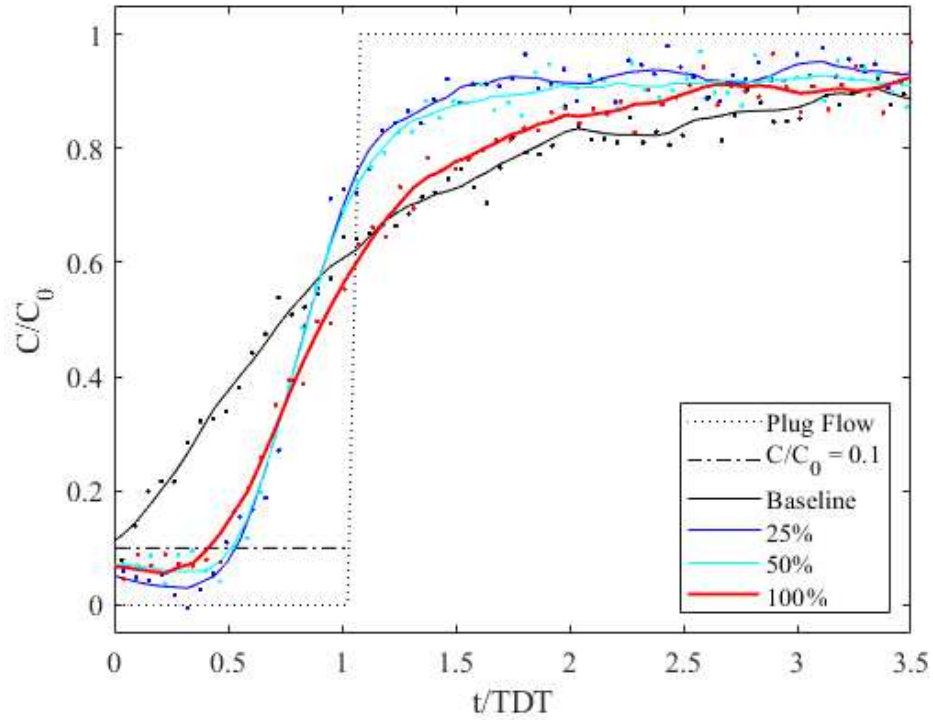


Figure B-3: Average RTD curves of various %RPM for 5 gpm ( $Re_{jet} = \sim 34,600$ ) for the BI/TO configurations.

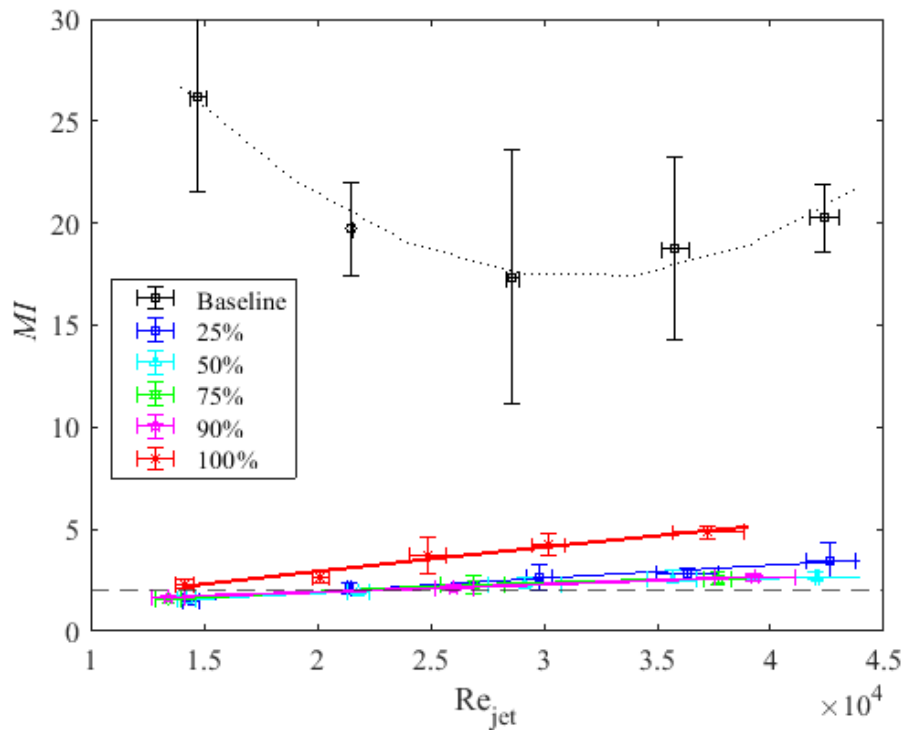


Figure B-4: Graph of MI of varying %RPM as a function of turbulent jet Reynolds number ( $Re_{jet}$ ) for the BI/TO configurations.

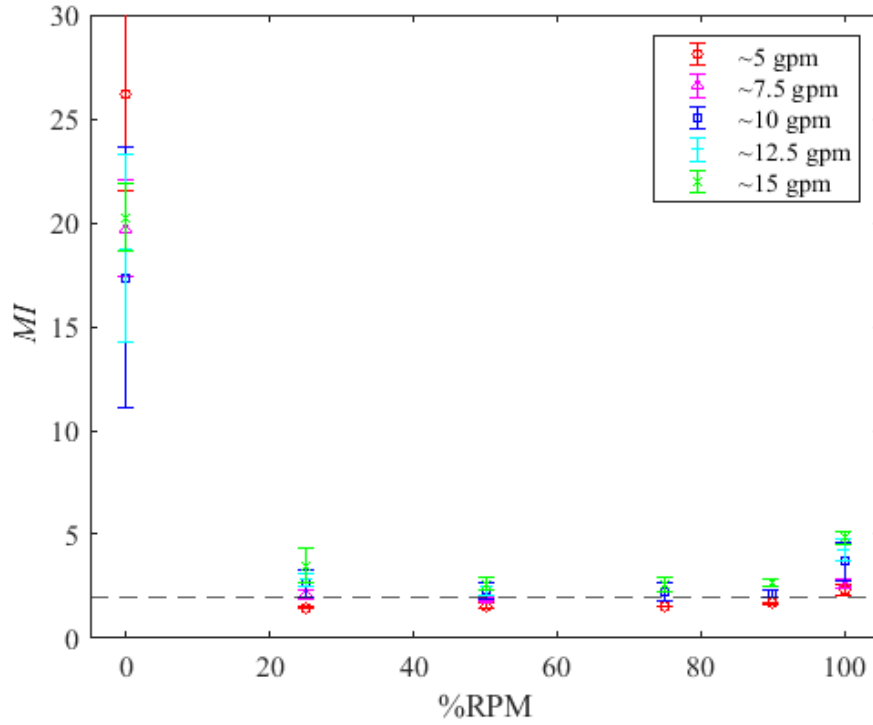


Figure B-5: Graph of MI of various flow rates as a function of % RPM for the BI/TO configurations.

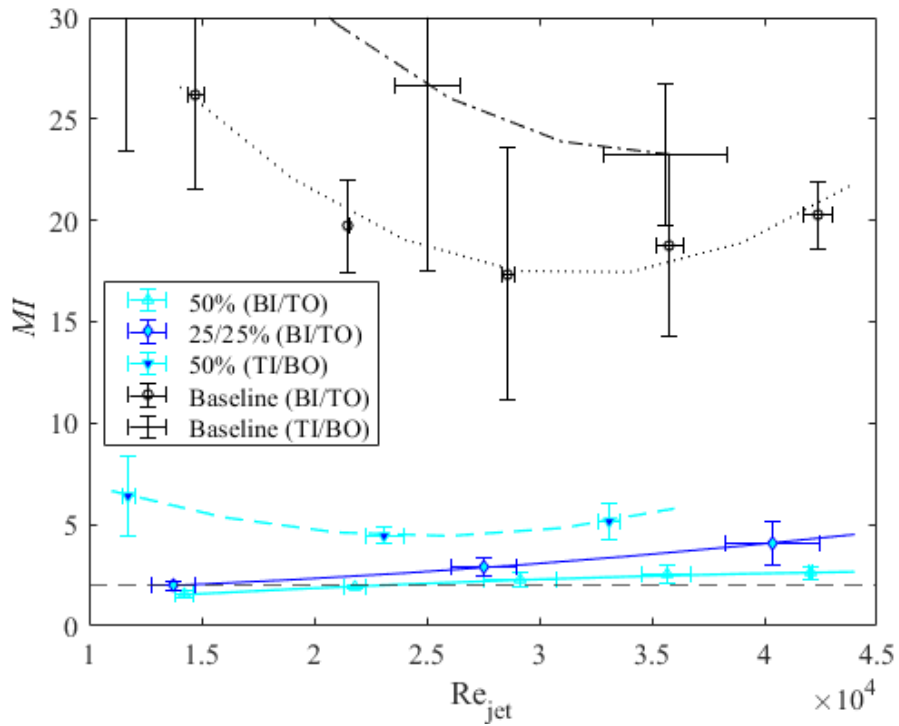


Figure B-6: Graph of MI compared to various turbulent jets of different configurations of %RPM = 50%; secured near inlet [50% (BI/TO)], split between inlet & outlet [25/25% (BI/TO)], and reverse direction [50% (TI/BO)].

Table B-1: Results of Kolmogorov-Smirnov test for RTD curves for the BI/TO configurations.

Q	%RPM	25%			50%			75%			90%			100%		
		h	p	ks	h	p	ks	h	p	ks	h	p	ks	h	p	ks
5 gpm	Baseline	1	0.0191	0.2346	1	0.0022	0.2840	1	0.0191	0.2346	1	0.0022	0.2840	0	0.1101	0.1852
	25%				0	0.1600	0.1728	0	0.1600	0.1728	1	0.0068	0.2593	0	0.5399	0.1235
	50%							0	0.1101	0.1852	1	0.0308	0.2222	0	0.1600	0.1728
	75%										1	0.0116	0.2469	0	0.1600	0.1728
	90%													0	0.0739	0.1975
7.5 gpm	Baseline	1	$5.5 \times 10^{-7}$	0.4507	1	$3.4 \times 10^{-11}$	0.5775							1	$2.0 \times 10^{-4}$	0.3521
	25%				1	$8.2 \times 10^{-6}$	0.4085							1	0.0459	0.2254
	50%													1	$2.0 \times 10^{-4}$	0.3521
10 gpm	Baseline	1	$4.3 \times 10^{-5}$	0.3803	1	$2.0 \times 10^{-4}$	0.3521	1	$4.3 \times 10^{-5}$	0.3803	1	$2.1 \times 10^{-7}$	0.4648	0	0.0724	0.2113
	25%				1	$1.4 \times 10^{-6}$	0.4366	1	$4.3 \times 10^{-5}$	0.3803	1	$3.4 \times 10^{-6}$	0.4225	1	0.0282	0.2394
	50%							1	$1.9 \times 10^{-5}$	0.3944	1	$2.9 \times 10^{-8}$	0.4930	1	0.0168	0.2535
	75%										0	0.5889	0.1268	1	$4.3 \times 10^{-5}$	0.3803
	90%													1	$1.4 \times 10^{-6}$	0.4366
12.5 gpm	Baseline	1	$1.0 \times 10^{-8}$	0.5070	1	$3.4 \times 10^{-6}$	0.4225							1	0.0098	0.2676
	25%				1	0.0055	0.2817							1	$8.2 \times 10^{-6}$	0.4085
	50%													1	0.0282	0.2394
15 gpm	Baseline	1	0.0168	0.2535	1	$2.0 \times 10^{-4}$	0.3521	1	$8.2 \times 10^{-4}$	0.3239	1	$2.0 \times 10^{-4}$	0.3521	1	0.0459	0.2254
	25%				1	0.0030	0.2958	1	$8.2 \times 10^{-4}$	0.3239	1	$1.9 \times 10^{-5}$	0.3944	0	0.1111	0.1972
	50%							1	0.0016	0.3099	1	$2.0 \times 10^{-4}$	0.3521	0	0.0724	0.2113
	75%										0	0.5889	0.1268	1	0.0055	0.2817
	90%													1	$4.1 \times 10^{-4}$	0.3380

\*Note: yellow shading represents a rejection of the null hypothesis at 5% significance

Table B-2: Results of Kolmogorov-Smirnov test for RTD curves of different %RPM = 50% configurations.

Q	%RPM	Baseline (TI/BO)			50% (BI/TO)			25/25% (BI/TO)			50% (TI/BO)		
		h	p	ks	h	p	ks	h	p	ks	h	p	ks
5	Baseline (BI/TO)	1	0.0483	0.2099	1	0.0022	0.2840	1	0.0308	0.2716			
	50% (BI/TO)							1	0.0039	0.2222	1	$6.8 \times 10^{-7}$	0.4198
	25/25% (BI/TO)										1	$2.7 \times 10^{-10}$	0.5185
	50% (TI/BO)	0	0.3116	0.1481									
10	Baseline (BI/TO)	0	0.1327	0.1852	1	$2.0 \times 10^{-4}$	0.3521	1	$1.3 \times 10^{-5}$	0.3883			
	50% (BI/TO)							1	$1.6 \times 10^{-6}$	0.4217	0	0.1785	0.1748
	25/25% (BI/TO)										1	0.0022	0.2840
	50% (TI/BO)	1	0.0191	0.2346									
15	Baseline (BI/TO)	0	0.9956	0.0657	1	$2.0 \times 10^{-4}$	0.3521	1	0.0158	0.2472			
	50% (BI/TO)							0	0.1327	0.1852	1	0.0020	0.2956
	25/25% (BI/TO)										0	0.2263	0.1605
	50% (TI/BO)	1	0.0483	0.2099									

\*Note: yellow shading represents a rejection of the null hypothesis at 5% significance